DISSERTATION

EXPERIMENTAL REALIZATION OF TWO-ISOTOPE COLLISION-ASSISTED ZEEMAN

COOLING

Submitted by

Mathew Hamilton

Department of Physics

In partial fulfillment of the requirements

For the Degree of Doctor of Philosophy

Colorado State University

Fort Collins, Colorado

Fall 2013

Doctoral Committee:

    Advisor: Jacob Roberts

    Stephen Lundeen
    Martin Gelfand
    Randy Bartels

ABSTRACT

EXPERIMENTAL REALIZATION OF TWO-ISOTOPE COLLISION-ASSISTED ZEEMAN

COOLING

The work presented in this thesis focuses on the demonstration and initial evaluation of a novel non-evaporative cooling method called collision-assisted Zeeman cooling. For this realization, an ultracold gas consisting of a mixture of ^{87}Rb and ^{85}Rb was used. Cooling was accomplished through interisotope inelastic spin-exchange collisions that converted kinetic energy into magnetic energy. Continual optical pumping spin polarized the ^{85}Rb which ensured that only kinetic energy reducing collisions occurred and the scattered pump photons carried entropy out of the system. Thus, cooling of the ultracold gas can be achieved without requiring the loss of any atoms in order to do so. This represents a theoretical advantage over forced evaporative cooling, which is the current state-of-the-art cooling technique in most experiments.

This thesis discusses the details of collision-assisted Zeeman cooling, as well as how the theory of the technique has been extended from cooling a single species to cooling with two species. There are many predicted advantages from using two rather than one species of atom in this type of cooling: greater flexibility in finding favorable spin-exchange collision rates, easier requirements on the magnetic fields that must be used, and an additional means to mitigate reabsorption (the primary limitation in many if not most non-evaporative cooling techniques).

The experimental considerations needed to prepare a system that simultaneously trapped two isotopes to be able to perform collision-assisted Zeeman cooling are discussed. Because this cooling scheme is highly reliant on the initial conditions of the system, a focused experiment examining the loading of the optical trap with both isotopes of Rb was conducted and the results of that experiment are described here.

The first experimental observations of spin-exchange collisions in an ultracold gas mixture of Rb are described as a part of this work. The experiments where collision-assisted Zeeman cooling were demonstrated are then described and evaluated. In this first implementation of the cooling technique the initial densities were too low and optical-pump-induced heating and loss too high for achieving the full predicted performance of the cooling technique. Through additional modeling, these limitations were understood and the necessary improvements for the next iteration of CAZ cooling experiments are laid out at the end of this work.

ACKNOWLEDGMENTS

All of the work presented within this thesis was accomplished through the efforts of many. Without the contributions and commitments of others this endeavor would not have been possible. As such, I would like to take a moment to thank those who have made particularly significant contributions to the project.

Above all I would like to thank my advisor, Jacob Roberts, whose dedication has made this all possible. His intelligence and knowledge, which extends beyond the academic, has been invaluable for my graduate education. From explaining complex physical and experimental phenomena related to research, to the sometimes colorful lunch-time conversations covering all walks of life, I have been sincerely grateful to have him as a resource and friend. In addition, Jake's patience and compassion cannot be overstated. I know I have contributed my fair share of nonsense to the lab, and Jake's ability to remain good natured as his students learn has been exceptional. I am especially grateful for his support and tolerance while I attempted graduate school and starting a new family at the same time. I very much appreciate the time we have had working together.

There have been a fair number of individuals, including graduate and undergraduate, who have also aided this research in essential ways. While I do appreciate all of their contributions, there are a few that I would especially like to acknowledge. First off, Rebekah Ferrier and Anthony Gorges, the two primary graduate students to work on the apparatus with me. Tony was responsible for a large amount of the preparation and construction of the experiment (as well as being a typical catalyst for some of those colorful lunch conversations). And although he inadvertently drenched me while we were working with the circulated water system, he did an excellent job with the project for which I am most grateful. Becky has taken the reins of the experiment since the conclusion of the work presented here, which she was integral to the

TABLE OF CONTENTS

asymmetry in the m-state populations. Thus there are more atoms in either the $m_F = 1$ or the $m_F = -1$ compared with the at rest situation. Note that these states are more sensitive to one circularly polarized state than the other. The resulting imbalance in scattering events inhibits atomic motion and causes cooling.

Figure 1.5: Polarization Gradient Cooling: Sisyphus.
In Sisyphus cooling, **(a)** two counter-propagating linearly polarized (red-detuned from the $F' = 3/2$ state) laser beams create a polarization gradient of varying ellipticity. Individual points along the path change smoothly between linear and alternating circular polarizations. **(b)** For an atom with an $F = 1/2$ ground state, the two magnetic sub-levels will be degenerate in regions of linear polarization but separated in regions of circularly polarized light. Thus an atom moving through the light field (from left to right in the figure) must climb a potential hill (black arrow) and lose kinetic energy every time its energy level switches from being the lower to the higher of the two. When an atom is in the higher of the two energy levels, it will be pumped into the lower (red arrows), with the scattered photon carrying away entropy. This is because the polarized light pumps atoms to the lower of the two ground state levels, as shown in panels **(c)** and **(d)**

Figure 1.6: Concept Behind a Magneto-Optical Trap (MOT).
(a) The one dimensional magnetic field gradient shown as light blue arrows, will cause a shift in the $F = 1$ excited state magnetic sub-levels of an atom. These atoms are in the $F = 0$ ground state and subjected to a red-detuned optical molasses shown as red arrows. The red dotted line represents the detuned cooling laser transition. The polarization of the cooling light and direction of the magnetic field are chosen such that atoms far from center become closer to resonance of one of the lasers such that the imbalance of photon scatters acts as a restoring force, trapping the atoms in space. **(b)** For more complex atoms such as 87Rb in the $F = 2$ ground state, the idea still holds. For example, an atom in the region to the left and in the $m_F = 2$ state experiences more photon scattering from the σ^+ polarized beam which is closer to resonance than the σ^- polarized beam, pushing it toward center. This is true for every magnetic sub-level as shown for the right side of the trap.

Figure 1.7: Cartoon of Evaporative Cooling.
On the left, atoms (white circles) confined in an atom trap, of trap depth d. The average kinetic energy of the atoms relative to d is indicated by the light blue line. On the right, thermal collisions have caused some atoms to loose energy and others to gain energy. If an atom has more energy than d (red circles), it is lost from the trap. Lost atoms have greater-than-average kinetic energy. Thus the atoms remaining in the trap have a lower average kinetic energy than before the loss, as indicated by the shift to the dark blue line. Evaporation continues until the average kinetic energy is approximately ten-percent of the trap depth.

Figure 1.8: Forced Evaporative Cooling in a Magnetic Trap.
Atoms (circles) are confined in a magnetic trap if in the m-state for the potential shown above, and expelled if in the m-state for the potential below. As atoms orbit the zero point of the trap's magnetic field on the left, more energetic atoms will enter regions of higher magnetic field where they can be selectively transitioned by a resonant RF field (purple) to the repulsive potential owing to the greater Zeeman shift of these atoms (green) compared to cooler ones in the cloud. After these atoms are transitioned (right) they are expelled from the trap (red). The average kinetic energy of the remaining atoms is reduced (dashed blue lines), and the RF field can be set (yellow) to expel progressively cooler atoms.

Chapter 1

Introduction

The ability to successfully cool atoms to micro-Kelvin temperatures is a relatively recent triumph of physics which has driven many efforts to better understand the quantum mechanical nature of our world. Although there exist multiple methods to efficiently cool atoms to this regime, there are still reasons to investigate new cooling techniques. By far, evaporative cooling [1,2] is the most successful means to cool atoms. Evaporative cooling is capable of achieving very low temperatures with relatively high atom cloud density. While evaporative cooling is very robust and experimentally straightforward to implement, it does suffer from some intrinsic drawbacks which leave room for improvement, foremost of which is the loss of atom number from the sample. In addition, a fair amount of experimental complexity is required for evaporative cooling to work. Also, in some situations, a long period of time is necessary for evaporative cooling to be effective. Not only is there interest in improving the speed and efficiency of cooling atoms, but whether or not it is possible to implement a cooling technique that performs on par with evaporative cooling is a valid physics challenge. Thus the study of new cooling techniques is an intriguing area of physics.

The work presented in this thesis focuses on the experimental realization and study of a novel atomic cooling technique called two-isotope collision-assisted Zeeman cooling, or two-isotope CAZ cooling for short. Two-isotope CAZ cooling is inherently an all-optical cooling technique, and as such, this introduction will focus on providing a broad overview of the field of laser cooling and trapping. A brief overview of the basic concepts behind laser cooling and trapping will be given. Also some of the motivations for this work are discussed. To place this work in better context, several common cooling techniques will be described as a frame of

reference for this work. Of course, given the scope of this thesis chapter, only an overview of these different cooling techniques can be presented.

1.1 Basics of Laser Cooling and Trapping

At the heart of laser cooling and trapping is the interaction of light with matter. Specifically, the interaction of individual atoms (or molecules) with an external optical field, typically the light field of a laser. These interactions take two primary forms: the scattering force on the atoms due to the individual photons in the light field, and dipole forces resulting from the atom's presence in the electrical component of the optical field [3]. Together these forces make up the radiation pressure that can be used to cool and confine atoms. Although radiation pressure can be useful in studies of not just atoms but ions [4,5], molecules [6], and even macroscopic particles [7] or objects [8], the focus here will be on neutral atoms, typically the alkali metals. In particular, the two abundant isotopes of rubidium, ^{85}Rb and ^{87}Rb, will be referenced often throughout this thesis as they are the isotopes used in the experiment described herein. Thus figure 1.1 will be a valuable reference throughout this work as it shows the relevant structure of the electronic energy levels of both isotopes. What follows is a description of how radiation pressure can be used to both cool and confine neutral atoms.

1.1.1 Cooling Using Radiation Pressure

Almost all laser cooling techniques begin by cooling atoms using radiation pressure. Radiation pressure is the workhorse of optical cooling. As such, the use of radiation pressure to cool and confine atoms was worthy of the 1997 Nobel Prize in Physics. On average, a gaseous atom at room temperature travels about 300 m/s. In order to be trapped that speed needs to be reduced by almost three orders of magnitude. This can be done by taking advantage of the scattering force due incident photons. Shown in figure 1.2, scattering can change the momentum of the atom by the photon momentum, $\hbar k$, it imparts upon the atom when absorbed. When the
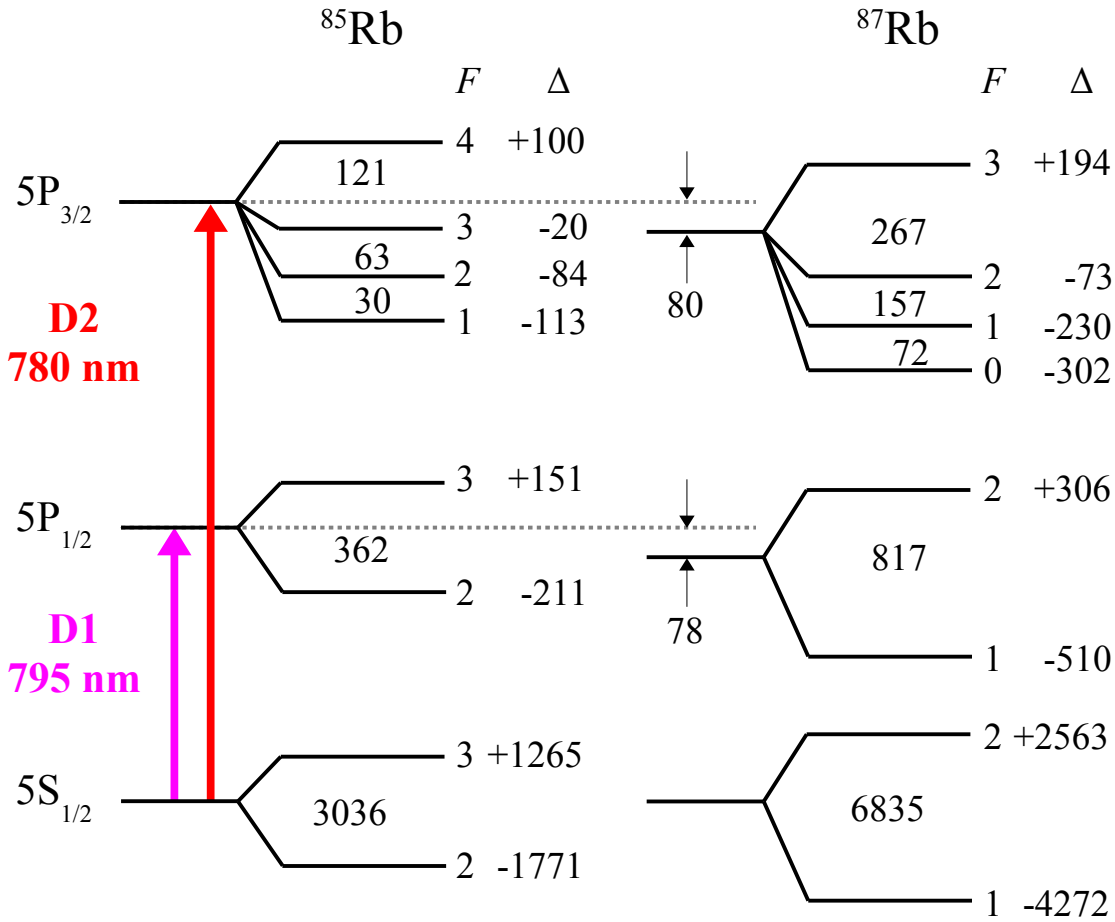
Figure 1.1 Energy Level Structure for ^{85}Rb and ^{87}Rb.
Relevant energy levels including hyperfine structure for the isotopes of Rb used in this research. Any optical transition used was near the D1 or D2 lines. Hyperfine states are resolved with the frequency difference between levels denoted. Also included are the $F = J + I$ values of each hyperfine state. Note that the nuclear spin of ^{85}Rb is 5/2 while for ^{87}Rb it is 3/2, thus the difference in F values between each isotope. The Δ values indicate the energy level shifts of the hyperfine interaction. Not shown are the degenerate (at zero magnetic field) magnetic sub-levels. These sub-levels are vital to this research. Each hyperfine level has $2F + 1$ magnetic sub-levels which are labeled by the quantum number m_F. All **splitting frequencies are in MHz** unless otherwise stated. Diagram not to scale.
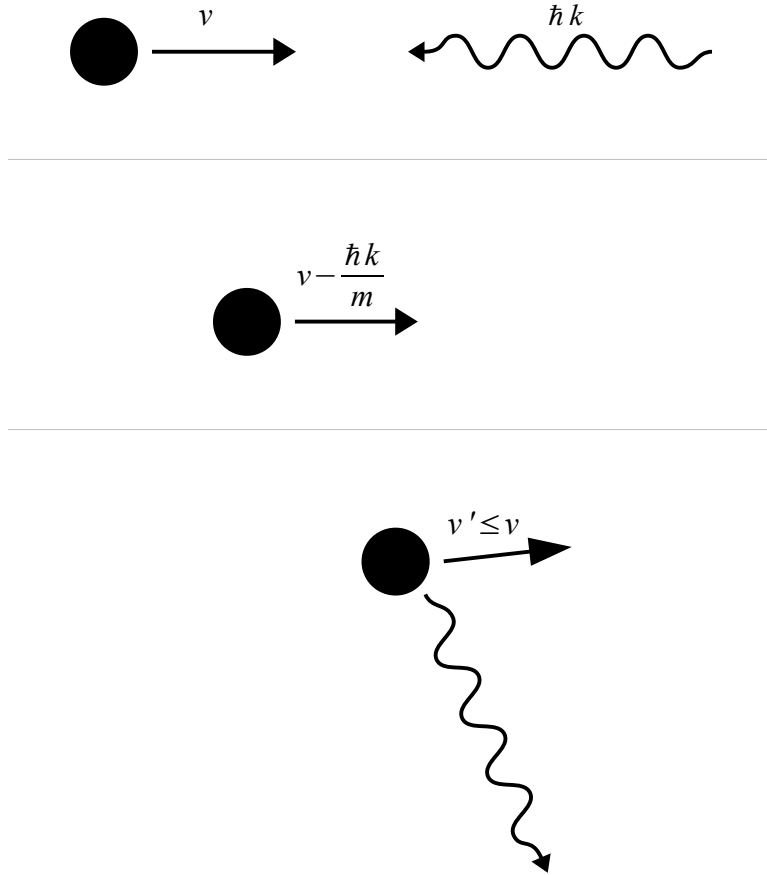
Figure 1.2 Radiation Pressure Due to Scattering of Photons.
(top) An atom moving with velocity v directly into a light field made up of photons with momentum $\hbar k$ will be (middle) slowed a small amount upon absorbing one of the photons. (bottom) When the atom re-emits the photon through spontaneous emission, it receives a second kick to its velocity, which will now be less in magnitude than the initial velocity (v' ≤ v). Since spontaneous emission results in a photon emitted in a random direction, the recoil due to the emission is also random. Thus after many scattering events the spontaneous photons average zero contribution to the atomic velocity, and each scattering event will on average reduce the atomic momentum by $\hbar k$ in the direction toward the light source. Many scattering events will result in a substantial decrease to the atomic kinetic energy. Scattered photons carry away that excess energy by appearing slightly bluer than incident photons in the lab frame.

atom is moving opposite of the propagation direction of a beam of light, the momentum change due to absorption will reduce the velocity of the atom. The excited atom must then emit a photon as it returns to its electronic ground state, completing the scattering event. The emitted photon also imparts a momentum kick to the atom (equal and opposite of its own), but when the emission process is spontaneous the direction of the emission is random. Thus the emission of many scattered photons averages to have zero change on the momentum of the atom. The result of this is that for an atom moving into a light beam a scattering event reduces the velocity by $\hbar k/m$ on average, where m is the mass of the atom. This means that many scattering events will reduce the kinetic energy of the atom. The difference in energy is carried away by the scattered photons which, in the lab frame, appears to be bluer than the incident photons from the cooling laser. All laser cooling techniques must have some mechanism to remove entropy from the atoms they are cooling. Typically, as with this case, it is the scattered photons which carry it away.

In order for atoms to be cooled out of a thermal vapor [9], they must be cooled in all three spatial directions. This is facilitated by using what is called optical molasses [10]. To understand how optical molasses works, first consider the one-dimensional case of an atom in the light field of two counter-propagating red-detuned laser beams, as shown in figure 1.3. Because the lasers are red-detuned, they will have a less-than-optimal scattering rate with the atom. Now if the atom is moving parallel to the propagation direction of the light, then the beam the atom is moving toward will be Doppler blue-shifted closer to resonance while the beam the atom is moving away will be red-shifted further from resonance. Therefore the atom will experience more scattering events from the beam it is moving toward and thus atomic motion is retarded regardless of direction. Extending this to three-dimensions is straightforward: have
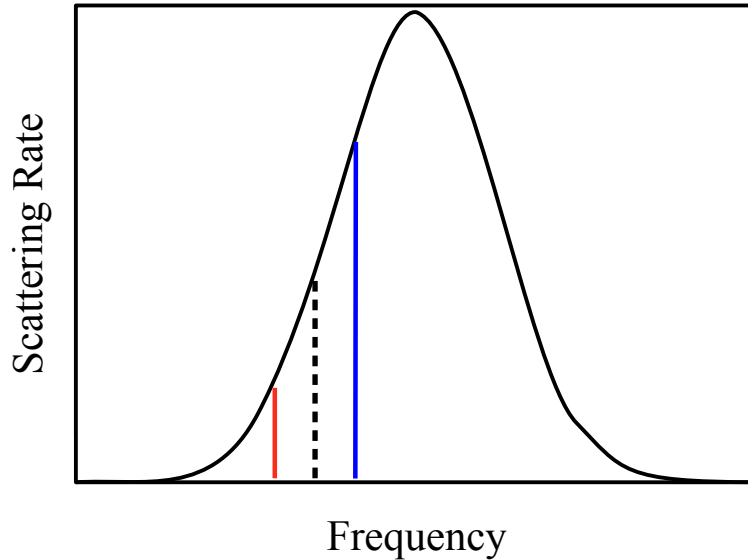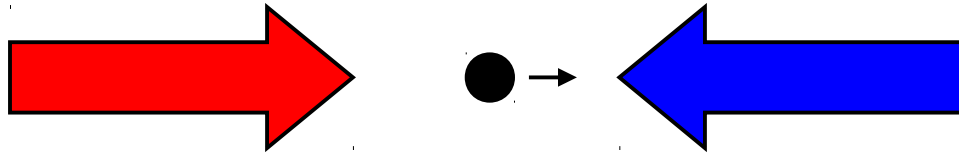
Figure 1.3 Doppler Cooling and Optical Molasses.
An atom moving in a light field will experience a Doppler shift in the observed frequency of the light. When moving toward the light source, the frequency is blue-shifted; when moving away, the frequency is red-shifted as depicted above. If the atom is moving in a light field made up of counter-propagating beams of a frequency slightly red-detuned of the atomic resonance (laser frequency indicated as the dotted line in the graph below), the beam the atom is moving into will be blue-shifted closer to resonance while the counter-propagating beam will be red-shifted further from resonance. This results in an imbalance of scattering rates as a result from the two counter-propagating beams and is depicted in the graph below.   Because there are more scattering events in the direction of motion, the atom experiences a viscous force inhibiting motion which is why the counter-propagating red-detuned beams are dubbed an optical molasses.

counter-propagating beams along each orthogonal spatial direction. This produces a three-dimensional light field which is velocity dependent and results in velocity damping.

An optical molasses will not cool the atoms to the point that they are stationary. The reason for this is that while the spontaneously emitted photon has no contribution on the momentum of the atom on average, it does impart a random instantaneous momentum shift. Therefore the atom is in motion at any given time, but on average has zero velocity. This sets a limit on the actual temperature that the atoms can be cooled to via optical molasses. This Doppler limit is dependent on the upper state lifetime of the atom and is given by:

$$T_D = \frac{\hbar \gamma}{2 k_B}$$

(1.1)

where k_B is the Boltzmann constant, and γ is the inverse of the excited state lifetime. For rubidium, the value of γ is $2\pi \times 5.98$ MHz giving a Doppler limit of 143 μK. However when put into practice, optical molasses produces clouds of some types of atoms (including Rb) with a temperature on the order of tens of micro-Kelvin [11], well below the Doppler limit. This is due to a sub-Doppler mechanism called polarization gradient cooling which affects the atoms when sufficiently slow. There are two different types of polarization gradient cooling mechanisms [12] which both rely on the optical pumping of the magnetic sub-levels of the atoms. Both can be understood by looking at the polarization field of two overlapped counter-propagating laser beams. Induced orientation cooling arises from the situation where the opposing beams are comprised of circularly polarized light of opposite handedness, while the Sisyphus cooling mechanism is the result of perpendicular linear polarizations.

For the case of induced orientation cooling, shown in figure 1.4 (adapted from reference 12), the polarization of the counter-propagating light beams is circular. In the frame of reference of the atom, each beam appears to have a polarization of opposite handedness of each other. The
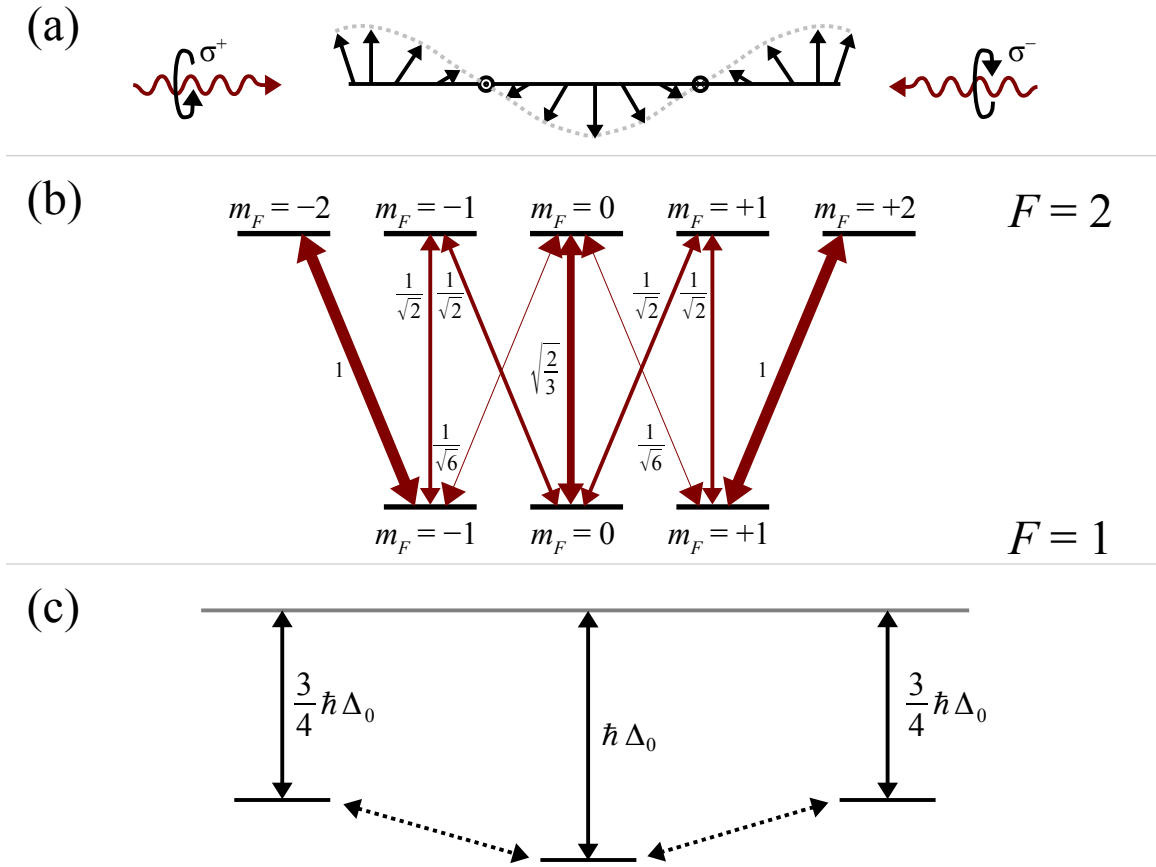
Figure 1.4 Polarization Gradient Cooling: Induced Orientation.
In induced orientation cooling, **(a)** two counter-propagating circularly polarized laser beams create a polarization gradient of fixed magnitude but changing direction resembling a helix. At any point the field is linear with the quantization axis along the direction of the polarization. Due to the relative transition strengths characterized by the Clebsch-Gordan coefficients, shown to the left of the transitions in panel **(b)**, atoms which are at rest will have a larger population in the $m_F = 0$ state. **(c)** This results in induced light shifts in the ground state hyperfine sub-levels due to the different linear transition strengths which favor the $m_F = 0$ state. Atomic motion that is slow enough causes a coupling between m-states (dotted arrows) resulting in motion dependent asymmetry in the m-state populations. Thus there are more atoms in either the $m_F = 1$ or the $m_F = -1$ compared with the at rest situation. Note that these states are more sensitive to one circularly polarized state than the other. The resulting imbalance in scattering events inhibits atomic motion and causes cooling.

light field that results is linearly polarized, but the polarization direction changes with spatial position. As shown in figure 1.4a, the polarization vector traces out a helix through space. For an atom at rest at any given point in space, the polarization field is linear and the logical choice for the quantization axis is along the polarization direction. Examination of the relevant Clebsch-Gordan coefficients (see figure 1.4b) reveals that the population distribution of the steady-state ground state sub-levels is non-uniform, with a larger population of atoms in the $m_F = 0$ state. For example, a Rb^{87} atom would have a relative population of 9/17 in the $m_F = 0$ state and a population of 4/17 in both the $m_F = \pm 1$ states. Note that the induced light-shifts in the sub-levels resulting from the relative transition strengths of the linear light (due to the Clebsch-Gordan coefficients) also favor the $m_F = 0$ state. When the atom is in motion (and sufficiently slow- that is the rotation speed of the polarization axis is much slower that the induced light-shift of the ground state sub-levels), the changing of the quantization axis produces a coupling between adjacent magnetic sub-levels in the atom. This can be shown to be equivalent to a fictitious magnetic field along the rotation axis. The coupling between adjacent levels distorts the steady-state ground state population compared to the at-rest situation. This leads to a velocity-dependent difference between populations the $m_F = -1$ and $m_F = +1$ states. For an atom moving toward the σ^+ light source, the imbalance favors the $m_F = +1$ state while the opposite state is favored when moving into the oppositely polarized light. Referring back to the Clebsch-Gordan coefficients in figure 1.4, we see that for an $F = 1$ atom in the $m_F = +1$ state there is a six-times more likelihood that a σ^+ photon will be absorbed than a σ^- photon. This means that the radiation pressure exerted by the two circularly polarized light beams is unbalanced for atoms in the $m_F = \pm 1$ states. Since atom motion induce a ground state sub-level population difference and atoms in the $m_F = \pm 1$ states experience unbalanced radiation pressure, atoms in motion experience a velocity-dependent force which acts as a viscous force opposing the motion of the

atom. Note that the cooling light can transfer atoms between the $m_F = \pm 1$ states through coherent Raman transitions [13,14]. These transitions serve to efficiently redistribute the ground state population. Thus coherent transitions are a vital part of effective sub-Doppler cooling. As with Doppler cooling, scattered photons in the lab frame are bluer than the cooling laser frequency and facilitate the removal of energy from the sample. Although the example shown here was for an $F = 1$ ground state atom, the mechanism similarly applies to other atoms so long as the cooling transition shares a similar structure ($F' = F + 1$). This force allows cooling to break the Doppler limit, but it it is not the only type of polarization gradient cooling that allows this.

Sisyphus cooling also cools below the Doppler limit, but the mechanism is different. The polarization gradient resulting from opposite handedness circularly polarized light produces no change in the atomic ground state energy levels as a function of position. Conversely, when the opposing beams are perpendicular linearly polarized beams there is a spatial-dependent energy shift in the ground state sub-levels. Cooling in this configuration is best understood by consideration of the simplistic case of an atom with an $F = 1/2$ ground state and an $F' = 3/2$ excited state, as summarized in figure 1.5 (adapted from reference 15). The counter-propagating orthogonal linearly polarized beams produce a polarization gradient as shown in figure 1.5a which varies in space. The ellipticity of beam alternates between circularly polarized and linearly polarized. Circularly polarized points alternate handedness every quarter wavelength, while linearly polarized points reside mid-way between the circularly polarized points and are perpendicular to adjacent linearly polarized points. Between the linearly and circularly polarized points are smoothly varying elliptical polarizations. The light-shift of the magnetic sub-levels of an atom is dependent on the local polarization of the light field. For an atom with $F = \frac{1}{2}$, a (red-detuned) σ^+ polarization will shift the energy of the $m_F = \frac{1}{2}$ lower than the $m_F = -\frac{1}{2}$ state, while a σ^- polarization will result in opposite shifts. Linearly polarized regions shift the states equally.

Figure 1.5 Polarization Gradient Cooling: Sisyphus.
In Sisyphus cooling, **(a)** two counter-propagating linearly polarized (red-detuned from the $F' = 3/2$ state) laser beams create a polarization gradient of varying ellipticity. Individual points along the path change smoothly between linear and alternating circular polarizations. **(b)** For an atom with an $F = 1/2$ ground state, the two magnetic sub-levels will be degenerate in regions of linear polarization but separated in regions of circularly polarized light. Thus an atom moving through the light field (from left to right in the figure) must climb a potential hill (black arrow) and lose kinetic energy every time its energy level switches from being the lower to the higher of the two. When an atom is in the higher of the two energy levels, it will be pumped into the lower (red arrows), with the scattered photon carrying away entropy. This is because the polarized light pumps atoms to the lower of the two ground state levels, as shown in panels **(c)** and **(d)**.

Thus as a function of position, the two magnetic sub-levels will oscillate between being higher and lower than each other as shown in figure 1.5b. Furthermore, when in a region of σ^+ polarization atoms are pumped into the $m_F = \frac{1}{2}$ state, while in σ^- polarization the atoms are pumped into the $m_F = -\frac{1}{2}$ state (figure 1.5c & d). Thus the atoms tend to spend more time in the lower energy state at any given position in the polarization field. For an atom in motion, optical pumping puts the atom into the lowest energy state when in the region of circularly polarized light; the atom then moves toward a region of opposite handedness circular light and loses kinetic energy as the internal energy increases due to the changing light shift. However, once exposed to the opposite handedness circularly polarized light, the atom is then pumped to the other magnetic sub-level which is now the lowest energy state. The excess energy is carried away by scattered photons. Since the atom loses its kinetic energy by continually climbing internal energy hills, the Greek myth of Sisyphus who was condemned to roll a stone up a hill forever is invoked and thus this type of polarization gradient cooling is named Sisyphus cooling.

Both forms of polarization gradient cooling are conceptually simple when only one dimension is considered; however, an optical molasses works in all three spatial dimensions. Extending either theory to three dimensions is non-trivial since the polarization field resulting from the three pairs of counter-propagating beams is not only more complex, but is sensitive to minute deviations in the experimental beam paths. In addition, the motion of a given atom through the field will result in a unique polarization gradient that the atom moves through, which also changes when the motion of the atom changes due to scattering events with other atoms as well as photons from the cooling light field. It is most probable that both forms of polarization gradient cooling are at work in an optical molasses, regardless of the beam polarizations used. It is the combination of the unbalanced radiation pressure of induced orientation cooling and the

optical pumping of Sisyphus cooling that produces temperatures below the Doppler limit in an optical molasses.

While polarization gradients allow the Doppler limit to be broken, they cannot cool to arbitrarily low temperatures. Atoms are continuously scattering photons, and each scatter imparts a small amount of recoil energy ($E_R = \hbar^2 k^2/(2m)$). If a single atom were at rest in the light-filed, it would scatter photons and subsequently move due to the photon recoils. Thus it would be expected that the limiting temperature of this atom would be on the order of a few photon recoil energies (for Rb, $E_R/k_B = 0.18$ μK). However, there are additional density-dependent effects to consider when a large sample of atoms are cooled. As the atoms are cooled, their density increases. This in turn increases the optical depth of the sample of atoms which increases the rate of reabsorption; that is, the rate that scattered photons are re-scattered. Reabsorbed photons not only cause additional heating by imparting additional photon recoils in a direction that is random, but they upset the relationship between the atoms spin polarization and light polarization necessary for the coherent transitions of effective sub-Doppler cooling [16-19]. Thus the lowest possible temperature achieved by sub-Doppler cooling is much greater than the photon recoil energy.

The random momentum kicks of scattered photons in the optical molasses result in the atom exhibiting a random walk reminiscent of Brownian motion. This means that while an optical molasses can cool atoms, it cannot trap them. As soon as an atom walks out of the laser field of the optical molasses it will be lost. Since cooled atoms are not much use if they they are not around, a brief description on how to confine atoms cooled by an optical molasses will be given in the following section.

1.1.2 Trapping Cold Atoms

To trap atoms, some sort of spatially-dependent restoring force must keep the atoms in a region of space. The magnetic structure of the atom can be used to provide this restoring force. Consider the 1D case of an atom in the $F = 0$ ground state in an optical molasses tuned to an $F = 1$ excited state with an applied magnetic field gradient such as that shown in figure 1.6a. Here the optical molasses comprises of counter-propagating, opposite circularly polarized beams. The magnetic field gradient is such that the center of the trap is at zero field. The magnetic field then increases in strength with position from center. The increasing magnetic field strength causes atoms further from the center of the trap to experience a greater Zeeman shift in the excited state energy magnetic sub-levels than those close to center. This results in different scattering rates between the two circularly polarized optical molasses beams. This is a consequence of the optical molasses beams being red-detuned from the atomic resonant frequency, meaning one of the excited state transitions is brought closer to resonance while the other is shifted further from resonance. The direction of the field is chosen such that excitations to the $m_F = -1$ ($m_F = +1$) excited state are closer to resonance with the light field in regions physically nearer to the source of the σ^- (σ^+) photons. Thus when an atom is displaced from the center of the trap toward the source of the σ^- (σ^+) light, it experiences an imbalance in radiation pressure since the σ^- (σ^+) light will drive only transitions to the $m_F = -1$ ($m_F = +1$) excited state that has been brought closer to resonance. The strength of the radiation pressure imbalance is position dependent, causing a greater restoring force further away from the center of the trap. The concept is extended to three dimensions by using the magnetic field produced from an anti-Helmholtz (AH) coil pair centered on a region with a three-dimensional optical molasses. Some care is needed to make sure the optical molasses beams have the correct polarization given the direction of the magnetic field along the beam path. The full configuration in all three spatial

Figure 1.6 Concept Behind a Magneto-Optical Trap (MOT).
(a) The one dimensional magnetic field gradient shown as light blue arrows, will cause a shift in the $F = 1$ excited state magnetic sub-levels of an atom. These atoms are in the $F = 0$ ground state and subjected to a red-detuned optical molasses shown as red arrows. The red dotted line represents the detuned cooling laser transition. The polarization of the cooling light and direction of the magnetic field are chosen such that atoms far from center become closer to resonance of one of the lasers such that the imbalance of photon scatters acts as a restoring force, trapping the atoms in space. **(b)** For more complex atoms such as ^{87}Rb in the $F = 2$ ground state, the idea still holds. For example, an atom in the region to the left and in the $m_F = 2$ state experiences more photon scattering from the σ^+ polarized beam which is closer to resonance than the σ^- polarized beam, pushing it toward center. This is true for every magnetic sub-level as shown for the right side of the trap.

dimensions is called a magneto-optical trap, or MOT. For atomic structure that is more complicated, the MOT still works because the Zeeman shift will bring one optical molasses beam closer to resonance than the other regardless of the ground state the atom is in. This can be seen in figure 1.6b which summarizes the spatial dependence of the Zeeman shifts of a Rb[87] atom in a MOT and shows how the radiation pressure imbalance is facilitated.

The MOT is a very robust tool for cold atom studies, but it is generally only a starting point for most experiments. This is because MOTs contain a large amount of scattered light and AC stark shifts of the energy levels of the trapped atoms. As such, most studies are actually done in traps whose environments are better controlled. These traps function through a variety of different mechanisms. Magnetic traps [20] operate on the interaction energy of the magnetic moment of the atom with an external magnetic field. Optical dipole traps [21] work on a similar mechanism but with an induced electric dipole of an atom in the electric filed of an intense laser field. This is a very important type of trap for this research and will be discussed later in section 3.2. Optical lattices [22] trap atoms in periodic potentials created by the interference pattern resulting from the overlap of multiple optical trap beams. Although each of the mentioned examples provide a unique set of benefits, challenges and limitations, they will only be discussed insomuch as they are relevant to the research presented in this work. For now, some of the motivations for using traps other than a MOT will be covered in the following section.

1.2   Usefulness of Cooling Beyond the MOT Limit

Although the MOT is a simple yet powerful tool for the cooling of neutral atoms [23,24], and is used in hundreds of experiments, the minimum temperature and maximum density of a MOT are correlated and limited [16,18,25]. This is a result of relying on both Doppler and sub-Doppler cooling [12,26,27], which themselves are limited as discussed earlier. The minimum temperature of a MOT is limited by photon scattering events as well as reabsorption effects.

Meanwhile, the maximum density of a MOT is limited by light-assisted collisional losses and scattering forces. Taking cold atoms to regimes beyond these limitations, however, offers many additional benefits.

Perhaps the most powerful original motivation to extend beyond MOT limits is the creation of a Bose-Einstein Condensate (BEC) [28-30]. BEC systems have been used to study the fundamental quantum physics of bosons [31,32], including systems in one or two dimensions [33-36]. BECs consisting of molecules [37] have also been studied. Due to the wave-like properties of BEC atoms, an atom interferometer can be constructed which has applications in inertial sensing [38]. BECs may be useful in the construction of scanning electron microscopes [39] and atom lasers [40]. It is also possible to pursue the development of quantum computers which utilize BECs [41,42]. These are but a few of the myriad of examples in the broad field of BEC science. Further information can be found in references 43-46.

In addition to creating degenerate gases of bosons, degenerate gases of fermions may be created as well [47]. Studies of Fermi Degenerate Gases (FDG) lead insight into the fundamental quantum physics of fermions [48,49]. In addition, a FDG can be very useful in modeling certain condensed matter problems, being considerably easier to make and manipulate. Similarly, FDG systems can give insight into superconductivity as well as particle pairing [50]. FDG can even be used to model high energy and astrological systems such as quark-gluon plasmas and neutron stars [51].

One does not need to go to degeneracy to take advantage of conditions beyond the MOT limit. Studies of ultracold gases beyond MOT limits can be used for a number of fundamental physics experiments. Some examples include: exploring the physics of non-degenerate systems of very high phase-space density [52-54], measurement of the electron dipole moment [55], study of systems of high quantum state fidelity which are useful for quantum computation

[56,57], atom interferometry [58], development and improvement of atomic clocks [59]. This is just a partial list of examples where ultracold atoms are useful in fundamental physics research.

Although non-evaporative cooling techniques were part of the race to make the first BEC, they were never successful in making a BEC [60,61]. Until recently[62], all gaseous BECs have been created using the technique of evaporative cooling. Not only is BEC creation by non-evaporative means an outstanding experimental challenge, but it would also allow a technical advantage. Non-evaporative cooling would enable novel experiments studying interesting physics which would otherwise be difficult or impractical using evaporative cooling. The following section discusses both evaporative cooling and non-evaporative cooling in more detail.

1.3 Evaporative Cooling vs. Non-Evaporative Cooling

1.3.1 Evaporative Cooling

To understand the benefits of non-evaporative cooling methods it is first instructive to describe the technique of evaporative cooling [63]. Evaporative cooling is the state-of-the-art cooling technique for ultracold gas experiments, being the most successful at cooling atoms to the lowest temperatures with relatively high densities. The technique is so successful that the creation of virtually every BEC utilizes some degree of evaporative cooling. As the name implies, cooling is achieved by evaporation in this technique. As illustrated in figure 1.7, atoms of the highest energy are allowed to escape the trap carrying away a larger-than-average amount of thermal energy. Once the high energy atoms are removed from the sample, the remainder are out of equilibrium. Upon redistributing their energy the atoms will come back into a Maxwell-Boltzmann distribution but one of lower temperature- since the higher energy atoms are removed, the remainder of the sample has a lower average kinetic energy.

Naturally a trap evaporates off atoms until those remaining in the trap thermalize to a Maxwell-Boltzmann distribution with a temperature well below the trap depth (assuming no

18

Figure 1.7 Cartoon of Evaporative Cooling.
On the left, atoms (white circles) confined in an atom trap, of trap depth d. The average kinetic energy of the atoms relative to d is indicated by the light blue line. On the right, thermal collisions have caused some atoms to loose energy and others to gain energy. If an atom has more energy than d (red circles), it is lost from the trap. Lost atoms have greater-than-average kinetic energy. Thus the atoms remaining in the trap have a lower average kinetic energy than before the loss, as indicated by the shift to the dark blue line. Evaporation continues until the average kinetic energy is approximately ten-percent of the trap depth.

other loss mechanisms). In typical traps, evaporation ceases once that temperature is approximately one-tenth of the trap depth [64]. This temperature is generally well above the BEC transition temperature. However, lower temperatures are possible if atoms with higher-than-average kinetic energy can be selectively and continuously removed from the trap. When encouraging more evaporation using a technique called forced evaporative cooling, incredibly low temperatures can be achieved. Forced evaporative cooling is the technique which allows the creation of BECs, and can be achieved different ways. What follows is a description of forced evaporative cooling in magnetic traps and optical dipole traps.

1.3.1.a   Forced Evaporative Cooling in Magnetic Traps

Although the work presented in this thesis could not have been done in a magnetic trap, the first creation of a BEC was done in a magnetic trap and the use of magnetic traps remains in widespread use today. For this reason, forced evaporative cooling in a magnetic trap will be discussed here in brief. Magnetic traps confine atoms in a region of minimum magnetic field magnitude by taking advantage of the magnetic moment of the atom. The interaction of the magnetic moment of an atom with an external field is given by:

$$H = -\vec{\mu} \cdot \vec{B} \tag{1.2}$$

where μ is the magnitude of the magnetic moment of the atom in external magnetic field B. When a magnetic field gradient is superimposed on a uniform magnetic field atoms minimize energy by seeking out regions of either the lowest or highest field strength, depending on the sign on μ (which is dependent of the Landé g-factor and magnetic quantum number of the trapped state). The interaction energy is minimized in a region of minimum magnetic field magnitude for an atomic magnetic moment that is anti-parallel to the external magnetic field. Note that owing to Earnshaw's theorem, magnetic field minima cannot exist in free space (only saddle points can exist) due to the vector nature of the field. However the magnitude of the magnetic

field can have a minimum and so long as the field does not change too rapidly, the magnetic moment of an atom will follow the field adiabatically. A magnetic atom trap is basically this type of configuration, where the field is designed so that there is a region of local minimum field strength where the atoms which have magnetic moments which are anti-parallel to the magnetic field are trapped. Because an atom with magnetic moment parallel to the magnetic field would have a maximum interaction energy in regions of lowest magnetic field strength, the magnetic trap is very sensitive to the particular spin-state that the atom is in. Thus atoms trapped in a magnetic trap are generally spin-polarized to be at the very least in a trappable state.

Atoms which are trapped in a magnetic trap are typically confined to nearly parabolic trapping potentials in all three spatial directions. This means that trapped atoms will orbit the trap center (region of magnetic field minimum). More energetic atoms will, at their extremes, orbit further away from the center of the trap where the local magnetic field strength is stronger. In turn, this causes the more energetic atoms to periodically experience a greater Zeeman shift than less energetic atoms in the trap. This is important because it gives a means to selectively remove more energetic atoms. The atoms can be selectively addressed using radio frequency (RF) transitions which can move atoms from one spin-state to another for a narrow range of external magnetic field strengths. Thus the higher energy atoms can be put into spin-states which are not trappable by the magnetic potential. Once these higher energy atoms are in an untrappable state, they will leave the trap with above average kinetic energy. The remaining atoms will consequently have a lower average kinetic energy. Figure 1.8 summarizes the process which is called forced RF evaporation. Once the atoms remaining in the trap have rethermalized and no longer have sufficient kinetic energy to put atoms into orbits where the RF field will remove them from the trap, the RF can be changed to remove slightly less energetic atoms. Thus the atoms remaining in the sample are made colder and colder.

Figure 1.8 Forced Evaporative Cooling in a Magnetic Trap.
Atoms (circles) are confined in a magnetic trap if in the m-state for the potential shown above, and expelled if in the *m*-state for the potential below. As atoms orbit the zero point of the trap's magnetic field on the left, more energetic atoms will enter regions of higher magnetic field where they can be selectively transitioned by a resonant RF field (purple) to the repulsive potential owing to the greater Zeeman shift of these atoms (green) compared to cooler ones in the cloud. After these atoms are transitioned (right) they are expelled from the trap (red). The average kinetic energy of the remaining atoms is reduced (dashed blue lines), and the RF field can be set (yellow) to expel progressively cooler atoms.

Forced RF evaporation is a very effective means to cool atoms beyond MOT limits. However, it tends to take a long time (often on the order of a few minutes to cool to degeneracy), and not all atomic species are magnetically trappable. In addition, if it is desirable to do an experiment that utilizes untrappable states, then the atoms must be transferred to another trap which will usually induce heating. In cases such as these the use of an optical dipole trap might be preferable since the atoms can be evaporated directly.

1.3.1.b   Forced Evaporative Cooling in Optical Dipole Traps

Studies for this thesis utilize an optical dipole trap, which can also be used for forced evaporative cooling. An optical dipole trap need not have atoms in a particular spin-state in order to be trapped because it is the electric dipole moment of the atom interacting with the electric field component of an optical field which provides the trapping potential. Thus RF transitions will be unable to selectively remove more energetic atoms as is the case in a magnetic trap. However, the trap depth of an optical trap scales with the intensity of the laser used which is readily adjustable [65]. If the trap depth is slowly lowered, as shown in figure 1.9, then atoms in the trap will more likely obtain enough energy through thermal collisions to escape the lower trap depth. Therefore more atoms will be evaporated out of the trap, cooling the remaining atoms. Although the process of lowering the trapping potential by decreasing the trapping laser intensity also relaxes the confinement strength of the trap. This makes forced evaporative cooling in an optical trap more difficult than in a magnetic trap since the density of the trapped atoms will decrease as the sample cools. In turn, this reduces the collision rate of the atoms and limits the rate the atoms can be further cooled. However, it is possible to overcome this issue using more advanced techniques [66].
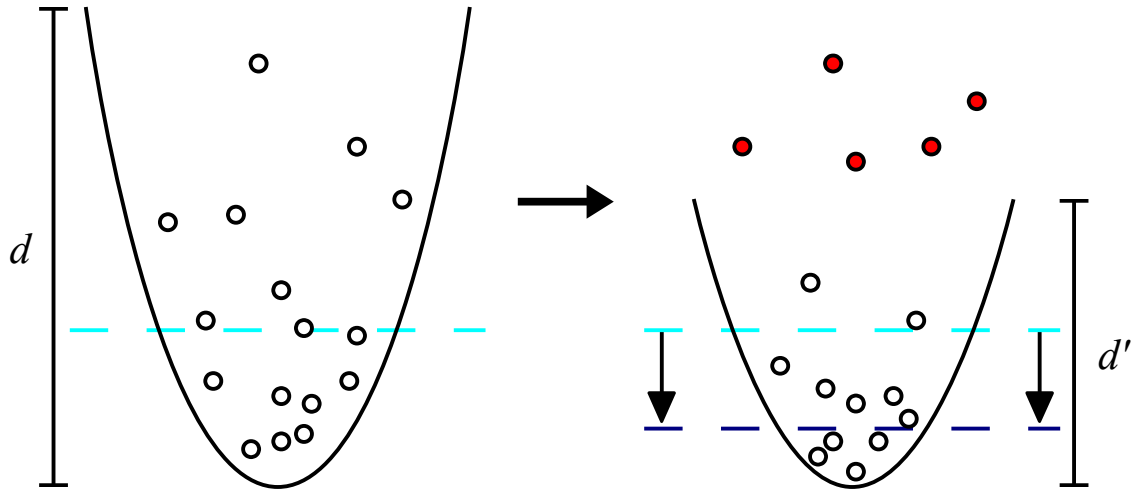
Figure 1.9 Forced Evaporative Cooling in an Optical Trap.
(left) Thermalized atoms in an optical trap of depth d can be cooled further by (right) intentionally lowering the optical tarp depth to d'. Due to the lower trap depth, more atoms will be able to be evaporated (red) causing the remaining atoms to have lower average kinetic energy (dashed blue lines). Although forced evaporation in an optical trap also relaxes the confinement strength of the trap, reducing the density, the cooling it facilitates is great enough that there is a net increase in the phase-space density. This assumes that the lowering of the trapping potential is done slow enough that the atoms are allowed to rethermalize.

1.3.1.c Limits of Evaporative Cooling

Evaporative cooling is a fine experimental technique with many benefits. So long as the ratio of rethermalizing collisions to loss-inducing collisions is about 100 to 1, then evaporative cooling works very effectively. Atoms can be prepared with very low temperatures and high densities. The amount of cooling is dependent on the temperature of the gas, which has a benefit over optical cooling schemes which are limited by the photon recoil energy. Evaporative cooling has facilitated relatively simple and robust systems to create BECs [67].

With all its success, evaporative cooling still has disadvantages. Even though it is fairly easy to decrease the trap depth in traps with harmonic potentials such as those found in magnetic and induced-dipole traps, non-harmonic potentials tend to require much experimental complexity to implement evaporative cooling [68]. Also, in the case of magnetic traps, evaporative cooling tends to be very slow (on the order of a few minutes to reach BEC temperatures). Perhaps most importantly, the primary mechanism to remove energy from the sample is to remove atoms from the sample. Thus evaporative cooling intrinsically requires loss. Typically samples are reduced by 95-99% of their initial populations to reach BEC temperatures. These limitations restrict the type and scope of experiments which can be done using evaporative cooling.

1.3.2 Non-Evaporative Cooling Techniques

Non-evaporative cooling methods have been around for some time and were even part of the race to BEC [60,69-73]. However, despite the interest and investment into non-evaporative cooling techniques only one [62] has has thus far been able to achieve a BEC on its own. Non-evaporative techniques have more commonly been successfully used as a pre-cooling stage for evaporative creation of BEC with notable improvement in number of atoms remaining in the condensate [74], but the final push to BEC almost always uses evaporative cooling. The principal limitation of non-evaporative cooling techniques is generally reabsorption [75].

Reabsorption will be discussed in more detail in section 2.3.3. Some examples of non-evaporative cooling methods include: velocity-selective coherent population trapping [76], gray optical molasses [77], in-lattice polarization gradient cooling [78], one-way atom wall [79,80], Raman cooling [60,69,73,81], and collision-assisted Zeeman (CAZ) cooling [82]. Raman cooling will be discussed briefly in the remainder of this chapter, as it is the most successful of these methods to date and illustrates the typical limitations of non-evaporative cooling methods. Meanwhile CAZ cooling is covered in detail in chapter 2.

The Raman cooling technique uses two counter-propagating beams each of opposite circular polarization to drive two-photon coherent Raman transitions. Since the beams are counter-propagating the transition is very velocity sensitive and thus requires specific detunings in order to affect atoms of a given velocity. The relevant energy levels of such a transition are depicted in figure 1.10. The basic idea is to first put all the atoms into a single m_F state where various velocity-selective Raman pulses are then used to pump some of the atoms into a different magnetic sub-level. This is done by choosing the detunings of the Raman lasers such that the absorption/emission cycle of the Raman pulse removes $2\hbar k$ of momentum from the atoms and reduces their velocity. The pumped atoms end up in a state of greater magnetic entropy (since atoms are no longer in a single polarized state) at the cost of kinetic energy. This entropy is then removed via the spontaneous emission resulting from optically pumping the atoms back into their initial state, closing the cooling cycle.

Aside from the advantage of being a loss-less cooling scheme capable of cooling below the limits of a MOT, Raman cooling has several other features making it an appealing technique. Not only is Raman cooling relatively fast since it relies on optical pumping rates, but it can be done in a configuration that helps the mitigation of reabsorption [81,83]. This is done by cooling the atoms in an optical lattice in the so-called Festina-Lente regime [84] where the trapping
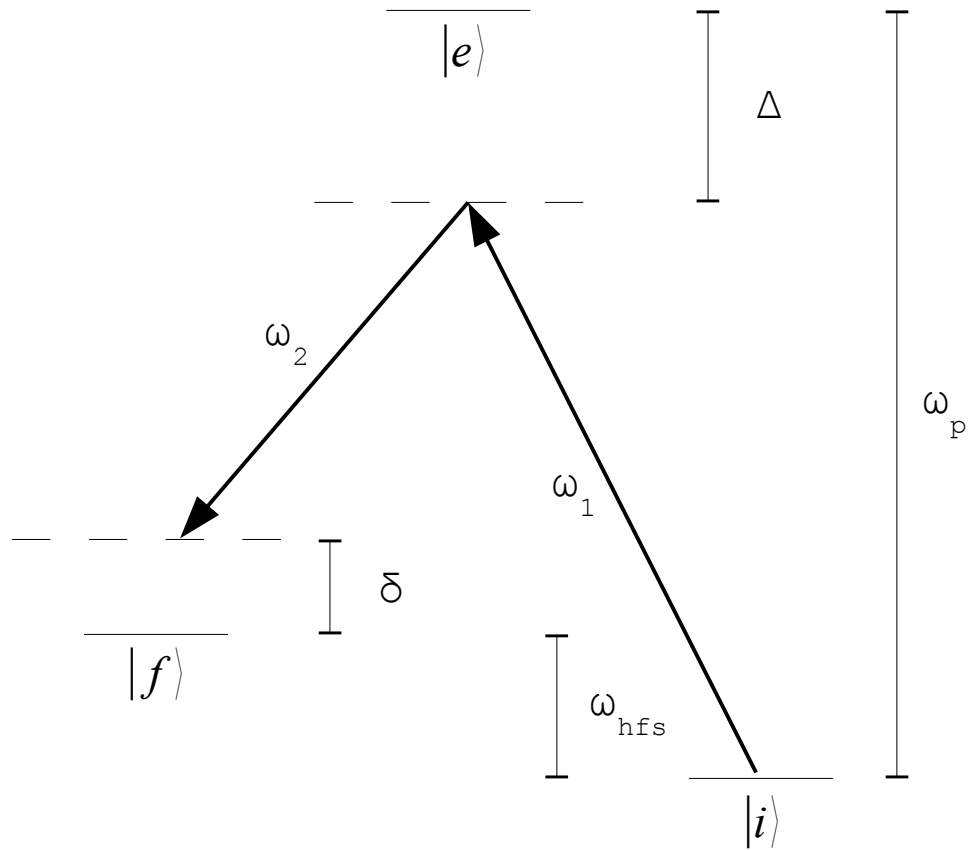
Figure 1.10 Energy Level Diagram for Raman Cooling.
Two counter-propagating beams with opposite circular polarizations of angular frequency ω_1 and ω_2 drive coherent population transfers from initial state i, to final state f, through an excited state e. initial and final states are in different hyperfine levels separated by the hyperfine level splitting ω_{hfs}. The beams are detuned with values of Δ and δ such that they only interact with specific velocity classes.

27

frequency is much greater than the spontaneous scattering rate. This relies on a technique called Raman sideband cooling, where atoms are moved between vibrational states of the individual lattice sites.

Although Raman sideband cooling has successfully reduced reabsorption effects, it nevertheless becomes limited by them prior to reaching the phase-space density necessary for BEC. Density can be made very high, and temperature can be made very low, but not necessarily enough at the same time with Raman cooling. In fact, measurements indicated that the lowest achievable minimum temperature using Raman cooling increased with increasing density, in such a way that the total achievable phase space density was limited. Also the setup required for Raman cooling schemes is fairly complex, requiring the setting of multiple timed pulses over a range of beam detunings. Such a setup can be time-consuming to tweak and optimize [85]. A non-evaporative cooling method that offers opportunities to avoid some of these limitations, is CAZ cooling, which is the primary focus of this work. The theory of CAZ cooling is given in chapter 2.

References for Chapter 1

[1] K. B. Davis, M-O Mewes,and W. Ketterle, Appl. Phys. B **60**, 155-159 (1995).
[2] N. Masuhara, J. Doyle, J. Sandberg, D. Kleppner, and T. Greytak, Phys. Rev. Lett. **61**, 935-938 (1988).
[3] S. Chang, and V. Minogin, Phys. Rep. **365**, 65-143 (2002).
[4] G. Horvath, R. Thompson, and P. Knight, Contemp. Phys. **38**, 25 (1997).
[5] M. Johanning, A. Varón, and C. Wunderlich, J. Phys. B: At. Mol. Opt. Phys. **42**, 154009 (2009).
[6] G. Meijer, ChemPhysChem, **3**, 495 (2002).
[7] A. Ashkin, Proc. Natl. Acad. Sci. U.S.A. **94**, 4853 (1997).
[8] P. Cohadon, A. Heidmann, and M. Pinard, Phys. Rev. Lett. **83**, 3174 (1999).
[9] A. Cable, M. Prentiss, and N. Bigelow, Opt. Lett. **15**, 507 (1990).
[10] S. Chu, and L. Hollberg, J. Bjorkholm, A. Cable, and A. Ashkin, Phys. Rev. Lett. **55**, 48 (1985).
[11] P. Lett *et al.* Phys. Rev. Lett. **61**, 169 (1988).
[12] J. Dalibard and C. Cohen-Tannoudji, J. Opt. Soc. Am. B **6**, 2023 (1989).
[13] S. Chang, T. Kwon, H. Lee, and V. Minogin, Phys. Rev. A **60**, 3148 (1999).
[14] P. van der Straten, S-Q. Shang, B. Sheehy, H. Metcalf, and G. Nienhuis, Phys. Rev. A **47**, 4160 (1993).
[15] S. Chu, Rev. Mod. Phys. **70**, 685 (1998).
[16] C. Townsend, N. Edwards, C. Cooper, K. Zetie, and C. Foot, Phys. Rev. A **52**, 1423 (1995).
[17] G. Hillenbard, C. J. Foot, and K. Burnett, Phys. Rev. A, **50**, 1479 (1994).
[18] G. Hillenbrad, K. Burnett, and C. Foot, Phys. Rev. A **52**, 4763 (1995).
[19] K. Ellinger and J. Cooper, Phys. Rev. A 55 4351 (1997).
[20] V. Bolpasi *et al.*, J. Phys. B: At. Mol. Opt. Phys. **45**, 235301 (2012).
[21] J. Yin, Phys. Rep. **430**, 1-116 (2006).
[22] I. Bloch, J. Dalibard, and S. Nascimène, Nature Physics **8**, 267-276 (2012).
[23] E. Rabb, M. Prentiss, A. Cable, S. Chu, and D. Pritchard, Phys. Rev. Lett. **59** , 2631 (1987).
[24] C. Wieman, G. Flowers, and S. Gilbert, Am. J. Phys. **63**, 317 (1995).
[25] K. Ellinger, J. Cooper, P. Zollar, Phys. Rev. A **49**, 3909 (1994).
[26] H. Metcalf, P. van der Straten, J. Opt. Soc. Am. B **20**, 5 (2002).
[27] M. Drewsen *et al.*, Appl. Phys. B **59**, 281-298 (1994).
[28] M. Anderson, J. Ensher, M. Matthews, C. Wieman, and E. Cornell, Science **269**, 198 (1995).
[29] K. Davis *et al.*, Phys. Rev. Lett. **75**, 3969 (1995).
[30] C. Bradley, C. Sackett, J. Tollett, R. Hulet, Phys. Rev. Lett. **75**, 1687 (1995).
[31] T. Weber, J. Herbig, M. Mark, H. Nägerl, and R. Grimm, Science **299**, 232 (2003).
[32] Y. Takasu *et al.*, Phys. Rev. Lett. **91**, 040404 (2003).
[33] M. Singh *et al.*, J. Phys. B **41**, 065301 (2008).
[34] G. Cennini, C. Geckeler, G. Ritt, T. Salger, and M. Weitz, Fortschr. Phys. **54**, 719 (2006).
[35] T. Kinoshita, T. Wenger, and D. Weiss, Science **305**, 1125 (2004).
[36] L. Tolra *et al.*, Phys. Rev. Lett. **92**, 190401 (2004).
[37] S. Jochim *et al.*, Science **302**, 2101 (2003).
[38] J. Fang, and J. Qin, Sensors **12**, 6331 (2012).
[39] T. Gericke, P. Würtz, D. Reitz, C. Utfeld, and H. Ott, Appl. Phys. B **89**, 447 (2007).
[40] G. Cennini, G. Ritt, C. Geckeler, and M. Weitz, Phys. Rev. Lett. **91**, 240408 (2003).
[41] D. DeMille, Phys. Rev. Lett. **88**, 067901 (2002).
[42] G. Brennen, C. Caves, P. Jessen, and I. Deutsch, Phys. Rev. Lett. **82**, 1060 (1999).
[43] F. Dalfovo, S. Giorgini, L. Pitaevskii, and S. Stringari, Rev. Mod. Phys. **71**, 463 (1999).
[44] A. Leggett, Rev. Mod. Phys. **73**, 307 (2001).
[45] O. Morsch, and M. Oberthaler, Rev. Mod. Phys. **78**, 179 (2006).
[46] I. Bloch, J. Dalibard, and W. Zwerger, Rev. Mod. Phys. **80**, 885 (2008).
[47] S. Giorgini, L. Pitaevskii, and S. Stringari, Rev. Mod. Phys. **80**, 1215 (2008).
[48] T. Fukuhara, Y. Takasu, M. Kumakura, and Y. Takahashi, Phys. Rev. A **98**, 030401 (2007).
[49] B. DeMarco, and D. Jin, Science **285**, 1703 (1999).
[50] S. Granade, M. Gehm, K. O'Hara, and J. Thomas, Phys. Rev. Lett. **88**, 120405 (2002).
[51] M. Alford, A. Schmitt, K. Rajagopal, and T. Schäfer, Rev. Mod. Phys. **80**, 1455 (2008).
[52] R. Newell, J. Sebby, and T. Walker, Opt. Lett. **28**, 14 (2003).
[53] K. Honda *et al.*, Phys. Rev. A **66**, 021401 (2002).
[54] A. Sommer, M. Ku, G. Roati, and M. Zwierlein, Nature **472**, 09989 (2011).

References for Chapter 1 Continued

[55] C. Chin, V. Leiber, V. Vuletić, A. Kerman, S. Chu, Phys. Rev. A **63**, 033401 (2001).

[56] D. Petrosyan and G. Kurizki, Phys. Rev. Lett. **89**, 207902 (2002).

[57] G. Brennen and I. Deutsch, Phys. Rev. A **61**, 062309 (2000).

[58] J. Baudon, R. Mathevet, and J. Robert, J. Phys. B: At. Mol. Opt. Phys. **32**, R173 (1999).

[59] R. Wynands and S. Weyers, Metrologia **42**, S64 (2005).

[60] H. Lee, C. Adams, M. Kasevich, and S. Chu, Phys. Rev. Lett. **76**, 2658 (1996).

[61] D. J. Han *et al.*, Phys. Rev. Lett. **85**, 724 (2000).

[62] S. Stellmer, B. Pasquiou, R. Grimm, and F. Schreck, (2013). arXiv:1301.4776v1.

[63] W. Ketterle, and N.J. van Druten, Adv. Atom. Mol. Opt. Phy. **37**, 181 (1996).

[64] K. O'Hara, M. Gehm, S. Granade, and J. Thomas, Phys. Rev. A **64**, 051403 (2001).

[65] M. D. Barrett, J. A. Sauer, and M. S. Chapman, Phys. Rev. Lett. **87**, 010404 (2001).

[66] J.-F. Clément *et al.*, Phys. Rev. A **79**, 061406 R (2009).

[67] H. Lewandowski, D. Harber, D. Whitaker, and E. Cornell, J. Low Temp. Phys. **132**, 516 (2003).

[68] N. Poli, R. Brecha, G. Roati, and G. Modugno, Phys. Rev. A **65**, 021401(R) (2002).

[69] V. Vuletic *et al.*, Phys. Rev. Lett. **81**, 5768-5771 (1998).

[70] A. Aspect *et al.*, Phys. Rev. Lett. **61**, 826-829 (1998).

[71] H. Perrin *et al.*, Euro. Phys. Lett. **46**, 141-147 (1999).

[72] D. Boiron *et al.*, Phys Rev. A **52**, R3425 (1995).

[73] M. Kasevich, S. Chu, Phys. Rev. Lett. **69**, 1741 (1992).

[74] T. Kinoshita, T. Wenger, D. Weiss, Phys. Rev. A **71**, 011602 (2005).

[75] Y. Castin, J. Cirac, and M. Lewenstein, Phys. Rev. Lett. **80**, 5305 (1999).

[76] J. Lawall *et al.*, Phys. Rev. Lett. **75**, 4194 (1995).

[77] D. Boiron, A. Michaud, P. Lemonde, Y. Castin, and C. Salomon, Phys. Rev. A **53**, R3734 (1996).

[78] S. Winoto, M. DePue, N. Bramall, and D. Weiss, Phys. Rev. A **59**, R19-R22 (1999).

[79] M. Raizen, A. Dudarev, Q. Niu, and N. Fisch, Phys. Rev. Lett. **94**, 053003 (2005).

[80] E. Schoene, J. Thorn, and D. Steck, Phys. Rev. A **82**, 023419 (2010).

[81] A. Kerman, V. Vuletić, C. Chin, and S. Chu, Phys. Rev. Lett. **84**, 439 (2000).

[82] G. Ferrari, Eur. Phys. J. D **13**, 67-70 (2001).

[83] I. Bouchoule *et al.*, Phys. Rev. A **65**, 033402 (2002).

[84] Y. Castin, J. Cirac, and M. Lewenstein, Phys. Rev. Lett. **80**, 5305 (1998).

[85] C. Chin, University of Chicago, private communication

Chapter 2

Collision-Assisted Zeeman Cooling Theory

A promising non-evaporative cooling method that has potential advantages over existing non-evaporative cooling methods is collision-assisted Zeeman (CAZ) cooling [1]. This method utilizes both optical pumping and collisions between atoms while taking advantage of the Zeeman effect in order to facilitate cooling. The general outlines of the physics behind this cooling were actually proposed in the 1950s [2]. Kinetic energy is converted to magnetic energy through inelastic collisions, and the magnetic energy is then removed from the system by optically pumping the atoms back to their original state. Utilizing magnetic energy levels to remove kinetic energy and cool an atomic vapor has already been successful in what is known as demagnetization cooling [3], and spin gradient demagnetization cooling [4].

While CAZ cooling was presented theoretically in the literature using a single isotope [1], the work presented in this thesis extends the technique to use two isotopes. Using two isotopes should make CAZ cooling more efficient to implement and features several advantages over other non-evaporative cooling methods. At higher temperatures, CAZ cooling removes more energy per photon scatter than Raman cooling, for instance. It is comparatively simple experimentally- the only adjustment needed as the gas cools is tuning a DC magnetic field. CAZ cooling cools in all three spatial directions. There are several technical and physical advantages to using CAZ cooling with multiple species: the magnitude of the required magnetic fields are much reduced, there is more flexibility in the optical pumping, and there are a greater number of options available for obtaining good spin-exchange collision rates. In addition, two-isotope CAZ cooling has an additional a degree of freedom that can be used to address reabsorption effects. The primary disadvantage is that sufficiently dense initial conditions need to be obtained in order to get acceptable cooling rates.

This chapter will first introduce the elements necessary to perform CAZ cooling. Following this is a brief summary of the original CAZ cooling concept, cooling a single atomic species. Then the two-isotope extension of CAZ cooling developed for this work is presented. Finally the advantages and limitations of two-isotope CAZ cooling are discussed.

2.1   Elements of Collision-Assisted Zeeman Cooling

There are three primary elements to CAZ cooling: spin-exchange collisions, a magnetic field, and optical pumping. In order to have spin-exchange collisions, the atoms (or molecules) being cooled must have spin-state structure in their ground state. This means that the sum of electronic and nuclear angular momentum of the atom must not be zero. The requirement that $F = J + I \neq 0$ ensures that the atom has multiple angular momentum projection states (magnetic sub-levels), which are denoted by the quantum number m. The magnetic field is needed to split the normally degenerate m-states so that m-changing spin-exchange collisions will transfer kinetic energy to Zeeman energy. Optical pumping makes it possible to put the population in states that result in a net transfer of kinetic energy into Zeeman energy due to spin-exchange collisions. Optical pumping also replenishes the initial states after the spin-exchange collisions have occurred as well as pumps Zeeman energy out of the system, allowing it to cool.   This section focuses on the physics of each element separately, and then how they come together in a successful CAZ cooling implementation.

2.1.1   The Magnetic Field

An external magnetic field lifts the degeneracy of m-state sub-levels through the Zeeman effect. The Zeeman effect arises from the interaction of the atom's magnetic moment with the magnetic field as given by the Hamiltonian:

$$H_{Zeeman} = -\vec{\mu} \cdot \vec{B}$$ (2.1)

where the magnetic field strength is B, and the total magnetic moment is given by μ. To first order, the shift in energy levels due to the Zeeman effect is:

$$\Delta E_{Zeeman} = -g_F \mu_B B m_F \qquad (2.2).$$

Here, μ_B is the Bohr magneton ($\sim 9.27 \times 10^{-24}$ J/T), m_F is the magnetic sub-level that the atom is in, and g_F is the gyromagnetic ratio, or g-factor, of the atom. The derivation of equation (2.2) and how to calculate the value of g_F can be found in appendix A. The atomic g-factor is the consequence of the various angular momentum components of the atom having different contributions to the total magnetic moment. The atomic g-factor for the lower hyperfine ground state of ^{85}Rb is $-1/3$, and of ^{87}Rb is $-1/2$. The difference arises out of the fact that the two isotopes have different values for the nuclear spin, I (5/2 for ^{85}Rb, 3/2 for ^{87}Rb). The different g-factors cause the two Rb isotopes to have different first-order splittings between adjacent m_F states due to the Zeeman effect:

$$\Delta E_{Zeeman\,85Rb} = -\frac{1}{3}\mu_B B$$

$$\Delta E_{Zeeman\,87Rb} = -\frac{1}{2}\mu_B B \qquad (2.3).$$

The Zeeman shift of equation (2.2) is the result of first-order perturbation theory and works very well for weak magnetic fields (that is fields resulting in Zeeman energy shifts much less than the hyperfine splittings). However, the Zeeman shift at higher magnetic fields begin to have significant contribution from second-order effects. In addition, there are situations where the second-order effects are more relevant for CAZ cooling (as will be discussed later). Thus it is useful to keep in mind that the second order Zeeman shifts in energy are given by [1]:

$$\Delta E_{Zeeman,\,2} = (-1)^F \hbar \omega_{HF} \left(4 - m_F^2\right) \left(\frac{\mu_B B}{2\hbar \omega_{HF}}\right)^2 \qquad (2.4)$$

where $\hbar\omega_{HF}$ is the energy splitting of the ground state hyperfine levels in the absence of a magnetic field (note that the full unperturbed treatment of the Zeeman shift is given by the Breit-Rabi equation [5]). Qualitatively, the second-order Zeeman effect modifies the energy of the m_F states symmetrically about the state $m_F = 0$, which experiences the greatest shift in energy. The qualitative differences in first-order and second-order Zeeman effects can be seen in figure 2.1. The first-order Zeeman shifts are uniform between adjacent m_F states and dominate when the external magnetic field is weak. Second-order effects are not uniform between adjacent states, shift the $m_F = 0$ state (while first-order effects do not), and are only significant at higher field strengths. Second-order effects can nevertheless be important in a weak field regime in certain configurations, for example the originally proposed single isotope CAZ cooling scheme discussed in section 2.2.

2.1.2   Optical Pumping

The next element of CAZ cooling is the process of using photons to prepare atoms in a specified state, called optical pumping. Originally used to create the population inversion of the first lasers, optical pumping has found a place as a valuable tool for atomic physics. In cold atomic physics, optical pumping is commonly used to put atoms into specific hyperfine states or set up a sample with a specific distribution of m_F states.

The process is conceptually simple and is summarized in figure 2.2. A pump laser is chosen such that its wavelength and polarization will excite atoms which are in an undesired quantum state. The excited atoms then decay through spontaneous emission. The decay process is governed by the relevant Clebsch-Gordan coefficients, but pump laser parameters are generally chosen so that decays occur preferentially into the preferred quantum state. Atoms which do not decay into the preferred state are excited again by the pump laser until they do end up in the preferred state. Ideally once in the desired state, the atoms no longer have an excited
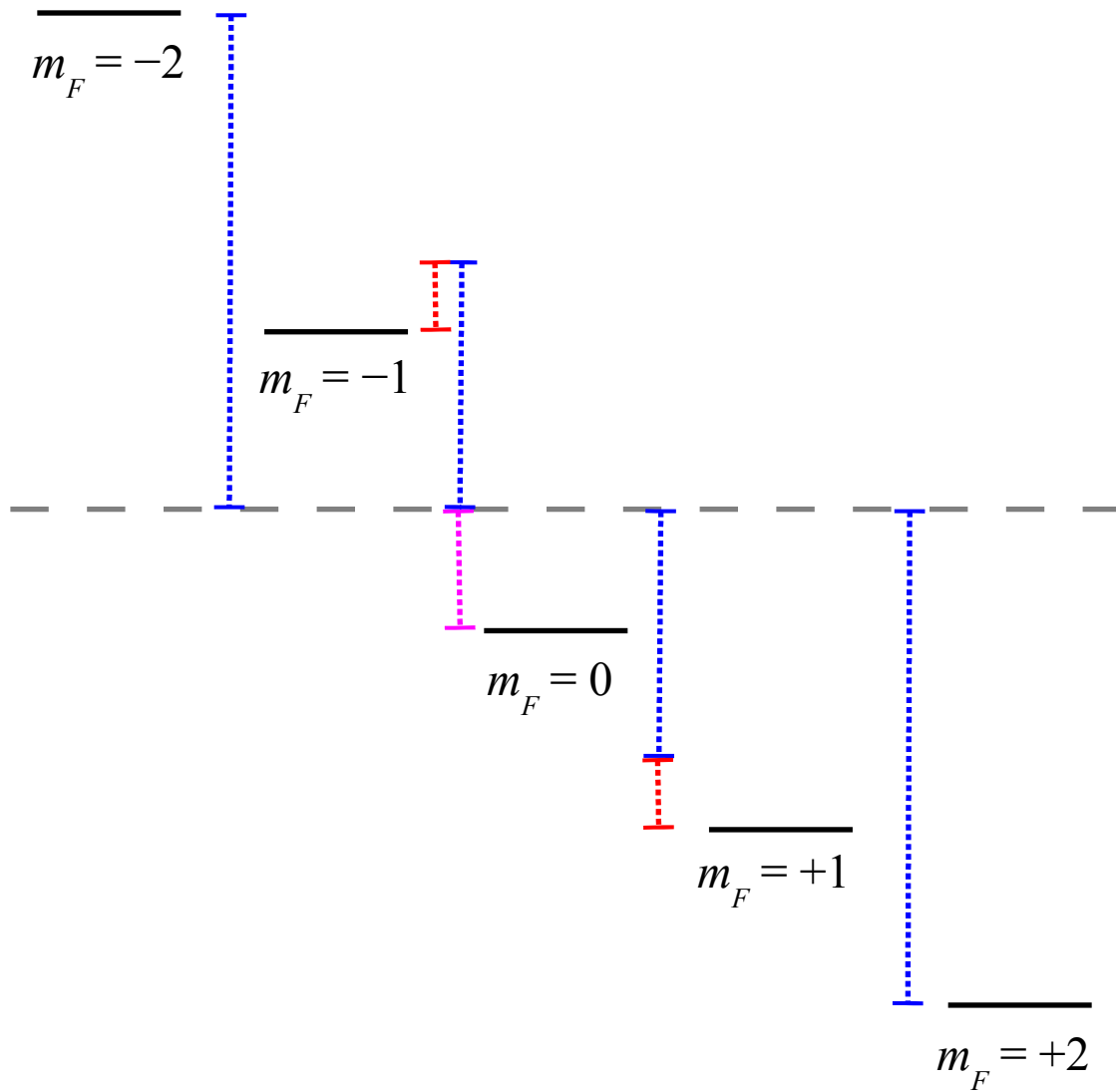
Figure 2.1 Difference in 1ˢᵗ and 2ⁿᵈ Order Zeeman Shifts.
The exaggerated qualitative difference between a first-order (blue) and second-order (red and pink) Zeeman shift in the energies of an atomic $F = 2$ state. For weak fields the first-order shift dominates.   Second-order effects are more relevant at higher field strengths and in certain configurations.   The dashed gray line indicates where the energy levels are degenerate in the absence of a magnetic field.   First-order effects cause adjacent m_F states to have the same magnitude energy splittings and do not affect the $m_F = 0$ state. Conversely, second-order effects shift the energy of the $m_F = 0$ state and result in nonuniform adjacent m_F state level splittings. Second order shifts are of different colors to emphasize that they are non-uniform across the m_F state distribution.
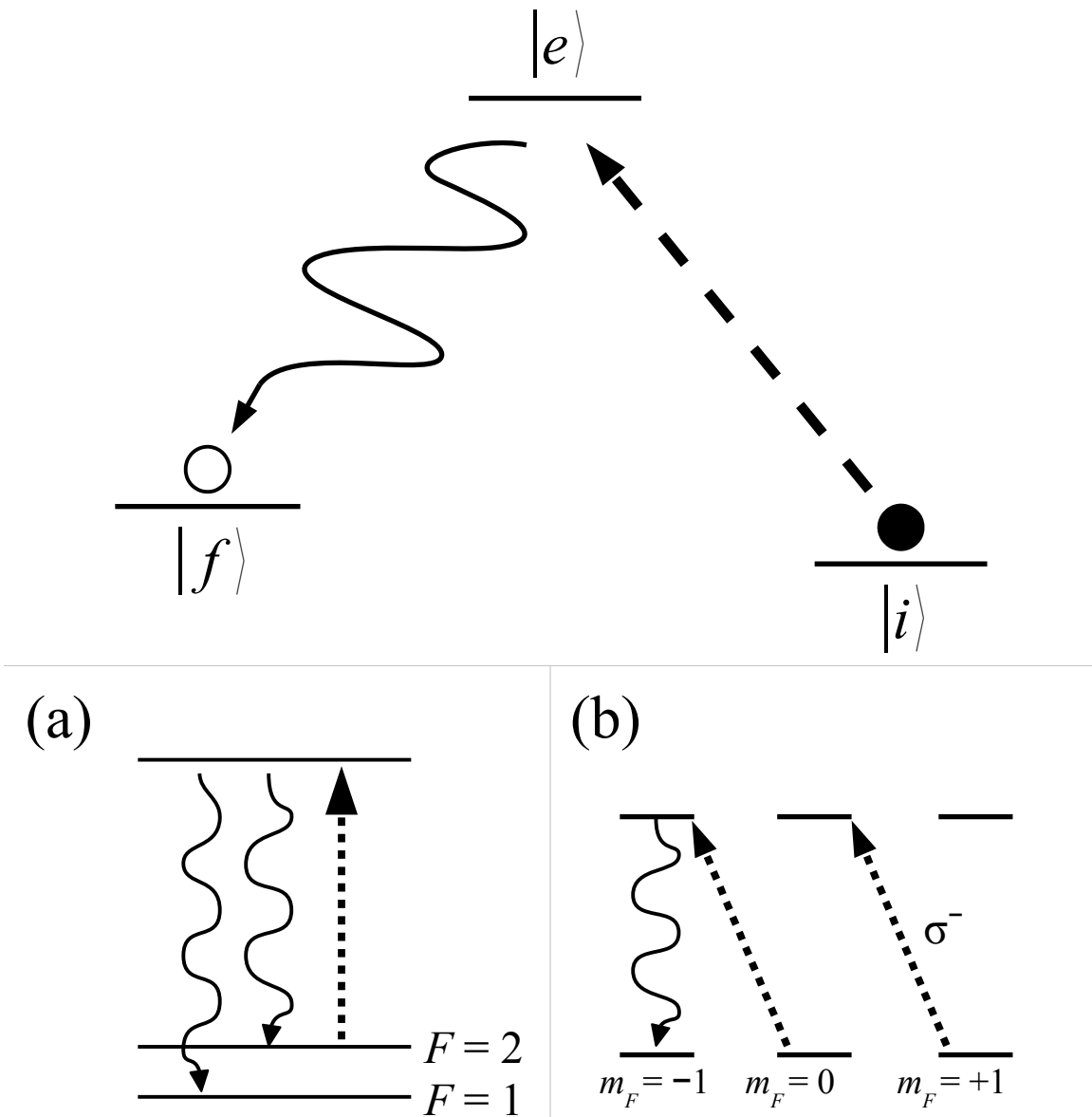
Figure 2.2 Basics of Optical Pumping.
Atoms in an initial energy state ($|i\rangle$) can be "pumped" into a final energy state ($|f\rangle$) by using a laser (dashed line) that excites atoms through an intermediate excited state ($|e\rangle$). Spontaneous emission (wavy line) de-excites atoms to the final state. Atoms in the final state cannot be excited by the pump laser due to the choice of system and laser. For example **(a)** the final state may be at a different energy level that does not have any states accessible at the laser resonance frequency as when pumping into a specific hyperfine state, or **(b)** atoms may be pumped into a specific m_F state by using a polarized pump beam between energy levels with the same F value (not all decay paths are shown in **(b)** for clarity).

state available at the pump laser resonance frequency and thus become completely transparent to the pump beam. Again, appropriate choice of laser parameters ensures that this is the case.

As an example consider optical pumping that puts ^{87}Rb atoms into the lower ($F = 1$) ground state. The splitting of the ground state hyperfine levels of ^{87}Rb (which is 6853MHz) can ensure that the pump beam tuned to the $5S_{1/2}$ $F = 2$ to, say, $5P_{3/2}$ $F' = 2$ state is resonant with atoms in the $F = 2$ ground state, but not the $F = 1$ ground state. Thus, atoms in the $F = 2$ ground state will scatter the pump light while atoms in the $F = 1$ ground state will not (approximately). When an atom scatters photons from the pump light, it is momentarily excited to the $5P_{3/2}$ $F' = 2$ state where it will decay to either of the ground state hyperfine levels. Atoms that decay back to the $F = 2$ ground state will scatter with more pump photons until the entire population of atoms is in the $F = 1$ ground state. This type of pump, depicted in figure 2.2(a), thus prepares the ^{87}Rb in the lower hyperfine ground state.

Note that the atom is at a lower energy level after the pumping. This is because the spontaneously emitted photon carries away excess energy. In an alternative pumping scheme, the $F = 1$ ground state of ^{87}Rb can be spin polarized using a laser resonant with the $F' = 1$ excited state that is also circularly polarized while the atoms are exposed to a uniform magnetic field (to set the quantization axis of all the atoms as well as the light). Such a setup, shown in figure 2.2(b), will prevent the polarized atoms from being resonantly excited because the circularly polarized light can only excite $\Delta m = \pm 1$ transitions ($\Delta m = -1$ in the example in the figure due to the σ^- polarization of the pump). Thus it is not possible for the polarized atoms at the end of the m_F state distribution to be pumped since there is no such m_F state available in the excited state (no $m_F = -2$ state in the excited $F' = 1$ state). Also note that since the atom populations change from occupying many states to less or even just one state, the spontaneously emitted photons carry away entropy from the system.

The examples given are some of the simpler pumping schemes possible. More complex schemes can involve multiple energy levels and/or additional pump lasers. The general idea of any scheme is that all atoms in undesired states are excited, while atoms in a target state remain untouched. Eventually excited atoms will decay and some number of them end in the target state while the others are excited again until they too end up in the target state. The efficiency of the pump process is dependent upon the specific states used and the Clebsch-Gordan coefficients that govern the decays. Ideally atoms are pumped into the desired state using as few photons as possible.

2.1.3 Spin-Exchange Collisions

The final element needed for CAZ cooling to operate is a spin-exchange collision [6]. In general terms, a spin-exchange collision is an inelastic collision between particles which results in a change in the spin states of the colliding pair. Spin-exchange collisions preserve angular momentum, so the sum of the m-state values of the colliding pair prior to the collision must be equal to the sum of the m-state values after the collision [7].

Spin-exchange collisions can be thought of as a consequence of the mixing of the total angular momentum states of the atoms relevant to the collision. In order to make a discussion of these collisions more concrete, collisions between ground state alkali atoms will be considered. Further, quantum statistics will not be considered in this example for simplicity. This is actually the case, for instance, in collisions between two different types of alkali atoms. For a pair of these atoms with a large internuclear separation, the electronic spin of each atom couples with the nuclear spin of the respective atom. This means that at large internuclear separation the hyperfine state basis is the most natural, and the spin state (i.e. hyperfine state) of each of the two atoms can be described individually. When the two atoms have a small internuclear separation however, electron exchange effects become more important and the singlet ($S = 0$, where

38

$\vec{S} = \vec{s}_1 + \vec{s}_2$ and $\vec{s}_i = 1/2$ is the valence electron spin) and triplet ($S = 1$) basis states are the most natural, describing the spin state of the entire system. This is because the difference in the ability of the electrons to overlap in space due to Fermi statistics produces very large energy differences between these spin states when the atoms are close to one another.

A general picture of collision can be constructed by considering two atoms approaching one another from a far distance. Far away, the atom spin states are expressed in the individual atom hyperfine basis; close in, in the electron pair singlet/triplet basis. At a particular separation as the atoms approach, the hyperfine basis is projected onto the electron spin basis. In reality, this is not a sudden projection, but this is a reasonable model of the situation. During the collision, the singlet and triplet portions of the wavefunction pickup a phase factor dependent on the scattering length of each state. Typically the singlet and triplet states will have different scattering lengths due to the different interatomic potential depths between the singlet and triplet states. Thus the singlet and triplet states pick up different phase factors during the collision, which are then projected back into the hyperfine basis as the atoms move away post-collision. The net result is that the hyperfine states before and after the collision will in general be different.

For the alkali metals, the transition zone between near and far internuclear separation is approximately 20 angstroms. The shape of the singlet and triplet potentials will be dependent upon the species involved in the collision, and the spin-exchange collision rate will be dependent on how different the singlet and triplet scattering lengths are. Predicted spin-exchange collision rates for ^{85}Rb and ^{87}Rb are shown in figure 2.3 [8].

2.1.4 Combining the Elements

To reiterate, the necessary components for a successful CAZ cooling setup are: a magnetic filed to break the degeneracy of the ground state magnetic energy levels, optical
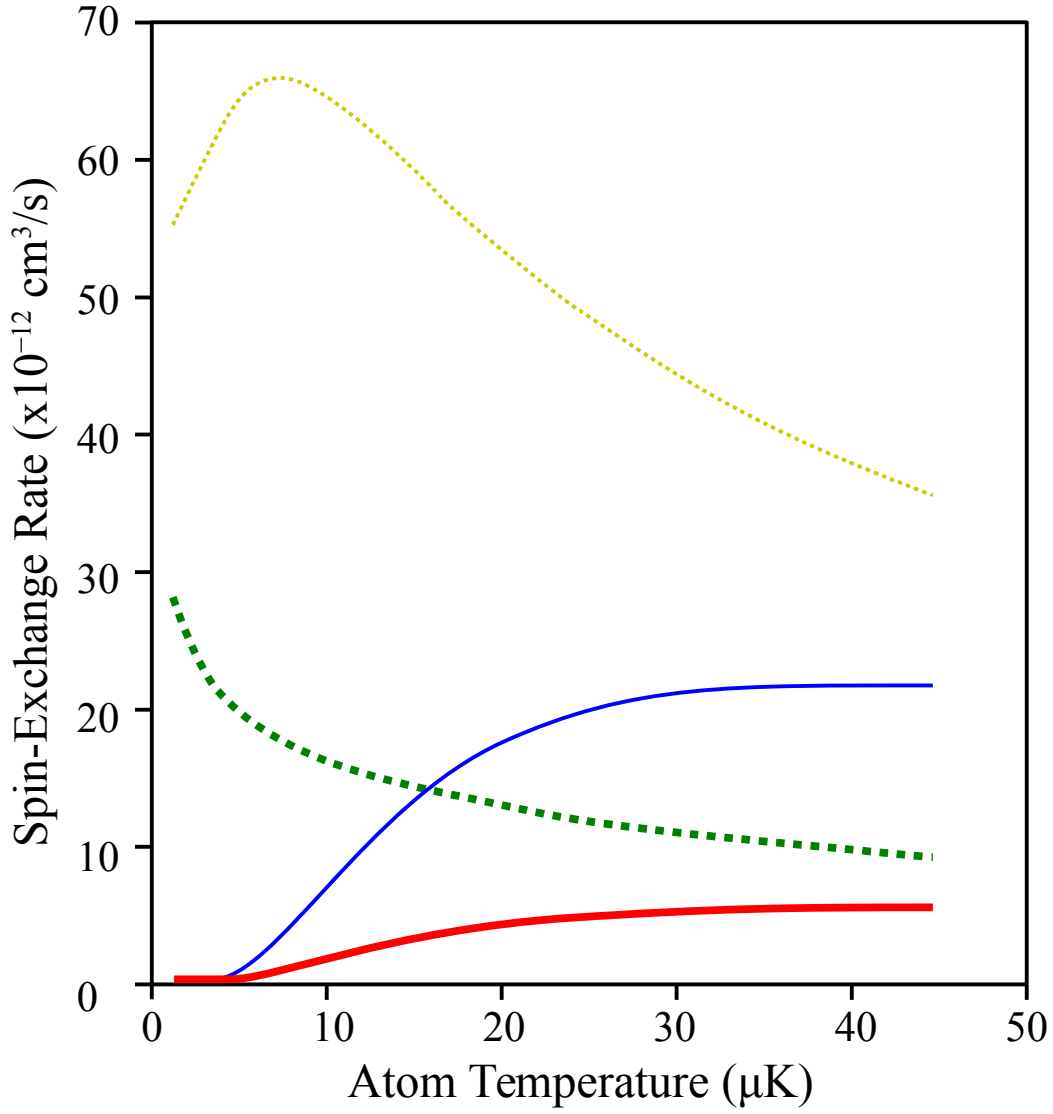
Figure 2.3 Spin-Exchange Collision Rates for ^{85}Rb and ^{87}Rb.
Predicted spin-exchange collision rates calculated from a thermal average over a Maxwell-Boltzmann distribution for (solid) ^{85}Rb $F = 2$, $m_F = -1 \rightarrow -2$ with

Red (thick):	^{87}Rb $F = 1$, $m_F = -1 \rightarrow 0$
Blue:	^{87}Rb $F = 1$, $m_F = 0 \rightarrow 1$

and (dashed) ^{85}Rb $F = 2$, $m_F = -2 \rightarrow -1$ with

Green (thick):	^{87}Rb $F = 1$, $m_F = 0 \rightarrow -1$
Yellow:	^{87}Rb $F = 1$, $m_F = 1 \rightarrow 0$

for a Rb mixture in a 2 G magnetic field. The solid curves are rates of kinetic-energy-reducing collisions which are most relevant to CAZ cooling. The dashed curves are the reverse rates which are higher owing to the fact that they are exothermic.

pumping of the atoms into a spin-polarized state, and spin-exchange collisions to convert kinetic energy into magnetic energy. The Zeeman is responsible for the breaking of the degeneracy of the ground state energy levels. A uniform field of varying strength may be used to control the magnitude of the induced energy splitting between magnetic sub-levels. Because this method requires the use of states that are not magnetically trappable, it cannot be done in a magnetic trap. This requirement makes an optical dipole trap an ideal tool for providing a trapping potential since individual magnetic sub-levels are not affected by the trapping potential [9].

Once the degeneracy of the *m*-states is broken, atoms may be optically pumped into a spin-polarized sample where all the atoms are in the same *m*-state. The spin-polarized atoms undergo spin-exchange collisions that change the *m*-states of the colliding atoms while preserving the sum of their *m* values. Typically, the change of *m* value of the atom is ± 1; however larger changes are possible. Spin-exchange collisions of atoms that change non-degenerate *m*-states can also change the kinetic energy of the atoms since colliding atoms may have different amounts of magnetic energy before and after the collision. Ensuring that the energy transfer of spin-exchange collisions results in a reduction of kinetic energy is accomplished by choice of the spin-polarized state. This is achieved by optically pumping atoms into an *m*-state that when undergoing spin-exchange collisions will always result in a kinetic-energy-reducing collision. Spin-exchange collisions occur naturally [9], and if they happen at a sufficient rate then they can be a very effective tool to transfer energy. After undergoing spin-exchange collisions, atoms are then repumped into the initial spin-polarized state by the optical pump. The optical pump also removes entropy from the gas via scattered photons that carry away entropy. Thus the optical pump allows the process to be repeated and the sample to cool.

Specific examples of CAZ cooling setups are described in the next two sections. Section 2.2 briefly covers the original proposal for CAZ cooling of a single isotope. The extended treatment of CAZ cooling of two isotopes used in this work follows in section 2.3.

2.2 Single Isotope CAZ Cooling

CAZ cooling was originally conceived to be performed with one isotopic species [1], and relies on the second-order Zeeman shift of the m_F states of an atom when subjected to an external magnetic field. Figure 2.4 shows schematically an example of the process for $F = 1$ ground state alkali atoms such as ^{87}Rb. Thus it is assumed that the atoms being cooled have hyperfine structure (e.g. are alkali metal atoms). Here we consider two atoms, both optically pumped into the $m_F = 0$ state. Contributions to the shifts in ground state energy levels due to the first-order and second-order Zeeman shifts are shown in panel (b). The qualitative difference between the types of shifts are important when considering a spin-exchange collision between the two atoms. Conservation of angular momentum requires that the sum of the m_F states after the collision be equal to what it was before. Since both atoms start in the $m_F = 0$ state, the only possibility after a spin-exchange collision is to have one atom in the $m_F = +1$ state and the other in the $m_F = -1$ state. In a situation where only first-order effects are relevant, the total magnetic energy of the system before and after the collision is equal. This is because first-order Zeeman shifts are linear with the m_F value of the magnetic states across a hyperfine level. Thus, to first-order in the Zeeman shift, any spin-exchange collision of isotopically similar atoms in the same hyperfine state increases the magnetic energy of one atom the same amount it decreases the magnetic energy of another, resulting in no net change in (and thus no transfer between kinetic and) magnetic energy.

However, when second-order effects are also considered, the combined state $m_{F1} + m_{F2} = 0 + 0$ will be at a lower magnetic energy than the combined state $m_{F1} + m_{F2} = 1 + (-1)$. Therefore
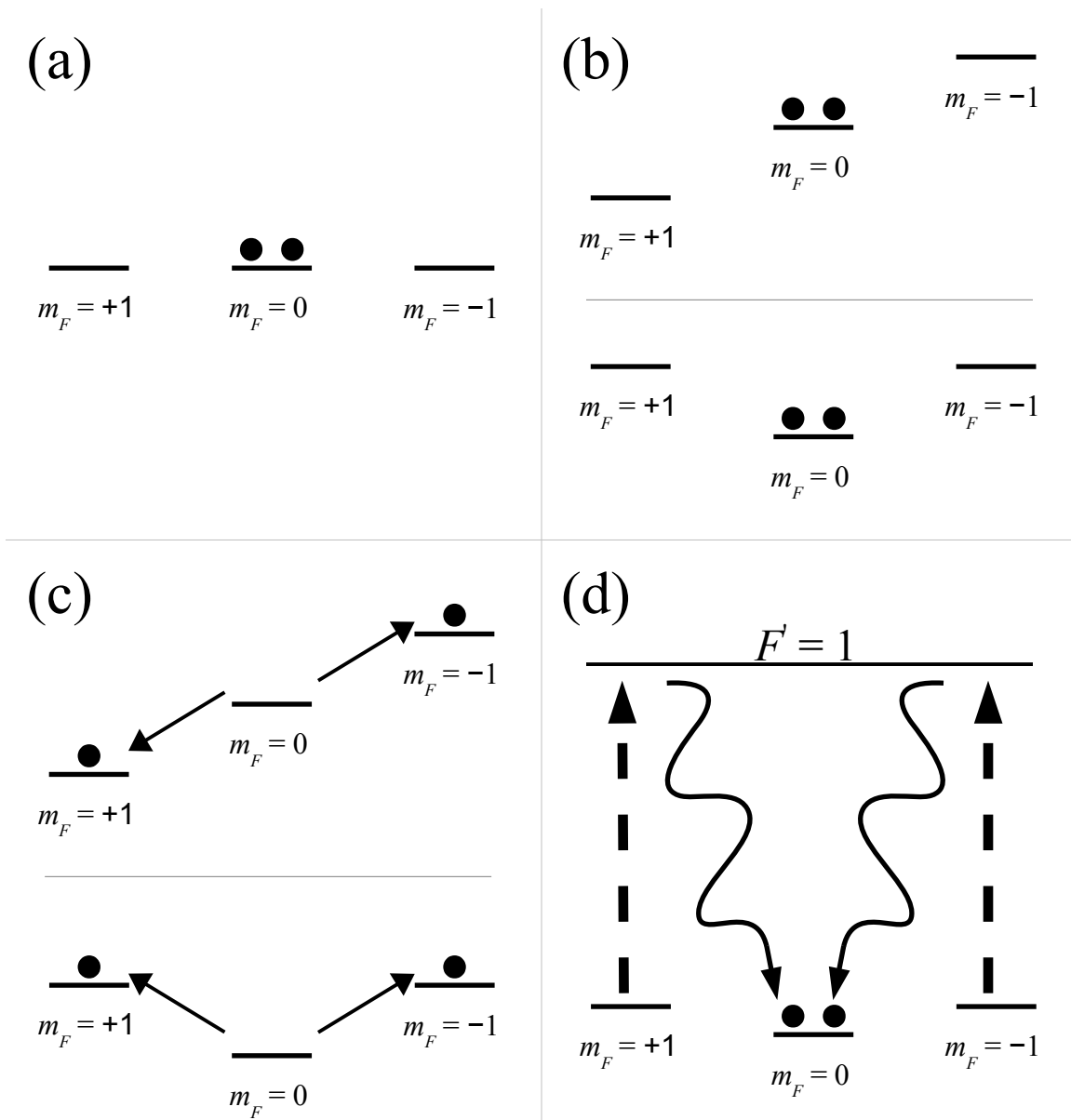
Figure 2.4 Sequence of Events in Single Isotope CAZ Cooling.
(a) Consider two atoms in an $F = 1$, $m_F = 0$ ground state. **(b)** In the presence of an external magnetic field the m_F energy levels split as a result of the Zeeman effect. The unscaled shifts due to first-order (top) and second-order (bottom) effects are shown. **(c)** A spin-exchange collision between the two atoms causes one atom to move into the $m_F = +1$ state and the other into the $m_F = -1$ state. Note that the total energy after the collision is the same to first-order but different to second-order in the Zeeman shift. **(d)** The atoms are then optically pumped back to $m_F = 0$ ground state through the $F' = 1$ state, completing the cooling cycle.

43

an $m_{F1} + m_{F2} = 0 + 0 \rightarrow 1 + (-1)$ collision will leave the atoms in a higher magnetic energy state, with the excess energy coming out of the pair's kinetic energy.

Cooling can be realized by adding a linearly polarized optical pumping beam resonant with the $F' = 1$ excited state since it then pumps the atoms out of the $m_F = \pm 1$ ground states. Because the Clebsch-Gordan coefficient for the $m_F = 0 \rightarrow m_F' = 0$ transition is zero for this transition, atoms that decay back to the initial $m_F = 0$ state will be unaffected by the optical pump beam. The cycle can repeat and every time the atoms are optically pumped back to the initial state spontaneous photons carry away entropy and the sample cools.

The reliance on the second-order Zeeman effect contributes to some of the limitations of single-isotope CAZ cooling. Being relatively small, second-order Zeeman shifts require relatively high magnetic fields to be appreciable, which results in greater experimental difficulty. Using an insufficiently strong magnetic field results in the amount of heat removed per cooling cycle being much too low, and this in turn causes the cooling to be slow. The use of higher magnetic fields poses additional problems for the cooling scheme. The optical pumping becomes more difficult. This is because the natural linewidth of most convenient atoms is much smaller than the first-order Zeeman shifts at high magnetic field. Since both the $m_F = +1$ and the $m_F = -1$ states must be repumped, this means that multiple pump lasers of different frequencies are required, adding to the experimental complexity. With the large first-order Zeeman shift, there will be some mixing of the ground and excited level m-states meaning $m_F = 0 \rightarrow m_F' = 0$ transitions are more likely to occur and are more difficult to suppress. The high magnetic field will also open up high-loss collision channels; for example, dipole relaxation collisions [10] which are inelastic collisions where spin angular momentum is transferred to the atom's orbital motion.

The major limiting factor considered in the original theory paper on this topic was the reabsorption of optical pumping photons due to optical thickness issues. This will indeed likely be a problem, and has been a significant limitation for other non-evaporative cooling methods. We will discuss this issue more in the context of two-isotope CAZ cooling, where there is predicted mitigation of this problem.

Finally, many of the alkali metals which make the best candidates for single-isotope cooling have small (e.g. Na) or very small (e.g. ^{87}Rb) predicted intra-isotope spin-exchange collision rates. These small rates lead to impractically small achievable CAZ cooling rates.

2.3 Two Isotope CAZ Cooling

While CAZ cooling with two types of atoms proceeds in much the same way as with one type of atom, there are benefits to using two atoms. One of the key benefit of using two isotopes in a CAZ cooling experiment is that it is possible to cool utilizing first-order Zeeman shifts. Since first-order Zeeman shifts are so much greater in magnitude, the requisite magnetic fields are much smaller. This means that all of the issues associated with high magnetic fields in the single-isotope case are no longer a major concern. The basic steps of the process are shown schematically in figure 2.5. For simplicity, only two of the m_F states in the hyperfine ground state of an atom of each isotope are considered. To take advantage of first-order Zeeman shifts, the isotopes chosen for the experiment need to have have different atomic g-factors. This causes the Zeeman shifts of adjacent m_F states to be different for the two different isotopes, as shown in panel (b) of the figure. When the two isotopes undergo a spin-exchange collision, as shown in panel (c), one isotope gains magnetic energy while the other loses magnetic energy due to the requirement that angular momentum be conserved. When properly prepared, the net result is an increase of the total magnetic energy (reducing kinetic energy) of the two particle system. One of the isotopes is then optically repumped to its initial state (panel (d)), with the scattered pump

(a)

$|i_1\rangle$ $|f_1\rangle$

$|f_2\rangle$ $|i_2\rangle$

(b)

$|i_1\rangle$

$|f_1\rangle$ E_1

$|f_2\rangle$

$|i_2\rangle$ E_2

(c)

$|i_1\rangle$

$|f_1\rangle$ E_1

$|f_2\rangle$

$|i_2\rangle$ E_2

$$\Delta E_{collision} = E_2 - E_1$$

(d)

$|i_1\rangle$

$|f_1\rangle$

$|f_2\rangle$

$|i_2\rangle$
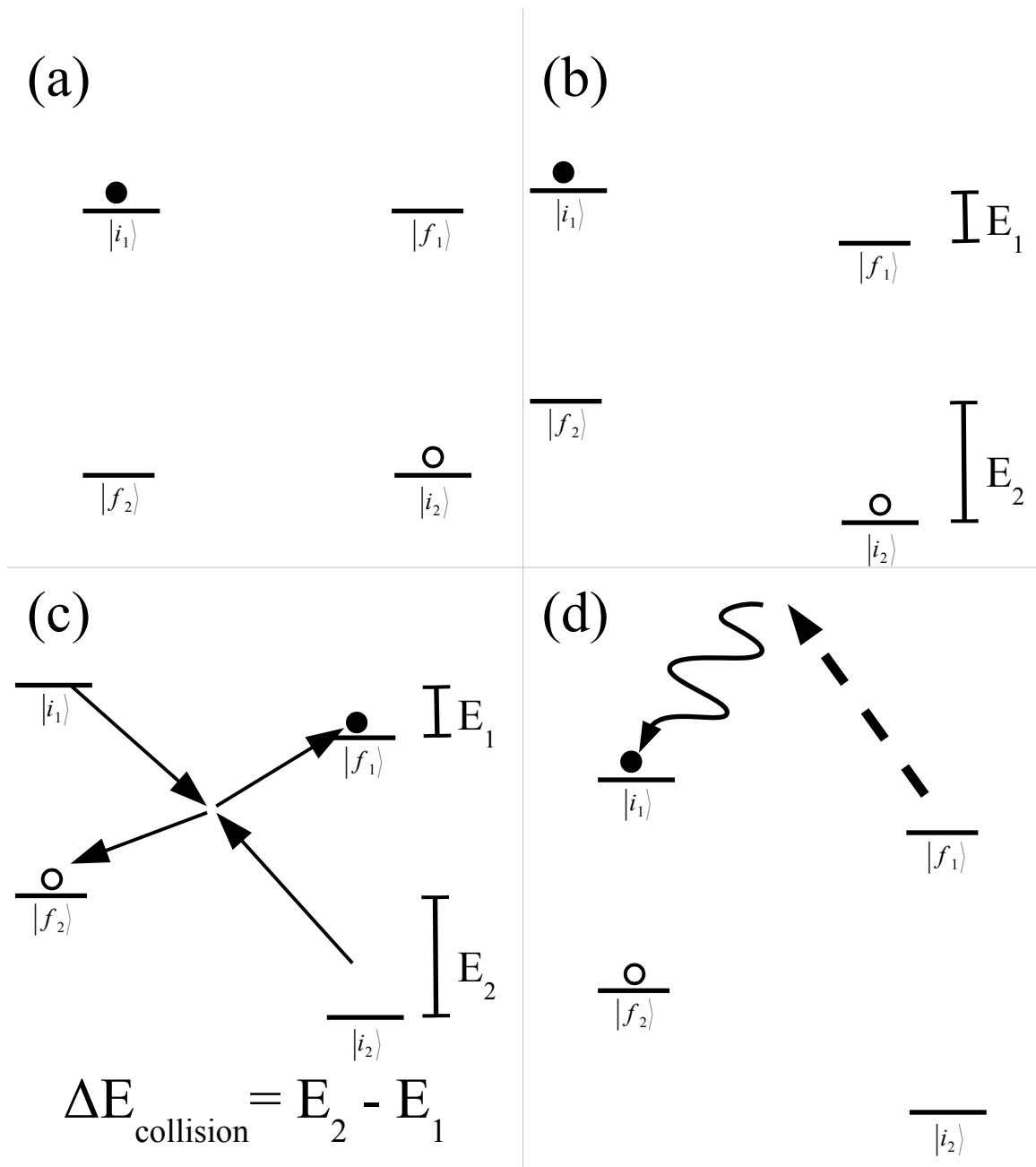
Figure 2.5 Sequence of Events in Two-Isotope CAZ Cooling.
Depicted are only the magnetic sub-levels involved in a generic cooling cycle. **(a)** Consider two different isotopes (black/1 and white/2) in an initial m_F state. **(b)** Exposure to an external magnetic field causes energy levels of adjacent m_F state to separate with different splittings between the different isotopes. **(c)** That difference enables a change in energy after a spin exchange collision where kinetic energy is transferred to magnetic energy. **(d)** One isotope needs to be optically repumped to its initial spin state allowing additional collisions with other atoms of the second isotope.

photon carrying entropy away from the system, thus facilitating cooling. The repumped isotope is then ready to collide with another atom of the second isotope, repeating the cooling cycle. Each cycle removes an amount of kinetic energy equal to the difference in the ground state Zeeman splittings of the two isotopes.

The two-isotope setup only requires a single optical pump so long as the second state can be redistributed. In order to remove entropy, only one of the two isotopes has to have its state populations manipulated irreversibly. Coherent state population transfers can therefore be used for one of the two isotopes, simplifying the required amount of optical pumping. The two-component nature of this approach allows for the possibility to adjust the densities of the two isotopes independently so that the one with near resonant light present can be kept optically thin to reduce light-induced losses while the other is kept dense so that the collision, and thus cooling, rate is relatively high. This will be treated theoretically in detail below. The rest of this subsection includes details and advantages of CAZ cooling utilizing the two isotopes ^{85}Rb and ^{87}Rb.

2.3.1   CAZ Cooling of ^{85}Rb and ^{87}Rb

The isotopes ^{85}Rb and ^{87}Rb were used in this work to realize CAZ cooling. The process is summarized in figure 2.6. Shown are the $F = 1$ and $F = 2$ hyperfine ground states of ^{87}Rb and ^{85}Rb respectively. When subjected to a magnetic field, the m_F states of each isotope shift in energy by different amounts on account of the difference in g-factors. The importance of the difference becomes evident when one considers a spin-exchange collision between isotopes which will result in a net change of kinetic energy equal to the difference of equation (2.3):

$$\Delta KE_{spin-exchange} = -\frac{1}{6}\mu_B B$$ (2.5).

47
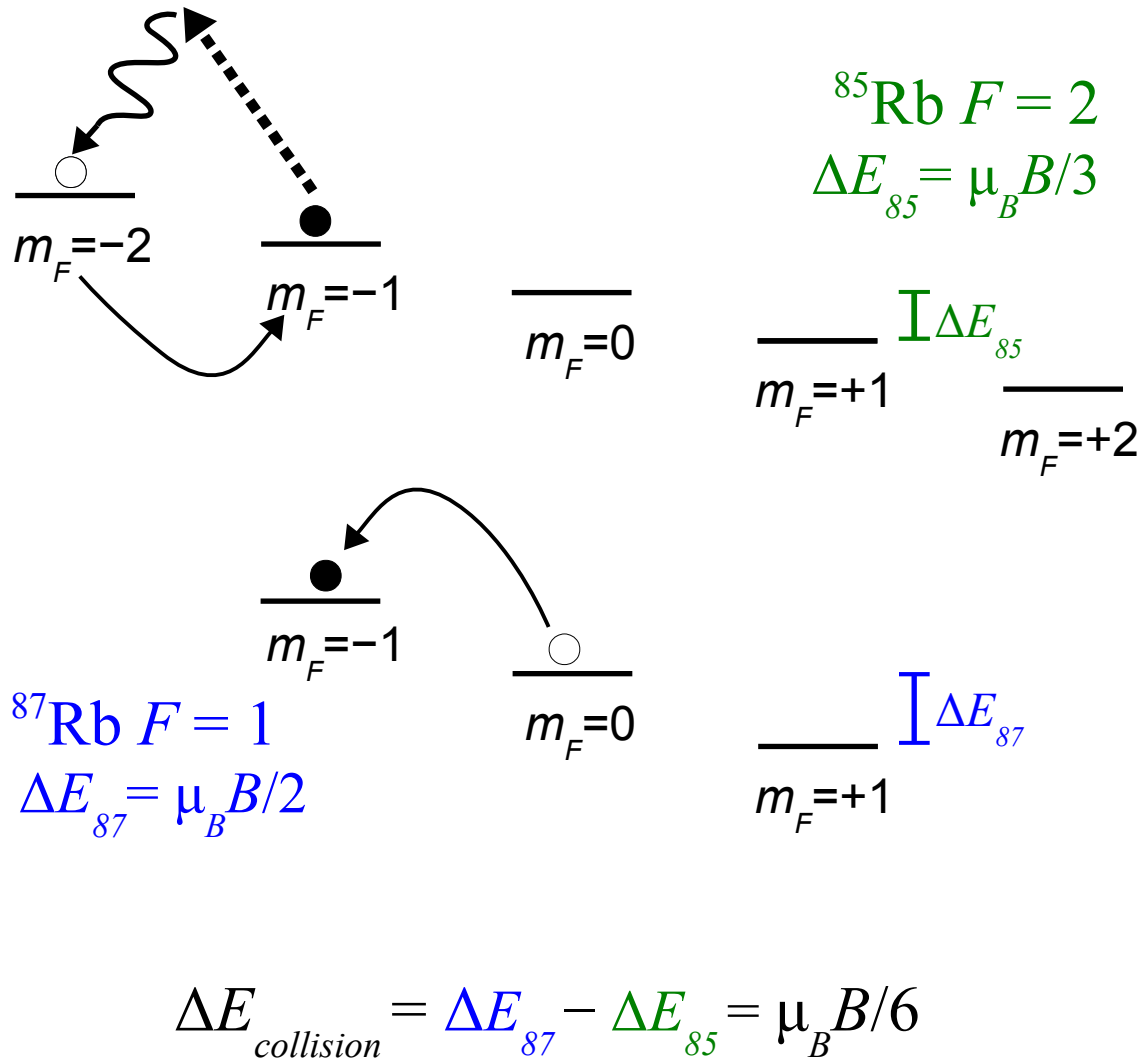
Figure 2.6 Collision-Assisted Zeeman Cooling of ^{85}Rb/^{87}Rb.
Diagram depicting CAZ cooling in an $^{85/87}$Rb mixture. The Zeeman shifted m_F state energy levels of the $F = 2$ hyperfine ground state of ^{85}Rb is shown above with the $F = 1$ hyperfine ground state of ^{87}Rb shown below. Spin-exchange collisions cause state changes from the open circles to the filled circles. Each collision results in a $\frac{1}{6}\,\mu_B B$ gain of magnetic energy with an equal amount of kinetic energy being removed from the colliding pair. ^{85}Rb is optically pumped back into its initial state, keeping it spin-polarized. This ensures that only kinetic-energy-reducing collisions take place. Scattered pump photons carry away entropy, and the atoms cool.

48

The spin-exchange collision shown in the figure results in an $m_F = -2 \rightarrow m_F = -1$ change in the ^{85}Rb and an $m_F = 0 \rightarrow m_F = -1$ change in the ^{87}Rb. Because the energy spitting of the ^{87}Rb levels is greater, the system experiences a net gain in the magnetic energy levels. This increase in magnetic energy comes at the expense of kinetic energy, which means that the colliding pair must have at least $^1/_6$ $\mu_B B$ worth of kinetic energy in order for the spin-exchange collision to occur.

The required kinetic energy to initiate a spin-exchange collision given in equation (2.5) acts as an energy barrier for the collisions to occur. This energy barrier is dependent on the magnetic field strength. Thus if the magnetic field strength is set too high compared to the thermal energy of the atoms in the gas, then few colliding atoms will have enough kinetic energy to initiate a spin-exchange collision. Conversely, if the magnetic field strength is too low, then only a small amount of energy is removed per CAZ cooling cycle and the cooling is not as efficient as it could be. The most efficient cooling will occur when the average kinetic energy of atoms is about equal to the energy barrier set by the magnetic field. Ideally, the kinetic energy of the collision would be just enough to break the spin-exchange collision barrier and the atoms would emerge with only the recoil energy imparted by the pump photon. As the sample cools, the optimal magnetic field strength will decrease. Since the magnetic field strength is controlled by a direct current, it is fairly easy to adjust the barrier height as the experiment is running and thus maintain the highest possible cooling rate. One of the appeals of this type of a CAZ cooling setup is that the primary experimental parameter to be adjusted is a DC magnetic field, which is a relatively straightforward adjustment to make.

So long as the ^{85}Rb atoms undergoing spin-exchange collisions are in the $m_F = -2$ state, only kinetic-energy-reducing collisions will occur. This is because only states with a greater value of m_F are available in the ^{85}Rb energy manifold to exchange spins with an ^{87}Rb atom.

Keeping the ^{85}Rb in the $m_F = -2$ state is the role of the optical pump. Details involving the optical pump will be discussed in section 2.3.2. Since the resonant frequencies to the first excited states of the two isotopes of Rb are different by a few thousand MHz, the near-resonant pump beam for the ^{85}Rb will be far from resonance for the ^{87}Rb. Thus, in principle, the ^{87}Rb can be kept at a much higher density to ensure a high inter-isotope spin-exchange collision rate while the ^{85}Rb is kept optically thin to help mitigate light-induced losses. While it is possible to have intra-isotope spin-exchange collisions between two ^{87}Rb atoms, the net change on the energy balance is zero since the Zeeman splittings are the same between the two colliding atoms. Additionally, the spin-exchange collision rate for two Rb atoms of the same isotope is extremely small compared to that of the inter-isotope spin-exchange collision rate [11].

While the ^{87}Rb depicted in figure 2.6 is in the $m_F = 0$ state prior to the spin-exchange collision, there is no reason that it could not be in the $m_F = +1$ state instead. The change in the kinetic energy in both cases is the same. However, ^{87}Rb atoms in the $m_F = -1$ state do not have any available states for a spin-exchange collision with the spin-polarized ^{85}Rb. Eventually all the ^{87}Rb will end up in the $m_F = -1$ state after having spin-exchange collisions with the ^{85}Rb. This is just the natural consequence of allowing only kinetic-energy-reducing collisions to occur. Spin-exchange collisions will cease at this point, and the cooling of the sample will stagnate. This can be avoided if the ^{87}Rb is periodically exposed to an RF field tuned to drive transitions of $\Delta m_F = \pm 1$ in the ^{87}Rb ground state. This will allow kinetic-energy-reducing spin-exchange collisions to occur again.

The RF field will "scramble" the m_F state populations of the ^{87}Rb, as opposed to driving coherent transfer of atoms from the $m_F = -1$ state to the $m_F = +1$ state. This is because the field will be applied before the population imbalance gets to be very large, which prevents the cooling rate from slowing down too much. This means that in an ideal case, if the $m_F = -1/0/1$ state

population fractions were 0.4/0.4/0.2, they might transfer to 0.2/0.4/0.4. However the transfer will only be perfect if there is the RF power is large enough and there is no noise. These are factors that simply need not be worried about too much in order to have decent performance. Therefore we will discuss the RF field transfer as one that mixes or scrambles the state populations instead of as a perfect coherent transfer.

Since the splittings between m_F states are dependent on the applied magnetic field, the scrambling field will need to be tailored to the conditions of the experiment. It is necessary that the two isotopes used have sufficiently different Zeeman shifts so that the spin-polarized isotope is not scrambled as well. This means that the frequency difference between the RF transitions of the two isotopes must be greater than the rate in which the scrambling needs to occur. As an example, when the [87]Rb populations need to be scrambled once every 100ms, the difference between the RF transitions of the [87]Rb and [85]Rb must be much greater than 10 rad/s. In practice, this is generally easily realized. Any atomic candidate for use in CAZ cooling will also be capable of being scrambled due to the requirement that both isotopes have ground state spin structure in order for two-isotope CAZ cooling to work. Since this technique is applicable to any isotope in CAZ cooling, it is very valuable for its versatility. The use of an RF field to scramble an isotope allows for only a single isotope to require optical pumping.

2.3.2 Optical Pumping Schemes

The optical pump serves not only to spin-polarize [85]Rb and ensure that only spin-exchange collisions resulting in a decrease in kinetic energy occur, but it also is the means by which heat is removed from the system. For an isolated system such as a sample of cold gas, this is the equivalent of removing entropy. Collisions occurring within the sample have only the ability to increase entropy of the atom cloud by the second law of thermodynamics. For example this can be seen when the spin-polarized [85]Rb undergoes spin-exchange collisions with [87]Rb,

relaxing its spin-state distribution. Thus an irreversible process is needed to extract entropy from the system. For CAZ cooling this is achieved by the spontaneous emission of the scattered optical pump photon. So long as spontaneous emission is occurring to one of the isotopes, the sample will cool. Because the optical pump is so vital to the operation of CAZ cooling several schemes for pumping will be discussed here.

2.3.2.a   Direct Optical Pumping

There are several strategies available for spin polarizing a sample of atoms. Probably the most straightforward and easy to implement is what we call direct optical pumping of the atoms. This consists of an appropriately polarized beam, σ^- in our case (see figure 2.7(a)), incident on the ^{85}Rb atoms that pumps them to the excited state and changes the m_F sub-level by -1. Atoms in the $m_F = 0$ ground state will be pumped to the $m_F = -1$ excited state, atoms in the $m_F = +2$ ground state will be pumped into the $m_F = +1$ excited state, et cetera. When pumping on the $F = 2 \rightarrow F' = 2$ D1 transition, atoms in the $m_F = -2$ ground state will be approximately unaffected since there is no resonant $m_F = -3$ excited state available. Excited atoms then decay back to the ground state through spontaneous emission whose photons carry entropy away from the sample. This decay process will put the atom into one of three possible m_F states ($\Delta m_F = \pm 1, 0$ from the excited state, if available) determined by the relevant Clebsch-Gordan coefficients. It is possible that the Clebsch-Gordan coefficients favor a decay resulting in a $\Delta m_F = +1$ transition which would move the atom the wrong way through the spin-state distribution; however, since the excitation moves the atom exclusively in the desired direction, the worst-case scenario is that the atom ends up where it started. The best-case scenario will put the pumped atom in the ground state with $\Delta m_F = -2$ from its initial state. Most importantly, after considering all possible pumping paths, there is on average a net migration towards the desired spin polarized state.
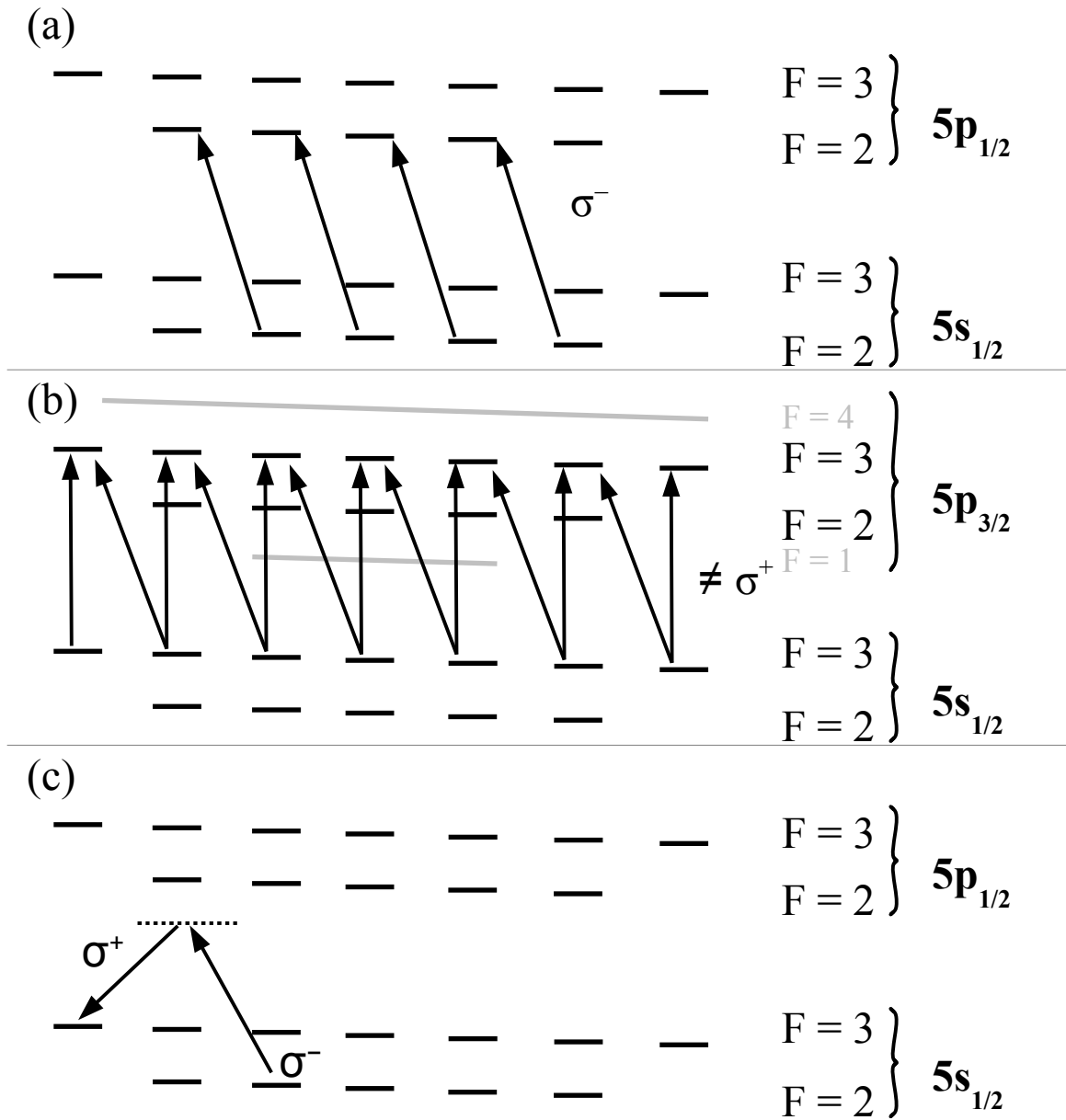
Figure 2.7 Optical Pumping for Spin-Polarization of ^{85}Rb.
Diagram of the various pumping laser transitions useful for spin-polarization of ^{85}Rb. **(a)** Direct optical pumping uses circular polarized light. **(b)** An repump is necessary for all pumping schemes with polarization set as elliptical with no σ^+ polarization component. **(c)** A Raman transition pump (only one shown) uses two polarized beams which coherently transfers atoms over via a virtual state to be cycled by the repump laser. The goal of each pumping method is to put atoms into a state with a high probability to end up in the $F = 2$, $m_F = -2$ ground state.

In addition to decaying into different magnetic sub-levels, the atoms may also decay into an upper hyperfine m_F state. This is an issue for several reasons. For one, these atoms will negatively affect the cooling efficiency since they are unlikely to have much spin-polarization, and are thus capable of spin-exchange collisions which result in an increase in the kinetic energy of the sample. More importantly, the g-factor for the upper hyperfine state is opposite in sign as compared to the lower hyperfine state. This means that atoms undergoing spin-exchange collisions that would reduce kinetic energy in the lower hyperfine ground state will actually increase kinetic energy in the upper hyperfine ground state on account of the fact that the Zeeman shift is in the opposite direction. So instead of removing $^1/_6\mu_B B$ of kinetic energy, upper hyperfine ground state interisotope spin-exchange collisions instead add $^5/_6\mu_B B$ of kinetic energy. In addition, atoms in the upper hyperfine ground state have a higher loss rate from the trap due to hyperfine state changing collisions. The same physics that produces spin-exchange collisions that change m-states can also change hyperfine states. Thus when spin-exchange collisions are present exothermic hyperfine state changing collisions are also present. Due to the relatively large splitting of the hyperfine states (3036 MHz for ^{85}Rb), these collisions release enough energy that the colliding pair will be lost from any experimentally realizable optical trap. The collision rate for hyperfine changing collisions in ^{85}Rb is 3×10^{-12} cm^3/s [10]. Therefore upper hyperfine ground state ^{85}Rb atoms must be cleared out quickly. Clearing the ^{85}Rb upper hyperfine ground state population can be handled by utilizing a secondary optical pumping beam (repump), as shown in panel (b) of figure 2.7. The repump is set along the $F = 3 \rightarrow F' = 3$ transition on the D2 line of ^{85}Rb, and is set to have no σ^+ polarization component that would work against the spin polarization. Hence, there will be a net migration of atoms to the desired state. A pure σ^- beam is undesirable because the linear component ensures that atoms cannot get stuck in the $F = 3$, $m_F = -3$ ground state which has no σ^- transition.

The advantage of direct optical pumping is that it is relatively easy to implement experimentally. It does rely on near-resonant light, so there will be a trade-off between the optical pumping rate and light-assisted collisional losses [12-14]. In general in optical traps, light-assisted collisional losses increase for light that is closer to resonance. Thus increasing the pump beam intensity will increase the pumping rate (and by extension cooling rate) as well as the loss rate. Light-assisted collisional losses can be decreased by detuning the optical pumping light. However, that also slows the optical pumping rate and so any possible improvement is dependent on the interplay between these two effects. Therefore it is important to observe the loss rate versus the pumping rate as a function of pump beam detuning, since the interplay of all the factors could be favorable or not. If the situation arises that the spin polarizing pump becomes too slow to be practical (i.e. the sample cannot be kept spin polarized) or induces too much loss, then a different pumping scheme must be employed.

2.3.2.b   Combination Microwave-Optical Pumping

One alternative to direct optical pumping is the combination of optical and microwave pumping. In this situation, resonant microwaves are used to excite ground state atoms into the upper hyperfine state so that they can then be optically pumped (by use of the same repump beam discussed in the direct optical pumping scheme). Since spontaneous emission occurs from the atoms pumped out of the upper hyperfine ground state, entropy is removed from the system, which is then able to cool. The primary advantage of this approach is that it requires one less optical pumping beam which can induce near-resonant losses. However, the efficiency of the pumping process becomes reliant on the microwave coupling into the system. If the experimental apparatus was not specifically designed to efficiently deliver microwaves to the sample region, then the spin polarizing pump can be limited by the efficiency of the microwaves which are delivered to the target. If transitions cannot be resonantly selected, then an adiabatic

rapid passage can be used (adiabatic rapid passage is the subject of section 3.6). Good microwave coupling to the atoms would ideally involve using a glass vacuum chamber, good quality microwave antenna, and high-quality microwave source.

2.3.2.c Pumping Using Raman Transitions

The final, and most ideal in principle, spin polarization method to be discussed here utilizes Raman transitions. Here, a two-photon pumping process moves atoms across the distribution and into the upper hyperfine ground state, seen as an example in figure 2.7(c). Note that $\Delta m_F = -2$ transitions are driven in this realization of the Raman-based optical pumping, in contrast to typical Raman transitions (see appendix B). The repump laser then cycles the atoms back to their lower hyperfine ground state and also carries away entropy from the system through scattered photons. This Raman transition needs two beams of opposite circular polarization: one to drive atoms out of a non-extreme m_F state and into an excited virtual state, the other to simulate emission out of the virtual state into the upper hyperfine ground state while further pumping the atoms into the desired spin orientation.. The frequencies of the Raman beams are set such that virtual state is not too near an internal energy state. The difference in frequencies between the two Raman beams is set so as to be resonant with the desired transition. For example, in the case of spin polarizing ^{85}Rb, the difference in laser frequencies will roughly match the ground state hyperfine splitting of 3036 MHz. If the two Raman beams are co-propagating then the Raman transition is not sensitive to the velocity of the individual atoms. This method is most efficient at moving atoms across the m-state distribution as compared to the other techniques discussed here. This is due to the fact that pump cycles nearly always result in forward progress towards spin polarization. The drawback of this method is that it takes more work to setup experimentally. In addition, there becomes an added complication when adjusting the Zeeman splittings by changing the magnetic field- the frequency difference of the Raman

beams must also be adjusted. This should not be particularly difficult, but care would need to be taken to ensure that the Raman transition is properly set. For more detail on this novel application of Raman transitions see appendix B.

2.3.3   Advantages and Limitations

There are several features of two isotope CAZ cooling that make it attractive compared to other non-evaporative cooling methods. For example, the spin-exchange collision energy barrier that determines the greater part of the energy removed per cooling cycle is controlled by a DC magnetic field- an adjustment that is easy to achieve experimentally. Compared to Raman cooling, which has had the greatest success as a non-evaporative cooling technique, two isotope CAZ cooling removes a large amount of energy per photon scatter. Raman cooling typically only acts on the atoms in the direction of laser propagation, but CAZ cooling operates in all three spatial dimensions, allowing it to cool more efficiently.

It should be mentioned that a cooling scheme that takes advantage of the Zeeman energy splittings does not require spin-exchanging collisions to be the specific type of inelastic collision to transfer kinetic into Zeeman energy. In fact, another reported use of magnetic energy level splittings for cooling, called demagnetization cooling [3], relies on dipolar collisions instead of spin-exchange collisions. Spin-exchange collisions are s-wave collisions, while dipolar collisions are less common p- and d-wave collisions. This is likely to prove beneficial for two isotope CAZ cooling since the collision rates are generally faster and will thus convert kinetic energy into Zeeman energy more rapidly. For demagnetization cooling performed with chromium atoms in reference 3, cooling was reportedly limited by optical pumping polarization effects due to imperfect control of the external magnetic fields. The number of atomic species that demagnetization cooling can performed on is relatively limited, while two isotope CAZ cooling offers more possibilities.

Another non-evaporative cooling technique that operates on a slightly different mechanism is called spin gradient demagnetization cooling [4]. In spin gradient demagnetization cooling, a strong magnetic field gradient is used to spatially separate spin states in an optical lattice. As the field gradient is relaxed, spin states begin to mix owing to a non-zero tunneling probability between lattice sites. Mixing of the spin states increases the entropy of the spin state distribution, which comes at the expense of kinetic energy. While this type of cooling is in the same "family" of cooling techniques as demagnetization and CAZ cooling, it is not a cycled cooling scheme. Thus it is more valuable as a one time enhancement to the minimum temperature of an ultracold sample that is best done after another non-evaporative cooling method has been used.

Compared to single isotope CAZ cooling, two isotope CAZ cooling operates at much lower magnetic field strengths. This is beneficial because high magnetic fields can cause dipole relaxation collisions as well as complicate the optical pumping process. In addition, the second isotope in two isotope CAZ cooling adds additional freedom to the experimental design. The larger number of possible isotopic combinations allows for a large range of optical pumping configurations as well as provides many opportunities for a finding a high spin-exchange collision rate.

For a perfect idealized CAZ setup the coldest temperature attainable would be dependent only on the photon recoil energy imparted by a single spin polarization pump photon. For ^{85}Rb the recoil energy is: $E_R/k_B = 180$ nK. Split between the three spatial directions of the two isotopes in the system, that would correspond to a gas temperature of 30 nK. This number assumes only a single photon is needed to optically repump an atom, which in practice is not possible. More likely to be limiting factors are reabsorption, three-body recombination, and an inadequate cooling rate compared to trap lifetimes and external heating due to an inadequate initial density

of the atoms. Fortunately owing to the unique features of two-isotope CAZ cooling there should be ways to reduce both reabsorption and three-body recombination should they become a major issue. Should the initial density be too low for a sufficiently high spin-exchange collision rate, the lifetime of the atoms in the trap will be too short compared with the cooling rate. Improving the initial conditions would be the solution in such a scenario. The remainder of this section discusses these limitations in turn.

2.3.3.a   Three-Body Recombination of ^{85}Rb

A potential limiting factor specific to the ^{85}Rb – ^{87}Rb system is the three-body recombination of ^{85}Rb. In a three-body recombination event, three atoms have an inelastic collision resulting in a bound molecule and an energetic atom. This results in both heating of the sample as well as loss from the trap. The three-body recombination rate of ^{85}Rb is relatively high [15], around 5×10^{-25} cm^3/s. This means that at an atom density of around 10^{12} cm^3/s or so (about an order of magnitude higher than the current trap conditions right after loading), the trap lifetime of the ^{85}Rb in the optical trap will be on the order of one second due to three-body losses. As the gas cools and its density increases, so will the recombination rate. One possible mitigation technique is to reduce the confinement of the optical trap as the cooling proceeds. The phase space density will remain the same for adiabatic changes in the potential and thus the cooling will continue to be effective. Since the density dependence of the three-body recombination rate scales stronger than that of the spin-exchange rate, reducing the density in a three-body recombination limited regime will improve the ratio of the cooling rate to the three-body loss rate. Thanks to the lack of dependence on trapping geometry for CAZ cooling, this can be done multiple ways. Not only could the trap depth be relaxed by reducing the optical intensity, but the trap geometry could be changed in a way that allowed the atoms to spread out. If the three-body recombination rate cannot be reduced sufficiently using density adjustments

during cooling then, thanks to the flexibility in choice of two-isotopes, other isotopic combinations can be used instead (such as ^{87}Rb and ^{6}Li).

2.3.3.b   Insufficient Initial Cooling Rate

In CAZ cooling, the spin-exchange collision rate and the optical repumping rate determine the cooling rate. The optical pumping rate is ultimately limited by reabsorption. Meanwhile, a low density of atoms will limit the spin-exchange collision rate. One of the appealing features of a CAZ cooling setup is that as a sample cools its density will increase and thus the cooling rate should increase with experimental run time. However, if the initial cooling rate is not sufficient then this benefit will never be realized. This is due to the finite lifetime of the trap (in our setup trap lifetime is between two and three seconds). What this means is that if the lifetime is too short in comparison to the initial cooling rate then CAZ cooling will not have much practical utility.

Should the initial cooling rate be the limiting factor, there are several possibilities available to try to improve the situation. For one, the loading of the optical trap can be optimized to achieve the maximum phase-space density possible. Alternatively, the optical trap itself could be changed to provide a situation which is more conducive to a strong cooling rate. Deeper traps can hold more atoms at higher densities. Improving the quality of the vacuum chamber would allow for more time for CAZ cooling to work. If the parameters of the apparatus itself cannot be tweaked in a manner to improve the initial conditions, then changing the isotopes in the mixture could be an avenue if there is a reasonable expectation that the spin-exchange collision rate would be significantly better with a different isotopic combination. Unfortunately several of these solutions require major experimental reconfiguration.

2.3.3.c Reabsorption

When a laser cooled cloud of atoms is optically thin, the scattered photons are able to carry away entropy and facilitate the cooling of the gas. However, if the cloud is optically thick to the laser light, scattered photons will be reabsorbed. Figure 2.8 depicts a cartoon of the process. Reabsorption [16,17] occurs when the photon mean free path is shorter than the spatial extent of the atom cloud. Thus the size, density, and geometry of the atom cloud play an important role in reabsorption. In addition, the intensity and detuning of the laser light affect reabsorption.

Reabsorption is a hindrance to cooling because scattered photons have a random direction, polarization, and phase. This is detrimental to cooling because the scattered photon imparts a random momentum kick when it is re-scattered that adds heat to the sample. As a cloud of atoms cools its density will increase causing the cloud to become more opaque to optical pumping light and reabsorption effects become more severe. Thus the optical pumping rate can become limited to a relatively slow rate for optically thick gasses. This can become the main limit to CAZ cooling if the optical pumping rate becomes slow compared to the spin-exchange collision rate. Ideally the optical pumping rate would be infinitely fast, and the cooling rate would be limited by the spin-exchange collision rate. However reabsorption effects in gases of high optical depth force the need to reduce the optical pumping rate through lowering the laser intensity or increasing laser detuning. Reabsorption is an intrinsic issue that tends to be the limiting factor in non-evaporative cooling methods [18]. As such a brief discussion of the scaling of the reabsorption rate on experimental parameters follows.

There are two types of reabsorption effects which can limit non-evaporative cooling methods: one-photon and two-photon. The one-photon reabsorption event is conceptually
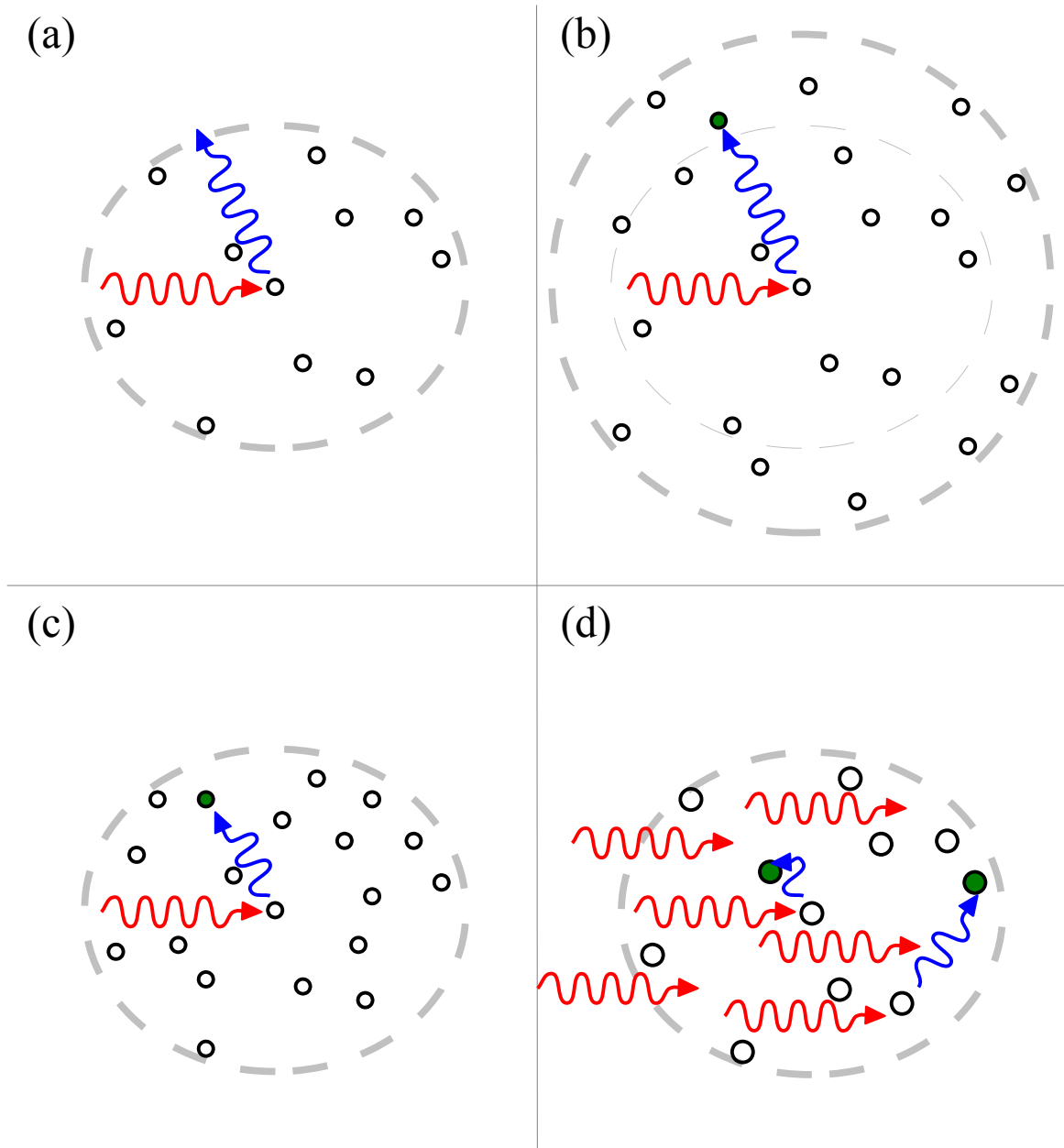
Figure 2.8 Cartoon of Reabsorption of Scattered Photons.
(a) In laser cooling, scattered photons carry away entropy from the cloud (dashed line) of cold atoms. Incident photons are red, and scattered photons are blue. If scattered photons are reabsorbed by other atoms in the sample (green), the cooling efficiency is decreased. **(b)** A larger atom cloud size of equivalent density, or **(c)** fixed sized cloud of higher density will undergo more reabsorption events. In addition, **(d)** laser parameters such as intensity and detuning can increase the reabsorption rate by increasing the number of scattering events or increasing the effective scattering cross-section respectively.

intuitive- the scattered photon is simply scattered by another atom. When the optical depth of the atom cloud is not too thick, the rate of such scattering events follows the relation:

$$R_{reabsorption} \propto R \sigma\, n\, l \qquad (2.6).$$

Where R is the cooling rate, σ is the reabsorption cross-section, n is the density of the atom cloud, and l is the average spatial extent of the cloud. The cooling rate is assumed to be proportional to the scattering rate of optical pumping photons with an individual atom and is thus dependent on the parameters of the optical pumping laser (at sufficiently large detunings):

$$R \propto \frac{I_L}{\Delta^2} \qquad (2.7).$$

Thus the laser intensity I_L, and laser detuning Δ, can be adjusted in tandem in a way that maintains a constant cooling rate. This is desirable because the cross-section for one-photon scattering only depends on the laser detuning so Δ may be adjusted to reduce the reabsorption effects. For one-photon reabsorption the cross-section scales as:

$$\sigma_1 \approx \frac{1}{1 + c_1 I + c_2 \Delta^2} \qquad (2.8).$$

Here, I is the intensity of the scattered light, and the c values are constants. The value for $c_2 \Delta^2$ is much greater than one; therefore, σ_1 is proportional to Δ^{-2} for low intensities. The one-photon reabsorption rate ($R_1 = R_{reabsorption}$ for a single photon) at a constant cooling rate is thus strongly dependent on detuning, scaling in the limit of large detuning as:

$$\frac{R_1}{R} \propto \frac{1}{\Delta^2} \qquad (2.9).$$

This is fortunate because it means one-photon reabsorption effects can be mitigated by detuning the cooling laser. Unfortunately two-photon reabsorption events do not share this dependence.

Two-photon reabsorption scattering occurs when the scattered photon from one atom combines with a pump laser photon to both excite and then induce stimulated emission in a

second atom. Two-photon reabsorption is facilitated through a coherent Raman transition where the second atom is pumped through a virtual state. Figure 2.9 demonstrates the process. Since the physics involved in this type of event is quite different, the two-photon scattering cross-section scales very differently [16]:

$$\sigma_2 \approx \frac{R}{1 + \alpha R} \tag{2.10}$$

Here, α is another constant. For sufficiently strong cooling rates consistent with efficient cooling, the cross-section tends to a constant and so does the two-photon reabsorption rate at a fixed cooling rate:

$$\frac{R_2}{R} = constant \tag{2.11}$$

Since the two-photon reabsorption rate is proportional to the cooling rate, it can only be reduced at the cost of decreasing the effectiveness of the cooling. While reabsorption can be fairly easily managed when primarily due to one-photon scattering, eventually the two-photon scattering will take over and limit the final attainable temperature. For this reason, non-evaporative cooling methods tend to be limited by reabsorption.

This is likely to be the case in CAZ cooling as well. However, changing the laser parameters is not the only possible way to mitigate reabsorption. For example, reabsorption has been successfully mitigated through the modulation of the optical pumping light [19].

In addition to this, two-isotope CAZ cooling offers extra means to suppress reabsorption effects as described below. This will be done by modeling the CAZ cooling rate and examining the theoretical differences between the technique utilizing one and two isotopes. This will put into perspective how two-isotope cooling compares with cooling of a single atomic species alone when temperatures are cold enough that reabsorption effects are prominent.
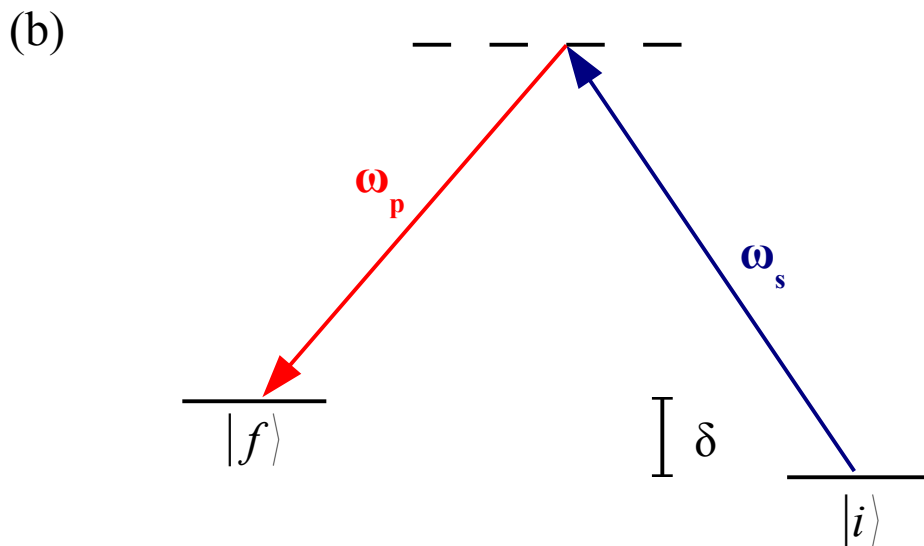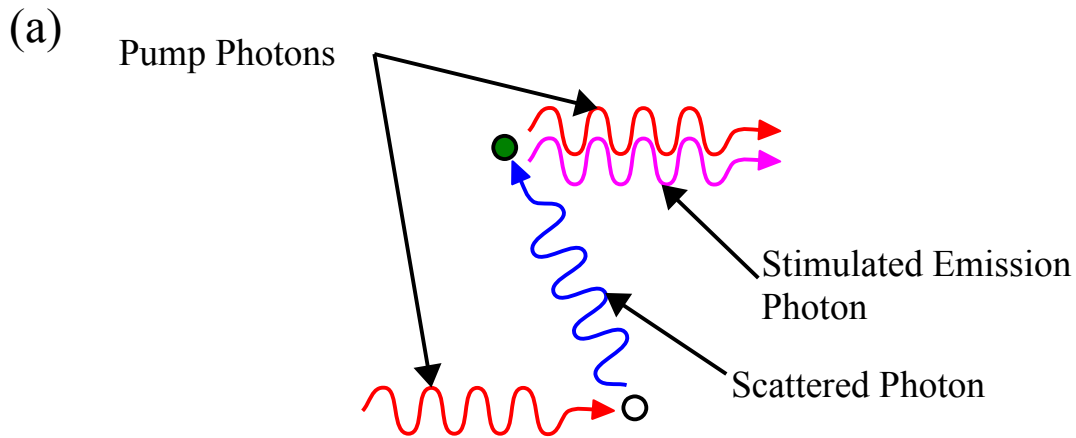
Figure 2.9 Two-Photon Reabsorption Event.
(a) Cartoon of a two-photon reabsorption event, where a scattered photon (blue) from an optically pumped atom (white circle) combines with a pump photon (red) to drive an excitation and stimulated emission (pink) in another atom in the sample (green circle). **(b)** The unscaled energy levels involved include an excited virtual state (dashed line). Initial and final states of the reabsorbed atom may be different because the scattered photon frequency (ω_s) may be different than the pump photon frequency (ω_p) by a shift (δ) resulting from a relative difference between velocities of the two atoms involved. δ may be positive or negative, and the order of the roles of the scattered and pump photon may be reversed dependent on the particular situation of the event.

2.4   Cooling Rate of Two Isotope CAZ Cooling

This section details a theoretical model developed for describing the CAZ cooling rate. There are several motivations for the development of such a model. For one, the model allows the prediction of the CAZ cooling rate for a given spin-exchange collision rate and under some assumptions about the optical pumping rate. Later (section 2.4.2), the model will be used to show theoretically that a two-component cooling arrangement, such as two-isotope CAZ cooling developed in this work, can dramatically increase the cooling rate at low temperatures over a comparable one-component cooling setup. Finally, the model will be used to compare the experimentally observed cooling rate to expectations (see chapter 5).

2.4.1   Model

Despite the number of m_F states in a system like that of ^{85}Rb and ^{87}Rb, it is possible to write a simple analytical expression for the two isotope CAZ cooling rate that has a wide range of validity. This is possible through using detailed balance considerations and the fact that certain collision channels are dominant for the magnitude of magnetic fields likely to be used. In this analytic expression it is assumed that the two different atoms are in sufficient thermal contact so that their temperatures are not widely different, that both gases are in kinetic thermal equilibrium, that the applied magnetic field is not too far from the optimal value, and that there is not a strong (i.e. much greater than factor of 2) variation in spin-exchange rates as a function of m_F state. It is also assumed that the optical pumping is efficient. This means that in our system, the ^{85}Rb atoms are perfectly pumped from the $m_F = -1$ to the $m_F = -2$ at a fixed rate such that there will be no significant portion of the atoms in any of the other m_F states. The ^{87}Rb atoms' m_F state populations are assumed to be rebalanced frequently enough that they do not deviate significantly from their average values during the cooling. All of these assumptions are reasonable in the $^{85/87}$Rb mixture investigated in the work of this thesis and can be expected to

apply to many other gas mixtures as well. In addition, it is assumed that the atoms are confined in a harmonic potential. Under these assumptions, we define the optically pumped state as the non-spin polarized state of the optically pumped isotope (for the Rb mixture, this is the [85]Rb $F = 2$, $m_F = -1$ ground state). The rate of change of the number of atoms in the optically pumped state is given by:

$$\frac{dN_{np}}{dt} = k_f \frac{N_{sp} N_c}{V} - k_s \frac{N_{np} N_c}{V} - \frac{1}{\tau_{OP}} N_{np} \tag{2.12}$$

where N_{sp} is the number of the optically pumped atoms in the spin polarized state (the [85]Rb atoms in the $m_F = -2$ state for the rubidium system), N_{np} is the number of optically pumped atoms which are not in the spin polarized state ([85]Rb atoms in the $m_F = -1$ state), and N_c is the number of atoms of the non-optically-pumped isotope which are available for spin-exchange collisions with the optically pumped isotope ($N_c = N_1$ is the total population of [87]Rb). In principle, two different terms would be used in place of N_c with values dependent on the state distribution of the non-optically-pumped isotope; however, under the assumptions of this simple model the population distribution is rebalanced fast enough that the distribution is uniform. The trap volume is defined such that the average atom density is N/V, and the optical pumping rate is characterized by the $1/e$ time τ_{OP}. The terms k_f and k_s are spin-exchange rate coefficients weighted by the assumed state distribution. In the absence of a magnetic field these terms will be equal, but due to the nature of the cooling scheme, there exists an energy barrier for kinetic-energy-reducing spin-exchange collisions. Thus, these collisions occur at a slower rate given by:

$$k_f = k_s \exp\left(\frac{-\Delta}{k_B T}\right) \tag{2.13}$$

where once again Δ is the change in Zeeman energy in a spin-exchange collision that changes $|m_F|$ by 1 ($\mu_B B/6$ for [85]Rb and [87]Rb). The exponential term in equation (2.13) is required so that the proper ratio of the populations of N_{np} to N_{sp} would be achieved in thermal equilibrium.

Given the assumption that all of the population of the optically pumped atoms (N_2) resides in the states N_{sp} and N_{np} ($N_2 = N_{sp} + N_{np}$), the steady-state solution to equation (2.12) can be found for the population of N_{np}:

$$N_{np} = \frac{k_s \exp\left(\frac{-\Delta}{k_B T}\right) N_c N_2}{\frac{1}{\tau_{OP}} V + N_c k_s \left(1 + \exp\left(\frac{-\Delta}{k_B T}\right)\right)} \tag{2.14}$$

As atoms are optically pumped from N_{np} to N_{sp} the energy of the gas is reduced. The rate of this energy reduction though optical pumping gives the cooling rate of the gas. The rate in which energy is removed from the system, R_{rm} due to the optical pump is given by:

$$R_{rm} = \frac{1}{\tau_{OP}} N_{np} (\Delta - \kappa) \tag{2.15}$$

Here, κ is the average of the energy that is imparted per *successful* optical-pumping-driven population transfer. Under the assumption that the optical pumping process is the only significant contributor to changes in the total energy of the system, and since the energy of the system is related to the temperature ($E = 3(N_1 + N_2) k_B T$), the instantaneous two isotope CAZ cooling rate is given by:

$$\frac{dT}{dt} = \frac{-1}{\tau_{SE}} \frac{\exp\left(\frac{-\Delta}{k_B T}\right) N_2}{3 k_B (N_1 + N_2)} (\Delta - \kappa) \frac{1}{1 + \frac{\tau_{OP}}{\tau_{SE}}\left(1 + \exp\left(\frac{-\Delta}{k_B T}\right)\right)} \tag{2.16}$$

here, N_1 and N_2 are the total number of atoms of the non-optically-pumped and optically-pumped isotopes, respectively. The spin-exchange time-constant is defined such that $1/\tau_{SE} = k_s n_1$ where n_1 is the average non-optically-pumped atom density and k_s is the spin-exchange collision rate weighted assuming equal m_F state populations for the non-optically-pumped atoms. In the limit of fast optical pumping, $\tau_{OP} \rightarrow 0$, the two isotope CAZ cooling rate is simply:

$$\frac{dT}{dt} = \frac{-1}{\tau_{SE}} \frac{\exp\left(\frac{-\Delta}{k_B T}\right) N_2}{3 k_B (N_1 + N_2)} (\Delta - \kappa) \qquad (2.17).$$

Heating must occur during optical pumping since photons are spontaneously scattered. Each photon scatter results in a random recoil momentum kick being imparted to the scattering atom that on average increases its kinetic energy. In addition, κ can also depend on the densities of the atoms in the gas. For instance, if the gas of optically-pumped atoms (N_2) is optically thick, then reabsorption will increase the amount of energy imparted per optical pumping cycle as photons scatter multiple times before leaving the gas [16]. Additionally, density-dependent collisions may produce not only losses but heating during the optical pumping cycle. These heating mechanisms represent a limit to the lowest achievable temperatures [1].

Since the value of Δ is set by the strength of the applied magnetic field, for any set of conditions the cooling rate can be maximized. In the limit of fast optical pumping (i.e. τ_{OP} goes to zero), the optimal value of $\Delta = k_B T + \kappa$ and the optimal cooling rate is:

$$\frac{dT_{opt}}{dt} = \frac{-1}{\tau_{SE}} \frac{\exp\left(-1 - \frac{\kappa}{k_B T}\right) N_2}{3 (N_1 + N_2)} T \qquad (2.18).$$

We note that the cooling rate varies little around the optimal value of Δ, and so setting Δ to precisely its optimal value is not a critical requirement for effective cooling.

2.4.2 Performance at Low Temperatures with Reabsorption

One of the main motivations for developing the CAZ cooling rate model is so that theoretical comparisons between the two-isotope technique and single isotope CAZ cooling can be made. Of particular interest is the low temperature range, where high densities result in reabsorption leading to the likely limit of the cooling technique. Intuitively, the expectation is that having the ability to reduce the number of optically pumped atoms will result in a reduced

reabsorption rate. Having a second non-optically-pumped species present means that the overall collision rate can be kept high and thus the cooling rate will be higher than with one isotope alone. Thus, the expectation is that reabsorption will be reduced in a two-component system at low temperatures delaying the onset of becoming reabsorption limited. Having a model for the cooling rate means that this expectation can be quantitatively tested theoretically.

Reabsorption reduction is a general feature of a two-isotope collision-based-cooling system and is not limited to two isotope CAZ cooling. While the focus of a two-isotope system is because of the [85/87]Rb system studied experimentally in this work, this analysis is generally applicable to other two-component cooling systems including atom/molecule systems as well. This benefit can be seen by examination of the difference between a straightforward model of single isotope cooling and the two isotope cooling model just developed. The single-isotope model is very similar to two-isotope case, with the cooling rate modeled by the first-order differential equation:

$$\frac{dT_1}{dt} = -k_s \frac{\exp\left(\frac{-\Delta}{k_B T}\right) N_1}{\xi k_B (N_1)} \left(\Delta - \alpha - \beta \frac{N_1}{V^{2/3}}\right) \tag{2.19}$$

where again k_s is the collision rate (spin-exchange collision rate for CAZ cooling), Δ is the amount of energy removed per cooling cycle (ideally $\frac{1}{6} \mu_B B$ for our setup), k_B is the Boltzmann constant, T is the temperature, N_1 is the number of atoms in the trap, V is the effective volume of the trap (which we will assume is equal to $\eta T^{3/2}$, where η is a constant, for the computations done here), and finally ξ is a dimensionless factor relating total energy to temperature. Note that in the previous treatment, a 3D harmonic trap was assumed so that $\xi = 3$. In addition, the heating term κ has been explicitly separated into two terms: a constant α that characterizes optical pump heating that is not density dependent, and a term dependent on β which characterizes optical-thickness-dependent optical pump heating (such as reabsorption).

The cooling rate changes as the energy removed per cooling cycle, Δ, is adjusted (done experimentally in two isotope CAZ cooling by setting the magnetic field strength). The maximum value of the cooling rate given by equation (2.19) occurs when Δ is set to the value:

$$\Delta_{optimal} = k_B T + \alpha + \frac{\beta N_1}{\eta^{2/3} T} \tag{2.20}$$

This optimal value for the energy removed per cooling cycle yields a maximum cooling rate of

$$\frac{d T_{1,max}}{dt} = -k_s \exp\left(-1 - \frac{\alpha}{k_B T} - \beta \frac{N_1}{\eta^{3/2} k_B T^2}\right) \frac{N_1}{\eta T^{1/2} 2 \xi} \tag{2.21}$$

Note that in the absence of optical pump induced heating, the optimal energy barrier is just $k_B T$. When the optical pump induces heating, Δ must be increased in order to ensure that cooling still occurs. This in turn will reduce the cooling rate since the collisions will be reduced on account of the energy barrier being greater than the average kinetic energy of the atoms. While the cooling rate never reaches zero, it does fall exponentially as the temperature of the gas is reduced.

Extending the treatment to two isotopes, we assume that the cooling collisions are the result of inter-isotope collisions. We will also assume that N_1 is the isotope we are most interested in cooling, and thus the newly introduced isotope, N_2, is the isotope that is to be optically pumped. In addition, we will assume that the two isotopes are in good thermal contact such that their temperatures are the same. The cooling rate of the two-isotope situation is just a modification of equation (2.17):

$$\frac{d T_2}{dt} = -k_s \frac{\exp\left(\frac{-\Delta}{k_B T}\right) N_2}{\xi k_B (N_1 + N_2)} \left(\Delta - \alpha - \beta \frac{N_2}{V^{2/3}}\right) \tag{2.22}$$

71

Again, this cooling rate can be maximized by optimal choice of Δ. In addition, we will assume that the number of atoms of the second isotope can be adjusted as the experiment progresses. Therefore we can also find an optimal value of N_2:

$$N_{2,optimal} = \frac{1}{2}\left(\sqrt{N_1^2 + \frac{4 N_1 k_B T^2 \eta^{2/3}}{\beta}} - N_1 \right) \qquad (2.23).$$

Assuming the optimal values of Δ (similar to equation (2.20) but with $N_1 \rightarrow N_2$) and N_2 yields a maximum two-isotope cooling rate of

$$\frac{d T_{2,max}}{dt} = -k_s \exp\left(-1 - \frac{\alpha}{k_B T} - \beta N_1\left(\frac{1-\varsigma}{2 k_B T^2 \eta^{2/3}} \right) \right) \frac{N_1}{\xi \eta \sqrt{T}} \frac{\varsigma-1}{\varsigma+1} ;$$

$$\varsigma \equiv \sqrt{1 + \frac{4 k_B T^2 \eta^{2/3}}{\beta N_1}} \qquad (2.24).$$

With equations (2.21) & (2.24), a relative comparison can be made between single and dual isotope cooling in the presence of heating due to reabsorption. Normally, the cooling rates will be dependent on the specific values of the various constants; however, to see if the two-isotope cooling rate is potentially better than the single isotope cooling rate, only representative behavior is needed. Thus, k_s, η, ξ, k_B, and N_1 can all be set to one in order to put the temperature and time into arbitrarily scaled units so that the two cases may be compared. Such a comparison is shown in figure 2.10, which plots the cooling rates for both single and dual isotope cooling as a function of atom temperature for $\alpha = 0.1$ and $\beta = 1$ as well as the ratio of the two rates. For this comparison, N_2 was never allowed to be greater than N_1. This is because at higher temperatures, N_2 optimizes toward infinity which may be bit difficult to achieve experimentally. A clear improvement in the cooling rate can be seen in figure 2.10 in the dual isotope case once $N_2 < N_1$. This is due to the optically pumped atom density being decreased in order to minimize reabsorption effects. Both cooling rates fall rapidly toward zero as the temperature is reduced;
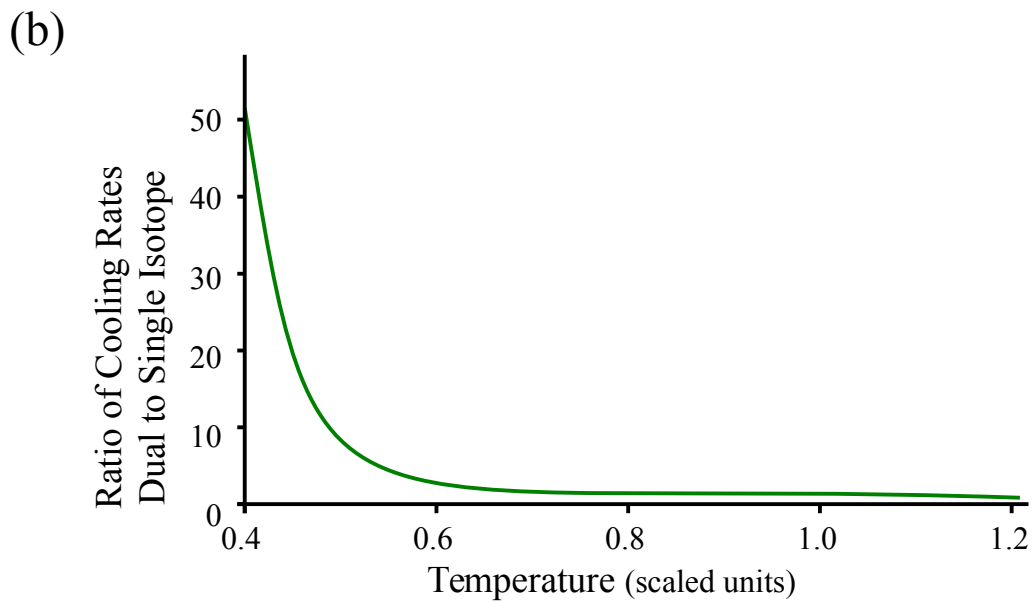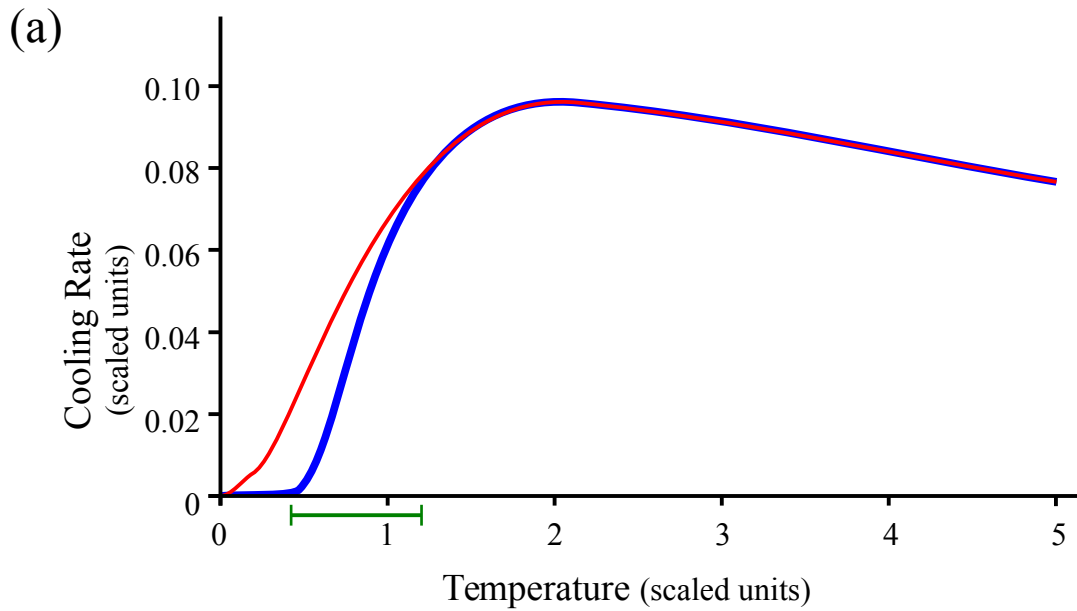
Figure 2.10 Single & Dual Isotope Cooling Rate Comparison.
(a) Comparison of the representative single isotope (blue) and dual isotope (red) cooling rates in arbitrarily scaled units where $\alpha = 0.1$ and $\beta = 1$. Rates assume that the optimal energy per cooling cycle is removed. In addition, the dual isotope cooling rate assumes that the atom number of the optically pumped species can be set to an optimal value at all times (and is no greater than the other species). For the temperature range indicated in green, **(b) the ratio of the two rates are plotted to emphasize the difference.**

however, the two-isotope cooling rate falls less rapidly which is very apparent when looking at the ratio of the two rates.

In a practical application, the cooling rate cannot be made arbitrarily low. This is because heating and loss is always present at some level. These effects set a limit on the minimum cooling rate that a system can sustain that is dependent on the experiment and apparatus. Since the benefit of a two-isotope cooling scheme is most manifest at lower temperatures and cooling rates, whether or not there is a practical benefit depends on the parameters of the specific case. For example, if a system operates in the regime shown in figure 2.10 and the heating and loss rates of the system require at least a cooling rate of 0.08, then there will be no benefit from two-isotope cooling. This is because the system cannot effectively operate at the low cooling rates where single isotope and two-isotope cooling differ. However, should the system require a cooling rate of at least 0.008, then the system can be cooled to regions where two-isotope cooling outperforms single isotope cooling. In such a scenario, cooling using a single isotope would be able to progress to an atom temperature of 0.555, while two-isotope cooling would reach temperatures of 0.213. A system with even less heating and loss would see even a greater advantage due to two-isotope cooling. Consider a system requiring a cooling rate of 0.002 or greater. The minimum temperature that could be reached for single isotope cooling is 0.462, compared to the minimum achievable for two-isotope cooling of 0.111. While a factor of a little over 4 in temperature may seem modest, the phase-space density scales as the cube of the temperature. Thus the factor of 0.462/0.111 improvement in temperature translates to almost two orders of magnitude of improvement in phase-space density.

Again, the particulars of the situation will determine if the addition of a second isotope would be worthwhile. The stronger the effect of reabsorption, the more likely a benefit can be realized with the addition of a second isotope. However, if reabsorption effects are relatively

weak (or density independent heating effects are strong), such as the case show in figure 2.11(a), then the region of parameter space where a benefit can be achieved becomes less accessible.

This simple model also assumes that the number of atoms of the optically pumped species can be controllably reduced. It is often more convenient, and certainly easier, to run an experiment with a set number of atoms (neglecting trap losses), as was the case for the experiments presented in this thesis. Nevertheless, two-isotope cooling can still be beneficial in such a case, as can be seen in figure 2.11(b). Figure 2.11(b) shows a family of cooling rates each with a different set value for N_2. The thick black curve represents the case where $N_2 = N_1$ (both set to one, with $\alpha = 0.1$ and $\beta = 1$, which matches behavior of the single isotope case shown in figure 2.10). Red curves represent $N_2 < N_1$, where N_2 is reduced in steps of 0.1. Blue curves represent $N_2 > N_1$, where N_2 is incremented in steps of 1. The challenge with a set number of atoms is finding the lowest possible atom number that still produces appreciable cooling rates at high temperatures but also provides a benefit at lower temperatures.

Finally, any additional two-isotope effects are not accounted for by this model. Many factors play a part in determining if a two-isotope system can effectively mitigate reabsorption effects. Accounting for all of them is beyond the scope of this thesis. However, this simple model does clearly show that there is a theoretical advantage in cooling with two-isotopes, and as far as we are aware this is the first treatment (theoretical or experimental) to examine advantages of cooling in a two-component system. When in the presence of significant reabsorption, the two-isotope strategy could easily improve the cooling rate by a factor of 10 for low temperatures. Investigation of any system of two-isotope cooling has the potential of determining experimentally whether or not the performance predicted in this model can be achieved. However in order to make such tests effectively, there needs to be a sufficient initial cooling rate in order to reach the reabsorption limited temperature range in the first place.
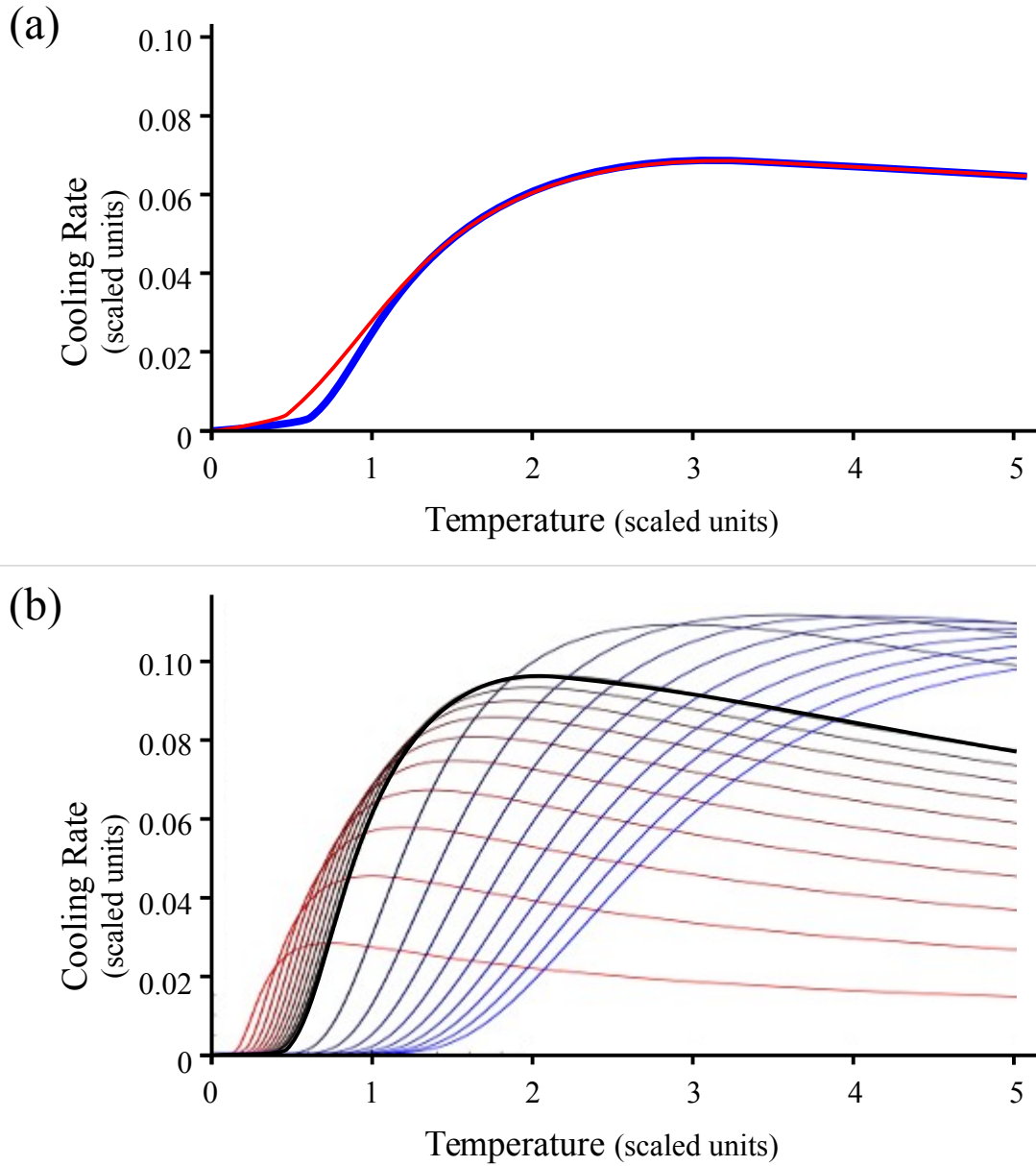
Figure 2.11 Additional Two-Isotope Cooling Considerations.
(a) Comparison of the single isotope (blue) and dual isotope (red) cooling rates similar to Figure 2.10, but with $\alpha = 1$ and $\beta = 1$, representing the case where density independent heating is more comparable to density dependent heating. **(b)** Family of curves representing $\alpha = 0.1$, $\beta = 1$, optimal Δ, and fixed N_2. The thick black curve represents $N_1 = N_2$ (same as single isotope). Red curves are reductions of 0.1 for $N_2 < N_1$, and blue curves are increments of 1 for $N_2 > N_1$. When N_2 is always optimal, the cooling rate curve traces out the far edge of the family of curves.

For typical conditions in our optical trap, an initial CAZ cooling rate can now be calculated. Conditions after loading the FORT are typically a density of 5×10^{11} cm^{-3} of ^{85}Rb and a density of 4×10^{11} cm^{-3} of ^{87}Rb, trapped at a temperature of 10 μK. The expected spin-exchange collision rate at this temperature from figure 2.3 is 2.7×10^{-11} cm^3/s. Initial observations are not expected to be reabsorption limited (i.e. β = 0), and a minimum estimate of the optical pump induced heating term is κ = α = 2 μK. Assuming CAZ cooling is conducted under these conditions and in a magnetic field of about 1 G, the expected cooling rate would be 6 μK/s. This is a respectable cooling rate in that it implies a $1/e$ cooling time of 1.7 s. Thus, the expected initial cooling rate seems to promise rapid cooling. So long as any potential difficulties in the implementation of the cooling technique can be overcome, CAZ cooling should show advantageous performance at low temperatures.

In order to realize CAZ cooling, several modifications needed to be made to an existing system capable of trapping $^{85/87}$Rb. Chapter 3 will discuss these modifications as well as several others useful for examination of CAZ cooling in more detail in future work.

References for Chapter 2

[1] G. Ferrari, Eur. Phys. J. D **13**, 67-70 (2001).

[2] A. Kastler, J. Phys. Radium **11**, 255–265 (1950).

[3] M. Fattori *et al.*, Nature Physics **2**, 765 (2006).

[4] P. Medley, D. Weld, H. Miyake, D. Pritchard and W. Ketterle, Phys. Rev. Lett. **106**, 195301 (2011).

[5] G. Breit and I. I. Rabi, Phys. Rev. **38**, 2082 (1931).

[6] W. Happer, Rev. Mod. Phys. **44**, 169-250 (1972).

[7] H. T. C. Stoof, J. M. V. A. Koelman, and B. J. Verhaar, Phys. Rev. B **38**, 4688-4697 (1988).

[8] S. Kookouline, University of Central Florida, private communication

[9] J. Stenger, *et al.*, Nature **396**, 345 (1998).

[10] James Burke, Ph. D. Thesis, University of Colorado, (1999).

[11] C. Myatt, E. Burt, R. Ghrist, E. Cornell, and C. Wieman, Phys. Rev. Lett. **78**, 586 (1997).

[12] M. Prentiss, *et al.*, Opt. Lett. **13**, 452-454 (1988).

[13] D. Sesko, *et al.*, Phys. Rev. Lett. **63**, 961-964 (1989).

[14] L. Marcassa, *et al.*, Phys. Rev. A **47**, R4563-R4566 (1993).

[15] J. Roberts et al., Phys. Rev. Lett. **85**, 728 (2000).

[16] Y. Castin, J. Cirac, and M. Lewenstein, Phys. Rev. Lett. **80**, 5305 (1998).

[17] J. Cirac *et al.*, Europhys. Lett. **35**, 647 (1996).

[18] D. J. Han *et al.*, Phys. Rev. Lett. **85**, 724 (2000).

[19] A. Gorges, A. Foxley, D. French, C. Ryan and J. Roberts, Phys. Rev. A **76**, 033420 (2007).

Chapter 3

Experimental Apparatus and Techniques

The system used for obtaining the measurements presented in this thesis was built with the ultimate goal of achieving CAZ cooling. Much of the details of the construction and design parameters are documented in Ref. [1]. At the beginning of this work, the apparatus had been optimized for loading both naturally occurring rubidium isotopes from a MOT into an optical trap at the same time. Thus far the system had been used for characterization of effects relevant to CAZ cooling [2-5], but not the cooling itself. As such, several substantial planned improvements had to be made in order for CAZ cooling to be realized. This chapter will briefly summarize the basics of the system prior to this work and then detail the changes necessary in order for CAZ cooling to be realized for the first time. While these changes were being made to the system, several additional upgrades were also made in anticipation of future work. Since these improvements were not used as part of this work, yet they are likely to be useful for extending CAZ cooling to longer durations, they will be covered in appendix C.

The typical experimental procedure for a CAZ sequence is as follows: atoms of ^{85}Rb and ^{87}Rb are collected into two overlapping MOTs from which roughly 10^6 atoms of each isotope are loaded into an optical dipole trap. The MOTs are turned off after the loading of the optical trap. The trapped atoms are then exposed to an external magnetic field. Atoms of ^{85}Rb are spin-polarized and spin-exchange collisions occur between the two isotopes. Afterward all fields are shut off and the atoms are released from the optical trap prior to imaging. The resulting image is analyzed to obtain atom number and temperature data. This general procedure may be useful to keep in mind while reading this chapter.

3.1 Simultaneous ^{85}Rb & ^{87}Rb Optical Trapping System

The experiments described in this thesis were conducted within an ultra high vacuum ($\sim 10^{-9}$ Torr) chamber filled with a thermal Rb vapor. The chamber itself was made of stainless steel and featured multiple access ports to allow the various laser beams admittance. In addition to the optical access ports, there were numerous electrical feedthroughs that allowed currents to be run to interior coils, antennas, and the Rb getters which produced the background thermal Rb vapor. The vacuum was maintained by an ion pump.

The thermal Rb vapor was the source of atoms which were collected in a MOT. The system utilized two MOTs simultaneously, one to trap ^{85}Rb and the other to trap ^{87}Rb. The MOTs were prepared using standard techniques [6], and are depicted schematically in figure 3.1. During the initial loading period of the MOTs, the ^{85}Rb MOT trapping beams had an average peak intensity of 2.5 mW/cm$^{2.}$. Each of the six beams were detuned 12 MHz to the red of the D2 line of ^{85}Rb. Meanwhile, the ^{87}Rb MOT operated with an average peak intensity of 4.8 mW/cm^2. The detuning of its six trapping beams was 20 MHz to the red of the ^{87}Rb D2 line. Each MOT confined a cloud of either Rb isotope containing roughly 2×10^8 atoms at the start of an experimental run. The trapping and hyperfine repump beams of each MOT each had their own electronically controlled shutter, which allowed them to be turned on or off as needed during the experiment. This also allowed the system to be run with either isotope alone or both at the same time, which was useful for evaluating the performance of the system. The hyperfine repump beams were also sent through acousto-optic modulators (AOMs) which allowed their intensities to be controlled.

The MOTs served as preparatory trap for the atoms which were then transferred, or loaded, into a far off-resonance trap (FORT). A FORT is an optical dipole trap which operates far from any atomic resonance. In this case, the FORT was produced by a 10.6 μm infrared CO_2
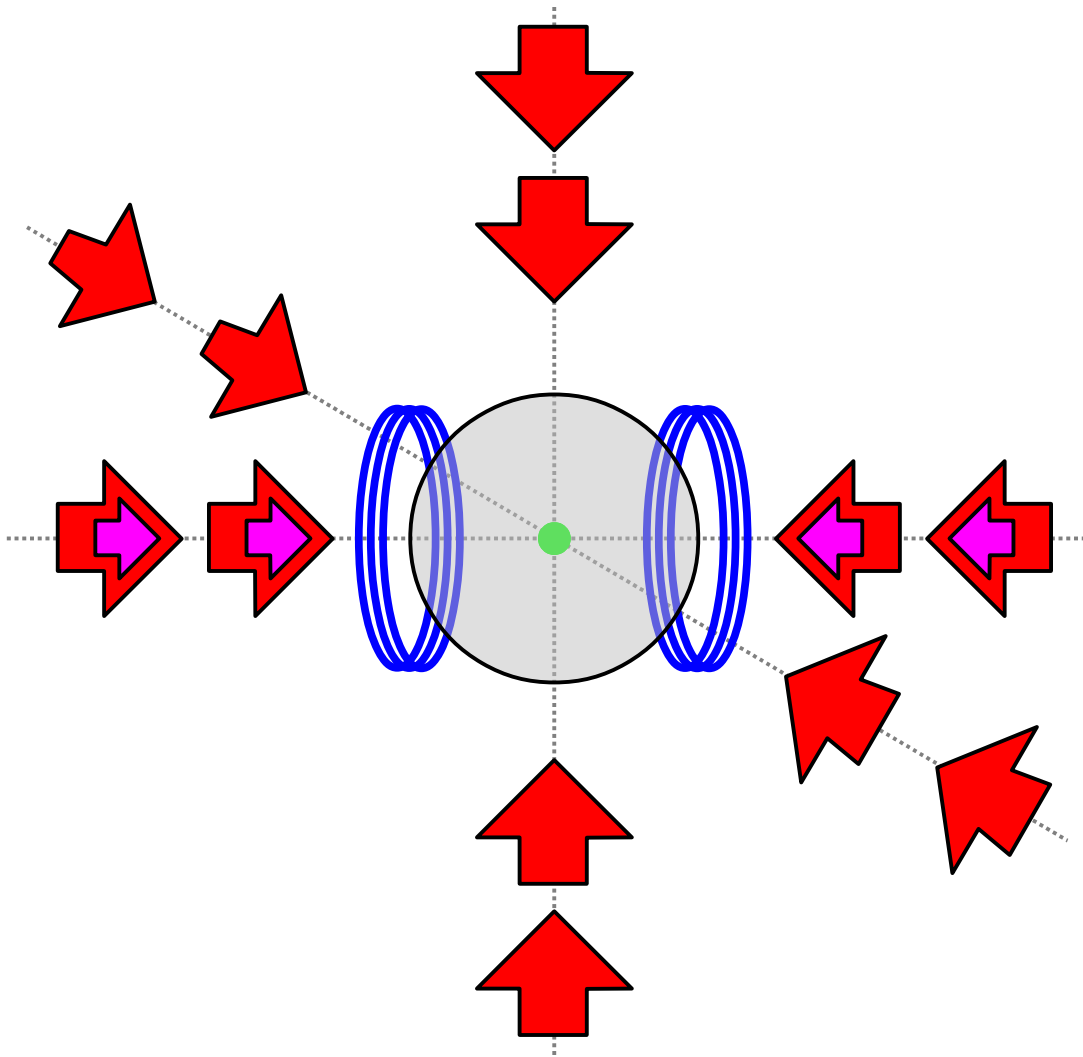
Figure 3.1 Schematic of Overlapping MOT Configuration.
MOT trapping beams (red arrows) are sent into the vacuum chamber (gray circle) along orthogonal directions. In actuality, three beams are sent through the chamber which are then retroreflected. The AH coils (blue) are located outside of the chamber and define the axial MOT direction.   The hyperfine repump beam (pink arrows) is overlapped with the axial trapping beam. There are two sets of MOT trapping and hyperfine repump beams which are overlapped and represented by the double arrows in the schematic.   Each MOT utilizes different frequency light tuned to cool and trap either ^{85}Rb or ^{87}Rb. This results in two clouds of trapped atoms (green) which are overlapping in the center of the vacuum chamber. Each cloud contains approximately 2×10^8 atoms at about 20 μK.

laser that produced a 20 Watt beam once it entered the vacuum chamber after all the beam shaping optics. All experiments described in this thesis were done within the FORT which was turned on and off by an AOM. Atoms were loaded into the FORT from the MOT through a series of compressed MOT (CMOT) stages [7]. During the CMOT stages, the MOT trapping laser detuning was increased and the hyperfine repump power was significantly attenuated. Two CMOT stages were used for loading the FORT. During the first CMOT stage, MOT laser detuning was set to 20 MHz to the red of the cycling transition for both isotopes of Rb. During the second CMOT stage detunings were increased to 33 MHz to the red of the cycling transition for both isotopes. Both CMOT stages utilized a reduction in hyperfine repump power to about 10 μW/cm^2 for each isotope. Also during the second CMOT stage, the FORT was turned on and atom transfer from MOT to FORT began. Multiple CMOT stages were used because FORT loading performance was observed to be better with them than without. Timings for these CMOT stage were generally about 10 ms for the first and as much as 40 ms for the second, and were set to values which maximize the number of atoms loaded into the FORT. Originally, following the second CMOT stage the anti-Helmholtz (AH) coils were turned off and the trapping laser detunings further increased in an optical molasses stage. However, it was found that loading behavior was more robust when the AH coils were left on, replacing the optical molasses stage with a third CMOT stage. During this last CMOT stage the ^{85}Rb trapping laser detuning was increased to 80 MHz and the ^{87}Rb trapping laser detuning was increased to 90 MHz. This final loading stage typically lasted 30 ms for optimal performance in our system. The physics of the loading process is discussed in section 4.1.

At the conclusion of the loading process, the hyperfine repump lasers are turned off. After a 1 ms delay the trapping lasers were turned off as well which put all the atoms trapped in the FORT into the lower hyperfine ground state. With the MOT lasers turned off the remaining

MOT atoms fall away. Further detail about getting the system to this point can be found in reference 1. The loaded FORT is the starting point of the CAZ experiments conducted for this thesis.

The vacuum chamber also housed a couple of tools useful for CAZ cooling. First, a conical microwave antenna that allowed microwave radiation to be coupled to trapped atoms. This can be useful as part of a microwave/optical spin-polarization scheme as was discussed on page 55. In addition, the microwave antenna also makes it possible for the m_F state distributions of the atoms to be probed (see section 3.5). This is a vital diagnostic tool that enabled us to observe the effectiveness of the spin-polarization. Another piece of equipment internal to the vacuum chamber was a coil of wire used to produce an RF field which will prevent buildup of ^{87}Rb in the $m_F = -1$ state by scrambling the ^{87}Rb m_F state distribution (section 3.7). This prevented the CAZ cooling from otherwise stagnating.

Upon completion of an experimental sequence, the temperature and the number of one of the isotopes of Rb was measured via absorption imaging. In absorption imaging, a probe beam is directed through the trap region and onto a charged-coupled device (CCD) camera. The probe laser is tuned to the resonant frequency of the cycling transition of the atoms being imaged. Being resonant light, the probe beam will be absorbed by atoms in its path causing a shadow to be cast on the CCD camera. The image captured of the atom cloud shadow can then be compared to an image of the probe in the absence of any atoms to obtain the optical depth of the cloud. In turn, the optical depth is used to calculate the density of the atoms. Assuming that the density distribution is Gaussian, the root-mean-squared widths are then used to define the radial and axial extents of the atom cloud (further detail about the imaging process can be found in chapter 3.3.1 of reference 1).

Prior to imaging, the atoms were typically released from the trap and allowed to ballistically expand for 5 ms. By observing the radial width of the atoms in the image, it was then inferred how much the atoms had expanded in the radial direction. Because the radial extent of the atoms in the optical trap is far smaller than the expanded size of the atoms, the radial rms size of the atoms can be divided by the expansion time to get the atoms' rms velocity directly. The initial size correction is estimated to be far less than 1%. From this, the energy in the radial direction was computed directly. For the axial direction, we cannot directly infer the amount of expansion due to the relatively large extent of the atom cloud in the axial direction. Thus a calibration was developed to relate the observed axial extent to the axial energy. To make the calibration, ^{85}Rb was trapped and held for over three times the estimated elastic collision equilibration time for the establishment of thermal equilibrium. Then the axial extent and radial energy were measured as the temperature of the gas decreased due to evaporation. In thermal equilibrium the axial and radial energies are equal, thus linking the radial energy to axial extent creates a calibration of axial energy versus axial extent. Once the radial and axial energies are known, the total energy of the atom cloud may be calculated. The total energy is taken to be equal to $3Nk_BT$. Therefore, the calculated total energy and the total number of atoms N observed from the image may be used to determine the temperature of the gas.

During imaging, the hyperfine repump beam of the imaged atoms is kept on to ensure that all atoms are in the upper hyperfine ground state and in resonance with the probe beam ($F = 2 \rightarrow F' = 3$ and $F = 3 \rightarrow F' = 4$ transitions for ^{87}Rb and ^{85}Rb, respectively). If the hyperfine repump beam is left off, then only atoms which were in the upper hyperfine state will be included in the image. This gives us a means to measure the hyperfine state distribution by comparing absorption images with and without the hyperfine repump beam being on during imaging. In addition, microwave transitions can be used with a sufficiently strong magnetic field

to excite specific m_F states to the upper hyperfine ground state and to be resonant with the probe light. In this way, the m_F state distribution of atoms can also be obtained in addition to the hyperfine state distribution, total atom number and density, and the temperature of the atoms trapped in the FORT. Because the absorption imaging process destroys the atom cloud and can only image one isotope at a time, many observational trials must be done to obtain a clear picture (and sufficient statistics) of what is happening during a given set of experimental conditions.

The multiple observations produce a statistical uncertainty of any measurement, which in general is represented as error bars on the reported data. However, there are also systematic errors which will be discussed here since most results are comparative in nature. Our atom number measurements have an estimated systematic uncertainty of 30%. There are multiple factors that contribute to this: uncertainty in the pixel size of the CCD camera, uncertainty in the probe light frequency, uncertainty in the polarization of both the probe light and the atoms while being imaged (which affect Clebsch-Gordan coefficients), and uncertainty in the quantization axis direction. Temperature measurements have a systematic uncertainty of 15%. Uncertainties in expansion time after atoms are released from the FORT prior to imaging, and pixel size calibration are contributing factors to the temperature systematic uncertainty. We can determine density to a much better degree than atom number because errors in atom number and temperature tend to off-set one another when due to error in camera pixel size calibration. For example, if the pixel size were actually 5% larger than presumed, then the atom number would be 10% more than reported, the axial extent would be 5% larger, and the radial temperature would be 10% more due to the miscalibration. Density scales as the number of atoms over both the axial size and the temperature, so the variation in the density would be 5%. Thus, the density varies by less than the overall number calibration.

The entire experiment was controlled with transistor-transistor logic (TTL) signals sent from a Viewpoint USA DIO-64 board controlled through a LabView computer interface. These TTL signals controlled shutters, RF and microwave switches, laser detuning settings, and AOM controllers among other things. Further details about the experimental setup at the start of this work can be found in reference 1. The remainder of this chapter focuses on detail of the individual components beyond those needed to simultaneously trap multiple isotopes. These are the tools that were used in this work to realize and evaluate CAZ cooling.

3.2   The Far Off-Resonance Trap

The CAZ cooling described in this thesis was done entirely within the optical trap. The optical trap was produced by a 50 Watt CO_2 laser operating at a wavelength of 10.6 μm (Coherent Inc. model GEM-Select 50). The trap itself consisted of a 20 Watt beam after losses from passing through beam shaping optics and an AOM which served to control the power and turn the trap on and off. Much time was spent characterizing and understanding the limits of loading the atoms into the far-off resonance trap (FORT) due to how crucial initial conditions are for successful CAZ operation. This section will discuss the physics of the FORT. Loading the atoms into the FORT is the subject of section 4.1. An upgrade that was made to the FORT that has the potential to be useful for extended CAZ cooling experiments, but not utilized in this work, is discussed in appendix C.

The force exerted by an electric field gradient on an electric dipole forms the basis on which optical traps operate. The electric field is supplied by an intense laser field, and the electric dipole is induced in a neutral atom. The interaction energy of such a system is given by:

$$U = -\vec{d} \cdot \vec{E} \tag{3.1}$$

where d is the magnitude of the electric dipole, and E is the magnitude of the electric field. In the case of neutral atoms in an optical dipole trap, d is actually induced by and proportional to

the electric field of the laser light which means that the interaction energy is proportional to E^2 or the intensity of the light. The precise strength of the interaction is dependent on the atom used and how close the frequency of light is to the atomic dipole transition resonance. An atom will have many of these resonances owing to the fact that the ground state can be coupled via dipole interaction to multiple quantum states. However, typically only one particular dipole resonance is dominant.

Areas of the highest intensity will have the largest shift in energy as they experience the greatest interaction. Thus, spatial variation in the light intensity will produce a spatial variation in the potential landscape. For example, the focus of a laser beam creates an intensity gradient which produces a potential well for atoms whose dipoles are aligned with the field. This is due to the interaction energy of equation (3.1) being the negative of the dot-product between the dipole and electric field, which means the ground state energy level is shifted to lower energy with greater interaction strength between the aligned vectors. This would be the case of atoms in a static electric field; however, the electric field produced by light is time varying. The effect this has on the interaction can be understood classically by considering the atom as a damped harmonic oscillator with resonant frequency at the dipole transition frequency. The oscillating electric field of the light acts as a driving frequency on the atom. When that drive frequency is less than the resonant frequency, the atom responds in phase. This means that for red-detuned light, the induced atomic dipole is aligned with the electric field and the interaction produces an attractive potential. Conversely, when the drive frequency is at a higher frequency than resonance, the atom will respond 180° out-of-phase. Thus, blue-detuned light induces a dipole anti-parallel with the electric field producing a repulsive potential. Both attractive and repulsive potential optical traps are commonly used. Attractive potentials are generally produced by the focus or overlap of red-detuned lasers confining the atoms in regions of maximum intensity.

Repulsive potentials are typically used by creating "light boxes" which consist of blue-detuned laser beams defining the edges of the trap keeping atoms in a region of minimum intensity [8].

The experiments of this thesis were conducted within a red-detuned optical trap producing an attractive potential where atoms are confined at and near the focus of a laser beam. The strength of the induced dipole and consequently the strength of the confining potential are dependent on the frequency of the trapping light. For a red-detuned laser this strength scales as the inverse of the detuning of the laser from the atomic resonance squared, at least when the light is sufficiently close to resonance with an atomic transition. While this alone would imply that a near-resonant beam would be preferred, producing the deepest potential, near-resonant photons also tend to both scatter off the atoms and produce light-assisted collisions.

Figure 3.2 shows a cartoon explaining light-assisted collisions. Shown are two-atom long-range interatomic potential curves as a function of internuclear separation. When both atoms are in the ground state, the potential curve is relatively flat (there is an r^{-6} van der Waals interaction, but at far internuclear separation the shift is relatively small compared with that of the excited state). Absorption of a photon excites the atom pair to the bound molecular potential above. This in turn causes the atoms to accelerate toward each other and pick up kinetic energy as the potential energy decreases. The pair remains on the excited potential for a time on the order of the excited state lifetime, then emits a spontaneous photon. The photon that is emitted will be less energetic than the one that was absorbed. The difference in energies of the absorbed and emitted photons is transferred to the kinetic energy of the atom pair. This gain in kinetic energy can be large enough that the atom pair will be able to escape the trap. Light-assisted collisions scale approximately as the inverse of the detuning squared when near resonance and in an optical trap. Since light-assisted collisions scale more strongly with detuning than the induced dipole, it is beneficial to use a trap that operates far off-resonance while compensating
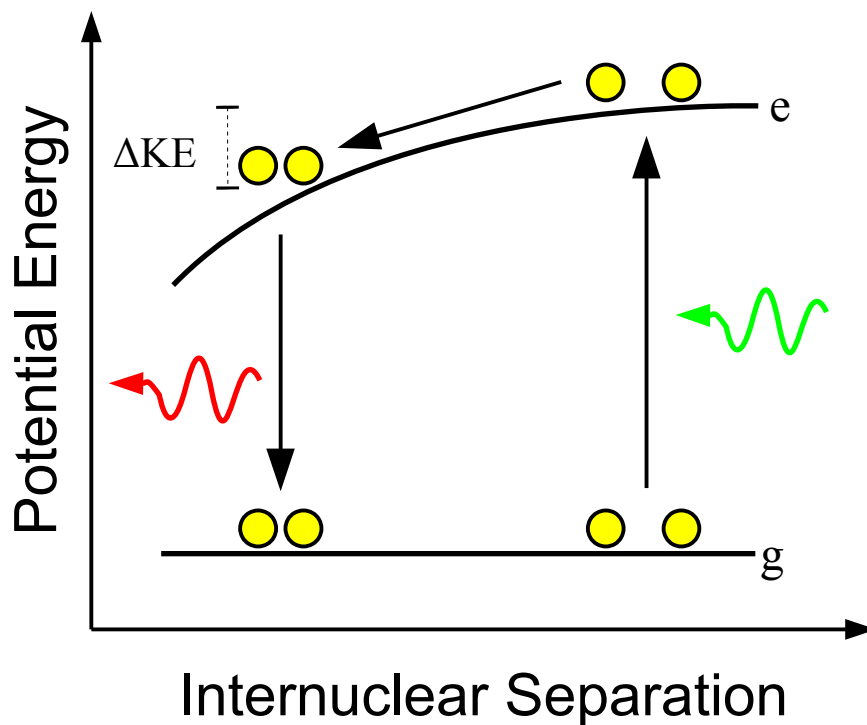
Figure 3.2 Light-Assisted Collision of a Two Atom Pair.
Potential energy curves of a two atom pair as a function of internuclear separation.
Absorption of a photon (green) puts the pair on the excited potential (e) where they are
accelerated toward each other. When the pair emits a spontaneous photon (red), returning to
the ground state (g), they have picked up kinetic energy (ΔKE) which can cause the pair to be
ejected from the trap. The emitted photon is less energetic than the absorbed photon,
conserving energy with the kinetic energy of the atom pair. The excited state energy potential
shown in this figure is attractive, however repulsive potentials exist as well. In reality the
upper state is much more complicated than a single state, but this illustrates the basic loss
mechanism.

by increasing the laser intensity to produce a deep trapping potential. Thus a far off-resonant trap (FORT) can be used to create a strong trap with very little loss.

The physical geometry of the FORT beam determines the shape of the trapping potential. The geometry of the FORT is determined by the electric field component of the light:

$$E = E_0 \psi \exp(i k z - i \omega t) \qquad (3.2)$$

for a beam of light with wavenumber k and angular frequency ω traveling along the z direction. Assuming the laser produces a Gaussian beam that is cylindrically symmetric, the electric field component of the beam is described by a cylindrically symmetric paraxial wave equation [9]:

$$\frac{1}{r}\frac{\partial}{\partial r}\left(r \frac{\partial \psi}{\partial r}\right) - i 2 k \frac{\partial \psi}{\partial z} = 0 \qquad (3.3)$$

where r and z denote the radial and axial directions receptively, and k is again the wavenumber of the laser light. Solutions to equation (3.3) take the form of the Laguerre-Gaussian or Hermite-Gaussian modes. These are transverse electromagnetic (TEM) modes with the lowest order mode (TEM$_{0,0}$ for Hermite-Gaussian modes) having a beam profile which is a simple Gaussian. The amplitude of the electric field of the TEM$_{0,0}$ mode is described by:

$$\left|\frac{E}{E_0}\right| = \frac{w_0}{w(z)}\exp\left[-\left(\frac{r}{w(z)}\right)^2\right] \qquad (3.4)$$

where w_0 is the beam spot size at its minimum and $w(z)$ is the beam size at an arbitrary position given by:

$$w^2(z) = w_0^2\left[1 + \left(\frac{z}{z_0}\right)^2\right] \qquad (3.5)$$

where z_0 is the Rayleigh length of the beam defined as:

$$z_0 = \frac{\pi n w_0^2}{\lambda_0} \qquad (3.6)$$

here, n is the index of refraction of the material the beam is propagating through (typically air or vacuum so in our case $n = 1$), and λ_0 is the wavelength of the light. The Rayleigh length is the distance from the minimum spot size to where the beam cross sectional area has doubled (spot size has increased by a factor of the square root of two). The spot size of the Gaussian is defined by the e^{-1} points of the electric field amplitude and are plotted as a function of the propagation of the beam in figure 3.3. The minimum spot size and the beam divergence are the most relevant beam parameters for the FORT trapping potential. The beam divergence is related to the other beam parameters by:

$$\frac{\theta}{2} = \frac{\lambda_0}{\pi\, n\, w_0} \tag{3.7}$$

The radial confinement of the trap is related to the spot size of the trap and the axial confinement is related to the beam divergence. Generally the tighter the confinement of the trap the better. This means that for a given spot size, a longer wavelength produces a more rapid divergence and thus stronger axial confinement. Thus, lower frequency lasers can in general have better confinement than higher frequency ones, holding the spot size constant.

For a laser sufficiently red-detuned from any atomic resonance, such as 10.6 μm CO_2 light trapping Rb atoms, the trapping potential can be found using the DC electric polarizability in a time-averaged electric field. The resultant time-averaged light-shift in energy is given by:

$$\Delta E = -\frac{1}{4}\alpha\, E^2 \tag{3.8}$$

α is the atomic polarizability, where the induced dipole strength is given by α times the electric field magnitude. For Rb, the atomic polarizability is 47.24 cm^3 [10] or 5.25×10^{-39} C m^2 V^{-1}. Using the polarizability of Rb, equations (3.4) & (3.8), and the measured beam power and size, trap parameters can be predicted. Knowing how much power is in the beam allows E_0 in equation (3.4) to be found since integrating over the intensity (E^2) distribution yields the
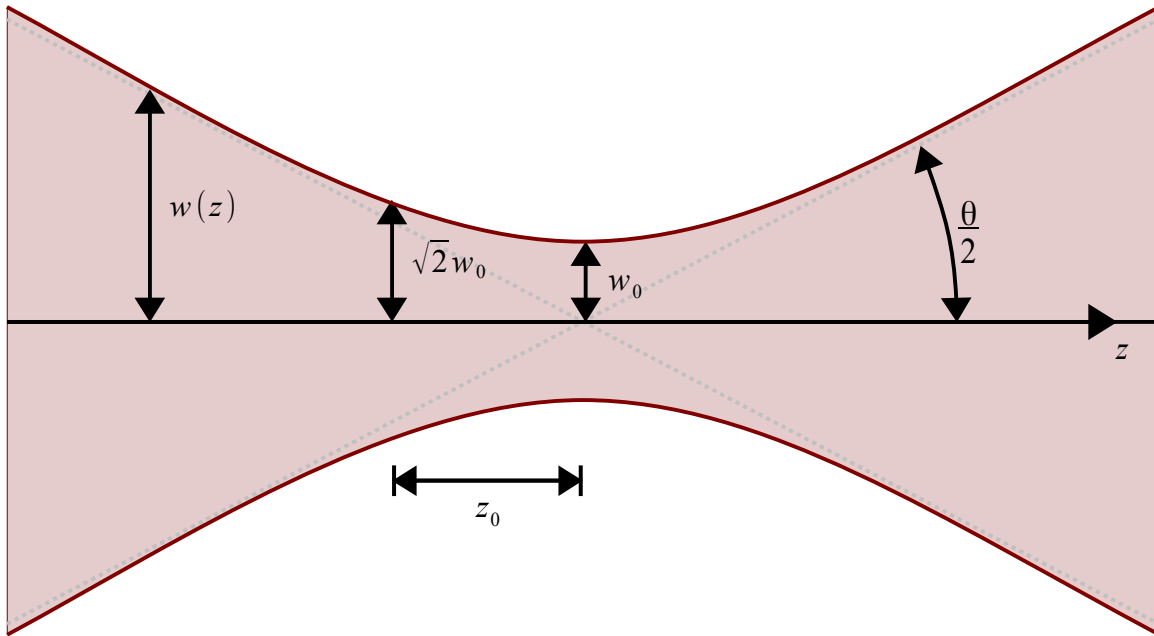
Figure 3.3 Shape of a Gaussian TEM$_{0,0}$ Beam.
A TEM$_{0,0}$ beam has a radial electric field and intensity distribution which is Gaussian in shape. Plotted above along the transverse direction are the e^{-1} points of the field which define the waist size of the beam, $w(z)$, which changes as the beam propagates in the z direction. The minimum spot size, w_0, is found at the focus of the beam. The beam diverges asymptotically from this point characterized by the angular spread of the beam, θ. The distance from the focus to $2^{1/2}w_0$ defines the Rayleigh length, z_0. These parameters are dependent on the wavelength of light used in the beam. Shorter wavelength light can be focused to a smaller spot size and will diverge less than light of a longer wavelength.

total power. Then the trap depth is found by the maximum of the trapping potential given in equation (3.8). The radial and axial trapping frequencies can be predicted by comparison of the second order term in the Taylor expansion of the trapping potential with the ground state energy level of an atom in a harmonic potential. For example, a 20 Watt beam of 10.6 μm light with a spot size of 90 μm, which is comparable to the trap used in the CAZ experiments, would produce a trap depth of just under 113 μK with a radial trapping frequency of about 370 Hz and an axial trapping frequency of 9.8 Hz.

This estimate assumes a pure $TEM_{0,0}$ beam which by definition has an M^2 value of 1. Real laser beams often exhibit some degree of deviation from purely Gaussian and this variation is characterized by the unit-less beam quality parameter, M^2 ("M squared"). The M^2 of a beam is found by the ratio of the beam parameter product (BPP) of the beam to the BPP of a Gaussian beam. The BPP is the product of the beam divergence with the minimum spot size. As an example, it is seen from equation (3.7) that a $TEM_{0,0}$ beam propagating in vacuum has a BPP of λ_0/π. Any distortion imposed on a beam will cause its M^2 to deviate from 1. The M^2 of a beam is often most easily determined by experiment. The M^2 of our CO_2 laser prior to the CAZ experiments was measured to be 1.6 in the vertical direction and 1.35 in the horizontal direction [1]. For simplicity we will look at a beam with an M^2 of 1.4 in both directions and calculate the change to the trapping parameters as an example. To approximate the trapping parameters for a beam with $M^2 > 1$, the same calculations as before are done but with the Rayleigh length multiplied by M^2. Repetition of the calculations for a 20 Watt, 10.6 μm beam with measured minimum spot size of 90 μm an assumed M^2 of 1.4 increases the expected axial frequency to about 13.8 Hz.

Recall from equation (3.6) that the Rayleigh length is proportional to the minimum spot size squared. Thus the minimum spot size is effectively larger by a factor of the square root of

M^2. This means that the minimum spot size could have been 76 μm had the beam had an M^2 of one. This would lead to a trap depth of 158 μK, a 520 Hz radial trapping frequency, and a 16 Hz axial trapping frequency. This means that the beam used in the prior experiments would have had a respectable improvement in the trap depth and confinement had it been a higher quality beam. It is likely that the deviation from an M^2 of 1 observed in our system is a consequence of non-linear thermal lensing effects occurring in the AOM used to turn the optical trap on and off. This will be an intrinsic limitation of a FORT since a high intensity, and thus high power, beam must be used to compensate for being far from resonance. High energy beams tend to cause thermal lensing effects in the optics and components such as the AOM.

The loss of trap depth and confinement strength due to laser beam distortion is not a total loss however. The trap depth is related to how tightly the beam is focused. This means that a very deep trap will result from a very tightly focused beam and as a consequence, the trap volume will be comparatively small. Conversely a relatively shallow trap will result in a larger trap volume. The trap volume becomes an important consideration for loading the trap with atoms. The larger the trap volume, the larger the capture region for atoms needing to be loaded. Therefore a shallow trap will capture more atoms, all other things being equal. For this reason, the FORT is kept intentionally shallow so as to allow a large number of atoms to be captured. However, a large volume trap will confine atoms at a lower density than if the same number of atoms were loaded into the smaller volume deeper trap. Because a high density of atoms is important in CAZ cooling for maximizing the cooling rate, a large number of atoms and a high density of atoms are desired. A system capable of first capturing a large number of atoms, then compressing them to a small volume would be able to satisfy both these goals. How this might be done is covered in appendix C.

3.3 Improvements in Magnetic Field Production

One of the key requirements for a CAZ setup is the need for a controlled magnetic field in the region where the atoms are cooled. As discussed earlier, this is what separates the energies of the magnetic sub-levels which enables kinetic energy to be transferred to magnetic energy. This section will discuss what is necessary to prepare the magnetic fields of a standard MOT-to-optical trap setup for CAZ cooling.

3.3.1 Anti-Helmholtz to Helmholtz Configuration

Once the optical trap has been loaded from the MOT, the MOT ceases to be of use and is turned off. However, many of the MOT components can be reused for CAZ cooling so as to reduce the footprint and amount of necessary equipment. The anti-Helmholtz (AH) coils are an example of such a piece of equipment. By reversing the current direction in one of the coils, a Helmholtz coil configuration can be utilized to produce the magnetic field necessary for CAZ cooling, as can be seen in the insets of figure 3.4. This can be a convenient approach to provide the requisite B-field since, contrary to a dedicated coil set up, it does not require much additional equipment, especially around the vacuum chamber itself. There are however, several factors which do need to be considered in order to reuse the AH coils.

The AH coils of our system consist of two coils of radius 3.8 cm and 36 loops located outside the vacuum chamber each 10 cm away from the optical trapping region. For the MOT, they run at a current of 20 A which produces a field gradient of about 4 G/cm. The requisite field strength for CAZ cooling is considerably less; 0.84 G matches the Zeeman splitting with the thermal energy of atoms at 9.4 μK and requires only 0.7 A of current. Thus not only does the current direction in one of the coils need to be switched, but the amount of current needs to be drastically changed as well. The equipment also needs to handle the relatively high power of the AH coils (>100W) when in the MOT configuration. A sufficiently fast and robust pair of relay
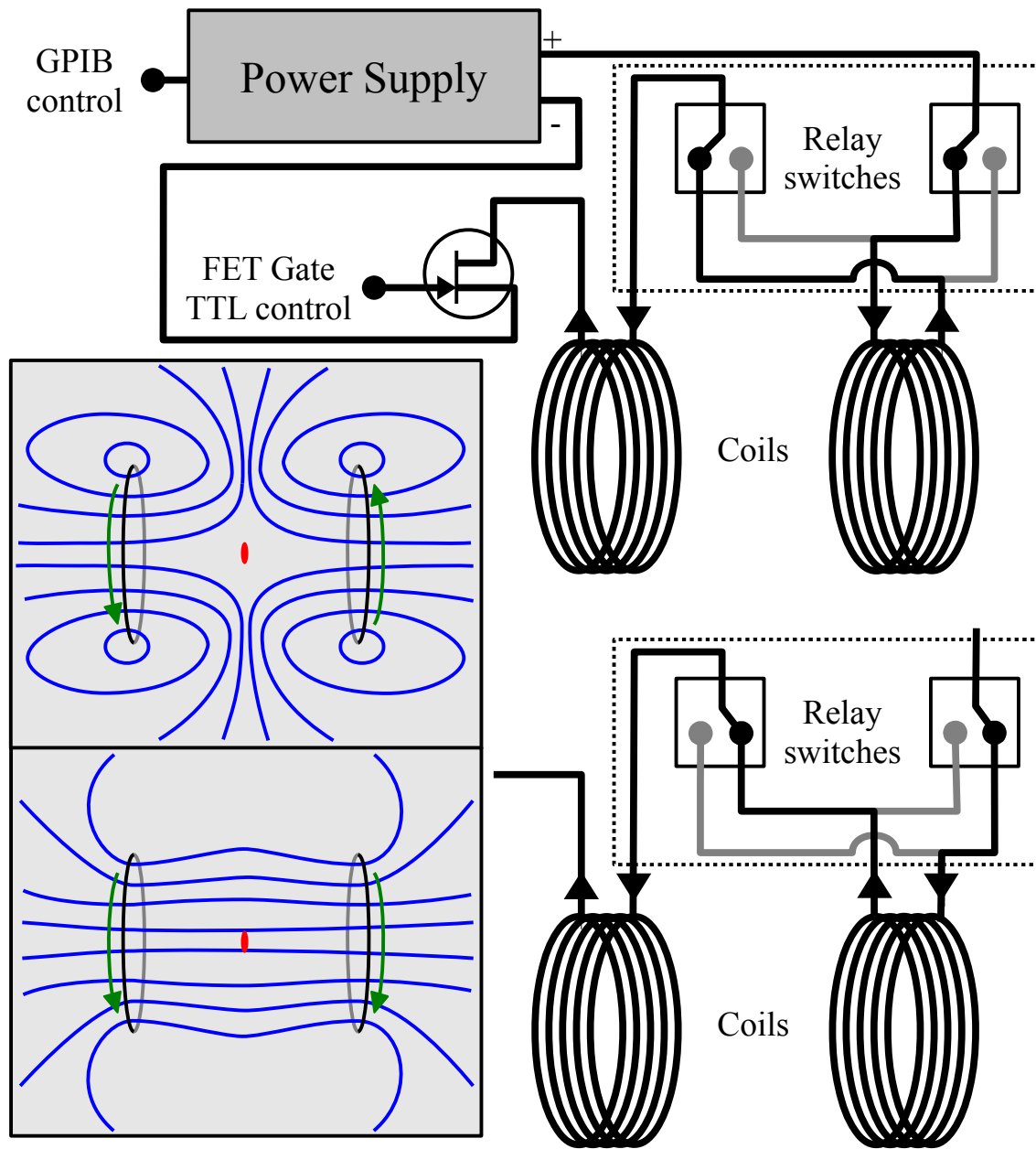
Figure 3.4 Layout of the AH to H Coil Configuration.
Schematic for the anti-Helmholtz to Helmholtz coil configuration. Previously coils were connected in series where the new system has a TTL controlled box (dashed box) containing two relay switches. The lower image of the box and coils shows the system in the Helmholtz configuration. Current direction (arrows) is controlled by the relays. GPIB controls the current level and the FET is used to disable output to the coils. The inset to the left shows the qualitative differences in the magnetic field (blue lines). The optical trapping region and beam direction is indicated in red.

switches can be utilized for changing the coils between anti-Helmholtz and Helmholtz configurations, and a GPIB controlled power supply can handle the necessary changes in output current, see figure 3.4.

Due to the amount of power running through the coils while in the MOT configuration as well as the high inductance of the coils, care must be taken to avoid changing the relays while current is running through the coils, otherwise one runs the risk of damaging the power supply. It is therefore wise to completely disable the power supply output prior to making the switch between configurations. In our system this is facilitated by a FET gate. Utilizing GPIB control to disable the supply output was considered but was ultimately abandoned due to timing issues. Our system is controlled through a LabView interface which sets sequence of TTL events which are in turn executed using an external board with its own timing chip (Viewpoint USA DIO-64). The GPIB commands are controlled by the computer and are thus subjected to the timing of the computer. Once the computer activates the DIO board there is no other synchronization between the computer and the board that produces the TTL pulse sequence running on its own internal clock. However, typical variation in timing between the DIO board and the computer is only ~10 ms. This typical variation is small enough that using GPIB to set the power supply output levels does not affect the experiment since the time that the coils are off (using the FET) is much longer. On occasion a major timing discrepancy (> 100 ms) was observed between the DIO board and computer GPIB. Had the system relied on using GPIB to turn off the power supply, then the relays would have been switched while the coils were running at the full 20 Amperes. For this reason, the disabling of the power supply was done using the FET controlled by TTL from the DIO board since the timing would then be consistent with the switching of the relays.

Even with the coil power supply disabled, switching the relays on and off is hard on the power supply as well as other electronics in the lab since electromagnetic energy tends to be

thrown around lab as a result of the switching. One of the control boxes for a laser utilized in the experiment (the probe laser) happened to be in relatively close proximity to the relays. This resulted in occasional loss of laser lock and a failed experimental run (since the probe was unable to image the atoms). Attempting to shield the relays was not successful at preventing the problem, but disabling the current lock on the laser usually prevented the issue.

When the coils are switched on or off, there is a delay before the current settles. To prevent any changes to the system while the coils were settling, 35 ms were given to let the system settle whenever the coils were turned on or off. Combined with time windows sufficiently large to allow the GPIB commands to work without issue and the entire coil switching process requires almost 100 ms, which is not enough to significantly affect the experiment adversely (trap lifetime is approximately 3 s for comparison). Allowing this ample time for coil adjustments is important to prevent the pump laser light from being turned on during the time when the magnetic field varies rapidly. If the laser light were to be turned on prematurely, then atoms could be either pumped into states with a high loss rate, or the sample could experience a large amount of optically induced heating.

3.3.2 Setting the Magnetic Field

For CAZ cooling to operate most efficiently, the magnetic field should be set to a value such that the average kinetic energy is equal to the amount of energy removed per cooling collision (equation (2.5)). It is then straightforward to see that the optimal field strength is proportional to the atom temperature:

$$B_{opt} = \frac{6}{\mu_B} k_B T \tag{3.81}.$$

This is the optimal magnetic field strength for a mixture of ^{85}Rb and ^{87}Rb (ignoring heating during the optical pumping process). Since CAZ cooling will inherently reduce the temperature

of a sample, it is evident that the optimal magnetic field strength will change as the cooling process progresses. For the first demonstration of CAZ cooling presented here, the magnetic field strength was kept constant so as to simplify the experiment. However, in order for the cooling technique to reach its full potential, the magnetic field will need to be adjusted as the sample cools. Changes to the experimental apparatus were made in anticipation of this, which is covered in appendix C.

The magnetic field strength was calibrated using resonant microwave spectroscopy. This may be done with either ^{85}Rb or ^{87}Rb in our system, which was loaded into the FORT without the other isotope present. Atoms were prepared in the lower hyperfine ground state, then the external magnetic field was turned on using a set current (set to produce a field on the order of a couple of Gauss). The approximate field strength at the position of the atoms may was estimated from the current used and the coil geometry. Due to the Zeeman effect, the magnetic field shifts the magnetic sub-level energy levels of the atom. Note that because the g-factors of the upper and lower hyperfine states have different signs (see appendix A), the m-states of each hyperfine state shift in opposite directions (for the same value of m_F). This produces a rich array of microwave transitions between the lower and upper hyperfine ground states. These transitions were then detected by imaging the atoms without the hyperfine repump light on after exposure to a microwave field set near the frequency of the hyperfine splitting. Only atoms which had been excited to the upper hyperfine ground state were visible by the probe light resonant with the D2 cycling transition. Thus as the microwave frequency was swept through the resonances between hyperfine ground states, some of the atoms came into and out of view of the probe light. Peaks in the number of atoms imaged with the probe correspond to resonances between hyperfine states. Because the Zeeman shifts are calculable, the expected microwave spectrum at a given field strength was simply compared with the observed microwave resonances. Repetition of the

process at different magnetic field strengths made it possible to develop a calibration of the set coil current to the magnetic field strength at the atom position.

3.4 Spin Polarization Components

With the appropriate magnetic field to setup and control the separation between m-states of the atoms in place, the next thing that must occur for CAZ cooling is the spin polarization of one of the atomic species. In the Rb mixture, it is the ^{85}Rb which is spin polarized. Only one of the spin polarizing techniques discussed in section 2.3.2 was used for our initial evaluations of CAZ cooling with Rb: direct optical pumping. This section discusses the experimental application of direct optical pumping to the $^{85/87}$Rb mixture.

The direct optical pumping scheme is the most straightforward and easiest to implement method of spin-polarization. All the steps of the direct optical pumping scheme are summarized in figure 3.5. The goal of an all-optical spin-polarization pump is to put all the ^{85}Rb atoms into the $m_F = -2$ lower ground hyperfine state while leaving those atoms unaffected by the pump light once they are there. Any excitation of these atoms will only add to heating of the atoms without any offsetting cooling. This goal is facilitated through the use of a pure σ^- polarized primary optical pumping beam. The primary optical pumping beam is set so that it excites atoms out of the $F = 2$ ground state and into the $5P_{1/2}$ $F' = 2$ excited state. Because no $m_F = -3$ excited state exists, the σ^- light cannot excite the $m_F = -2$ lower ground hyperfine state through a resonant transition. Thus the primary optical pumping beam serves to clear out any population in all but the $m_F = -2$ sub-level of the $F = 2$ ground state. The primary optical pumping beam does not affect atoms in the $F = 3$ ground state. This poses a problem because atoms in the $F' = 2$ excited state have a 7/9 chance to spontaneously decay to the $F = 3$ ground state. Thus most of the atoms will end up in a state which is not only inaccessible to the primary pump light but also not the intended spin-polarized state. For this reason, it is absolutely critical that a second optical
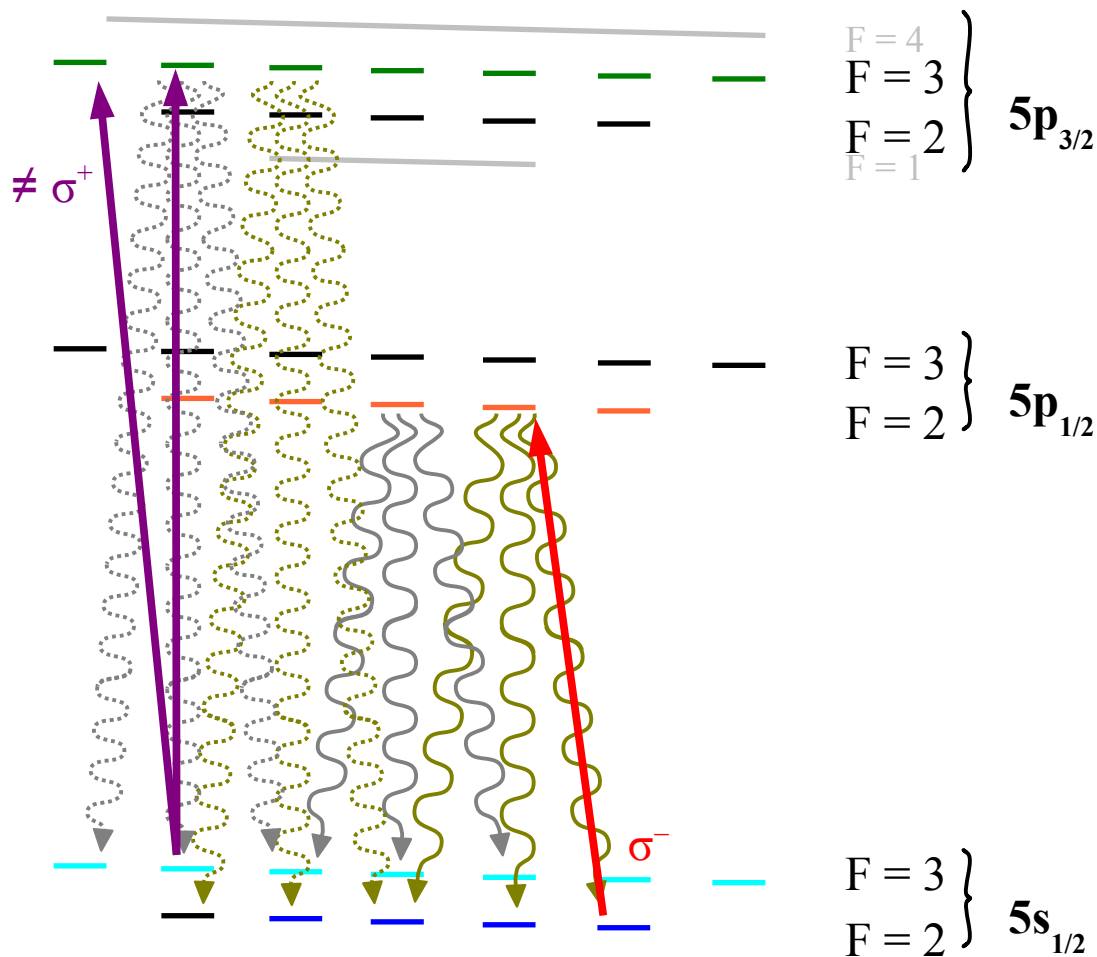
Figure 3.5 Spin-Polarizing Direct Optical Pumping of ^{85}Rb.
To effectively spin-polarize ^{85}Rb, atoms in the $F = 2$, $m_F = -2$ ground state must be unaffected by the optical pumping light. This is facilitated by the primary optical pump beam (red) which is made up of pure σ^- polarized light. This drives atoms out of each of the lower hyperfine ground states (dark blue) and into the lower hyperfine $5p_{1/2}$ excited state. The lack of an excited $m_F = -3$ state, ensures that atoms in the $m_F = -2$ ground state are unaffected with respect to resonant transitions. Any atom excited by the primary pump beam is in a state (orange) where they may decay spontaneously to the either the $F = 2$ (solid brown) or the $F = 3$ (solid gray) ground states. When an atom ends up in an upper hyperfine ground state (light blue), it will be cycled out by the repump beam (purple) consisting of light absent of σ^+ polarization. These atoms are pumped into a $5p_{3/2}$ $F = 3$ excited state (green) where they then decay back to the ground state (dotted brown and gray). For clarity the excitation and decay routes of only one of any similar colored state is shown.

repump beam is used. For the repump beam a 780 nm laser is used to drive atoms out of the $F = 3$ ground state and into the 5P$_{3/2}$ $F' = 3$ excited state. The desired polarization state of the repump is a combination of σ^0 and σ$^-$ polarization. Any σ$^+$ polarization serves to undo the spin-polarization process. Some σ^0 polarization is required in order to remove atoms from the $F = 3$, $m_F = -3$ ground state, which would otherwise be unaffected by the repump light. Leaving atoms in the upper hyperfine ground state is undesirable even it they are polarized because this state suffers a higher loss rate from the FORT. Although the spontaneous decays from the excited states may not necessarily result in net transfer of atoms toward the spin-polarized state (determined by the relevant Clebsch-Gordan coefficients), both the pump beams cause a strong migration of atoms toward spin-polarization state. In this way, all the atoms can end up in the desired spin-polarized state. Note that for the laser intensities and scattering rates used in this work, the Zeeman shifts due to the magnetic field prevent the formation of dark states.

While the aim of the spin-polarization is to avoid scattering and the resultant heating of the spin-polarized atoms, in practice there will always be some of this. Both imperfect beam polarization and off-resonant transitions are the cause of unavoidable scattering events resulting in heating. The magnitude of both of these effects can be estimated. In general, the scattering rate is given by:

$$R = \frac{\gamma}{2} \frac{\left(\dfrac{I_0}{I_{sat}}\right)}{1 + \left(\dfrac{I_0}{I_{sat}}\right) + 4\left(\dfrac{\delta}{\gamma}\right)^2} \qquad (3.82)$$

here, I_0 is the intensity of the light field, I_{sat} is the saturation intensity which is defined here as the circularly polarized light intensity needed to saturate the transition of the atoms in a maximally polarized state, γ is the inverse of the excited state lifetime, and δ is 2π times the laser detuning, Δ. The scattering rate of a specific transition due to a given polarization of the driving light field

can be found by modifying the I_0/I_{sat} term in equation (3.82) with the appropriate Clebsch-Gordan-based coefficients weighted by the proportion of the light field polarized along the transition,

$$\left(\frac{I_0}{I_{sat}}\right) \rightarrow C\left(\frac{I_0}{I_{sat}}\right)\Sigma \qquad (3.83)$$

where C represents a product of weighting coefficients relevant to the transition of interest, and Σ is the proportion of the light field which is correctly polarized along the transition. The term C can be reduced down to the product of two factors: one proportional to the reduced matrix element squared between the relevant ground and excited F states, and the other to account for the addition of the photon momentum (i.e. a Clebsch-Gordan coefficient). For our system which pumps out of the $F = 2$ ground state of ^{85}Rb, the only transfers between F states possible are to the $F' = 3$ and $F' = 2$ excited states which contribute a factor of 5/9 and 2/9 respectively. The factor for the addition of the photon momentum will depend on the particular transition of interest. For example, the off-resonant transition $F = 2$, $m_F = -1$ to $F' = 3$, $m_{F'} = -2$ requires a σ^- photon and contributes the Clebsch-Gordan coefficient: $(j_1\ j_2\ m_1\ m_2\ |\ j_1\ j_2\ j\ m)^2 = (2\ 1\ -1\ -1\ |\ 2\ 1\ 3\ -2)^2 = 2/3$ and thus $C = (5/9)\cdot(2/3) = 10/27$. Ideally, Σ would be 1 for σ^- transitions and 0 for all others, but the polarization is likely imperfect and some contamination of σ^0 polarized light can be expected. It should however, be a relatively small amount. Summation of all the possible rates multiplied by the photon recoil energy, $E_R/k_B = 0.18\ \mu K$ for ^{85}Rb, gives an idea of how much heating in micro-Kelvin can be expected.

For our system, the intensity of the primary optical pump beam is approximately 10 $\mu W/cm^2$, and the saturation intensity of Rb is 1.6 mW/cm^2. The primary spin-polarizing pump laser is detuned 37 MHz to the blue of the $F = 2 \rightarrow F' = 2$ transition on the D1 line of ^{85}Rb (the left pink line in figure 1.1) which has a γ value of $2\pi\cdot5.98$ MHz. Assuming that all the ^{85}Rb

has been spin-polarized and is in the $F = 2$, $m_F = -2$ ground state and that spontaneous decays into the other ground states are small enough to be negligible, an off-resonant heating rate of at least 2 µK/s can be expected if the beam consists of pure σ^- light. This increases linearly to almost 3 µK/s with a 2% portion of the beam (by intensity) comprising of linearly polarized light. Although this heating rate is non-negligible, it should not be in excess of what CAZ cooling can remove from the system. The estimate does not account for "backstreaming" of atoms where some number of atoms in the $m_F = -2$ state are pumped out due to imperfect beam polarization and off-resonant transitions. These atoms will require additional photon scatter events to be repumped back into the appropriate state which will result in additional heating. This is treated in more detail in chapter 5 where it was evident as a degradation of the expected cooling rate as compared to the cooling rate that was observed. How the direct optical pumping scheme is implemented into the system follows.

3.4.1   Direct Optical Pump Beam

The use of an all optical pump to directly spin polarize the ^{85}Rb was the first optical pumping scheme that we attempted. Since the MOT was no longer needed at this point in the experiment, the trapping lasers were used to provide the light. The primary spin polarizing optical pump acted on the D1 line of Rb at 795 nm and so the MOT repump laser was used as the primary spin polarization beam. The setup can be seen in figure 3.6. The MOT repump is switched on and off by an 80 MHz AOM which deflects the beam into the chamber. The through beam is then available for the spin polarizing pump. However, the MOT repump drives the $F = 2$ to $F' = 3$ transition of the Rb D1 line, and for the spin polarization pump the $F = 2$ to $F' = 2$ transition needs to be used. The laser diode locking range is limited, so it is not practical to use the electronic lock box to achieve such a frequency shift. A frequency shift of 80 MHz already exists in the beam as a result of the AOM which controls the MOT repump beam. Thus a
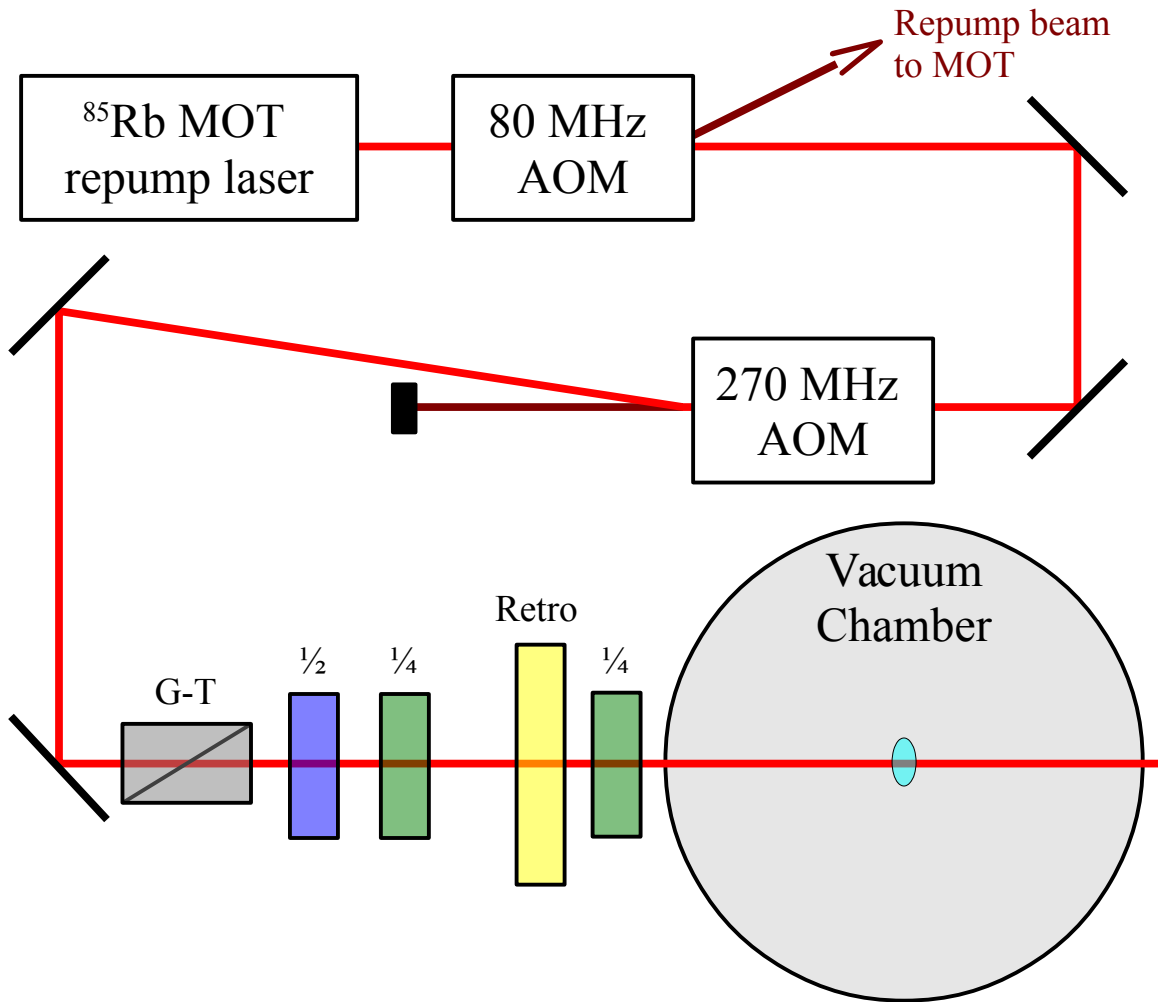
Figure 3.6 Spin Polarization Layout for Direct Optical Pump.
The direct optical spin polarizing pump beam is produced by the same laser used for repumping
^{85}Rb in the MOT. Since the MOT repump drives atoms to the upper hyperfine excited state
($F = 2$ to $F' = 3$), a second 270 MHz AOM is used to red shift the unused beam from the 80 MHz
MOT control AOM to bring the pump beam close to the lower hyperfine excited state resonance
($F = 2$ to $F' = 2$, 360 MHz to the red). The beam is then sent through a Glan-Thompson polarizer
(G-T) to be linearly polarized. A $\lambda/2$ waveplate (½, blue) adjusts the orientation of the linear
polarization. Next a $\lambda/4$ waveplate (¼, green) puts some ellipticity into the beam set to cancel
out any introduced by passing through the backside of the slightly transmissive axial retro-
reflection mirror (yellow). This ensures that the fixed $\lambda/4$ waveplate next to the chamber
changes the beam to σ^- circularly polarized light to pump the atoms (center of light blue oval).

270 MHz AOM was used to further shift the beam to the red. This brings the frequency close enough to the $F = 2$ to $F' = 2$ transition, which is 362 MHz away from the $F = 2$ to $F' = 3$. The electronic lock box can then be used to set the frequency. The 270 MHz AOM also serves as an on/off switch for the spin polarizing beam.

While the reuse of the MOT coils to provide the magnetic field necessary for CAZ cooling is convenient in many respects, it is however inconvenient in others. The largest problem being that the quantization axis of the system is then set to the axial direction of the MOT. The reason that this is inconvenient is due to the fact that our MOT uses retro-reflected trapping light. This means that the axial MOT beam path, which is reflected back on itself, lies along the magnetic quantization axis. To take advantage of purely circularly polarized light for the optical pumping process, the pump light must travel in the direction of the quantization axis otherwise it will always have some linear component. Therefore the deflected beam from the 270 MHz AOM must be directed to travel along the same direction as the axial MOT trapping beam. The optical pumping light cannot be coupled into the same beam path as the axial trapping beam because the retro-reflecting mirror has a $\lambda/4$ waveplate in front of it in order to reverse the handedness of the MOT beam. This means that the optical pumping beam would also switch handedness after being reflected and set up a polarization gradient just like the MOT beam. This is completely contrary to the goal of a pump beam of a single polarization.

To avoid setting up a polarization gradient, the optical pumping beam must come into the chamber from the other direction- through the back of the retro-reflection mirror. This can be done with a slightly transmitting mirror which allows a small amount of the optical pumping light to pass through while the MOT light traveling in the opposite direction will be mostly reflected. Only a small amount of optical pumping light is needed; indeed, in our system a 98% reflective retro-reflection mirror easily passes about 10 $\mu W/cm^2$ of optical pumping light for spin

polarization. Not only is this a sufficient amount of light for direct optical pumping to spin polarize ^{85}Rb at a reasonable rate, but we found that there was so much light that light-assisted collisions became an issue.

The spin-polarizing optical pump is required to pass through the back end of the partially reflective retro-reflecting MOT mirror, as well as a fixed $\lambda/4$ waveplate; both these optics cannot be avoided since are necessary for the MOT. Thus to set the spin-polarizing beam polarization, the following optics are used prior to the back of the retro-reflection mirror: a Glan-Thompson polarizer to linearly polarize the pump beam, a $\lambda/4$ waveplate oriented to change the ellipticity slightly in order to cancel out any ellipticity introduced by the birefringence of the retro-reflection mirror, and a $\lambda/2$ waveplate to orient the polarization axis correctly with the fixed waveplate next to the chamber. Ultimately the polarization was optimized experimentally due to the unknown birefringence of the chamber port windows.

3.4.2 Repump Beam

Regardless of spin polarization method used, ^{85}Rb atoms will need to be pumped out of the $F = 3$ hyperfine ground state. This can be accomplished utilizing the ^{85}Rb MOT trapping laser at 780 nm on the D2 line of Rb. Normally the main cycling transition of the MOT trapping beam is the $F = 3$ to $F' = 4$ transition; however, the $F' = 4$ excited state is undesirable because it cannot decay back to the $F = 2$ ground state. Thus the frequency must be shifted sufficiently to avoid transitions to the $F' = 4$ state. This is done by utilizing two 80 MHz AOMs to red-shift the beam a total of 160 MHz. This puts the excitation of the repump beam between the $F' = 2$ and $F' = 3$ hyperfine levels of the $5P_{3/2}$ state (recall figure 1.1).

The laser frequency lock boxes that are used in the experiment have four available channels allowing the laser to be locked to four different frequencies. The MOT trapping laser utilizes all four channels for the loading process of the FORT. This meant that the laser lock box

had to be modified in order to have independent control of the spin polarizing repump frequency. Additional circuitry was added to the lock box to allow for two additional frequency set points. The new setup utilizes TTL logic so that only three control channels (previously two) are necessary to choose any of the six set points (three bits having upgrade capability for up to eight set points). One of the new set points is used for locking to the spin polarizing repump frequency which is adjustable over a range of a little over 100 MHz.

The repump beam must be polarized in a fashion that minimizes any population pumping contrary to the spin polarization. A full σ^- circular polarized repump would not move atoms the wrong direction, but it would not pump atoms in the $F = 3$, $m_F = -3$ ground state. This is because the σ^- light will only couple to a $m_F = -4$ excited state which can only decay back to the $m_F = -3$ upper hyperfine ground state for no gain (in addition to such a transition being relatively far off resonance for the set frequency). Thus some amount of linear polarization is necessary to clear atoms out of the $F = 3$, $m_F = -3$ ground state since it drives to the $F' = 3$, $m_F = -3$ excited state and has only one decay option to the lower hyperfine ground state: the desired $m_F = -2$ state. Decays back to the $F = 3$ hyperfine level will be repumped until they drop back to the $F = 2$ ground state. This means that the constraints on the polarization of the repump beam is to have a combination of σ^0 and σ^- polarizations with no σ^+ circular polarization component. Therefore the light can easily be sent along any direction so long as it has the appropriate elliptical polarization. Thus the only necessary polarization optics are a linear polarizer and a $\lambda/4$ waveplate.

3.5   Internal Microwave Antenna

Knowing about the m_F state population distribution of the atoms within the optical trap is vital for setting up and diagnosing CAZ cooling. This was accomplished utilizing a microwave antenna internal to the vacuum chamber capable of state-selective microwave excitation.

Although it is also possible to determine the state distribution using a Stern-Gerlach approach [11], due to the relatively high starting temperature of the atoms, the requisite time of expansion needed to resolve the states is too great for our system. The antenna was powered by a microwave generator with output sent through an amplifier, and connected by a BNC feedthrough into the vacuum chamber.

Measurement of the individual state populations is possible because there is a difference in the ground state hyperfine splitting between states with equal m_F values while in the presence of a uniform magnetic field, as can be seen in figure 3.7. For ^{85}Rb the frequency shift of the hyperfine splitting is approximately: 0.9 m_F B MHz/G. For ^{87}Rb the frequency shift is: 1.4 m_F B MHz/G. Using an input of 10 W with a 1% coupling efficiency, a Rabi frequency of 1 kHz can be expected in our system and the individual states were well-resolved to the microwave excitation. Thus resonant microwaves could be used to selectively excite atoms from a specific magnetic sub-level of the lower hyperfine ground state to the upper hyperfine ground state. Because atoms in the upper hyperfine ground state were in resonance with the probe laser, they could then be imaged using absorption imaging as discussed earlier. Repeating the measurement for each m_F state would allow the entire population distribution to be obtained. By sweeping the microwave frequency, multiple states or all states can be excited to the upper hyperfine ground state. This makes it possible to use the microwave antenna as part of the pumping process as described in section 2.3.2.b.

The vacuum chamber is metal, being made of stainless steal, and thus there is a concern about establishing microwave standing waves within the chamber. A standing wave microwave field will inevitably have nodes and hot spots of microwave radiation. The pattern of microwave "hot" and "cold" regions will be dependent on the chamber geometry as well as the specific frequency of microwaves used. Furthermore, field strength will fall off sharply with distance
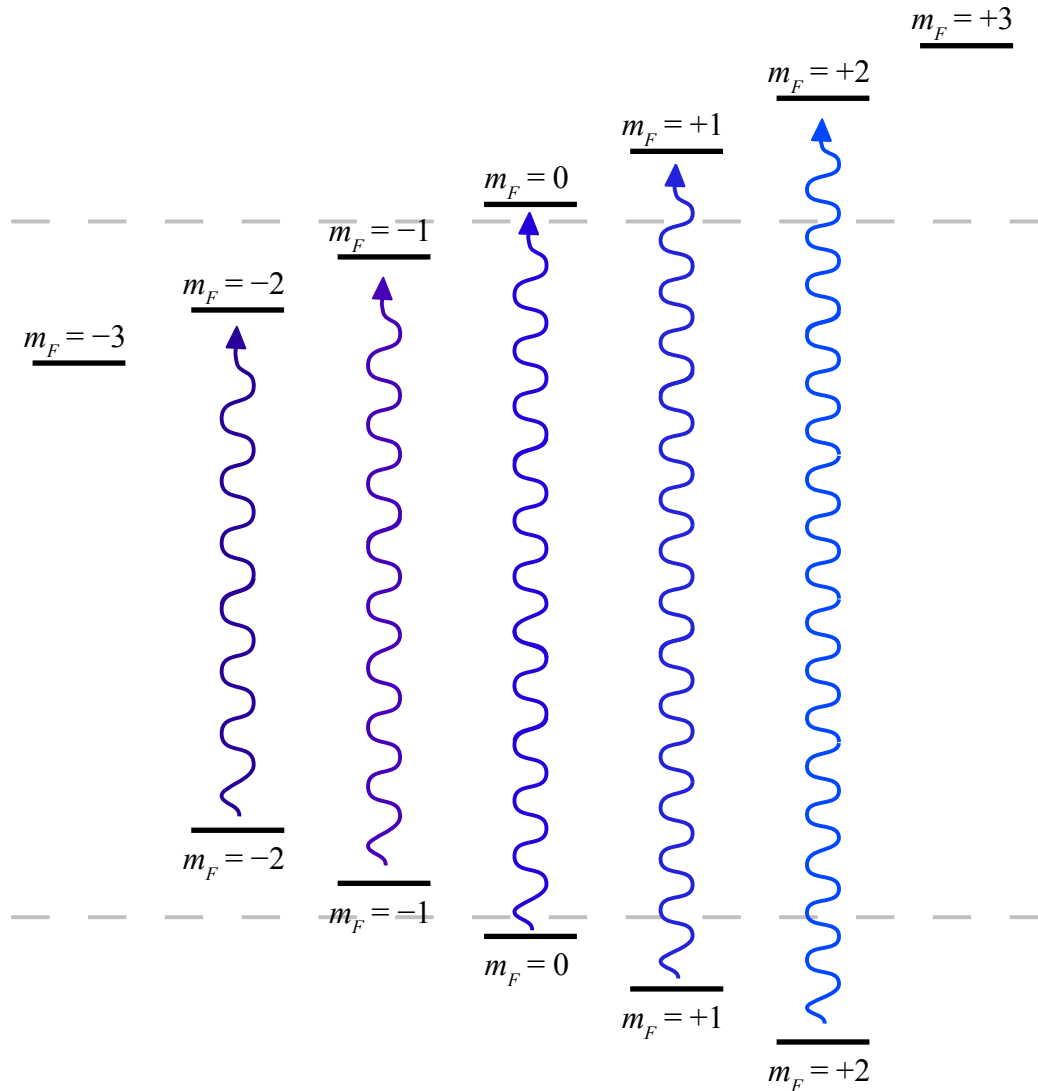
Figure 3.7 Probing the m_F State Distribution of ^{85}Rb.
When in the presence of a magnetic field the magnetic sub-levels of ^{85}Rb become separated, as is qualitatively depicted here for the $F = 2$ and $F = 3$ ground states. Because states of the same m_F value are shifted opposite directions for the two ground state hyperfine levels, microwave excitations (shown in blue) between these states are at slightly different frequencies from one another. Thus resonant microwaves can be used to excite the population of a particular m_F state while leaving the other states untouched. Atoms excited to the $F = 3$ ground state are in resonance with the probe beam and can be imaged and counted. Repeating the process while changing which microwave resonance is used yields the entire m_F state population distribution of the atoms in the trap.

away from the microwave antenna. Due to the chamber geometry, this fall off of field strength is not easily determined. In fact, these considerations imply that there is likely a large variation in the amplitude of the microwaves across the trapping volume of the FORT. Observations confirmed that this was the case, as atoms trapped in a single m_F state could not be one-hundred percent transferred using coherent Rabi oscillations. However, microwave transfer of atoms can be successfully achieved using adiabatic rapid passage.

At the time that this work was completed, microwave coupling to the atoms was poor. This meant that it was not yet possible to measure the entire spin state distribution, or perform effective microwave/optical pumping. There was enough coupling that tasks such as setting the spin polarization and calibrating the magnetic field strength could be done by maximization of signal observed. However, it was not until subsequent experiments performed after this work that the full benefit of the internal microwave antenna was realized.

3.6 Adiabatic Rapid Passage

To measure the m_F state distribution of Rb in our system, an ability is needed to induce a total population transfer out of an individual lower ground state hyperfine magnetic sub-level and into the upper hyperfine ground state so that it can be imaged and measured. In principle this could be done utilizing Rabi oscillations between the levels. This requires a coherent source of resonant microwaves at the >3 GHz frequency separation between the ground state hyperfine levels. When the atoms are exposed to the coherent radiation, they undergo sinusoidal population transfers between the resonant energy levels at the Rabi frequency,

$$\Omega = \frac{\mu_{eff} B}{2 \hbar} \tag{3.84}$$

where μ_{eff} is the effective magnetic transition matrix element, and B is the peak magnetic field amplitude of the radiation field. If the atoms are instead exposed to a π-pulse of the resonant

radiation, one-hundred percent population transfer between states can occur. While this is a very effective method of population transfer, it requires a coherent source of radiation and is sensitive to variations in the π-pulse. The microwave source and delivery system used in our vacuum chamber is not expected to produce radiation that is capable of fulfilling these requirements, and indeed no evidence exists that our system is capable of the ideal coherent Rabi oscillations between hyperfine ground states. In addition, Rabi oscillations are also sensitive to inhomogeneities in the sample itself [12] which, due to the magnetic field variation across the trapping region, also exist in the m_F state resonant frequencies of our atoms. While π-pulses of resonant radiation is not an option for our system, one-hundred percent population transfer is nevertheless an option utilizing an adiabatic rapid passage [13].

In adiabatic rapid passage the radiation field is tuned off of the atomic resonance and is either swept through resonance, or the energy levels are swept so as to pass through resonance with the radiation. When the sweep is performed adiabatically, the entire population can be transferred [14]. To be adiabatic, the sweep must be slow compared to the Rabi frequency:

$$\frac{d\,\Delta(t)}{d\,t}\frac{1}{\Omega^2} \ll 1 \qquad (3.85)$$

where $\Delta(t)$ is the time-varying detuning of the radiation from atomic resonance. When the starting and ending detunings are far enough from resonance, that is greater than the Rabi frequency, a nearly full population transfer will occur. This can be understood by looking the evolution of a two-level dressed-state system subject to the time-dependent Schrödinger equation. Figure 3.8 shows a qualitative picture of the energy levels of the dressed-state system as a function of detuning from atomic resonance. The lower and upper dressed states of the two-level atom are shown as dotted lines which cross at the resonance frequency. If changes in the detuning are done non-adiabatically, the state populations follow these lines. However, when the
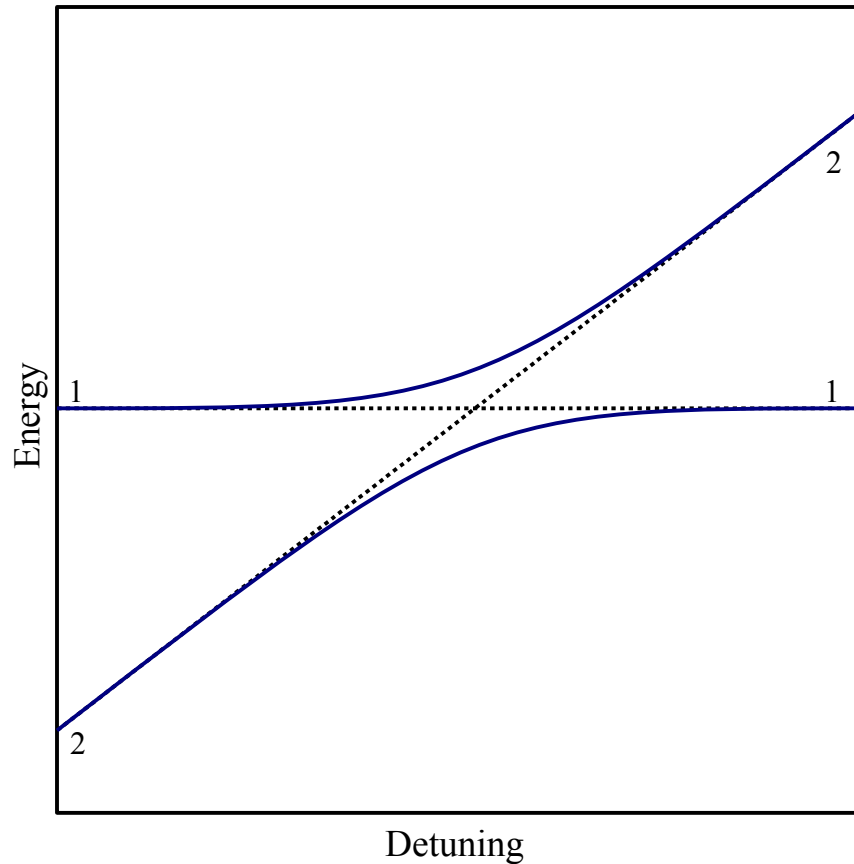
Figure 3.8 Adiabatic Rapid Passage via Avoided Crossing.
The energy levels of a two-level atom dressed with an exposed radiation field are shown as a function of detuning of the radiation from the resonance frequency of the atom. The dotted lines are the dressed energy levels of the two states denoted 1 and 2 representing the large-detuning lower and upper states of the two-level atom respectively. The lower state has been normalized to be zero, and the intersection of the two dotted lines occurs when the radiation field is in resonance with the two-state system. The process of changing the detuning rapidly compared to the Rabi frequency is diabatic and state populations stay on the dotted lines. However, if the detuning change slow, the process is adiabatic. The solid blue lines represent the energy levels of the adiabatic eigenstates of the dressed-state system. These states are a linear superposition of the diabatic states and do not cross due to interaction of the states. This produces what is known as an avoided crossing and the state populations remain on the blue curves for adiabatic processes.

detuning is changed adiabatically, the populations follow the adiabatic eigenstates which appear as solid blue lines in the figure. These states are a linear superposition of of the dressed lower and upper states of the two-level atom. Due to the interaction of these states with the driving field, the adiabatic energy levels do not cross. Instead there is an avoided crossing resulting in the populations of the two states being entirely switched after the detuning sweep. The requirement that the starting and ending detunings be far from resonance ensures the complete population transfer during the adiabatic sweep because the two adiabatic states approach the two atomic states asymptotically at far detunings.

Adiabatic rapid passage is much more robust than direct resonant population transfer. Even if there are inhomogeneities in the sample or driving light, slight variations in the adiabatic eigenstate energy levels still exhibit the avoided crossing behavior resulting in the complete transfer of atoms between energy levels. Extending these ideas to multiple-state atoms, such as the m_F state of Rb in a magnetic field, is fairly straightforward. So long as the detuning sweep is adiabatic, dressed state energy levels will have avoided crossings and populations will be adiabatically transferred between those levels. This makes adiabatic rapid passage a very useful tool for diagnostics such as measuring the m_F state distribution of ^{85}Rb in the CAZ cooling experiments.

3.7 Radio Frequency Scrambler for ^{87}Rb

Thus far, the described components of the CAZ cooling device are the bare-minimum needed to observe CAZ cooling. They allow the necessary control over the magnetic field as well as the spin-polarization and repumping of ^{85}Rb. While it is true that the ^{85}Rb can be cycled back to its desired initial state with this setup, it is not true that the cooling can continue to indefinitely. This is because the spin-exchange collisions shift the ^{87}Rb m_F state population toward the $m_F = -1$ state which cannot undergo additional spin-exchange collisions with the

114

spin-polarized ^{85}Rb. Once the ^{87}Rb is entirely in the $m_F = -1$ state, spin-exchange collisions will cease and the cooling will stagnate. Stagnation can occur relatively fast (~100 ms), so to be able to continue cooling the ^{87}Rb must be redistributed among m_F states periodically.

One way to handle the buildup of ^{87}Rb atoms unusable for cooling is to periodically subject them to an on-resonant RF field. This will scramble the m_F state populations of the ^{87}Rb, as discussed in chapter 2, page 50. Because the level splittings between m_F states of ^{87}Rb are different from those of ^{85}Rb (see equation (2.3)) there should be no worry about ^{85}Rb being depolarized. The RF field can be applied to the atoms using a coil of wire driven at the appropriate frequency.

In anticipation of the need to scramble the ^{87}Rb population distribution, a coil had previously been installed inside the vacuum chamber. The coil consists of ten turns of wire with a diameter of 3 cm and is suspended approximately 4 cm above the trapping region. The proximity to the atoms means that only moderate currents are needed to drive the radio wave excitations. Typically less than half an amp is enough to scramble the ^{87}Rb m_F states. The wire has a Kapton coating so as to prevent electrical shorts within the vacuum chamber since Kapton is an insulator and also does not significantly outgas. The wire connects to the outside of the chamber via BNC feedthroughs.

This completes the description of the experimental apparatus components that have been added to allow the implementation of CAZ cooling. Additional experimental apparatus enhancements were made in anticipation of future work to optimize CAZ cooling. These potentially useful improvements are covered in appendix C.

References for Chapter 3

[1] Anthony Gorges, Ph. D. Thesis, Colorado State University (2010).
[2] A. Gorges, A. Foxley, D. French, C. Ryan and J. Roberts, Phys. Rev. A **76**, 033420 (2007).
[3] A. Gorges, N. Bingham, M. DeAngelo, M. Hamilton, and J. Roberts, Phys. Rev. A **78**, 033420 (2008).
[4] M. Hamilton, A. Gorges, and J. Roberts, Phys. Rev. A **79**, 013418 (2009).
[5] M. Hamilton, A. Gorges, and J. Roberts, J. Phys. B: At. Mol. Opt. Phys. **45**, 095302 (2012).
[6] E. Rabb, M. Prentiss, A. Cable, S. Chu, and D. Pritchard, Phys. Rev. Lett. **59**, 2631 (1987).
[7] W. Petrich, M. H. Anderson, J. R. Ensher, and E. A. Cornell, J. Opt. Soc. Am. B **11**, 1332-1335 (1994).
[8] C.-S. Chuu, F. Schreck, T. Meyrath, J. Hanssen, G. Price, and M. Raizen, Phys. Rev. Lett. **95**, 260403 (2005).
[9] J. T. Verdeyen, *Laser Electronics* 3rd ed., (Prentice Hall, New Jersey, 2000) page 66.
[10] W. F. Holmgren, M. C. Revelle, V. P. A. Lonij, and A. D. Cronin, Phys. Rev. **81**, 053607 (2010).
[11] K. Corwin *et al.*, Applied Optics **37**, 3295 (1998).
[12] W. S. Warren, J. L. Bates, M. A. McCoy, M. Navratil, & L. Mueller, J. Opt. Soc. Am. B **3**, 488 (1986).
[13] N. V. Vitanov, T. Halfmann, B. W. Shore, and K. Bergmann, Annu. Rev. Phys. Chem. **52**, 763 (2001).
[14] J. S. Melinger *et al.*, Phys. Rev. Lett. **68**, 2000 (1992).

Chapter 4

Characterization of Dual Isotope Loading into the FORT

The cooling rate and cooling efficiency of collision-assisted Zeeman cooling is dependent on the rate of spin-exchange collisions between atoms in the gas. Samples of higher densities will have higher spin-exchange rates and will thus exhibit better CAZ cooling performance. For this reason, considerable effort was put into characterizing and optimizing the loading of the optical trap prior to performing the CAZ cooling experiment in order to ensure that the cooling observed was as efficient as possible. Much of this characterization was done in previous work and is summarized in Ref. [1]. This work included experiments to characterize and mitigate light-assisted collisional losses [2] and optimization of loading a single species into the optical trap [3]. Not included was the evaluation of dual-isotope loading which proved to perform worse than expected. Therefore the initial work was extended further and an improved treatment of dual-isotope optical trap loading was developed. This chapter presents this extended preparation work which appears in the literature in reference 4.

4.1   Basic Physics of Optical Trap Loading

The potential produced by a far off-resonant optical trap is conservative. Any atom which enters into the trap will eventually escape as shown schematically in figure 4.1. This is due to the fact that any energy barrier imposed by the trap is overcome by kinetic energy gained by the atom as it enters the potential well. This means a conservative potential alone can only capture atoms that are initially in the trapping potential with sufficiently small kinetic energy. Owing to the relatively small size of the trap, very few atoms are trapped directly when the FORT is initially turned on. This necessitates that atoms be cooled in order for a significant number to be trapped in the FORT. Cooling is facilitated by an optical molasses, which causes
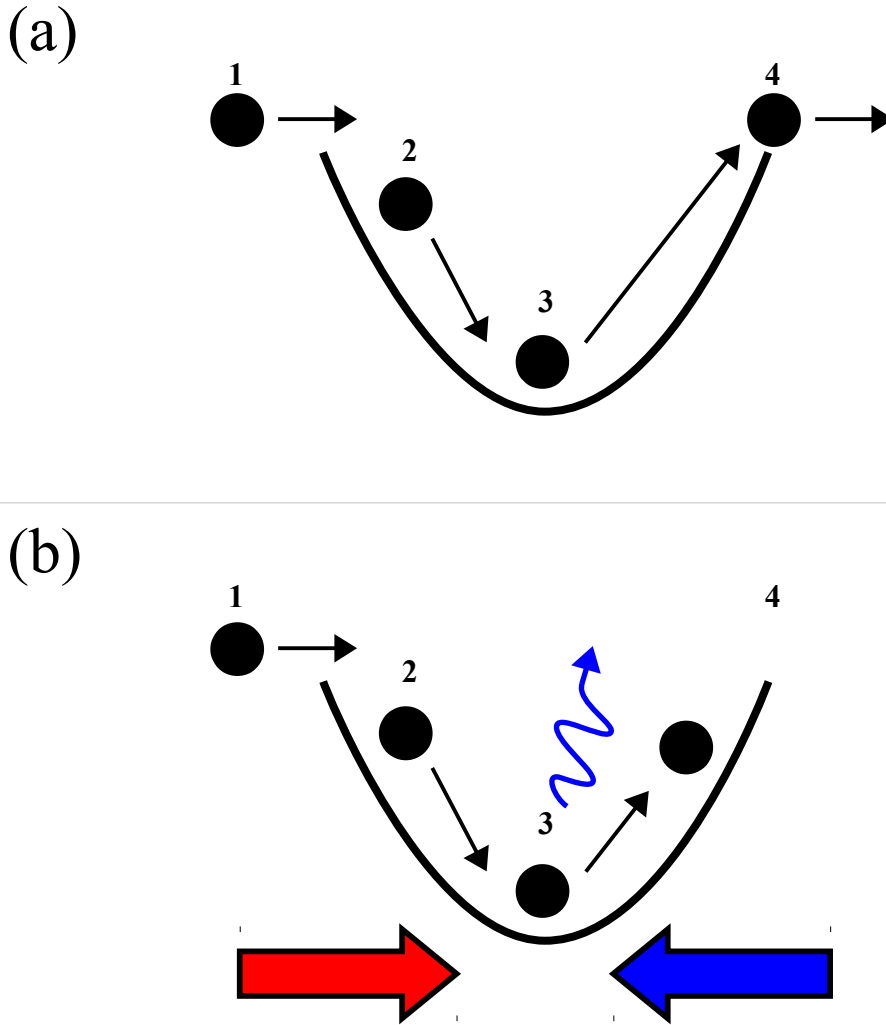
Figure 4.1 Trapping Atoms in a Conservative Potential.
Panel **(a)** shows, 1, an atom with some amount of kinetic energy, entering a conservative trap potential well. As the atom travels through the trap, 2, it gains kinetic energy as the potential energy decreases. At the potential minimum, 3, the atom has a maximum of kinetic energy which is enough for the atom to, 4, climb the other side of the potential well and escape the trap with the same kinetic energy as when it entered. In panel **(b)** an atom once again, 1, enters the trap, and, 2, gains kinetic energy. However, if the trap region is subjected to a cooling force such as in an optical molasses (indicated by large red and blue arrows), the atom will, 3, loose some energy through scattering of photons in the cooling light. If enough energy is lost in the cooling, 4, the atom will not be able to escape the potential well and is trapped.

atoms that venture into the FORT trapping region to lose kinetic energy. If a sufficient amount of energy is lost from an atom, it becomes confined to the optical potential and is trapped.

The total number of atoms loaded into the FORT will be dependent on the two competing processes of cooling into the trap and losses due to light-assisted collisions (see section 3.2). The previous work that was mentioned earlier [3] optimized the loading process for loading from either an ^{85}Rb or ^{87}Rb MOT into the FORT without the other isotope being loaded. When loading both isotopes simultaneously, one might expect that the performance of each isotope be nearly the same as when loading alone. This is because the cooling light used for each isotope is relatively far off resonance from transitions of the other isotope, giving little reason to suspect any significant change in behavior. However, the need for multiple light frequencies to be simultaneously present during dual isotope loading increases the number of possible light-assisted loss channels, even with off-resonant light. There are two sources of these additional loss channels: on- and off-resonant heteronuclear losses between isotopes, and off-resonant homonuclear losses. It is not immediately clear how much of an impact the additional losses will have on dual-isotope loading. Heteronuclear loss rates and off-resonant homonuclear loss rates are expected to be smaller than the on-resonant homonuclear loss rate because in general the collisions occur at shorter internuclear separation [5]. However, there are many additional loss channels. The ultimate effect on the performance of the FORT will depend on the comparison of the single-isotope loss rates with the sum of the large number of additional smaller-rate loss channels.

4.2   Overview of Simultaneous Dual-isotope Loading Experiment

By optimizing the simultaneous loading of ^{85}Rb and ^{87}Rb into the FORT, quantitative measurements of the relevant loss rates were made. The observed loading was compared with the loading expected from a model. This allowed us to determine how much an impact the

heteronuclear and off-resonant homonuclear losses had on the loading process under optimized conditions, as well as if there were any other mechanisms affecting load performance other than these additional losses. When comparing the loading performance to a quantitative model, it was found that the additional loss rates alone are not sufficient to explain the observed reduction in the number of both isotopes of rubidium. Instead, a reduction in the loading rate of the atoms into the optical trap was also required to match observations and predictions. Additional experiments showed that such loading rate reduction did indeed occur for an isotope when the other (i.e. non-resonant) isotope was present.

This hindrance to the trap load rate will in turn reduce the maximum number of atoms loaded into the optical trap. For a trap of constant volume, the density of atoms loaded in the trap is directly proportional to the number of atoms loaded into the trap. A high density of atoms loaded into the FORT is a vital initial condition for robust CAZ cooling (as well as other multi-species experiments). The loss in atom number due to the decreased load efficiency proved to be a major limitation to the best cooling performance we were able to achieve using CAZ cooling, emphasizing the importance of these measurements in evaluating CAZ cooling performance.

4.3 Modeling the Loading of the FORT

It is beneficial to begin our discussion of the dual-isotope loading experiment with the model of optical trap loading. We will start with modeling the case of single-isotope loading. As mentioned earlier, the number of atoms loaded into the FORT is a function of two competing processes: the rate of atoms loaded into the FORT and collisions leading to a loss of atoms from the FORT [6]. The rate of atoms loaded into the FORT is determined by the temperature of the atoms in the MOT, the number of atoms that enter the load volume per unit time, and the effectiveness of the cooling light in slowing the atoms in order that they become confined by the conservative optical potential. Losses are primarily induced by light-assisted collisions, but may

also include other losses such as collisions with background gas atoms. Thus, the number of single-isotope atoms loaded into the FORT is described by the equation [6]:

$$\frac{dN}{dt} = R(t) - \Gamma N - \beta' \frac{N^2}{V}$$

(4.1)

where N is the number of atoms in the FORT, V is the effective volume of the trap such that N/V gives the average density of atoms in the trap, $R(t)$ is the load rate of atoms into the trap, Γ characterizes single-body losses due to collisions with background gas atoms, and β' is an effective two-body loss coefficient characterizing the losses due to light-assisted collisions. On the time scales used in our experiment, single-body losses contribute much less than the two-body losses and thus the Γ term may be approximated as zero in our model. There is an observable time dependence of the load rate $R(t)$ which is caused by changes in our MOT density and position during the loading process [3]. The density of the MOT decreases as atoms are slowly lost from the MOT, and motion of the MOT arises from changes in the beam balance of the MOT as light forces change with time. The effective loss coefficient β' depends on not only the intensity and detuning of the various lasers used during loading, but also in principle the F and m_F population distributions of the trapped atoms. Nevertheless we observe that the effective loss coefficient β' has little to no variation during the course of loading, and can therefore be treated as a constant during the loading process.

The description of dual-isotope optical trap loading is very similar to the single-isotope case. However, there are the additional two-body loss mechanisms associated with the additional loss channels discussed above. Therefore, dealing with both isotopes requires two coupled differential equations of similar form as equation (4.1), with the addition of a two-body cross-loss term:

$$\frac{dN_{85}}{dt} = R_{85}(t, N_{87}, N_{87\text{MOT}}) - \Gamma_{85} N_{85} - \beta'_{85} \frac{N_{85}^2}{V} - \beta'_{85-87} \frac{N_{85} N_{87}}{V}$$

$$\frac{dN_{87}}{dt} = R_{87}(t, N_{85}, N_{85\text{MOT}}) - \Gamma_{87} N_{87} - \beta'_{87} \frac{N_{87}^2}{V} - \beta'_{85-87} \frac{N_{87} N_{85}}{V}$$

(4.2)

In equation (4.2), subscripts have been added to explicitly denote each isotope of Rb. The effective two-body cross-loss coefficient β'_{85-87}, assumes that cross-species collisions result in equal losses of both Rb isotopes. This is reasonable given the mass of each isotope is close to the other and the FORT trap depth is the same for both isotopes. Again, the single-body losses do not contribute significantly in our apparatus, so the terms Γ_{85} and Γ_{87} can be ignored. In addition, it should also be noted that all β' terms in equations (4.1-4.2) are effective two-body loss coefficients, and thus represent a sum over individual loss channels.

The time dependence of the loading rate R indicated in equation (4.2) was known from single-isotope loading experiments [3]. However, there was also observed to be a cross-isotope dependence of R as well, and so that dependence is also indicated in equation (4.2). This cross-isotope dependence acted as a hindrance to the loading over time and will be discussed in further detail below. One of the ways this reduction in load rate manifests itself is through a decrease in the maximum number of atoms loaded into the FORT.

4.4   Description of the Dual Loading Experiment

In order to examine performance of dual-isotope loading, the following experimental procedure was followed. Two overlapping magneto-optical traps were prepared, using standard techniques [7] (discussed in Chapter 3), inside a chamber containing a thermal Rb vapor. Each MOT trapped either ^{85}Rb or ^{87}Rb atoms and consisted of its own hyperfine pump laser as well as a cooling/trapping light field. The light field was formed by a laser beam which was split into three separate orthogonal beam paths. Each path was ultimately retroreflected back on itself. Each of the six trapping beams in the MOT had an average peak intensity of 2.5 mW/cm^2 for

^{85}Rb and 4.8 mW/cm^2 for ^{87}Rb. The laser beams of either MOT were allowed into the chamber using separate shutters, giving us the ability to take measurements with either isotope of Rb alone or both isotopes at the same time. We allowed each of the MOTs to accumulate $2{\times}10^8$ atoms prior to starting the loading sequence. The FORT was produced by a CO_2 laser operating at a wavelength of 10.6 μm, which was turned on and off non-adiabatically (less than 1 μs) via an acousto-optical modulator. The FORT itself consisted of a 30 W beam that produced a trap with a depth of 120 μK whose focus was overlapped with the MOT region. The optical molasses stage which facilitates loading into the FORT (see section 3.1) had the ^{85}Rb trapping laser set to 80 MHz to the red of its cycling transition, and ^{87}Rb laser set to 120 MHz to the red of its cycling transition. It is also during this stage that the FORT was turned on and loading occurred. The duration of this stage is referred to as the FORT loading time and was adjusted to examine loading. When we stopped loading, the hyperfine pump lasers were turned off for 1 ms prior to the MOT trapping lasers. This put all the atoms into the $F = 2$ or $F = 1$ hyperfine state for ^{85}Rb and ^{87}Rb respectively. The temperature of the atoms after loading was about 15 μK. The atoms were held in the FORT for 100 ms after loading ceased to allow any residual MOT atoms to fall away. The FORT was then turned off and the atoms were allowed to expand for 5 ms prior to being imaged by a charged-coupled device camera using absorption imaging. The resulting image could then be analyzed to determine the atom number as well as the temperature of the atoms loaded into the FORT.

4.5 Observations of the Dual Loading Experiments

4.5.1 General Observations

When both isotopes of Rb are loaded at the same time, we observe that the sum of the maximum number of atoms for each isotope trapped by the FORT drops by as much as a factor of 2 compared to what might be expected by summing the maximum number loaded of each

isotope alone. This is seen in figure 4.2, which depicts the atom number loaded into the FORT as a function of load time for both alone (open circles) and dual (full circles) loading of (a) ^{85}Rb and (b) ^{87}Rb atoms.

In order to determine the source of the near factor of two reduction in atom load number during dual loading, we first compared the measured dual-isotope FORT loading behavior to the behavior predicted by the model described by equation (4.2), using measured loss rates and under the initial assumption that the load rate was independent of the number of isotopes being loaded. To perform this comparison, a series of experiments designed to measure the load rate and all the coefficients β' under conditions relevant to the FORT loading were conducted. In each of these experiments, the general strategy was to alter our normal loading conditions to make one of the terms dominant over the others so that the dominant term could be measured. For example, to measure load rate as a function of time the number of atoms in the optical trap was kept small by delaying the time at which it was turned on; this ensures that the rate term dominates in equation (4.1) & equation (4.2) allowing us to map out $R(t)$. Once all of the load rates and loss coefficients were determined, the match between the model prediction and the measured data could be used to evaluate the validity of the model under the independent load rate assumption (i.e. assuming $R_{85/87}(t)$ not $R_{85/87}(t, N_{87/85}, N_{87/85MOT})$).

Under the independent load rate assumption, the load rate for either isotope was obtained from examination of single-isotope loading into the FORT. This is significantly easier than extracting the load rate directly from dual-isotope loading data. To solve for the coefficients in equation (4.1), we examined the loading at the peak of the loading curve where dN/dt is equal to zero following a technique developed in earlier work [3]. This begins with rearranging equation (4.1) with dN/dt equal to zero:
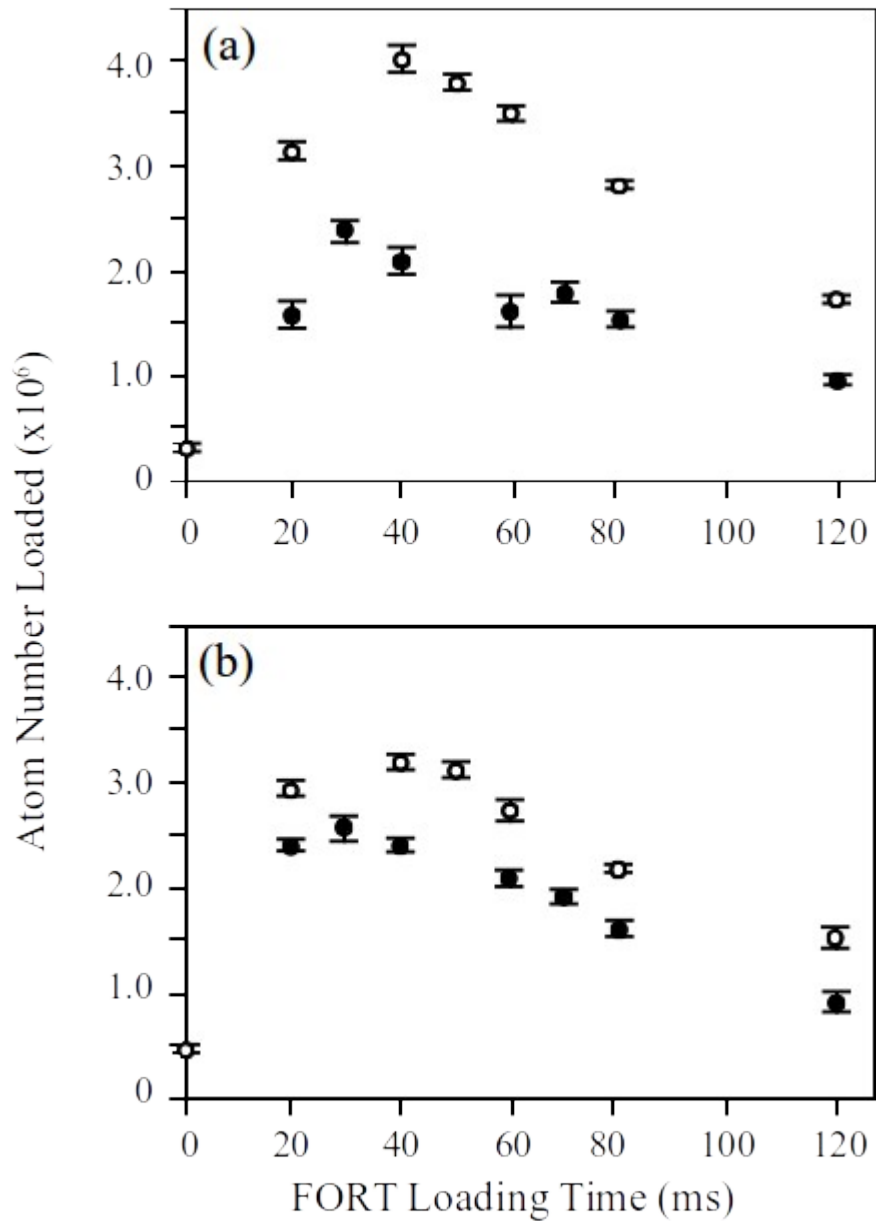
Figure 4.2 Typical FORT Loading Evolution of Atom Number.
The atom number loaded into the FORT as a function of time for both **(a)** ^{85}Rb and **(b)** ^{87}Rb. Open circles denote atom number during loading of the isotope alone, while full circles denote the isotopic atom number during loading while loading with the other isotope. The error bars denote statistical uncertainties. The loading data of an isotope alone was taken without the MOT light of the other isotope present. With the MOT light of the other isotope present, a decrease in maximum atom number of almost 10% in ^{85}Rb and less than 3% in ^{87}Rb has been observed, which is less than the reduction depicted in the figure.

$$\beta' = \frac{R_{peak} V}{N_{peak}^2} \qquad (4.3)$$

where we now need only be concerned with the peak number of atoms loaded into the trap, N_{peak}, and the instantaneous load rate into the FORT when the peak number of atoms are trapped, R_{peak}, and do not need to worry about the specifics of the time dependence of these parameters. While N_{peak} is directly obtainable from the load evolution depicted in figure 4.2, obtaining R_{peak} requires a second measurement at the time corresponding to the peak atom load. This is about 40 ms of loading for both sets of open point data depicted in figure 4.2. By delaying the turn on time of the FORT beam to that of the peak and taking short duration measurements, we obtained the load rate at the peak. This was then used to solve for the constant loss coefficient β' using the full loading behavior at the peak. The loss coefficient for ^{85}Rb and ^{87}Rb was observed to be $6.3 \pm 0.7 \times 10^{-11}$ cm^3/sec and $9.2 \pm 1.2 \times 10^{-11}$ cm^3/sec, respectively.

Once the single-isotope loss coefficient was obtained and we confirmed experimentally that it was constant in time, the time dependence of the load rate (using the load rate at the peak as a constraint) was modeled. A second order polynomial was sufficient to model the load rate over the time interval measured.

In order to accurately use the effective loss coefficients for dual-isotope loading, the populations in each of the ^{85}Rb and ^{87}Rb hyperfine states had to be measured. This is because the loss rates are hyperfine state dependent [2]. Typically, during the imaging of atoms trapped in the FORT the hyperfine pump laser light is turned on to put atoms into the upper ($F = 3$ for ^{85}Rb or $F = 2$ for ^{87}Rb) hyperfine state and into resonance with the probe light. To determine the hyperfine state distribution, we repeated the atom number measurements but rapidly shut off all other light followed by imaging without the hyperfine pump laser on. This gave us the number of atoms in the upper hyperfine state which could then be compared with the full number of

atoms from a standard measurement. We found that during our dual loading conditions approximately ten percent of atoms are in the upper hyperfine state for ^{85}Rb and about twenty percent for ^{87}Rb. The overall homonuclear light-assisted collisional loss rate can then be calculated based on the measured loss rates from individual loss channels and the hyperfine state population distribution.

To determine values for the homonuclear loss rates of individual loss channels, we loaded the FORT with the isotope of interest to its peak number before turning off its trapping laser or hyperfine pump laser. This will destroy that isotope's MOT, allowing those MOT atoms to fall away and cease the loading of that isotope into the FORT. The atoms which were already loaded into the FORT remain, and are rapidly pumped into a single hyperfine state. In the case of ^{85}Rb, turning off the trapping laser will put the atoms into the $F = 3$ hyperfine state and turning off the hyperfine pump laser will put them into the $F = 2$ hyperfine state. Similarly for ^{87}Rb, shutting off the trapping laser puts the atoms into the $F = 2$ hyperfine state, while blocking the hyperfine pump laser puts the atoms into the $F = 1$ hyperfine state. The decay of the atom number remaining in the FORT was then measured and used to extract the hyperfine state-specific loss coefficient. The homonuclear losses during single-isotope loading are not the same as homonuclear losses during dual-isotope loading. This is because the addition of the second isotope's MOT lasers introduces off-resonant losses. We explicitly measured these by examining the decay of one isotope loaded into the FORT alone with the off-resonant light of the other isotope turned on. For example, to obtain the off-resonant losses of ^{85}Rb single species in the $F = 3$ hyperfine state ^{85}Rb atoms were first loaded alone to their peak number. Next the trapping laser was shut off putting all the atoms into the $F = 3$ state where their decay from the trap was measured as a function of time both with and without the laser light for cooling the ^{87}Rb being present. Taking the difference between these two loss rates allows us to find the single species

loss rate of ^{85}Rb in the $F = 3$ state due to only the off-resonant ^{87}Rb cooling light. See Table 4.1 for loss rates driven by off-resonant light.

Table 4.1 Measured hyperfine state-dependent losses of both isotopes of Rb in units of 10^{-11} cm^3/sec. Off-resonant single species losses are the homonuclear losses experienced by the isotope pumped into the indicated hyperfine state while subjected to the off-resonant trapping light of the other isotope. Cross species losses refer to the losses between the indicated isotope and hyperfine state with the other isotope having a hyperfine state distribution typical of the distribution during a dual-isotope load. The numbers in parenthesis indicate the statistical uncertainties for each measurement. In addition, there is an overall systematic uncertainty of about 50 percent in these measurements.

Hyperfine State Dependent Losses	Off-Resonant Single Species	Cross Species
^{85}Rb $F = 3$	6.54(0.37)	16.81(0.63)
^{85}Rb $F = 2$	1.77(0.17)	4.33(0.47)
^{87}Rb $F = 2$	11.71(0.83)	8.07(0.40)
^{87}Rb $F = 1$	0.36(0.21)	0.08(0.39)

The values of the loss rates depicted in Table 4.1 are a result of the laser powers and detunings used in the loading of the optical trap as previously specified, as well as the complex inter-atomic potentials resulting from the hyperfine structure and distributions of the two isotopes. We find that the off-resonant homonuclear losses of the upper hyperfine states are about an order of magnitude greater than without the off-resonant light present. Note that the values for the on-resonant homonuclear losses quoted earlier in the text (page 126) are not directly comparable to the values listed in Table 4.1. This is because the values quoted for the on-resonant losses are a mixture of states while the off-resonant losses are measured with a specific hyperfine distribution. The values in Table 4.1 have an overall systematic uncertainty of about 50% due to systematic uncertainties in both number calibration and trap volume determination. However, since these uncertainties are expected to apply equally to all measurements the relative comparisons have a precision reflected by the statistical uncertainty quoted in the table.

Once the homonuclear losses are known, the decay measurements were then repeated with both isotopes loaded into the FORT to give us the hyperfine state dependent heteronuclear losses. This was done by modeling the decay of both isotopes present using the known homonuclear losses and fitting the heteronuclear losses to the data. This method requires knowledge about the time dependent behavior during the observed decay in the FORT of the isotope which is not pumped into any particular F state for the loading process. We find that the atom number of the other isotope can be well modeled by a simple interpolating function. For example, to measure the ^{85}Rb $F = 3$ heteronuclear loss rate, both ^{85}Rb and ^{87}Rb were loaded into the trap and then the ^{85}Rb trapping light was shut off. The ^{87}Rb atom number vs. time was approximated with an interpolating function and the ^{85}Rb decay was explicitly measured and fit. This allows us to solve either part of equation (4.2), with the rate term set equal to zero, as a decoupled solitary differential equation. All of the hyperfine state dependent losses measured in this way are summarized in Table 4.1. Upper state ($F = 3$ for ^{85}Rb and $F = 2$ for ^{87}Rb) heteronuclear losses are observed to be much larger than the lower state ($F = 2$ for ^{85}Rb and $F = 1$ for ^{87}Rb) heteronuclear losses. The larger upper state losses are not surprising since the relatively strong trapping lasers are nearly in resonance with those states.

Once the hyperfine-state dependent loss rates have been determined, they can be used to construct an effective loss rate β' for use in equation (4.2). To find the effective loss coefficients used in equation (4.2), the state dependent values are weighted by the observed hyperfine state distribution and summed. The weighing was performed using our best estimate of the actual hyperfine state distribution incorporating all of our available measurements. The weighted loss coefficients are the final piece of information required to construct a theoretical dual loading curve for either isotope of rubidium under the independent load rate assumption. These curves appear with the dual loading data in figure 4.3. The shaded area in figure 4.3 is due to the
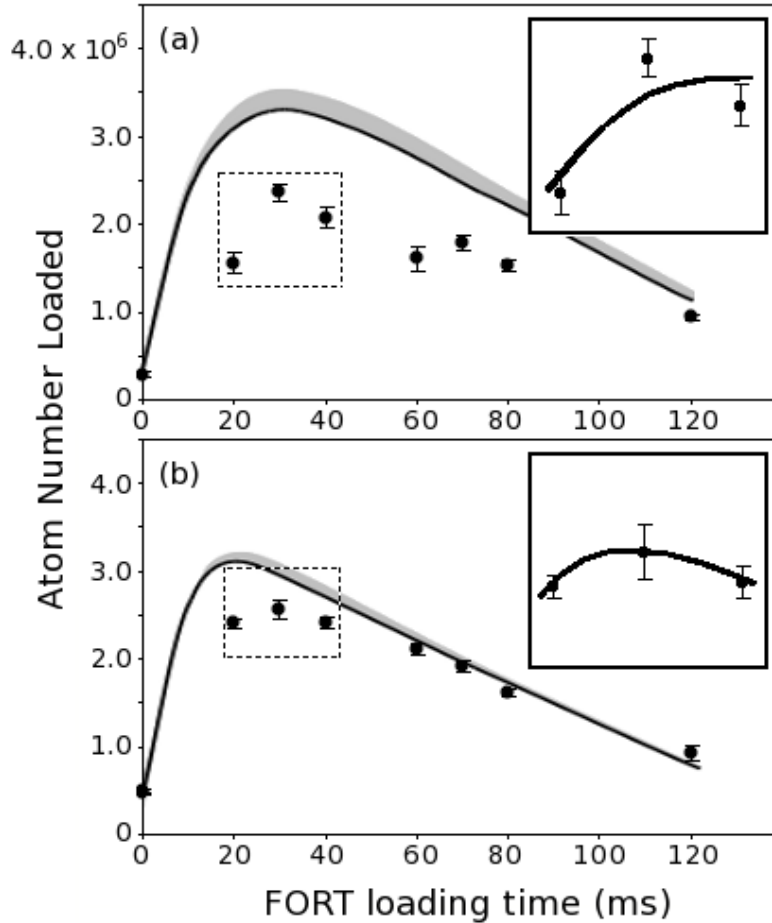
Figure 4.3 Dual-Isotope Independent Load Rate Assumption.
Model of dual-isotope evolution of atom number loaded into the FORT under the independent load rate assumption along with the actual dual loading data. Plotted separately are the individual isotopes of **(a)** ^{85}Rb and **(b)** ^{87}Rb, with the total number of atoms in the trap being the sum of the two. The points are the experimental values with error bars representative of statistical error of the measurement. The curves follow the model behavior of the coupled differential equations given in equation (4.2) with the observed load rate from single isotope loading and losses calculated explicitly from measured rates from individual loss channels. Due to our inability to separately determine individual channel loss rates ($F = 2 + 2$ vs. $F = 2 + 1$) that make up the ^{87}Rb effective homonuclear loss rate β'_{87}, the model prediction is shown as a band of possible values. Our observations indicate that actual behavior is likely to be close to the solid line. The insets show the best fit allowing for the variation of the load rate due to the presence of the other isotope near the peaks of the loading curves.

inability to separate homonuclear collisions between atoms which are both in the upper hyperfine state versus between an atom in the upper hyperfine state and an atom in the lower hyperfine state. This presents a problem when applying the homonuclear loss rate correction to handle the $F = 2$ state population reduction of ^{87}Rb due to the presence of ^{85}Rb. The solid line represents the case where it is assumed that the sole loss mechanism is between atoms in different hyperfine states ($F = 2 + 1$). Our previous work [3] found that the upper hyperfine state fraction was much smaller than the lower hyperfine state fraction which indicates that there are few collisions between two upper hyperfine state atoms compared with collisions between atoms in the upper and lower hyperfine states. This implies that the behavior is most likely best modeled by the region close to the solid line.

4.5.2 Observation of Cooling Efficiency Disruption

A comparison between the theory model and the observed dual isotope loading behavior shows a clear and significant difference between the two. These differences ultimately caused us to reexamine our independent load rate assumption. The assumption seemed reasonable because the resonant frequencies of the two isotopes are hundreds of natural linewidths apart, meaning that the atom response to the resonant light of the other isotope is minimal. The weak atom response to the resonant light of the other isotope was confirmed experimentally by adding the off-resonant light right when the optical trap is turned on so that the off-resonant light is present but the other isotope is not. However, additional measurements showed that the isotopes could have an effect on each others' load rates despite the large difference in resonant frequencies. This section will show why the assumption does not hold. These measurements were first reported in reference 1, and as such are only summarized here. However, additional analysis in the context of dual isotope loading is performed for the first time in this work, extending and

131

improving the understanding of these observations. Also, the rest of this chapter then relates these observations to the dual isotope trap loading performance in a detailed way.

To observe the cross-isotope hindrance to the load rate, we examined the loading of ^{87}Rb into the FORT with ^{85}Rb present. This was done by first preparing both ^{87}Rb and ^{85}Rb MOTs as if doing a dual-isotope experiment. During the FORT loading sequence, one or both of the ^{85}Rb lasers were turned off so that ^{85}Rb was not actively loaded into the FORT. However, ^{85}Rb atoms were still present while ^{87}Rb was loaded into the FORT. The number of ^{87}Rb atoms loaded into the FORT as a function of time was then measured and used to determine the load rate (in atoms/s). The experiment was repeated without having any ^{85}Rb present by either detuning the ^{85}Rb MOT lasers to the point that the MOT could not load, or by turning off the trapping or hyperfine pump beams of the ^{85}Rb MOT. The load rates of ^{87}Rb were then compared with and without ^{85}Rb present during the loading process. The results of these measurements are shown in figure 4.4 [1]. The load rates extracted from the data presented in figure 4.4 were $1.129 \pm 0.051 \times 10^8$ atoms/sec when loading ^{87}Rb alone, and $0.821 \pm 0.044 \times 10^8$ atoms/sec when loading in the presence of ^{85}Rb. This corresponds to a $27 \pm 5\%$ decrease in the overall loading rate of ^{87}Rb due to the presence of ^{85}Rb. It was found that this decrease was not sensitive to the values of the coefficient of the light-assisted collisional loss rates; variations of 50% on the values of the loss coefficients yielded no noticeable effect on the proportionate decrease of the load rate. Note that although ^{85}Rb was not actively loaded into the FORT, a small number (0.4×10^6) of ^{85}Rb ended up in the FORT trapping region during these measurements. This is partially due to atoms being immediately loaded upon turning on the FORT [8], but also due to non-trapped atoms passing through the trapping region during the experiment contributing to the net density of ^{85}Rb.

132
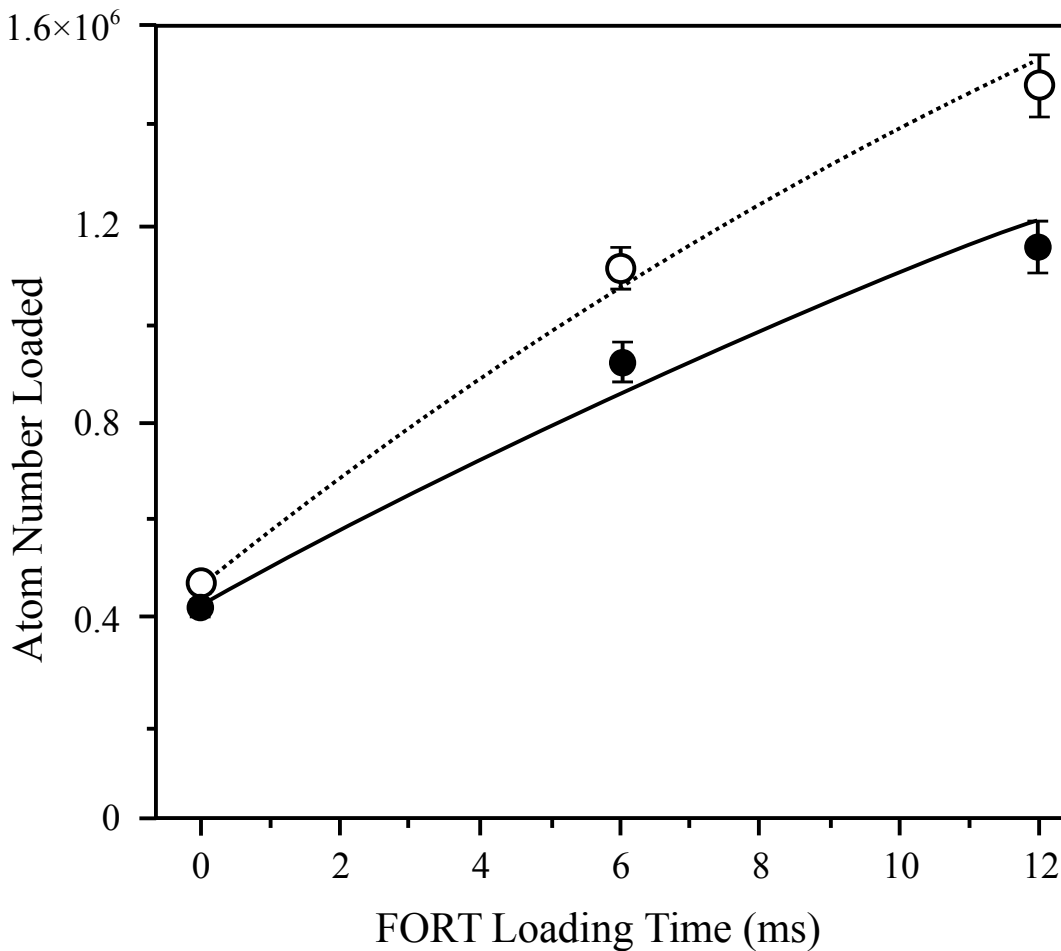
Figure 4.4 Observed Reduction in the ⁸⁷Rb Load Rate.
FORT loading data for ^{87}Rb with and without ^{85}Rb present. The plot shows number of ^{87}Rb atoms in the FORT versus load time. Open circles are ^{87}Rb alone, while full circles are ^{87}Rb in the presence of an ^{85}Rb MOT. Error bars reflect statistical error of the measurements. The dashed and solid lines are fits to the ^{87}Rb alone and ^{87}Rb in the presence of ^{85}Rb data respectively. Only minimal loading of ^{85}Rb into the FORT was allowed so as not to produce significant light assisted collisional losses. The impact of these losses can be seen in the reduction of the slope of the loading curve with higher atom number.

In addition to observing a decrease in the load rate due to the presence of another isotope, it was also found that the presence of both isotopes affected the hyperfine state distributions of the atoms. For these measurements both isotopes were loaded into the FORT. ^{85}Rb was loaded into the FORT for a selected time of 0-20 ms prior to being put into the $F = 2$ state. This allowed the ^{85}Rb atom number loaded into the FORT to be deliberately adjusted. The ^{87}Rb was allowed to continue loading before abruptly shutting off both trapping and hyperfine pump MOT beams so as to preserve its hyperfine distribution. Load time for the ^{87}Rb was adjusted to preserve the same number of atoms for the duration of the experiments. After allowing 100 ms for atoms to fall away once loading is completed, the atoms were imaged using standard absorption imaging techniques. Turning the hyperfine pump beam on or off during imaging allows for the hyperfine state distribution to be determined. The fraction of ^{87}Rb in the $F = 2$ state (Ω) was then compared for the experiment with and without ^{85}Rb present. Figure 4.5 [1] shows the fractional change in Ω ($\Omega_{\text{with 85Rb}}/\Omega_{\text{without 85Rb}}$) as a function of number of ^{85}Rb loaded into the FORT. The data shows that as the number of ^{85}Rb in the FORT increased, there was a measurable difference in the ground state distribution of ^{87}Rb. This strongly implies that the ^{85}Rb changes the optical pumping of ^{87}Rb in the FORT, which will affect the optical cooling rate and thus the load rate into the trap.

The observed reduction of load rate and cooling disruption cannot be explained by either reabsorption or typical cold collisions (elastic, hyperfine changing, spin-exchange, and light-assisted) for these scattering rates are too low because the associated cross-sections are too small. However, laser light will induce dipoles in the atoms which can interact, and it turns out that even off-resonant induced dipoles are not inconsequential for our experimental conditions. Estimates of the induced dipole-dipole forces show that they have a significant influence on the interatomic potential. This can be seen in figure 4.6 which shows some of the potentials of an

134
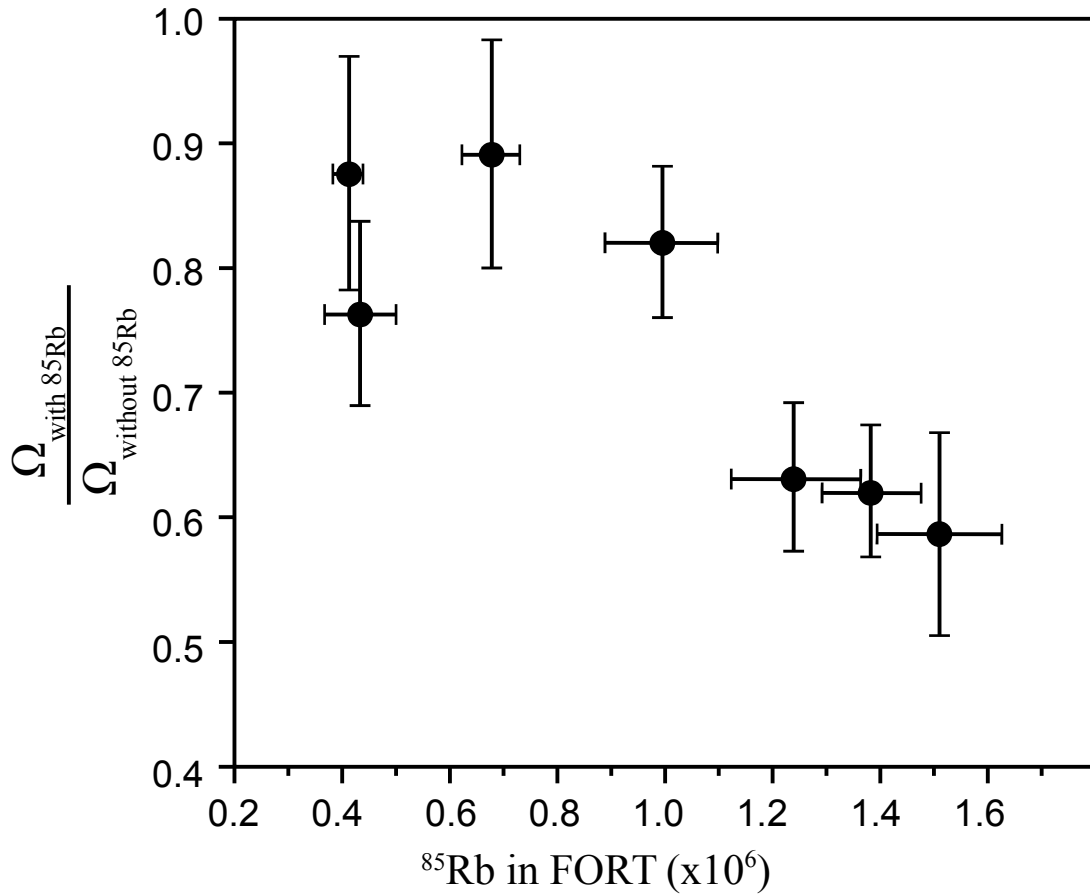
Figure 4.5 Disruption of Hyperfine State Distribution.
Change in the fractional amount of ^{87}Rb in the $F = 2$ ground state Ω as a function of number of ^{85}Rb loaded into the FORT. At small numbers of ^{85}Rb in the trap, there is small change in the ^{87}Rb state distribution. However, as the number of ^{85}Rb increases in the FORT, there is significant change to the ground state distribution of the ^{87}Rb. When ^{85}Rb was absent, the ratio $\Omega_{\text{with85Rb}}/\Omega_{\text{without85Rb}}$ was by definition 1 and the value of $\Omega_{\text{without85Rb}}$ was about 0.25.
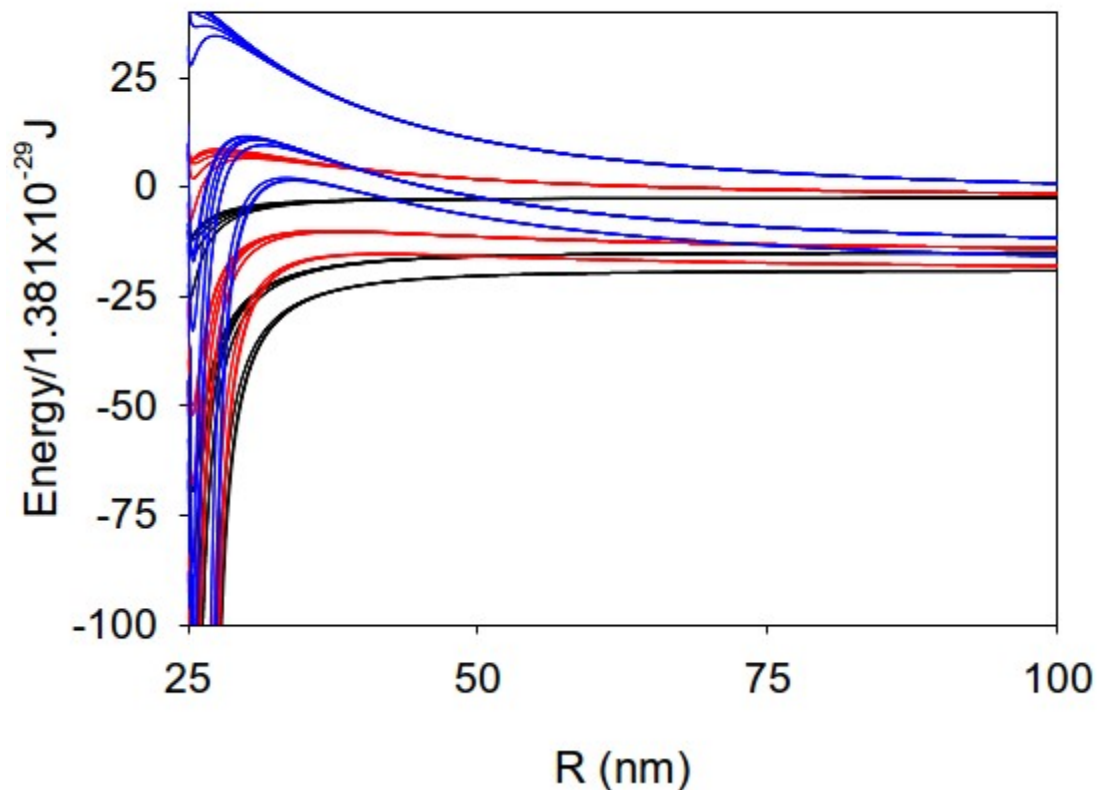
Figure 4.6 ^{87}Rb $F = 2$ Ground Dressed States.
The figure shows the results of a calculation of the ground $F = 2$ dressed states for an ^{87}Rb atom as a function of the distance away from an ^{85}Rb atom in its $F = 2$ state. The different colors refer to the $l = 0$, $l = 1$, and $l = 2$ entrance channels (black, red, and blue). Linear light is assumed and a collision direction along the direction of the light polarization. One can see that the interaction with the laser light decreases the potential at short radii, leading to a likely change in the collision cross section. In particular, the angular momentum barriers of higher angular momentum states are reduced.

The details of the potential change depending on the relative orientation of the atoms. However, the barrier reduction occurs to about the same degree for all orientations.

$F = 2$ ^{87}Rb atom and $F = 2$ ^{85}Rb atom dressed with the laser light as a function of internuclear separation. Note that the potentials are much lower at small internuclear separations, likely causing a change in collision cross-section. The effect on the potential barriers of higher angular momentum states indicate that the dipole-dipole interaction strength is large enough that previously closed collision channels (e.g. p-wave, d-wave) become accessible at temperatures present in the gas. This results in not only an increased elastic collision rate but an increased inelastic, m_F-state changing collision rate as well. While not leading to large increases in the atoms' kinetic energy, such collisions can decrease the load rate R by disrupting the m_F state coherences necessary for effective cooling [9]. A drop in load rate of 35±6% and 37±6% for ^{85}Rb and ^{87}Rb respectively accounts for the discrepancy in figure 4.3, consistent with the previously-measured load rate reduction after taking into consideration density variations in the MOTs between these measurements.

As a check, we investigated the necessary increase in heteronuclear losses which would remove the discrepancy in figure 4.3. We found that an increase of a factor of 2.5 would be sufficient, but this is well outside the uncertainty of our measurements. Thus our observations that the interisotope load rate influences must be included for a proper understanding of the dual isotope loading.

4.6   Conclusions of the Dual Loading Experiment

When loading ^{85}Rb and ^{87}Rb from MOTs into an optical trap it is expected that that off-resonant homonuclear and heteronuclear light assisted collisions reduce the maximum number of atoms loaded into the FORT for each isotope as compared to loading the isotopes alone. Through explicit measurements, these loss channels in a simultaneous load of ^{85}Rb and ^{87}Rb were characterized. It was found that the sum of the losses due to these additional channels is comparable to the sum of the on-resonant homonuclear losses during single-isotope loading.

However, these additional losses are not enough to explain the observed reduction in the number of atoms which can be loaded into the FORT. A reduction in the load rate for both ^{85}Rb and ^{87}Rb due to the presence of the other isotope can explain the discrepancy in a manner which is consistent with additional observations. The results thus indicate the significance of both light-assisted collisional losses and laser cooling efficiency disruption in the performance of loading ^{85}Rb and ^{87}Rb into a shallow FORT.

Although the magnitude of the heteronuclear losses observed was larger than initially hoped for, they are nevertheless consistent with expectations. On the other hand, the disruption to the load rate was unexpected, resulting in far less number of atoms being loaded into the FORT than would otherwise been expected from dual-isotope loading. Unfortunately this turned out to have a serious negative effect on the best CAZ cooling performance that could be achieved. This is because the load rate reduction resulted in initial conditions in the FORT which were well deficient of those needed to maximize the full power of CAZ cooling as predicted theoretically. However, it did not prevent observation and evaluation of CAZ cooling which is described in the remainder of this thesis. Even though the ultimate CAZ cooling performance obtained was disappointing, at least a couple of avenues exist which should allow improved performance. These are both are beyond the scope this thesis, but include using a different FORT loading method and/or cooling the atoms additionally once loaded into the trap. Additional cooling should permit a better starting density, and using a different loading technique may avoid these issues entirely.

It is expected that similar effects would be present in other experiments which load dual atom species into a FORT. This means that a loading disruption is likely to be an inherent additional limitation to the number of atoms which can be set up in a FORT in preparation for CAZ cooling or other similar experiments. Loading a mixture of two different atoms (rather than

two different isotopes) is expected to have a lesser disruption in the loading rate due to the greater difference in resonance frequencies of the two species. This means that the induced dipole in the non-resonant species should be smaller. Although testing whether this is the case is well beyond the scope of this thesis. Also, the specific magnitude of the effect is unclear for atomic combinations other than ^{85}Rb and ^{87}Rb, but it is potentially enough of a disruption to forestall the benefits of CAZ cooling.

References for Chapter 4

[1] Anthony Gorges, Ph. D. Thesis, Colorado State University (2010).

[2] A. Gorges, N. Bingham, M. DeAngelo, M. Hamilton, and J. Roberts, Phys. Rev. A **78**, 033420 (2008).

[3] M. Hamilton, A. Gorges, and J. Roberts, Phys. Rev. A **79**, 013418 (2009).

[4] M. Hamilton, A. Gorges, and J. Roberts, J. Phys. B: At. Mol. Opt. Phys. **45**, 095302 (2012).

[5] J. Weiner, V. Bagnato, S. Zilio, P. Julienne, Rev. Mod. Phys. **71**, 1 (1999).

[6] S. Kuppens, K. Corwin, K. Miller, T. Chupp, and C. Wieman, Phys. Rev. A **62**, 013406 (2000).

[7] E. Rabb, M. Prentiss, A. Cable, S. Chu, and D. Pritchard, Phys. Rev. Lett. **59** , 2631 (1987).

[8] J. Wu, R. Newell, M. Hausmann, D. J. Vieria, and X. Zhao, J. Appl. Phys. **100**, 054903 (2006).

[9] S. Chang, and V. Minogin, Phys. Rep. **365**, 65-143 (2002).

Chapter 5

Performance of Initial CAZ Cooling Experiments

The first experimental realization of two-isotope CAZ cooling is described in this chapter. These initial investigations had several objectives. The first was to observe experimental evidence of the previously unobserved spin-exchange collisions in an $^{85/87}$Rb gas. This was done through the observation of cooling that occurred as a result of these collisions. Spin-exchange collisions were indeed observed to contribute to the cooling of the gas, demonstrating experimentally the fundamental mechanism of CAZ cooling. Once the cooling was observed, the rate of cooling was measured quantitatively and compared with expectations. These comparisons were done with the intent of examining the observed cooling rate along with evaluating any heating mechanisms. Although each of these goals were met, substantial heating rates were observed much to our disappointment. This chapter presents the data obtained in these initial CAZ cooling investigations followed by a discussion of the limitations observed and possible solutions to address them. Future experiments planned for the apparatus will also be commented on at the end of the chapter.

5.1 CAZ Cooling Experimental Sequence

A basic description of the typical experimental sequence of events executed for the implementation and observation of two isotope CAZ cooling follows. This sequence began with the preparation and loading of the $^{85/87}$Rb atom mixture into the FORT as described in section 3.1 and evaluated in chapter 4. Atom counts for each of the isotopes were kept near 0.6 million for these measurements resulting in an average density of 5×10^{11} cm^{-3}. Note that the loading limitations described in chapter 4 make loading atoms at a higher density than this difficult. Thus, increasing the atom number would require increasing the volume of the optical trap. Once the FORT was loaded, the uniform magnetic field was turned on. Most of the CAZ cooling

experiments were conducted in a field, calibrated via microwave spectroscopy as described in section 3.3.2, of 0.84 G. This corresponds to an energy barrier of 9.4 μK times k_B, which is roughly optimum for the atoms which were typically at a temperature at or just below 10 μK upon being loaded into the FORT. Next, the ^{85}Rb was spin-polarized. Of the several optical pumping schemes discussed in section 2.3.2 to facilitate the spin-polarization, the experiments presented here used direct optical pumping. The optical pump beam was set at +37 MHz blue detuned from the $F = 2 \rightarrow F' = 2$ transition near the D1 line with an intensity of 12 μW/cm². For this intensity, and as a matter of experimental convenience, the primary optical pump was normally pulsed on for 30 ms every 115 ms. The optical repump beam, on the other hand, was left on continuously. The detuning of the repump was set to +24 MHz to the blue of the $F = 3 \rightarrow F' = 3$ transition near the D2 line. The intensity of the repump, totaling around 2 μW/cm², was set to be 75% σ⁻ polarization, 23% π polarization and 2% σ⁺ polarization. The duration of the cooling experiments was varied up to as long as 1.5 s, in order to observe the evolution of the cooling over time. The following sections will describe and present data from the first CAZ cooling experiments.

5.2   First Observation of Spin-Exchange Collisions

Spin-exchange collisions are an essential piece of the CAZ cooling process. Although the expectation was that spin-exchange collisions between the two isotopes of Rb would occur at a rate sufficient to make CAZ cooling successful (recall figure 2.3), the spin-exchange collision rate between the isotopes had not been experimentally observed. Thus the first set of experiments conducted was to confirm that spin-exchange collisions would indeed occur at the predicted rate. Because we can measure the widths of the Rb gases with very high reproducibility after release from the optical trap, the best way to search for the influence of the

spin-exchange collisions was to observe the temperature of the atoms after a single pulse sequence of CAZ cooling light as a function of magnetic field.

The kinetic-energy-reducing spin-exchange collision rate between atoms in an external magnetic field is sensitive to the strength of that magnetic field, while other effects that can alter the temperature of atoms, such as evaporation or light-interaction effects, are not significantly affected by the magnetic field at these field strengths. This makes the magnetic field an ideal experimental parameter to be adjusted to observe spin-exchange collisions. At this point, we were not interested in explicitly measuring the spin-exchange collision rate, so there was no need to eliminate other temperature altering effects so long as they could be kept constant throughout the experiment. For this preliminary measurement, there was also no need to have the spin polarization of ^{85}Rb set optimally. The ^{85}Rb did need to be sufficiently spin polarized to ensure that kinetic-energy-reducing collisions, as opposed to kinetic-energy-increasing collisions, would dominate to produce an observable signal. Also, because we were most interested in confirming spin-exchange collisions and did not wish to employ the RF scrambler, the duration of the optical pumping was kept to a minimum: a single 115 ms cycle of direct optical pumping.

The experiment was conducted as follows. Roughly 0.6×10^6 atoms of ^{85}Rb, and 0.8×10^6 atoms of ^{87}Rb were loaded into the FORT. The magnetic field was set between 0 and 2 G, resulting in a kinetic-energy-reducing spin-exchange collision energy-barrier of up to 22.4 μK. A single 115 ms cycle pulse of direct optical pumping light (as described in section 5.1) was applied, after which one of the isotopes was imaged. Once several images were collected for each isotope, the average total energy of the mixture was calculated using techniques discussed on page 84 in section 3.1.

The spin-exchange data collected is displayed in figure 5.1 which shows, as a function of magnetic field strength (given in units the kinetic energy spin-exchange collision barrier), the
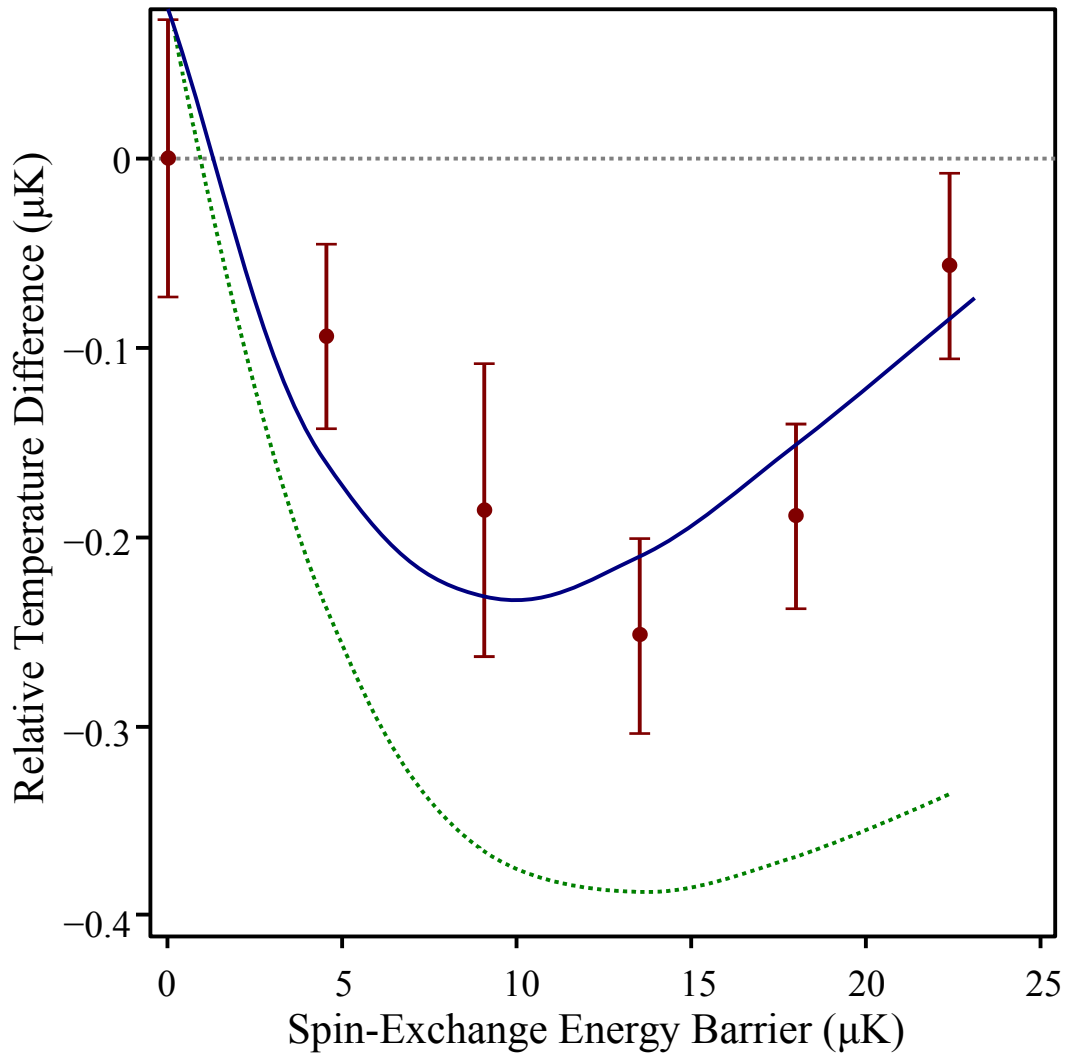
Figure 5.1 Observation of Spin-Exchange Collisions.
The relative temperature difference of the $^{85/87}$Rb gas mixture after spin polarization of ^{85}Rb as a function of magnetic field strength as compared to that at with no magnetic field. The initial optical pumping was not optimized, but that was not necessary for these measurements. Magnetic field strength is expressed in units of the spin-exchange collision energy barrier, $1/6\ \mu_B B$ in μK-equivalent units. Collected data is depicted by the points with error bars representative of the statistical uncertainty of the individual measurement. The lines are model fits accounting for backstreaming (solid blue) and ignoring backstreaming (dashed green) under the assumptions discussed in the text.

deviation in the atom cloud temperature as compared to the that with no magnetic field. The temperature of gas in the absence of the magnetic field is ~11 μK. Variation as a function of magnetic field is clearly apparent in figure 5.1. The probability that the data are consistent with zero cooling and that the observed variation with magnetic field is just due to random fluctuations is less than 2%. This suggests that the kinetic-energy-reducing spin-exchange collisions are indeed occurring in the sample. Despite the uncertainties, the data also displays a maximum reduction in the kinetic energy near the expected optimal magnetic strength of just under 1 G.

A modification to the CAZ cooling rate model developed in section 2.4.1 is needed in order to explain a too-rapid reduction in cooling at high magnetic field. The primary modification that is needed for the model is an accounting of the presence of what we call backstreaming. Backstreaming occurs when ^{85}Rb atoms in the spin polarized $F = 2$, $m_F = -2$ state are excited by the optical pumping light due to either off-resonant transitions ($F = 2$, $m_F = -2 \rightarrow F' = 3$, $m_F = -3$) or imperfect beam polarization ($F = 2$, $m_F = -2 \rightarrow F' = 2$, $m_F = -2$ or $F' = 2$, $m_F = -1$). Some of these atoms will decay into states other than the $F = 2$, $m_F = -2$ state, requiring additional photon scatter events to be repumped back into the $m_F = -2$ state. The presence of off-resonant scattering means that the $m_F = -2$ state is not dark to the optical pumping light. Thus atoms will continually scatter photons, which in turn leads to more heating. Additionally, with backstreaming present the gas will never be fully spin polarized. This reduces the energy removed by spin-exchange collisions per unit time as compared to a fully spin polarized polarized gas, a problem that worsens as the magnetic field is increased.

The backstreaming amount due to unavoidable off-resonant transitions can be estimated by comparing the on- and off-resonant scattering rates of purely σ⁻ polarized optical pump light. The scattering rate is given by equation (3.82) & (3.83):

145

$$R = \frac{\gamma}{2} \frac{\left(\dfrac{I_0}{I_{sat}}\right)}{1 + \left(\dfrac{I_0}{I_{sat}}\right) + 4\left(\dfrac{\delta}{\gamma}\right)^2} \tag{3.82},$$

$$\left(\frac{I_0}{I_{sat}}\right) \rightarrow C \left(\frac{I_0}{I_{sat}}\right) \Sigma \tag{3.83}.$$

To refresh on the terms, I_0 is the intensity of the light field, I_{sat} is the saturation intensity, γ is the inverse of the excited state lifetime ($2\pi \times 5.98$ MHz), and δ is 2π times the laser detuning, Δ. The term Σ is the proportion of the light field which is correctly polarized along the transition and the term C can be reduced down to the product of two factors: one proportional to the reduced matrix element squared between the relevant ground and excited F states, and the other to account for the addition of the photon momentum (i.e. a Clebsch-Gordan coefficient). The desirable on-resonant transitions occur on the ^{85}Rb $F = 2$, $m_F = -1 \rightarrow F' = 2$, $m_F = -2$ transition, while off-resonant transitions occur on the $F = 2$, $m_F = -2 \rightarrow F' = 3$, $m_F = -3$ transition. This means that the detuning term δ in equation (3.82) differs by $2\pi \times 362$ MHz between the on- and off-resonant transitions. Given that $I_0 \ll I_{sat}$ (10 µW/cm² $\ll$ 1.6 mW/cm²), the comparison of on- and off-resonant scattering rates comes down to the square of the detuning terms. The optical pump runs at +37 MHz blue detuned from the $F = 2$, $m_F = -1 \rightarrow F' = 2$, $m_F = -2$ transition, which is a detuning of -325 MHz for the off-resonant transition. This would result in a factor of 77 reduction in the scattering rate along the off-resonant transition. However, Clebsch-Gordan factors must be taken into account. Following the same procedure on page 103 in section 3.4 to calculate C in equation (3.83), Clebsch-Gordan factors reduces the scattering rate difference to a factor of about 10. Therefore backstreaming can be expected to occur on the order of around ten percent. Imperfect polarization and suppression of decays into the target state due to high optical density will cause the backstreaming to be somewhat more. However, the estimate obtained

above tends to overestimate the backstreaming fraction as not every atom pumped out of the $F = 2$, $m_F = -2$ state will wind up in the $F = 2$, $m_F = -1$ state due to the polarizing action of the repump beam. Note that measurements taken after the work in this thesis on an optimized CAZ setup found a backstreaming amount, defined as the steady-state population of ^{85}Rb in the $m_F = -1$ state in the absence of any collisions, of about 7 percent. This value is reasonable given the estimate here.

In the limit of perfect polarization of the optical pumping light, backstreaming is maximally reduced by setting the laser frequency to be exactly on resonance with the ^{85}Rb $F = 2 \rightarrow F' = 2$ transition. However, this produces the unfortunate side effects of more light-assisted collisions and optical thickness issues. Light-assisted collisions reduce the number of atoms in the trap and their rate increases as the light approaches the atomic resonance. The atoms also become more optically thick as the light is brought closer to resonance. A high optical thickness inhibits the optical pumping because it makes it more difficult for scattered photons to escape the gas. After all, scattered photons carry away angular momentum from the gas, allowing it to be spin polarized. Moreover, the resulting additional scatters that occur due to the high optical thickness result in an increase in the amount of heating imparted by the optical pump. The detuning of +37 MHz to the blue of the ^{85}Rb $F = 2 \rightarrow F' = 2$ transition used for the CAZ cooling experiments was chosen as a result of an optical pump detuning survey. It was found that optical pumping at the +37 MHz detuning was more effective and had lower loss than observed at detunings closer to resonance. Also it was found that the blue detuning induced less loss than red detuning, explaining why blue detuning was selected. This can be understood given previously observed behavior of light-assisted collisions in an optical trap [1].

Accounting for backstreaming in the simple model of section 2.4.1 can be done by modifying equation (2.12)

$$\frac{dN_{np}}{dt} = k_f \frac{N_{sp} N_c}{V} - k_s \frac{N_{np} N_c}{V} - \frac{1}{\tau_{OP}} N_{np} \tag{2.12}$$

by adding an additional backstreaming term to become:

$$\frac{dN_{np}}{dt} = k_f \frac{N_{sp} N_c}{V} - k_s \frac{N_{np} N_c}{V} - \frac{1}{\tau_{OP}} N_{np} + \frac{1}{\tau_{OP}} \zeta N_{sp} \tag{5.1}$$

where ζ characterizes the backstreaming. In addition, because the backstreaming induces heating and gas depolarization, the amount of energy removed by the optical pump is reduced from that in equation (2.15)

$$R_{rm} = \frac{1}{\tau_{OP}} N_{np} (\Delta - \kappa) \tag{2.15}$$

to:

$$R_{rm} = \frac{1}{\tau_{OP}} N_{np} (\Delta - \alpha) - \frac{1}{\tau_{OP}} \zeta (N_2 - N_{np})(\Delta + \alpha') \tag{5.2}.$$

Here we have also made the substitution: $\kappa = \alpha$ to simplify the analysis since density-dependent effects should be relatively small for these early conditions. In addition, the backstreaming term has a contribution from α' which characterizes the density independent heating due to the backstreaming transitions. The number of photons involved in a backstreaming scatter should be about the same as those induced by regular optical pumping, as such we will make the simplifying assumption of $\alpha' = \alpha$. Following the same procedure as in section 2.4.1, and in the limit of fast optical pumping, the rate of change in the atom temperature will have two terms. The first is a pure heating term which arises because there are no dark states when backstreaming is present. The lack of a dark state causes heating to occur even in the absence of any collisions:

$$\frac{dT_{pureheat}}{dt} = \frac{(\alpha + \alpha') N_2 R \zeta}{3 k_B (N_1 + N_2)(1 + \zeta)} \tag{5.3}$$

148

Since this term depends on neither the atom density nor the magnetic field strength, it will be constant for the data presented in figure 5.1 and may be ignored for this comparative analysis. The second term is the CAZ cooling term:

$$\frac{dT_{CAZ}}{dt} = \frac{k_s N_1 N_2 \left(\Delta + \alpha'\right)\zeta - \left(\Delta - \alpha\right)\exp\left(-\Delta / k_B T\right)}{3 k_B \left(N_1 + N_2\right) V \left(1 + \zeta\right)} \tag{5.4}.$$

Note that this matches equation (2.17) when the backstreaming term is set to zero, $\zeta = 0$, and $\kappa = \alpha$ (also, equation (5.3) vanishes in the absence of backstreaming). On average, it is expected to take 3.5 photon scatters to perform the optical pumping. Combined with the direction that the optical repump beam intersects with the optical trap, this implies that a reasonable value to be expected for the density independent loss terms is $\alpha' = \alpha = 2$ µK times k_B. Assuming a spin-exchange collision rate of 2.7×10^{-11} cm^3/s, accounting for evaporation, and using the same density, ^{85}Rb/^{87}Rb number ratio, and temperature conditions as the data collected produced the solid blue line in figure 5.1. For this model fit, the zero point (since the B = 0 temperature cannot be perfectly known) and ζ were fit parameters. This fit yields backstreaming of 9.5 percent, which is reasonable given our estimates. Note that in the absence of backstreaming effects, cooling is predicted to follow the green dashed line in figure 5.1. The difference between the two curves therefore shows how backstreaming can influence the atom cloud temperature. Meanwhile the acceptable agreement between the data and model with a reasonable amount of backstreaming is strong evidence that spin-exchange collisions are occurring as expected. It is reasonable to assume that spin-exchange cooling is indeed responsible for the observed behavior as we predict it should be, rather than some other mechanism

Two additional quick tests reinforced the observations of spin-exchange collisions. Both observations used the strategy of observing "CAZ heating," where spin-exchange collisions result in an increase in kinetic energy. CAZ heating may be observed with both unpolarized gas,

and a gas that is polarized in the "wrong" direction (i.e. ^{85}Rb polarized in the $m_F = +2$ state). Preparing the atoms for such an experiment is straightforward. Both isotopes of Rb are loaded into the FORT, and the external magnetic field is applied. The optical pump beam may or may not be turned on at this point depending on if it is desired to spin polarize the ^{85}Rb. The atom temperature is then measured as a function of time. Spin-exchange collisions will result in the sample of atoms gaining kinetic energy owing to the fact that magnetic sub-levels with lower Zeeman energy experience an increase in their population since they are energetically favorable. With none of the atoms in the sample spin polarized, spin-exchange collisions that result in both an increase and decrease in kinetic energy can occur. However, kinetic-energy-reducing collisions require the colliding atom pair to have at least $\frac{1}{6} \mu_B B$ of kinetic energy to facilitate the change in Zeeman energy. No such requirement exists for kinetic-energy-increasing collisions, which allows them to occur at a greater rate. The imbalance in spin-exchange collision rates is dependent on the magnetic field strength, and the effect is most pronounced when the energy barrier for kinetic-energy-reducing collisions is well above the average kinetic energy of the atoms in the cloud. Comparisons between holding unpolarized atoms in a low and high strength magnetic field indeed produced this characteristic behavior

Heating was also found to be more pronounced after applying the optical pump beam set with the opposite polarization. The opposite polarization of the optical pump beam spin-polarizes the sample and causes even more kinetic-energy-increasing collisions to occur, amplifying the effect of CAZ heating. The comparative heating rates under these conditions thus also indicate that spin-exchange collisions occur as expected in our system.

5.3 Realization of Two-Isotope CAZ Cooling

The observation of spin-exchange collisions showed that the basic principles of two isotope CAZ cooling could work. The next set of experiments conducted set out to demonstrate

CAZ cooling on a more practical scale, with the intent to analyze its performance. For these experiments, each isotope was observed individually as a function of CAZ cooling time. Measurements were taken before initiating CAZ cooling, after six 115 ms cycles of CAZ cooling light, and after twelve cooling cycles. For these experiments, the RF scrambler was used to ensure that the ^{87}Rb m_F state distribution was largely uniform. The scrambler consisted of the repetition of an 80 ms sweep from 540 MHz to 640 MHz run continuously during cooling. Several measurements were taken under different sets of conditions to evaluate CAZ cooling: the magnetic field strength set near the optimal value, the magnetic field strength set to a value well above optimal, without the magnetic field, and without the magnetic field or optical pumping light present.

A representative data set showing two isotope CAZ cooling can be seen in figure 5.2. Here, the average temperature of an $^{85/87}$Rb gas mixture is shown under four separate conditions. The data shown in black depict the case where the atoms are left unaltered in the FORT and acts as a baseline. These atoms have been loaded into the FORT and allowed to sit without any applied magnetic field or optical pumping light. The observed decrease in temperature is attributed to evaporative cooling. This was confirmed by significantly reducing the FORT trap depth during loading, which captures far less atoms at a lower temperature, then increasing the trap depth and observing that the cloud temperature remains unchanged over time.

The data shown in green in figure 5.2, show the case where the ^{85}Rb is optically pumped but in the absence of an applied magnetic field. Due to a lack of magnetic field, the energies of the m_F states remain degenerate and no CAZ cooling can occur. Thus this data is reflective of heating of the atoms as a result of the optical pumping light.

The blue data points represent the case of spin polarized ^{85}Rb in a high magnetic field. The field was set to 2.52 G which corresponds to a spin-exchange collision energy barrier ($\mu_B B/6$
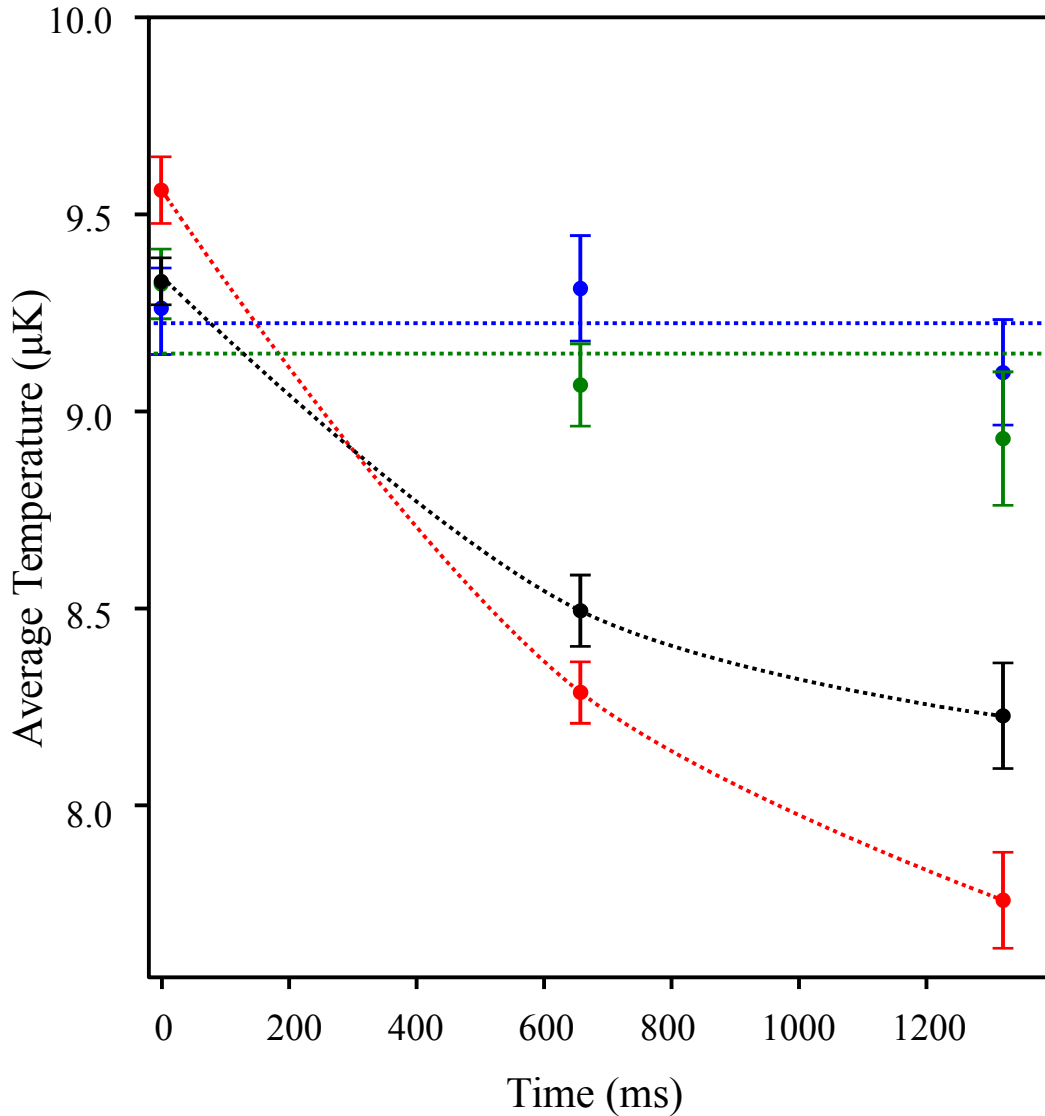
Figure 5.2 Observations of CAZ Cooling in $^{85/87}$Rb Mixture.
Temperature evolution of the Rb mixture showing the first realization of CAZ cooling. Shown are four conditions: (black) baseline data where no magnetic field and no optical pump light was used, (green) no magnetic field with pump light present, (blue) a magnetic field of 2.52 G causing a spin-exchange collision energy barrier of 28 μK, and (red) a 0.84 G magnetic field resulting in a near-optimal barrier of 9.4 μK. Comparison of the baseline and 0.84 G conditions indicates the successfulness of CAZ cooling. The high and zero field measurements give insight to the heating induced by the optical pump light. Points are data with error bars representative of statistical uncertainty of the measurement. Dashed lines are guides for the eye.

for the $^{85/87}$Rb system) of 28 μK times k_B. This is well above the average kinetic energy of atoms in the sample, preventing almost all of the kinetic energy reducing spin-exchange collisions from occurring. These data points therefore also represent optical pump induced heating. As an aside, high magnetic fields can also induce magnetic dipole collisions which cause heating; however, for Rb the expected collision rates [2] at the magnetic field strengths used in CAZ cooling is small, causing a heating rate of about 0.2 μK/s. Indeed, we have no evidence that these effects are significant in the CAZ cooling data, however we did observe them when the magnetic field was accidentally set too high- at 20 G.

The final data set shown in figure 5.2, depicted as red, represents successful CAZ cooling. In this case, ^{85}Rb is optically pumped with an applied magnetic field of 0.84 G, near the optimum value for the atoms at their starting temperature of just over 9 μK. There is a clear improvement in atom cooling when two isotope CAZ cooling is taking place which was originally quite encouraging. However, the decrease in temperature as a result of implementing two isotope CAZ cooling was much less than what was predicted. The deviation between predictions and observations were much larger than the systematic uncertainties of the system, as discussed on page 85 in section 3.1. The analysis to determine why the performance was weaker than expected is given in the next section.

5.4   Evaluation of CAZ Cooling Performance

The difference between the initial and final temperatures of the observed CAZ cooling data in figure 5.2 is slightly over 1.8 μK. Naively predicting the temperature change from the CAZ cooling rate model under the conditions that the data was taken with reasonable backstreaming yields an expected drop of 1.2 μK. However, it is important to note that that prediction would only be valid in a situation where there was no observed change in temperature for the baseline data. This is because the CAZ cooling theory thus far discussed only models the

heating and cooling rates directly associated with CAZ cooling. However, several important phenomena are omitted from this theory, an example of which is evaporative cooling.

Atom loss from the trap as a result of evaporation reduces not only the atom number but the average temperature of the atom cloud as well. This will have a significant impact on the performance of the cooling. For one, the amount of energy in the cloud is altered directly through evaporative loss. In addition however, changes in the atom density affect the CAZ cooling rate itself. Ignoring the presence of evaporative cooling thus gives a highly distorted view of the CAZ cooling that was actually achieved. The baseline data in figure 5.2 lost 49±5% of the atoms in the two-isotope mixture initially loaded into the FORT over the 1320 ms of experimental run time. Most of this loss was due to background gas collisions (which will neither significantly heat nor significantly cool the cloud). However, approximately 3% of the total number of atoms lost was due to evaporative cooling.

Although the amount of loss due to evaporation is small, atoms lost through evaporation carry away significantly greater-than-average kinetic energy. This has a substantial effect on the temperature as evident in the observed decrease in the baseline data of figure 5.2. The decrease in temperature combined with the observed loss in atom number implies that significant evaporation was present while CAZ cooling was occurring. The presence of evaporative cooling complicates the evaluation of CAZ cooling since the baseline data cannot be directly compared with the CAZ cooling data. This is because the evaporative cooling rate is dependent on the temperature of the atoms in the gas. When CAZ cooling lowers the gas temperature, it also reduces the evaporation rate. Thus there is an interplay between evaporative cooling, CAZ cooling, and the temperature of the atoms which masks the effects of CAZ cooling. Thus a

comparison between the final temperature of the baseline and CAZ cooling data runs will tend to underestimate the cooling effect due to spin-exchange collisions.

Ideally CAZ cooling in the presence of strong evaporative cooling should be characterized by only a mild effect on the final atom temperature combined with an improved final atom number due to the reduction of evaporative loss. At first glance, it would therefore seem useful to compare the atom losses between the CAZ cooling and baseline data since any improvement in atom number during CAZ cooling could be used as a measure of successful CAZ cooling. However, atom losses observed during every measurement of CAZ cooling suffered a greater loss of atoms than the baseline. The high magnetic field and zero magnetic field data provides insight as to why this is the case. Both these trials also had atom losses on top of those observed in the baseline data. These additional losses, just as those during CAZ cooling, are on average an extra 10% of the initial total atom number. This implies that the optical pump is inducing additional loss since the presence of optical pumping light is the common element between all the data sets that suffered greater atom loss rates. The optical pump light can cause loss via light-assisted collisions (see figure 3.2 and relevant discussion within section 3.2). Unfortunately between the relatively high optical-pump-induced loss of atoms and the low atom loss due to evaporation, any change in atom loss due to evaporation is not resolvable in our system.

Due to the many cooling (CAZ, evaporative), heating (optical pump, backstreaming), and loss mechanisms (background, evaporative, light-assisted) present during the experimental runs, a more sophisticated model than the CAZ cooling rate model was developed to characterize these various rates. This model not only utilizes the CAZ cooling rate model developed earlier in this thesis, but also accounts for loss due to background gas collisions. In addition, the model estimates atom and energy loss due to evaporation and the optical pump. This model can thus be

used with the data in figure 5.2 to infer how much each of these processes are affecting the Rb mixture.

The goal of the "evaporation model" was to be as simple as possible while still capturing all the physics relevant to these early CAZ experiments. Also by examining such a model, the imperfections in the initial application of the cooling technique can be identified so that future implementations can seek to minimize these problems. Several simplifying assumptions are made:

- The number of atoms are tracked with time as well as the total energy (temperature) of the gas. However, only the total number of atoms ($N = N_1 + N_2$) are tracked instead of each isotope of Rb separately. This simplification is justified since the two Rb isotopes are similar enough and in good enough thermal contact that both isotopes are affected roughly the same.

- Because only the total number of atoms are tracked, evaporation is characterized by an average effective cross-section. A cross-section with scattering length of $250a_0$ (where $a_0 = 5.29 \times 10^{-9}$ cm is the Bohr radius) is used, which is the average of the intra- and inter-isotope scattering lengths of the two Rb isotopes.

- Just like in the CAZ cooling rate model, it is assumed that the ^{87}Rb population distribution never deviates significantly from equal m_F state populations. Because the RF scrambler is used during CAZ cooling, this assumption should hold.

- The model uses the CAZ cooling rate accounting for backstreaming (section 5.2). To be consistent with the data a value of $\zeta = 0.06$ is used.

- Using the backstreaming CAZ cooling rate assumes that density-dependent optical-pump-induced heating is zero. That is, $\beta = 0$ and $\kappa = \alpha$. This approximation is still good for these conditions as the sample is not very dense. Indeed, the CAZ cooling model

predicts a difference of only a couple of tenths of a Kelvin at the end of the experiment run time when β is included.

- The density-independent heating term α' is set to α which is set for an average of 3.5 photon scatters per pumping event, a minimum estimate.

- Simple quadratic functions were fit to the trap volumes $V(t)$ observed in the data in order to capture the time-dependence of the density.

- The loss due to background gas collisions occur at the rate defined by our measured trap lifetime of $\tau = 1.71$ s.

- An effective trap depth of $d = 85.8$ μK was set by matching the model results to observed baseline conditions using the evaporation cross-section defined above. Any difference between this assumed depth and the true trap depth reflects imperfections in the assumption of just one species rather than treating both ^{85}Rb and ^{87}Rb separately, uncertainty in the average energy with which atoms escape from the optical trap, and residual imbalance between the radial and axial temperatures leftover from the optical trap loading.

- An optical pumping rate of $R = 20$ s^{-1} is used. This rate is consistent with estimates based off the direct optical pump beam duty cycle, its detuning, and its measured intensity.

- The initial conditions are fixed to the t = 0 data point.

- A loss rate that scales with the CAZ cooling rate could also be used to account for loss due to the optical pump light. However, the influence of this loss term on the final temperature is minor (less than 0.1 μK) -- it more accounts for the observed number loss. For simplicity of the following discussion, this term will be omitted.

Under all of the assumptions above, the CAZ cooling model accounting for evaporation is described by two coupled differential equations. The first models the total number of atoms in the FORT:

$$\frac{dN}{dt} = -\frac{N}{\tau} - \frac{N^2}{V(t)} \sigma_e \sqrt{\frac{16}{\pi} \frac{k_B T}{m}} \frac{d}{k_B T} e^{\left(\frac{-d}{k_B T}\right)}$$

(5.5)

where all the terms represent the same values as before as well as those defined in the list of assumptions above. The evaporative loss cross-section is given by the term $\sigma_e = 4\pi (250a_0)^2$. The time dependence of the volume was determined from the data. Images of the atoms are used to extract the axial extent and radial temperature. The radial temperature combined with measurements of the radial trap frequency determines the radial extent of the atoms. Assuming a Gaussian density distribution, the axial and radial extents are used to construct the trap volume such that the average density is equal to N/V. Plotting measured volumes as a function of time determines the form of $V(t)$. Equation (5.5) has two terms that affect the atom number: one that accounts for loss due to background gas collisions, and the other that accounts for the loss of atoms through evaporation. The form of the evaporation term was determined using estimation techniques of [3] assuming three-dimensional evaporation.

The second differential equation models the total energy of the gas:

$$\frac{dE}{dt} = -\frac{N}{\tau}(3k_B T) - \frac{N^2}{V(t)} \sigma_e \sqrt{\frac{16}{\pi} \frac{k_B T}{m}} \frac{d}{k_B T} e^{\left(\frac{-d}{k_B T}\right)}(d + k_B T) + \left(\Delta E_{CAZ}\right)$$

(5.6)

which is a sum of the losses of energy due to background gas collisions, evaporation, and changes in energy due to CAZ cooling. The CAZ cooling term ΔE_{CAZ} is initially set to zero so that the numerical solution to the system of equations can be found for the baseline data. The value of the effective trap depth d is adjusted until the evaporative terms in equations (5.5) & (5.6) best match the baseline data. This trap depth is then used when numerically solving the

system of equations during CAZ cooling. During CAZ cooling, the CAZ cooling term, ΔE_{CAZ}, in equation (5.6) is given by:

$$\frac{k_s f (1-f) N^2 R \left[(\Delta + \alpha') \zeta - (\Delta - \alpha) \exp\left(\frac{-\Delta}{k_B T}\right) \right] + f N V R^2 \zeta (\alpha + \alpha')}{\left(\exp\left(\frac{-\Delta}{k_B T}\right) + 1 \right) k_s (1-f) N + R V (\zeta + 1)} \tag{5.7}$$

Equation (5.7) is a modification on the earlier CAZ cooling rate model. Specifically, equation (5.7) is the rate of change in energy associated with the total CAZ cooling rate in the presence of backstreaming ($3k_B$ ($N_1 + N_2$) times the sum of equations (5.3) & (5.4)). Because the CAZ cooling rate model tracked the populations of each isotope individually, the following substitutions were made: $N_1 \rightarrow (1 - f)N$, and $N_2 \rightarrow f N$. Where the parameter f is the fractional number of ^{85}Rb atoms compared to the total number of atoms in the trap. For the CAZ cooling data in figure 5.2, $f = 0.32$. Note that the CAZ cooling term has contributions of both cooling due to CAZ, and heating (density-independent as well as a result of backstreaming) due to the direct optical pump light needed for this implementation of CAZ. The numerical solutions of this model under conditions observed for the baseline and CAZ cooling data are shown in figure 5.3. The model results are consistent with the data, an indication that the model captures all the physics relevant to CAZ cooling. As an additional check, numerical solutions using conditions of the high magnetic field and zero magnetic field data was also done. These results were consistent with no significant change in energy as was observed in the data. The model does not predict much of an improvement in total number of atoms (less than 2% of N) as a result of reduced evaporation due to CAZ cooling. However, as mentioned earlier this behavior was not observed during this implementation of CAZ cooling. Applying loss rate measurement techniques analogous to those in used chapter 4, found a significant ($1.50 \pm 0.75 \times 10^{-12}$ cm^3/s) light-assisted collisional loss rate under the CAZ cooling experimental
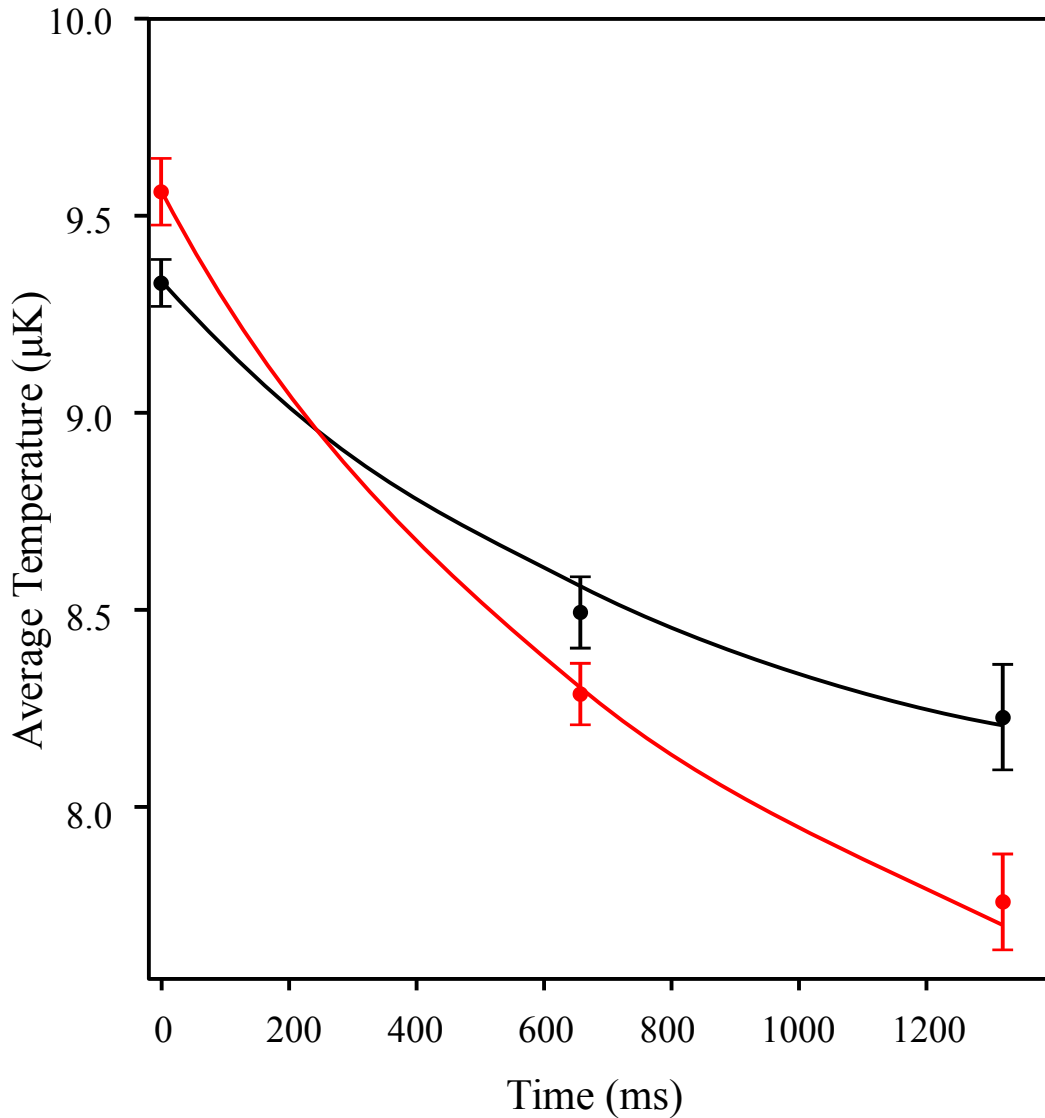
Figure 5.3 Modeling CAZ Cooling with Significant Evaporation.
Numerical solutions showing the temperature evolution of an [85/87]Rb mixture of atoms trapped in a FORT in the presence of significant evaporation (black) and with CAZ cooling in the presence of significant evaporation. The points are the observations of behavior as shown in figure 5.2. Lines are the numerical solutions to the evaporation model discussed in the text. While the model is very consistent with the atom temperature, it is less so with the atom number. The model predicts atom losses of about 55% of the total for both cases, but observations found that about 50% of the atoms were lost in the baseline data and 60% were lost during CAZ cooling. Atom loss is primarily due to background gas collisions, but greater loss is always observed when the spin polarization light is on. This implies that significant light-assisted collisional losses resulted from the optical pumping light.

conditions. If the light-assisted collision rate were to be reduced by increasing the laser detuning, then the backstreaming effects would worsen. Thus, in order to advance CAZ cooling further the direct optical pumping technique used for these results will need to be replaced with another spin-polarization technique.

5.5 Prospects for Cooling Performance Improvement and Future Investigations

Achieving CAZ cooling in the lab has been a significant milestone for the research project; however, much work remains to be done. This section will cover some of the immediate next steps for improvement of CAZ cooling sequence, potential solutions to additional limitations, and some of the long term goals of the research group.

5.5.1 Improving collision-assisted Zeeman cooling

The experiments of the immediate future will focus on the performance of the CAZ cooling in the $^{85/87}$Rb system. Currently the greatest challenges for efficient cooling are limitations in the pumping process and relatively poor initial conditions in the gas mixture. Work has already been started to address these issues while this thesis was completed. These improvements are discussed below.

The initial density and temperature of the atoms loaded into the FORT must be such that the CAZ cooling rate is sufficiently high compared to the lifetime of the trapped atoms due to background gas collisions. The two-isotope loading difficulties discussed in chapter 4 result in a significant limitation for the Rb system. For example, had the FORT been able to load twice as many atoms at the otherwise same conditions as those in the CAZ cooling data, the cooling rate would be dramatically improved by roughly a factor of two.

In principle the limitations due to initial conditions can be overcome though the use of different trapping techniques. For example, using hybrid magnetic/optical trap loading would vastly improve the number of atoms trapped [4]. In this loading scheme, atoms would be first

captured in a magnetic trap where they would be evaporatively cooled prior to being transferred to an optical trap (recall that CAZ cooling cannot be done in a magnetic trap). This avoids the light-assisted collisional losses inherent to MOT-to-optical trap loading. Alternatively, the use of pre-cooling of the atoms prior to CAZ cooling would remove unwanted evaporation and also result in higher initial densities. Also, as discussed in appendix C, modification of the optical trap geometry could be done to increase the density, improving the initial density.

The direct optical pumping of ^{85}Rb used in this initial realization of CAZ cooling resulted in a significant amount of light-assisted collisional loss and backstreaming. Reducing either of these issues, inherent to direct optical pumping, only comes at the cost of increasing the other. Optical-pump-induced heating and loss is in a sense more severe an issue than the initial conditions. This is because in an ideal environment where the trap lifetime was not a limiting factor and evaporative effects were non-existent, heating and loss from the optical pump will prevent the cooling from progressing to arbitrarily long timescales. To give an idea of the potential benefits of using a different optical pumping technique, consider figure 5.4. Figure 5.4 shows an additional solution of the model of the previous section for CAZ cooling in the presence of evaporation compared to the observations made in this study. For this new solution, optical-pump-induced heating terms including backstreaming have been set to zero. The model indicates that the temperature reduction with respect to the baseline case after 1.32 seconds due to CAZ cooling could be improved by a factor of 2.5 under the same initial conditions and cooling times as those observed in this first implementation of CAZ cooling if the ^{85}Rb could be spin-polarized without loss. Improving the optical pumping process can be done by utilizing one of the other spin-polarizing pumping techniques discussed in section 2.3.2. The implementation of these techniques lies beyond the work presented in this thesis. However, as this thesis was written, a pumping technique that utilizes both direct optical and microwave pumping has
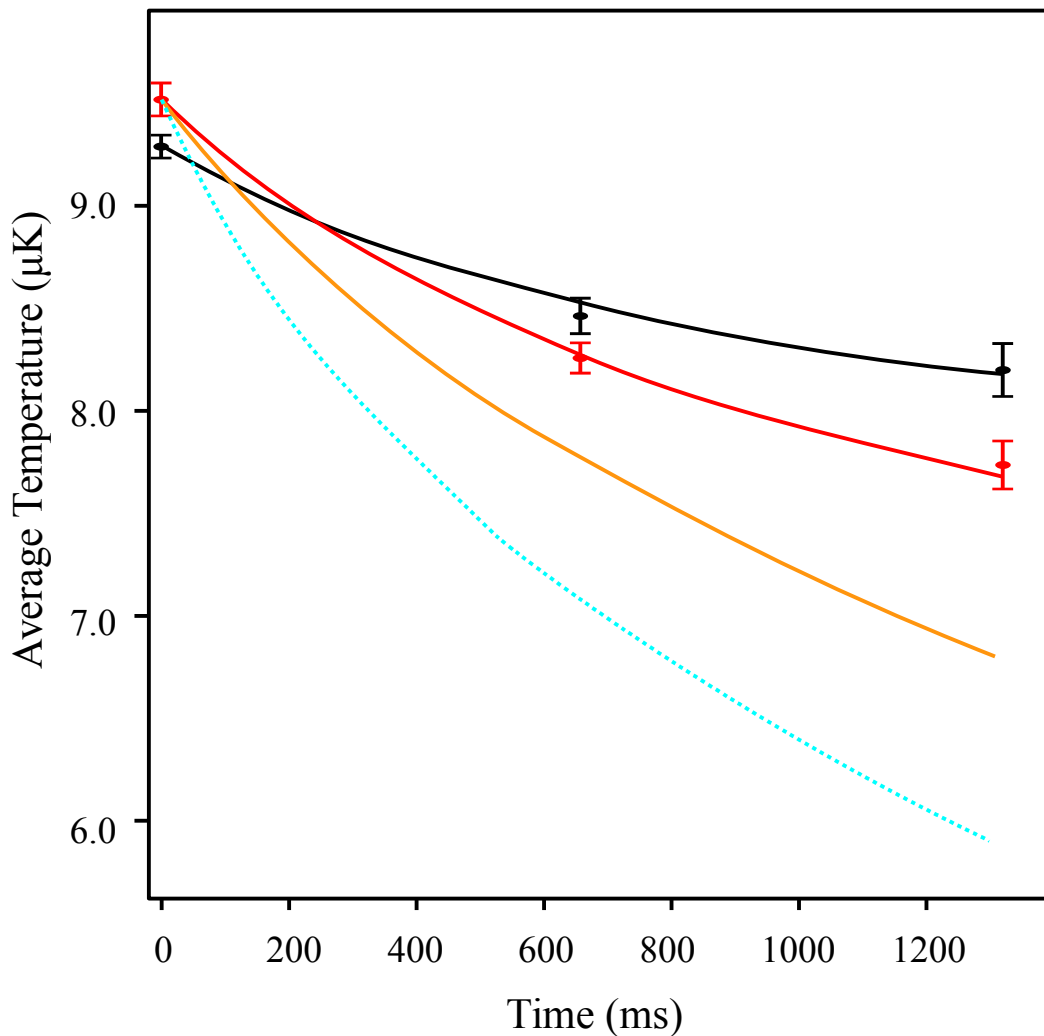
Figure 5.4 Predicted Performance with Improvements in Pumping & Density.
Numerical solutions showing how the temperature evolution of an [85/87]Rb mixture of atoms trapped in a FORT could be improved assuming no loss due to the spin polarization process. The red curve is the model solution to the observed CAZ cooling conditions, and the black curve is the baseline solution. Both include the data points for reference. The orange curve shows the maximum expected performance under the same initial conditions but with no loss due to the optical pumping process. The blue dashed curve includes no optical pumping loss with a doubling of initial atom number. While quantitative improvements due to a doubling of initial conditions are the similar to those due to perfect optical pumping on this timescale, in practice improving the optical pumping will provide better performance in the long run.

already been developed and put to use. This technique uses the direct optical pump beam to initialize the spin polarization, which is then maintained using microwave/optical pumping. This results in the quick preparation of atoms for CAZ cooling, as well as avoids light-assisted collisional losses for the majority of the experimental run. Further improvement to the optical pumping could be realized through Raman pumping the ^{85}Rb atoms from the $F = 2$, $m_F = -1$ state to the $F = 3$, $m_F = -3$ state as expanded on in appendix B. Raman pumping has the advantage of being very fast in principle, with no appreciable backstreaming of atoms. It is also a more efficient means to optically pump atoms into the desired state. And because Raman transitions utilize relatively large detunings, light-assisted collisions should be much lower, despite the relatively high intensities that would be used.

Should both the initial conditions and the inefficiencies due to the spin polarization process be improved from those reported in this thesis, the CAZ cooling rate should be high enough to warrant pushing toward the limits of the technique. For example, if all heating and loss due to the optical pumping process can be eliminated and if the initial densities of both rubidium isotopes could also be doubled, then the CAZ cooling would be expected to reach temperatures indicated by the blue line in figure 5.4. This much of an improvement represents a best-case scenario, and taking the model solution for these conditions out to longer cooling times is shown in figure 5.5.

Figure 5.5 demonstrates that substantial CAZ cooling could still be expected in our system if the spin polarization could be done without heating and loss and if the initial densities were doubled, all other things equal. This means that the magnetic field has been set to 0.84 G, which is only near optimal at the starting temperature. Although the final ~3 μK temperature that this prediction settles to is still above the BEC transition temperature of about 1 μK, the amount
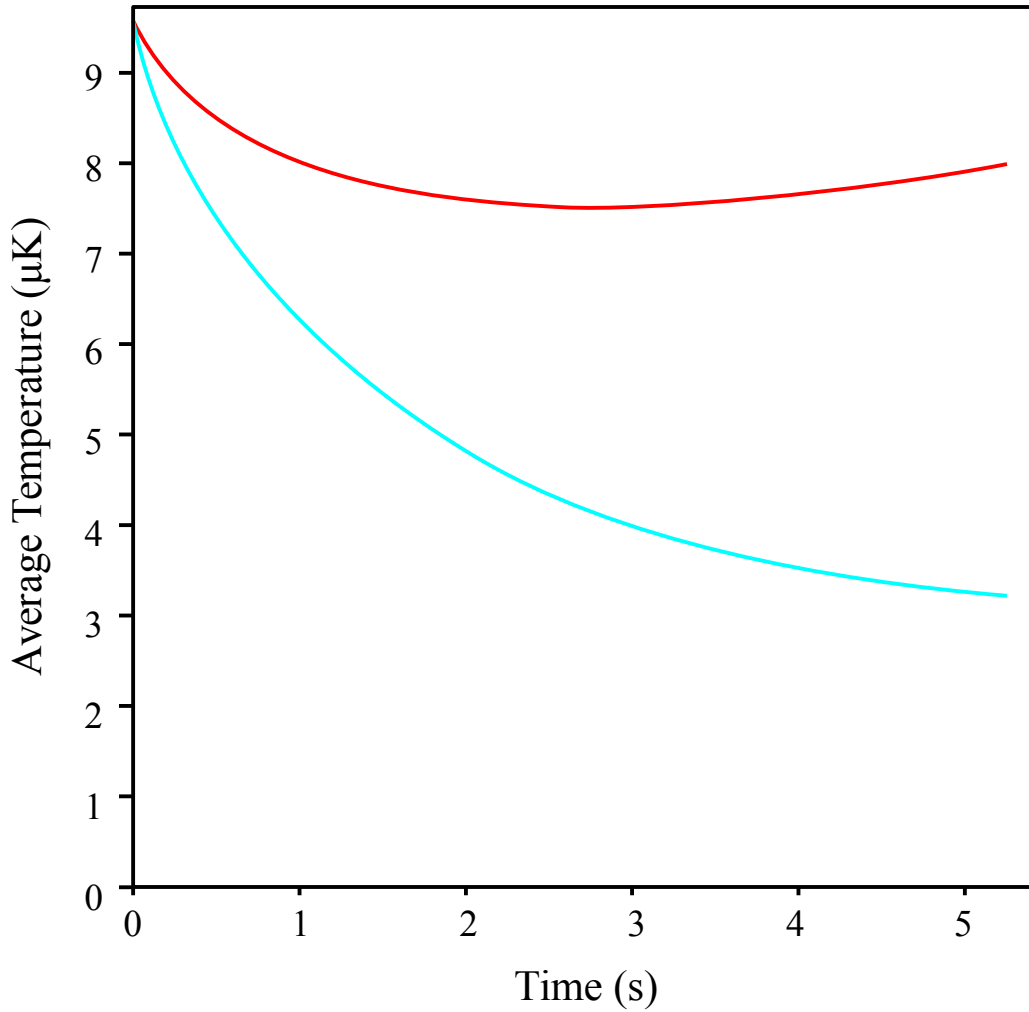
Figure 5.5 Predicted Improved CAZ Cooling for Extended Times.
Numerical solutions to the CAZ cooling model in the presence of evaporation for cooling times of several seconds. The blue curve shows expected performance if all optical-pump-induced heating and loss is eliminated and initial densities are doubled from those observed in this work. This represents a maximum expected improvement in performance for our system. To take the model to longer time frames than those observed with the data, a volume scaling of $V = \eta(T)^{3/2}$ is assumed with the constant η fit to the initial trap conditions observed. All other parameters are assumed equal to those observed in the CAZ cooling data reported in the text. Extending cooling times under the model for the reported CAZ cooling conditions is shown in red. For reference, the BEC critical temperature is around 1 μK.

of cooling is still respectable. This prediction was made under the earlier assumptions of no reabsorption effects and a spin-exchange collision rate that does not change with atom temperature, both of which are unlikely to hold over the span of temperatures. Thus the long-time estimate may be overly optimistic. However, there are also still means to improve the cooling which are not considered. For example, adiabatic compression of the optical trap, adjustment of the magnetic field during cooling in order to maintain an optimal energy barrier for the kinetic-energy-reducing spin-exchange collisions (both covered in appendix C), or improving the trap lifetime due to background gas collisions could all be done in order to improve the collision rate.

Improvements to the apparatus aimed to increase the initial densities and to utilize a different optical pumping mentioned have already been made and have allowed CAZ cooling experiments to progress beyond what is presented here. The cooling sequence now extends cooling times well beyond one second using a shortened cooling cycle. The improved cooling setup has enabled evaluation of CAZ cooling in greater detail. This has made it possible to separate out various extra cooling and heating effects leading to a better understanding of the limitations of CAZ cooling, and especially limitations of the $^{85/87}$Rb system- all topics for a future thesis.

5.5.2 Mitigation of Reabsorption

Should reabsorption effects become the limiting factor of an optimized CAZ cooling setup, there are several measures which can be taken to try to push the performance yet further. Although many of these available options have already been mentioned and discussed throughout this thesis as they became relevant, it is somewhat useful to summarize them here in one place.

The two component nature of the CAZ cooling being pursued offers a very straightforward means to combat reabsorption, as shown in section 2.4.2. Since only one of the isotopes in the sample is being optically pumped, there is no near-resonant light around for the other isotope. This means that only one isotope is in likely danger of reabsorption-related losses. Since the cooling rate is dependent on inter-isotope collisions, the density of the two-component mixture is more pertinent to the cooling than the density of either isotope alone. As can be seen in figure 2.10, there is a clear theoretical advantage to be gained by adjusting the relative abundance of the optically pumped isotope in a CAZ-like cooling scheme. In fact, the relative abundance adjustment need not be done in situ if the trap lifetime is able to support a relatively low initial cooling rate, as was shown in figure 2.11. Adjusting the proportions of each isotope initially loaded into the optical trap can be easily facilitated by changing the detuning of the MOT trapping lasers during the optical trap loading process. Reducing the optically pumped atom number as the cooling progresses could be done by use of a near-resonant laser beam incident on the outer edge of the atom cloud's axial direction to push some of the atoms out of the trap. Removal of atoms in this manner would also somewhat cool the cloud since only the higher energy atoms are able to reach the far edges of the trap potential. Again, the theory treatment in section 2.4.2 shows the utility of managing the optical depth to obtain the highest cooling rates.

The adjustable aspect ratio optical trap, discussed in appendix C, also provides a potential method to mitigate reabsorption. As the atoms cool, their density will increase. When the density increases to a point where scattered photons cannot escape the cloud reabsorption effects start playing a major role. An adjustable aspect ratio optical trap can counter the density increase. The trap volume can be made larger by relaxing the confining potential. This would allow the atoms to spread out more throughout the trap and thus reduce the atom density. A

relaxation of the trap potential can also be obtained by reducing the optical trap laser power, but only at the expense of being more likely to reintroduce evaporation losses. Relaxing the trap potential by adjusting the trap's aspect ratio will obviously change the shape of the trap. Normally the long and thin geometry of a standard optical trap is best because the spatial extent is small in the radial direction which allows more of the scattered photons to escape. However, with the ability to adjust the aspect ratio of the trap, parameters can be chosen such that the trap volume can be optimally relaxed and reabsorption maximally mitigated.

Also we have seen in past work that modulation of the pumping light can be used to reduce reabsorption effects [5]. In this previous work it was found that the two-photon reabsorption process could be mitigated by using pump light with multiple frequency components and a spatial interference pattern on a length scale smaller than the scattered photon mean path length. In such a situation, the phase of the spontaneously scattered light varies randomly with respect to the pump light at any given point in space due to the random distribution of atoms in the gas. This disrupts the phase coherence of the reabsorption process, reducing the amount of reabsorption. Using this technique, the previous work saw about a factor of two reduction in the reabsorption rate. Analytical calculations of the reabsorption rate for such a configuration indicated that the reduction scales linearly with number of additional frequency components used for the pump beam, given the net intensity of the pump is kept the same. This technique could be applied to the CAZ cooling system, and offers yet another way to mitigate reabsorption.

Even though reabsorption is not currently the limitation in our studies, it may well become a problem should CAZ cooling be pushed to its maximum (perhaps in a system other than an $^{85/87}$Rb mixture). Since reabsorption is related to the density of atoms and the density is related to the temperature, success in reducing reabsorption resulting in further cooling is likely

to result in a future problem with reabsorption. Having multiple means of mitigation available is thus a likely valuable asset. Using one or all of the above mentioned techniques may be needed to reach the maximum cooling potential of CAZ cooling.

5.5.3 Other Isotopic Combinations

Like reabsorption, three-body recombination is a density dependent effect. As a cloud of atoms cools and contracts, it becomes more susceptible to three-body losses. It is known that ^{85}Rb has a relatively high three-body recombination rate [6]. So, while initial investigations into the $^{85/87}$Rb mixture have demonstrated the technique experimentally, it may well be the fact that ultimately the largest applicability of CAZ cooling will be in other gas mixtures.

The requirements for potential CAZ cooling candidates are not particularly stringent. The two isotopes must have an appreciable spin-exchange collision rate, and they must not have high inelastic collisional losses. The spin-exchange collision rate between isotopes is generally hard to predict. This is because the rate depends strongly on the precise depth of the interatomic potential between the two isotopes. Atoms with a richer ground state spin structure will in general more likely have some collision channel with an appreciable rate. Conversely the alkali earths do not have ground state spin structure therefore CAZ cooling will not work with these atoms in their ground state. The choice of ^{85}Rb and ^{87}Rb used for the research presented in this thesis was made because their rates are relatively well known and out of convenience of experimental implementation for the first investigation of this cooling technique. The Rb mixture meets the basic requirements of high spin-exchange collision rate and low inelastic loss rate (with the exception of the three-body recombination rate of ^{85}Rb, which while high, is not high enough to be prohibitive to the technique until the cooling in the gas brought the temperature to much lower values than those examined here). ^{85}Rb and ^{87}Rb are also easily obtainable since both isotopes have high natural abundance. In addition, much of the equipment

(MOT trapping lasers, imaging laser, etc.) can be used for both isotopes since they share the same electronic atomic structure. This was viewed as a strong advantage for investigation of a previous untried technique. There are several other isotopic combinations that are particularly promising for CAZ cooling.

Among combinations of the alkali metals, Li/K, K/Rb, and Li/Rb, are the most promising candidates for CAZ cooling. The use of Cs atoms is not promising due to high inelastic collision loss rates. The inelastic collisions would lead to loss except when the Cs density is very low-opposite of that which is desired for CAZ cooling. Combinations of isotopes with the same nuclear spin would require second-order Zeeman shifts to be utilized for the cooling. For example, the isotopes of ^{39}K, ^{41}K, ^{87}Rb and ^{7}Li all have a nuclear spin of 3/2, thus combinations of these atoms would require second-order Zeeman effects to facilitate CAZ cooling. Although second-order Zeeman shifts are experimentally accessible, they are also inconvenient (e.g. magnetic fields on the order of 100 G). A combination of ^{87}Rb and ^{6}Li (or ^{40}K if its low natural abundance is not an issue) is therefore an interesting possibility, which would also allow for cold boson-fermion interactions to be studied. Another potential advantage of other combinations of isotopes is that perhaps the cross-species losses during optical trap loading, reported for ^{85}Rb and ^{87}Rb in chapter 4, could be reduced. Be that as it may, all the alkali metal combinations will likely suffer from similar optical pumping issues as the work of this thesis has seen. If alternative pumping processes cannot overcome these issues in the $^{85/87}$Rb system, then there is a high likelihood that they will be present in other alkali mixtures as well.

Perhaps more intriguing than combinations of alkali metals would be a combination of an alkali metal with a non-alkali metal. Elements such as Al, Cr, Er, and Ga have been successfully cooled and trapped and may provide additional opportunities for CAZ cooling. The isotope of ^{52}Cr is particularly interesting due to a lack of hyperfine structure which would allow it to be

optically pumped with a single laser beam. This also means that there is a lack of nearby transitions which would cause backstreaming effects to be nearly non-existent. The isotope still has a spin structure since the ground state has a total spin of 3, making it a viable candidate for CAZ cooling. Therefore in principle all the two-isotope advantages discussed in chapter 2 could be realized with a ^{52}Cr/^{87}Rb system.

5.6   Conclusions

The work presented in this thesis includes the first experimental evidence for spin-exchange collisions between ^{85}Rb and ^{87}Rb. Also, the first successful implementation of CAZ cooling was demonstrated. The implementation of CAZ cooling utilized two different isotopes (^{85}Rb and ^{87}Rb). This is an expansion of the original CAZ cooling theory [7], whose development was also presented in chapter 2. This included a simple cooling rate model that showed that cooling with two species was advantageous over cooling with a single species at low temperatures in the presence of reabsorption effects.

The performance of the CAZ cooling of the $^{85/87}$Rb mixture was below expectations even after accounting for lower than expected initial densities. Thus, the cooling was not pushed to the lowest possible temperatures that could be supported with the current apparatus. Background gas collisions, evaporation, and optical-pump-induced heating and loss were all observed during CAZ cooling. An extended model was developed to account for these additional processes. Using reasonable expectations for our system, the model indicated that these effects account for the observed sub-optimal performance. It was found that low initial densities and inefficiencies in the optical pump process prevented efficient cooling. The optical pump caused much more heating than was originally expected, and also induced a large amount of light-assisted collisions. In order to improve performance, a system redesign is therefore necessary.

The results of the initial CAZ cooling analysis shows that the physical principals of the technique are sound. All indications are that the observed cooling performance was due to technical limitations and not fundamental limitations. As such, the work presented here is invaluable for determining how the apparatus should be improved. It should be noted, though, while this work does show what problems must be avoided, it does not guarantee that CAZ cooling will perform at the level of the highest expectations. It does indicate important factors that must be considered in order for the technique to reach its full potential for success.

The expectation that CAZ cooling in our system could reach temperatures around 3 μK, or better with the system improvements discussed in chapter 3 and appendix C, is reasonable given the observed limitations and prospects on how they might be improved. Even if the planned improvements to the apparatus are not enough to make CAZ cooling efficient, the technique is flexible enough that mixtures other than $^{85/87}$Rb will likely benefit from its use. Many opportunities still exist for the cooling technique.

References for Chapter 5

[1] A. Gorges, N. Bingham, M. DeAngelo, M. Hamilton, and J. Roberts, Phys. Rev. A **78**, 033420 (2008).

[2] James Burke, Ph. D. Thesis, University of Colorado, (1999).

[3] W. Ketterle, and N.J. van Druten, Adv. Atom. Mol. Opt. Phy. **37**, 181 (1996).

[4] Y.-J. Lin, A. Perry, R. Compton, I. Spielman, and J. Porto, Phys. Rev. A **79**, 063631 (2009).

[5] A. Gorges, A. Foxley, D. French, C. Ryan and J. Roberts, Phys. Rev. A **76**, 033420 (2007).

[6] J. Roberts et al., Phys. Rev. Lett. **85**, 728 (2000).

[7] G. Ferrari, Eur. Phys. J. D **13**, 67-70 (2001).

Appendix A: The Zeeman Shift and g-Factors

The Hamiltonian describing the energy of an atom in an external magnetic field of magnitude B is given by equation (2.1):

$$H_{Zeeman} = -\vec{\mu} \cdot \vec{B} \tag{A.1}$$

The total magnetic moment, μ, used above is a weighted sum of the various angular momentum components of the atom: S the electronic spin, L the electronic orbital momentum, and I the nuclear spin. Each component is weighted by the appropriate g-factor (or gyromagnetic ratio) which characterizes the contribution of each piece of angular momentum (g_S, g_L, and g_I for S, L, and I respectively). This leads to a total magnetic moment of:

$$\mu = -\frac{\mu_B}{\hbar}\left(g_L \vec{L} + g_S \vec{S} + g_I \vec{I}\right) \tag{A.2}$$

where μ_B is the Bohr magneton which is approximately 9.27×10^{-24} J/T. The Hamiltonian for the Zeeman shift then becomes:

$$H_{Zeeman} = \frac{\mu_B}{\hbar}\left(g_L \vec{L} + g_S \vec{S} + g_I \vec{I}\right) \cdot \vec{B} \tag{A.3}$$

Under the assumption that the magnetic field is small, equation (A.3) can be further simplified. For example if the field is weak enough that the Zeeman shifts in energy are weak with respects to any fine structure of the atom, the quantum number $J = S + L$ may be used:

$$H_{Zeeman} = \frac{\mu_B}{\hbar}\left(g_J \vec{J} + g_I \vec{I}\right) \cdot \vec{B} \tag{A.4}$$

where g_J is the Landé g-factor.

The Landé g-factor can be found by evaluating the Zeeman shifts of a lone electron in the absence of nuclear spin [1,2]:

$$H_{Zeeman} = \frac{\mu_B}{\hbar}\left(g_S \vec{S} + g_L \vec{L}\right) \cdot \vec{B} \tag{A.5}$$

174

Solving requires evaluation of the vector dot product in terms of quantum numbers. This may be done by projecting the vectors along the vector J:

$$
\begin{aligned}
H_{Zeeman} &= \frac{\mu_B}{\hbar}\left(g_S \vec{S} + g_L \vec{L}\right)\cdot\frac{\vec{J}}{|J|}\frac{\vec{J}}{|J|}\cdot\vec{B} \\
&= \frac{\mu_B}{\hbar J^2}\left(g_S \vec{S} + g_L \vec{L}\right)\cdot\left(\vec{S}+\vec{L}\right)J_z B
\end{aligned}
\tag{A.6}.
$$

Here the second expression also assumes that the magnetic field is along the z-axis, thus J_z is the quantum operator for the projection of J along the z-axis. Carrying out the vector algebra yields:

$$
H_{Zeeman} = \frac{\mu_B}{\hbar}\left[g_L\left(\frac{J^2+L^2-S^2}{2J^2}\right)+g_S\left(\frac{J^2-L^2+S^2}{2J^2}\right)\right]J_z B
\tag{A.7}.
$$

The operators can then be expressed as quantum numbers, $J^2 = J(J+1)$, $J_z = \hbar\, m_j$, $L^2 = L(L+1)$, and $S^2 = S(S+1)$, which yields a Zeeman shift in energy of:

$$
\Delta E_{Zeeman} = g_J \mu_B B m_J
\tag{A.8}
$$

where the Landé g-factor has been used to simplify the evaluated bracketed terms in equation (A.7), and is thus defined as:

$$
\begin{aligned}
g_J = g_L &\frac{J(J+1)-S(S+1)+L(L+1)}{2J(J+1)}+g_S\frac{J(J+1)+S(S+1)-L(L+1)}{2J(J+1)} \\
&\approx \frac{3}{2}+\frac{S(S+1)-L(L+1)}{2J(J+1)}
\end{aligned}
\tag{A.9}
$$

where the approximation is the result of inserting the electronic g-factors: $g_L = 1$ and $g_S \approx 2$. This is the Landé g-factor to be used in .

However, can be further simplified if the magnetic field is weak enough that the Zeeman shift in energy is less than the hyperfine state separation. In this case, the quantum number $F = J + I$ may be used:

$$
H_{Zeeman} = \frac{\mu_B}{\hbar}g_F \vec{F}\cdot\vec{B}
\tag{A.10}
$$

where g_F is the g-factor of the entire atom. The atomic g-factor can be found using the same procedure as the Landé g-factor, but with the following substitutions in equations (A.5) through (A.8): $J \rightarrow F$, $L \rightarrow J$, and $S \rightarrow I$; which leads to the following definition for the atomic g-factor:

$$g_F = g_J \frac{F(F+1) - I(I+1) + J(J+1)}{2F(F+1)} + g_I \frac{F(F+1) + I(I+1) - J(J+1)}{2F(F+1)}$$

$$\approx g_J \frac{F(F+1) - I(I+1) + J(J+1)}{2F(F+1)}$$

(A.11)

where the approximation in the second expression is due to the nuclear g-factor g_I being much smaller than Landé g-factor g_J. The corresponding equation to equation (A.8) under the strong hyperfine interaction assumption gives the first-order approximation to the shift in energies due to the Zeeman effect, which is equation (2.2) in the text.:

$$\Delta E_{Zeeman} = g_F \mu_B B m_F$$

(2.2).

Calculating the first-order Zeeman shift then comes down to evaluating the atomic gyromagnetic ratio of the state in question. The relevant quantities to calculate g_F for the lower hyperfine ground states of the isotopes of Rb used in this work are given in the following table [3,4]:

Table A.1 Gyromagnetic ratios and angular momentum values of the lower hyperfine ground state of [87]Rb and [85]Rb. The gyromagnetic ratios, or g-factors, are measured values collected by reference 3 & 4. Using the angular momentum values with the equations and approximations discussed in the text, the lower hyperfine ground state g-factors, g_F, for each isotope can be determined to calculate first-order Zeeman shifts.

Term	Symbol	Value
Electron spin g-factor	g_S	2.002 319 304 3622(15)
[87]Rb electron orbital g-factor	g_L	0.999 993 69
[85]Rb electron orbital g-factor	g_L	0.999 993 54
Rb ground state Landé g-factor	g_J	2.002 331 13(20)
[87]Rb nuclear g-factor	g_I	$-0.000\ 995\ 141\ 4(10)$
[85]Rb nuclear g-factor	g_I	$-0.000\ 293\ 640\ 00(60)$
Electron spin	S	1/2
Rb ground state electron orbital momentum	L	0
Rb ground state total electron momentum	J	1/2

^{87}Rb nuclear spin	I	3/2
^{87}Rb lower hyperfine ground state atomic angular momentum	F	1
^{85}Rb nuclear spin	I	5/2
^{85}Rb lower hyperfine ground state atomic angular momentum	F	2

The values of the g-factors presented in Table A.1 are measured values and thus deviate slightly from those used in the text. The reason for the difference is due to quantum electrodynamics and the structure and mass of the Rb nucleus. Approximating the g-factors as discussed earlier and using the angular momentum values for each isotope of Rb, allows us to calculate the gyromagnetic ratio of the lower hyperfine ground state of Rb using equation (A.9) and equation (A.11):

$$^{85}Rb: g_F = -\frac{1}{3}$$
$$^{87}Rb: g_F = -\frac{1}{2}$$

(A.12).

These are the values used to find the first-order Zeeman shifts in equation (2.3):

$$\Delta E_{Zeeman85Rb} = -\frac{1}{3}\mu_B B$$
$$\Delta E_{Zeeman87Rb} = -\frac{1}{2}\mu_B B$$

(2.3).

References for Appendix A

[1] C. Nave, *Hyperphysics: Magnetic Interactions & the Landé g-Factor*, Georgia State University (1998).
[2] Also addressed in some textbooks, see for instance, D. Griffiths, *Introduction to Quantum Mechanics*, **2nd ed.** (Pearson Prentice Hall, New Jersey, 1995) page 277.
[3] D. Steck, "Rubidium 87 D Line Data," http://steck.us/alkalidata (revision 2.1.4, 23 December 2010).
[4] D. Steck, "Rubidium 85 D Line Data," http://steck.us/alkalidata (revision 2.1.5, 19 September 2012).

Appendix B: Spin-Polarization via Raman Transitions

The spin polarization technique for CAZ cooling that holds the most promise, yet is also the most complex, utilizes Raman transitions. Due to the experimental complexity required, this technique was not initially pursued for the realization of CAZ cooling. However, at the conclusion of the work presented within this thesis, pursuing the Raman spin polarization pump was expected to be the next step to improve CAZ cooling performance since CAZ cooling performance in this work was significantly hindered due to issues relating to the pumping process. The theory of pumping atoms for spin polarization using Raman transitions is covered in this appendix. Calculations will focus on those relevant to the spin polarization of ^{85}Rb.

The Raman spin polarization pump replaces the role of the direct optical pump beam (or the microwave-driven transitions) with a Raman transition. This is useful for many reasons. For one, the Raman pump will ultimately place the atoms into the $F = 3$, $m_F = -3$ upper hyperfine ground state. From here there is a large probability that they will decay down to the $F = 2$, $m_F = -2$ due to the action of the repump laser. Because the $m_F = -3$ state is the lowest energy state in the $F = 3$ hyperfine ground state, atoms pumped into this state cannot participate in CAZ "heating" collisions as described on page 149. Having atoms in this state also suppresses intra-isotope hyperfine changing collisions (see page 54). Because the electric dipole transitions are stronger than magnetic dipole transitions for experimentally realizable fields, the transfer rate for Raman pumping can be very fast. Finally, there is high state selectivity with Raman transitions, so for Raman pumping there are no expected problems with backstreaming, as discussed in section 5.2 on page 145.

This appendix covers basic Raman transition theory and applies it to the spin polarization of ^{85}Rb. A Raman pump model is devised and solved numerically to show that the technique should be feasible for use in CAZ cooling of an $^{85/87}$Rb mixture.

B.1   The Raman Transition

A Raman transition is caused by a two-photon coherent transition that changes the internal state of an atom. Shown schematically in figure B.1 is a Raman transition that changes the hyperfine ground state of an atom.   The transition requires two photons with energy difference equal to the hyperfine splitting of the initial and final states. The first photon excites the atom into a virtual state detuned from the atomic excited state, and the second photon stimulates emission into the desired final state.

By utilizing two lasers that are counter-propagating for the Raman photons, the transition can be made to be highly velocity selective as shown in panel (a) of the figure. To understand how this is the case, consider an atom with a velocity component in the propagation direction of one of the laser beams. Doppler shifts in the laser light cause one beam to be blue-detuned and the other red-detuned as compared to the lab frame owing to the fact that the beams are propagating in opposite directions. This creates a shift in the term δ in the figure compared to the zero velocity case, and so δ becomes a velocity-dependent quantity.   Thus the laser frequencies may be chosen so that only certain velocity classes are in resonance with the two-photon transition.

In contrast, co-propagating beams are insensitive to the velocity of the atom. Panel (b) of figure B.1 shows the case where the Raman beams are co-propagating. Here, both beams are Doppler shifted in the same way. Thus atoms in motion are still in resonance with the beams if the frequencies are set for atoms at rest (i.e. δ is approximately velocity-independent in this case for sufficiently large values of Δ). Velocity insensitive Raman transitions are useful for situations where all the atoms need to be addressed such as optical pumping for spin-polarization. The rest of this appendix assumes that the Raman beams are co-propagating and the Raman transitions are velocity insensitive.
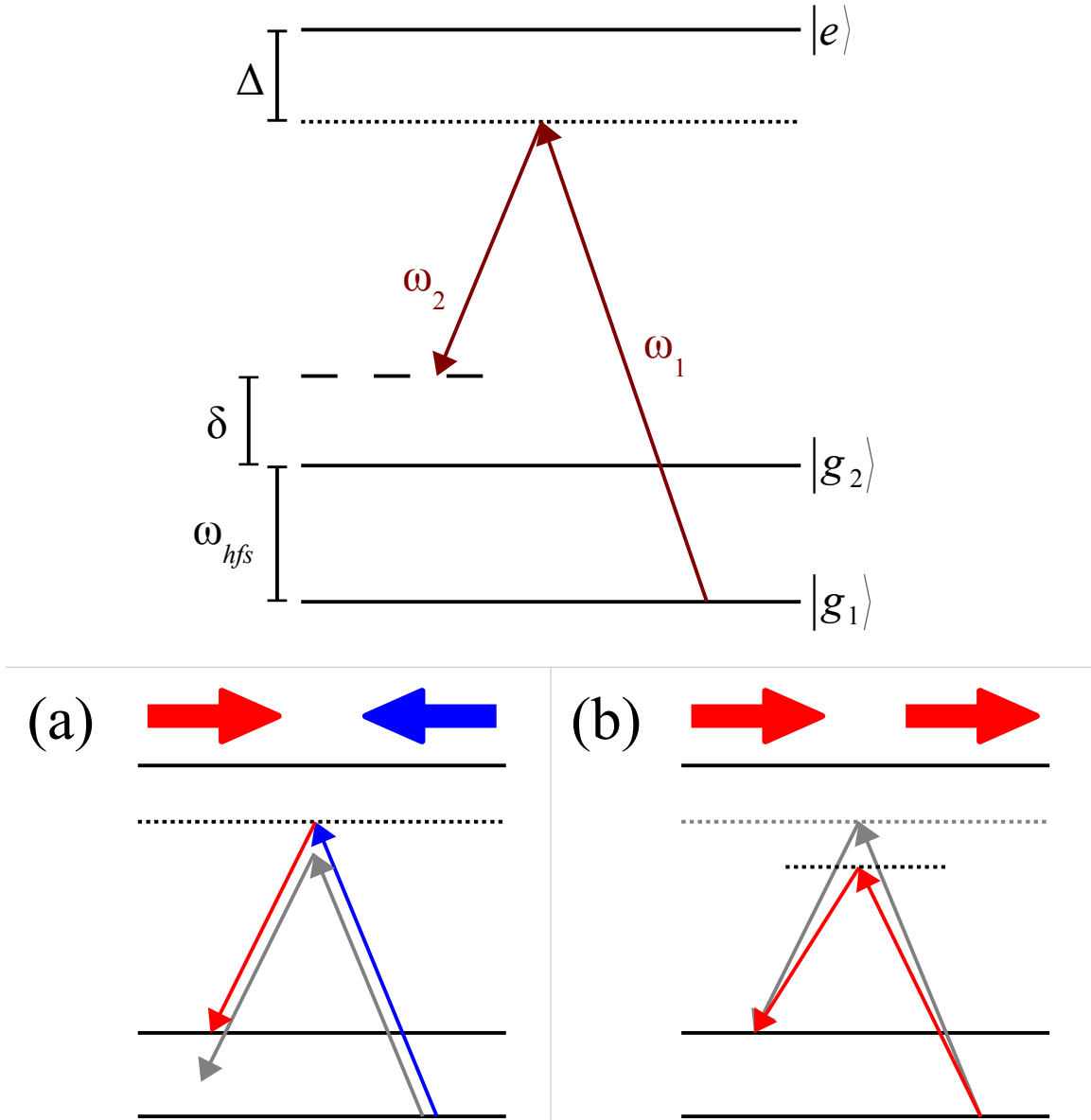
Figure B.1 A Basic Raman Transition.
A Raman transition changing the ground state hyperfine levels of an atom, with hyperfine splitting given by the by frequency ω_{hfs}. Two lasers with chosen frequencies of ω_1 and ω_2 drive the transition through a virtual excited state. In this case, the virtual state is red detuned from the excited state by Δ. There is a small two-photon detuning term, represented by δ, that includes any other shifts to the energy levels such as an induced AC Stark shift. **(a)** Counter- and **(b)** co-propagation beam configurations are velocity selective and velocity insensitive respectively. This is due to Doppler shifts in the Raman beams due to atom motion in the light field (indicated by the large arrows for an atom moving to the right). The small δ has been omitted in **(a)** and **(b)** for clarity.

Because a Raman transition is a coherent process, there is nothing to prevent the two photons from driving the reverse transition as compared to the one that is desired. This means that Raman transitions alone cannot be used to spin-polarize (i.e. optically pump) a gas due to the lack of an irreversible step. However, a Raman transition can take the role of either the direct optical pump beam or the microwave-driven transitions introduced in section 2.3.2. The spontaneous scattered photon of the repump beam provides the irreversible step which facilitates the spin polarization of the gas.

Understanding the evolution of the state populations can be done under the framework of Rabi oscillations. This is a semi-classical approach that models the behavior of a two level atom in the presence of a classical coherent light field. The light field drives transitions between the two states of the atom cyclically at what is known as the Rabi frequency. Here, we will formally define the Rabi frequency between two states, i and j, as:

$$\Omega_{ij} = -\frac{\langle i|\bar{d}_{ij}\cdot\vec{E}_0|j\rangle}{2\hbar}$$

(B.1)

where d_{ij} is the dipole moment of the transition and E_0 is the electric field amplitude and polarization of the light field. The Rabi frequency is proportional to the square root of the light intensity and can be calculated by [1]:

$$\Omega^2 = \frac{\gamma^2}{8}\left(\frac{I}{I_{sat}}\right)$$

(B.2)

where γ is the inverse of the excited state lifetime in angular units ($\gamma = 2\pi \times 5.98$ MHz for the 5P$_{1/2}$ state of ^{85}Rb); I is the laser intensity and I_{sat} is the saturation intensity of the transition ($I_{sat} = 1.6$ mW/cm^2 for Rb). Equation (B.2) represents a "base" Rabi frequency which will need to be modified via the appropriate Clebsch-Gordan coefficient factors in order to get the Rabi frequency of particular transitions.

For an atom that is known to be in one of the two states and in the driving light field, the probability of finding that atom in the other state oscillates between 0 and 1 at the Rabi frequency as long as the driving term is on-resonance. For systems with more than two states, such as those utilizing Raman transitions, the light field drives transitions according to the relative transition strengths between the relevant levels. This makes the time evolution of energy level occupancy potentially more complicated. However, it is generally still possible to ensure complete population transfer at regular intervals. The use of Raman transitions in controlling atomic state populations thus requires precisely timed pulses of Raman light. While this adds to experimental complexity, it is possible to calculate these timings from theory and adjust them experimentally. The remainder of this appendix details the theoretical treatment of a particular Raman transition in ^{85}Rb that would be useful for CAZ optical pumping.

B.2   Theory of ^{85}Rb Spin Polarization Using Raman Transitions

Spin polarization of ^{85}Rb using Raman transitions utilize the energy levels shown in figure B.2. The Raman transition moves atoms from the $m_F = -1$ lower hyperfine ground state into the $m_F = -3$ upper hyperfine ground state using circularly polarized light. From the $F = 3$, $m_F = -3$ state, the atoms are pumped back to the lower hyperfine ground via the optical repump beam as discussed in section 2.3.2. The goal is to have the atoms end in the $F = 2$, $m_F = -2$ lower hyperfine ground state, which is the desired spin polarized state. Because the 5p$_{1/2}$ state has hyperfine structure, there are two excited m_F states of concern each with a different detuning (Δ_1, Δ_2) from the laser frequencies that differ by the excited state hyperfine splitting. The detuning term δ accounts for any deviation from two-photon resonance given the frequencies of the two light fields in the limit of zero intensity.

In order for the two-photon transition to change the value of m_F by two, the hyperfine interaction must be exploited, otherwise Δm can only equal 0, $\pm$ 1. In principle, a $\Delta m = -1$
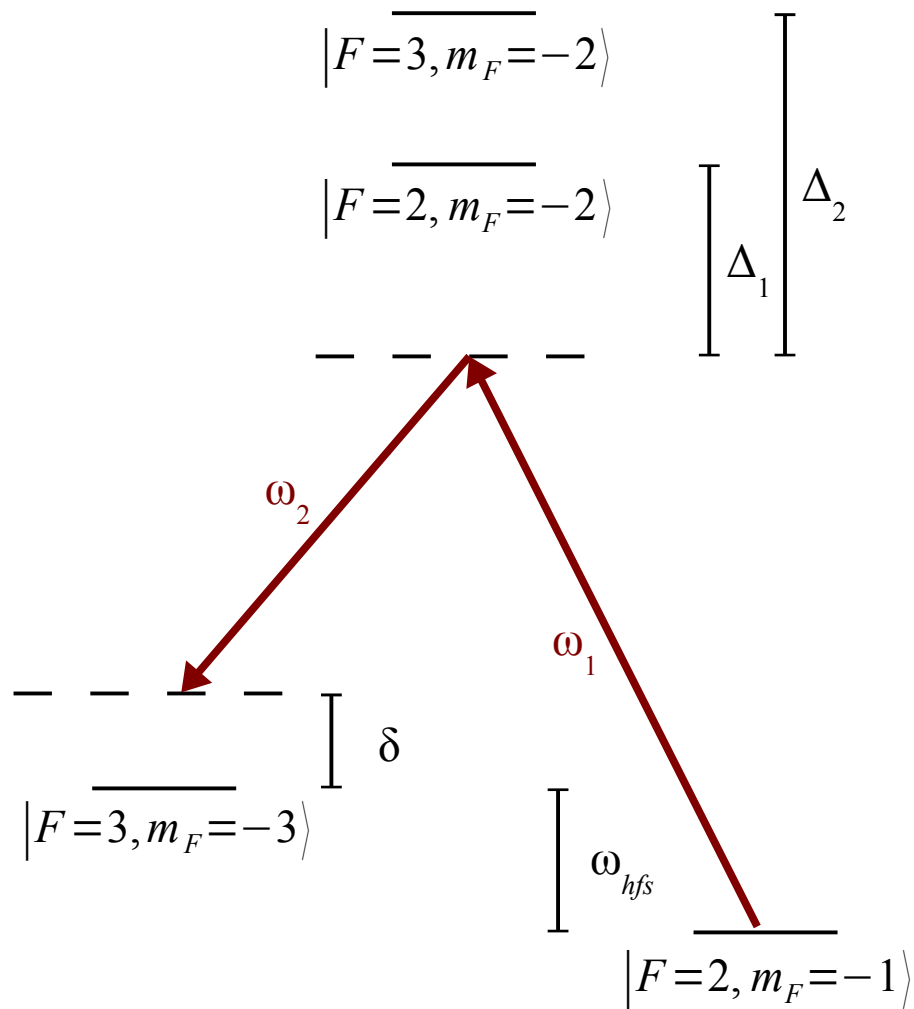
Figure B.2 Energy Level Diagram for Raman Pumping of ^{85}Rb.
Raman transitions along the D1 line may be used for spin polarization of ^{85}Rb. The transition pumps atoms from the lower to upper hyperfine states of the $5s_{1/2}$ ground state through a virtual state detuned from the $5P_{1/2}$ excited state. The hyperfine splitting (ω_{hfs}) of ^{85}Rb is 3.036 GHz. The laser frequencies ω_1 and ω_2 are defined by the various detunings (Δ_1, Δ_2, and δ) and are set to maximize the transition strength for as short a pulse as possible.

transition could be used, but then it would be possible to drive transitions out of the $F = 2$, $m_F = -2$ state, which is undesirable. Although such a transition would be suppressed in a magnetic field since the two-photon resonance frequency would be dependent on the initial m_F state of the ^{85}Rb, it is better to further suppress the transition via light polarization. The use of the hyperfine interaction also means that smaller values of Δ need to be used than would otherwise be the case. A consequence of this is that spontaneous emission will be more of an issue than is generally the case for $\Delta m = \pm 1$ transitions. Later in this appendix, the amount of spontaneous emission is quantified. Furthermore, since the hyperfine interaction is stronger along the D1, it is more desirable to have the Raman transition along the D1 line instead of the D2 line in order to make it easier to accomplish the $\Delta m = -2$ transitions.

Assuming a given pair of laser intensities with the correct circular polarization such that only transitions that decrease the m_F value occur, the pulse length and laser detuning must be chosen to maximize transfer. If the detunings are not set properly, then only partial coherent population transfer will occur due to spontaneous emission during the Raman transition. Similarly if the pulse length is not set correctly then either partial population transfer will occur, or the atoms will be transferred but part or all of the population will transfer back to the initial state. Ultimately the optimal settings will be determined experimentally. However, the theoretical treatment known as adiabatic elimination [1] can be used to determine where the experiment should be set at the start. The rest of this appendix will use this technique, which approximates the equations of motion that describe the relevant quantum energy levels in a classical light driving field. These equations of motion in the ^{85}Rb system are:

$$\dot{B}_1 = -i\,\Omega_1 e^{-i\Delta_1 t} B_3 - i\,\Omega_1' e^{-i\Delta_2 t} B_4$$
$$\dot{B}_2 = -i\Omega_2 e^{-i(\Delta_1+\delta)t} B_3 - i\,\Omega_2' e^{-i(\Delta_2+\delta)t} B_4$$
$$\dot{B}_3 = -i\Omega_1^* e^{i\Delta_1 t} B_1 - i\Omega_2^* e^{i(\Delta_1+\delta)t} B_2 - \frac{\gamma}{2} B_3 \qquad \text{(B.3)}.$$
$$\dot{B}_4 = -i\Omega_1'^* e^{i\Delta_2 t} B_1 - i\Omega_2'^* e^{i(\Delta_2+\delta)t} B_2 - \frac{\gamma}{2} B_4$$

Here, the B terms represent the probability amplitude of ^{85}Rb in each state and the Ω terms are the Rabi frequencies between individual energy levels. Figure B.3 explicitly defines these quantities.

The two terms which depend on the excited state lifetime (γ^{-1}) account for atoms "lost" due to spontaneous emission. This is not a physical loss of the atoms, but instead a loss of coherence. Given the polarization of the Raman beams, spontaneous emission is likely to be beneficial with regard to the spin polarization of ^{85}Rb. However, it is also a hindrance to optimal coherent transfer, and thus for the treatment developed here, it will be considered as a loss.

While the four equations of motion could be solved directly, they may be reduced to down two equations which are computationally quicker to solve. The approximation of adiabatic elimination assumes that the terms B_1 and B_2 oscillate much slower than the detunings Δ. Despite the fact that spontaneous emission plays a non-negligible role for some sets of parameters, Δ is much larger than any other relevant frequency in the system making the approximation valid. Making this assumption allows us to remove the time dependence of B_1 and B_2 in the bottom two equations and analytically solve for B_3 and B_4. These solutions may then inserted into the top two equations to yield two differential equations describing the time evolution of the population distribution of the two ground states coupled by the Raman transition:
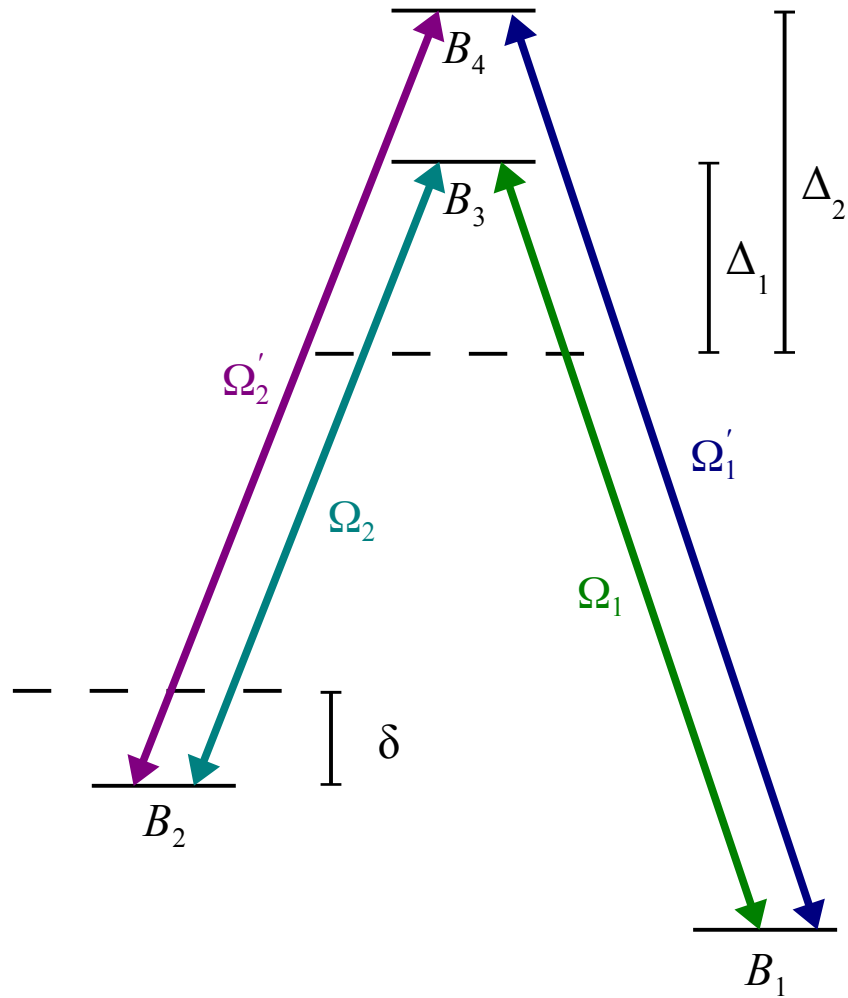
Figure B.3 Nomenclature for Adiabatic Elimination Theory.
Shown are the same states as in figure B.2 using the following definitions:

$$B_1 = |5s_{1/2}, F=2, m_F=-1\rangle$$
$$B_2 = |5s_{1/2}, F=3, m_F=-3\rangle$$
$$B_3 = |5p_{1/2}, F=2, m_F=-2\rangle$$
$$B_4 = |5p_{1/2}, F=3, m_F=-2\rangle$$

The Rabi frequencies, Ω, that couple these states are shown schematically by the colored arrows.

$$\dot{B}_1 = -\left[\frac{|\Omega_1|^2(\frac{\gamma}{2}-i\Delta_1)}{\Delta_1^2+\frac{\gamma^2}{4}} + \frac{|\Omega_1'|^2(\frac{\gamma}{2}-i\Delta_2)}{\Delta_2^2+\frac{\gamma^2}{4}}\right]B_1$$

$$-\left[\frac{\Omega_1\Omega_2^*(\frac{\gamma}{2}-i(\Delta_1+\delta))}{(\Delta_1+\delta)^2+\frac{\gamma^2}{4}} + \frac{\Omega_1'\Omega_2'^*(\frac{\gamma}{2}-i(\Delta_2+\delta))}{(\Delta_2+\delta)^2+\frac{\gamma^2}{4}}\right]e^{i\delta t}B_2 \qquad \text{(B.4a)},$$

$$\dot{B}_2 = -\left[\frac{|\Omega_2|^2(\frac{\gamma}{2}-i(\Delta_1+\delta))}{(\Delta_1+\delta)^2+\frac{\gamma^2}{4}} + \frac{|\Omega_2'|^2(\frac{\gamma}{2}-i(\Delta_2+\delta))}{(\Delta_2+\delta)^2+\frac{\gamma^2}{4}}\right]B_2$$

$$-\left[\frac{\Omega_2\Omega_1^*(\frac{\gamma}{2}-i\Delta_1)}{\Delta_1^2+\frac{\gamma^2}{4}} + \frac{\Omega_2'\Omega_1'^*(\frac{\gamma}{2}-i\Delta_2)}{\Delta_2^2+\frac{\gamma^2}{4}}\right]e^{-i\delta t}B_1 \qquad \text{(B.4b)}.$$

Note that the detunings Δ_1 and Δ_2 are separated by the excited state hyperfine splitting, 362 MHz. Thus the simplification of $\Delta_2 = \Delta_1 - (2\pi \bullet 362 \times 10^6)$ can be made (since Δ_2 is the detuning from the upper hyperfine excited state transition and the beam is red or negative detuned). Using equations (B.4) a numerical model can be put together to explore potential laser detuning and intensity combinations of the two Raman beams as well as provide estimates of the losses incurred during a complete population transfer.

Since the transitions involved are between specific m_F states, Rabi frequencies generated from equation (B.2) must be weighted by the relevant Clebsch-Gordan coefficients specific to these transitions. For each Rabi frequency there are three Clebsch-Gordan coefficients of concern, two of which are from the projection of the F, m_F states into the m_I, m_J basis:

$$|F, m_F\rangle \rightarrow |m_I, m_J\rangle \qquad \text{(B.5)}.$$

This is done because the photons will couple with the electron orbital momentum, thus m_J is the relevant quantum number and not m_F. The projections of the relevant states in our ^{85}Rb Raman transition are as follows:

$$B_1 = \left|5S_{1/2}; 2, -1\right\rangle \;\rightarrow\; -\sqrt{\frac{2}{3}}\left|\frac{3}{2}, \frac{1}{2}\right\rangle + \sqrt{\frac{1}{3}}\left|-\frac{1}{2}, -\frac{1}{2}\right\rangle$$

$$B_2 = \left|5S_{1/2}; 3, -3\right\rangle \;\rightarrow\; 1\left|-\frac{5}{2}, -\frac{1}{2}\right\rangle$$

$$B_3 = \left|5P_{1/2}; 2, -2\right\rangle \;\rightarrow\; -\sqrt{\frac{5}{6}}\left|-\frac{5}{2}, \frac{1}{2}\right\rangle + \sqrt{\frac{1}{6}}\left|-\frac{3}{2}, -\frac{1}{2}\right\rangle$$

$$B_4 = \left|5P_{1/2}; 3, -2\right\rangle \;\rightarrow\; \sqrt{\frac{1}{6}}\left|-\frac{5}{2}, \frac{1}{2}\right\rangle + \sqrt{\frac{5}{6}}\left|-\frac{3}{2}, -\frac{1}{2}\right\rangle$$

$$\text{(B.6).}$$

Since the electric field of the light can only couple matrix elements involving the same initial and final m_I in the m_I, m_J basis, only terms with the same m_I between initial and final state are needed. The third Clebsch-Gordan coefficient that is required handles the addition of the photon's angular momentum through the Wigner-Eckart theorem. For circular polarized light and both initial and final state of $J = \frac{1}{2}$, this coefficient is the square root of two-thirds. Light with σ^- polarization also carries a minus sign. Using this with the correct coefficients in equation (B.6) allows us to calculate the Rabi frequencies necessary for the model based off the Rabi frequency defined in equation (B.2):

$$\Omega_1 = \left(-\sqrt{\frac{2}{3}}\right)\left(-\sqrt{\frac{2}{3}}\right)\left(\sqrt{\frac{1}{6}}\right)\Omega = \frac{1}{9}\sqrt{6}\,\Omega$$

$$\Omega_1' = \left(-\sqrt{\frac{2}{3}}\right)\left(-\sqrt{\frac{2}{3}}\right)\left(\sqrt{\frac{5}{6}}\right)\Omega = \frac{1}{9}\sqrt{30}\,\Omega$$

$$\Omega_2 = \left(-\sqrt{\frac{5}{6}}\right)\left(\sqrt{\frac{2}{3}}\right)(1)\,\Omega = -\frac{1}{3}\sqrt{5}\,\Omega$$

$$\Omega_2' = \left(\sqrt{\frac{1}{6}}\right)\left(\sqrt{\frac{2}{3}}\right)(1)\,\Omega = \frac{1}{3}\,\Omega$$

$$\text{(B.7).}$$

The pair of differential equations (B.4) can now be solved numerically, and parameters can be adjusted to find the optimal values for the detuning of the two Raman lasers as well as the amount of time needed for complete population transfer.

B.3 Numeric Results of Adiabatic Elimination

Numerical solutions to equations (B.4) were examined in the detuning, Δ_1 range of −400 MHz to −1 GHz. For a set Δ_1, the value of δ was varied in the tens of kHz range and the state populations were observed for a Raman pulse duration up to about 50 μs. Initial conditions assumed that the entire population was in the $5s_{1/2}$, $F = 2$, $m_F = -1$ state. Both the absorption and emission Raman beams were set to have equal intensities of 52 μW/cm^2. The solutions were examined to find the conditions for maximum population transfer of the atoms which remain after losses from the excited state. The optimum value of δ was found with the pulse duration necessary for maximum population transfer, as well as the values of δ that caused only half of the atoms to be transferred (to give an idea how sensitive the detuning settings might be).

An example of some of the numerical solutions can be seen in figure B.4, which shows the time evolution of the relative population in the $5s_{1/2}$, $F = 3$, $m_F = -3$ state. Figure B.4 shows that with laser detunings of $\Delta_1 = -800$ MHz and $\delta = 55$ kHz (green curves), full population transfer (of the 92% of the atoms that have not lost coherence due to spontaneous emission, as shown by the dashed curve) can be expected after a Raman pulse lasting about 22 μs. Changing δ by ± 25 kHz reduces the transfer percent to about 50%, as can be seen in the blue curves, which gives some indication on how precisely the detunings need to be set. Figure B.5 shows how both the optimum value of δ (red, left axis), as well as the necessary Raman pulse length (blue, right axis) for total population transfer change over the range of Δ_1 from −400 MHz to −1 GHz. The "error bars" on the δ values indicate the range where population transfer is over fifty percent. The closer the Raman excited state is to the atomic excited energy level, the shorter the necessary pulse and the more forgiving the exact detunings used are in an absolute sense. Throughout the range of Δ_1 shown, the total number of atoms drops to approximately 92%. These results indicate that good Raman pulse transfer is possible at reasonable detunings
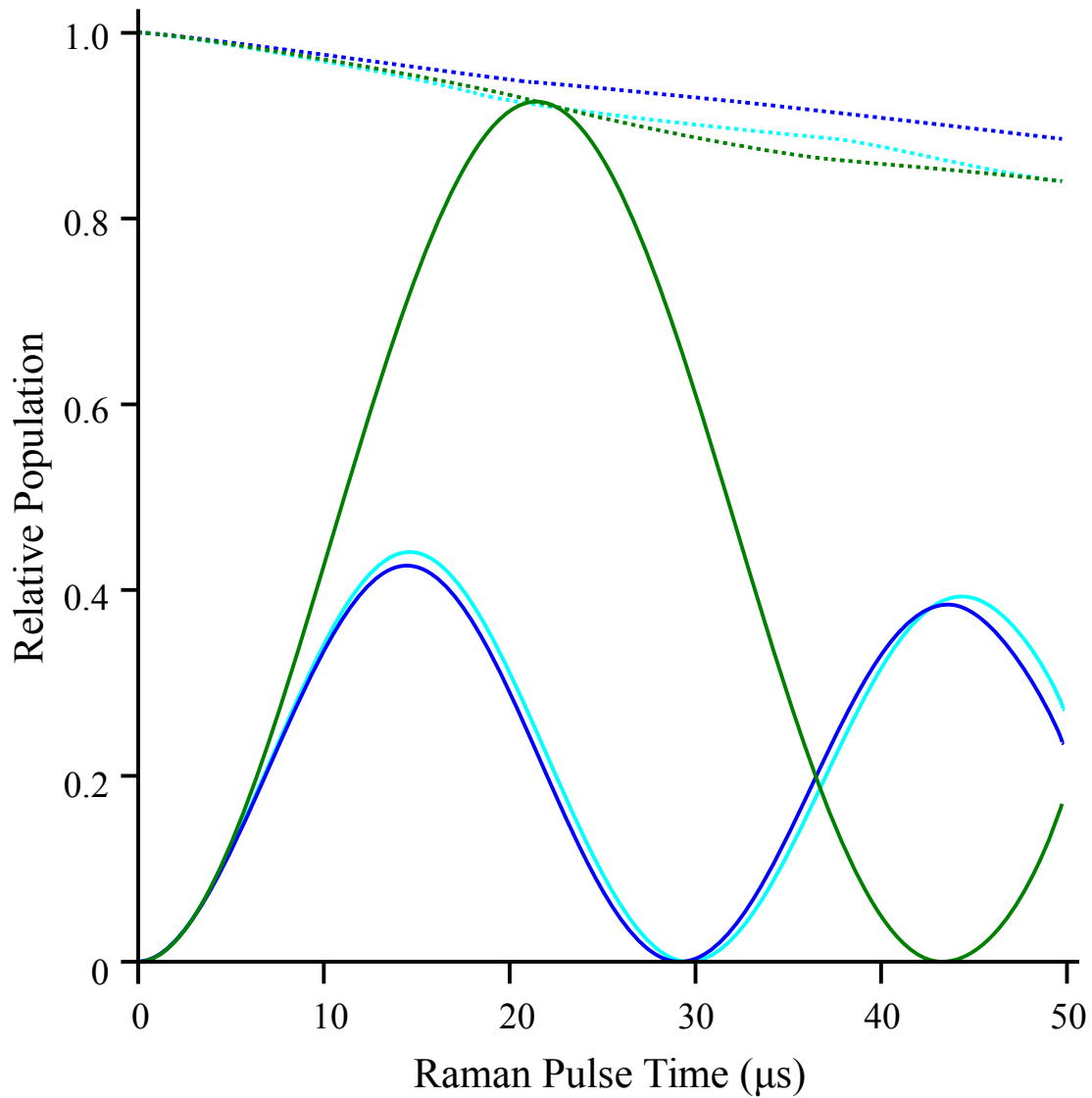
Figure B.4 Example Numerical Simulation of Raman Pumping.
The relative population of pumped atoms, in the state B_2 (solid lines), compared to the total number of atoms (dashed lines) as a function of Raman pulse time. Populations are normalized so that the total atom population at time zero is one, where all atoms are in the state B_1. The detuning parameter Δ_1 is set to -800 MHz. When the detuning parameter δ is at 55 kHz (green), one hundred percent of the atoms (of the 92% that remains) are transferred after a pulse of about 22 μs. The blue curves are at $\delta = 55 \pm 25$ kHz where roughly only half the population can be transferred. This gives a measure of how robust the Raman transition is.
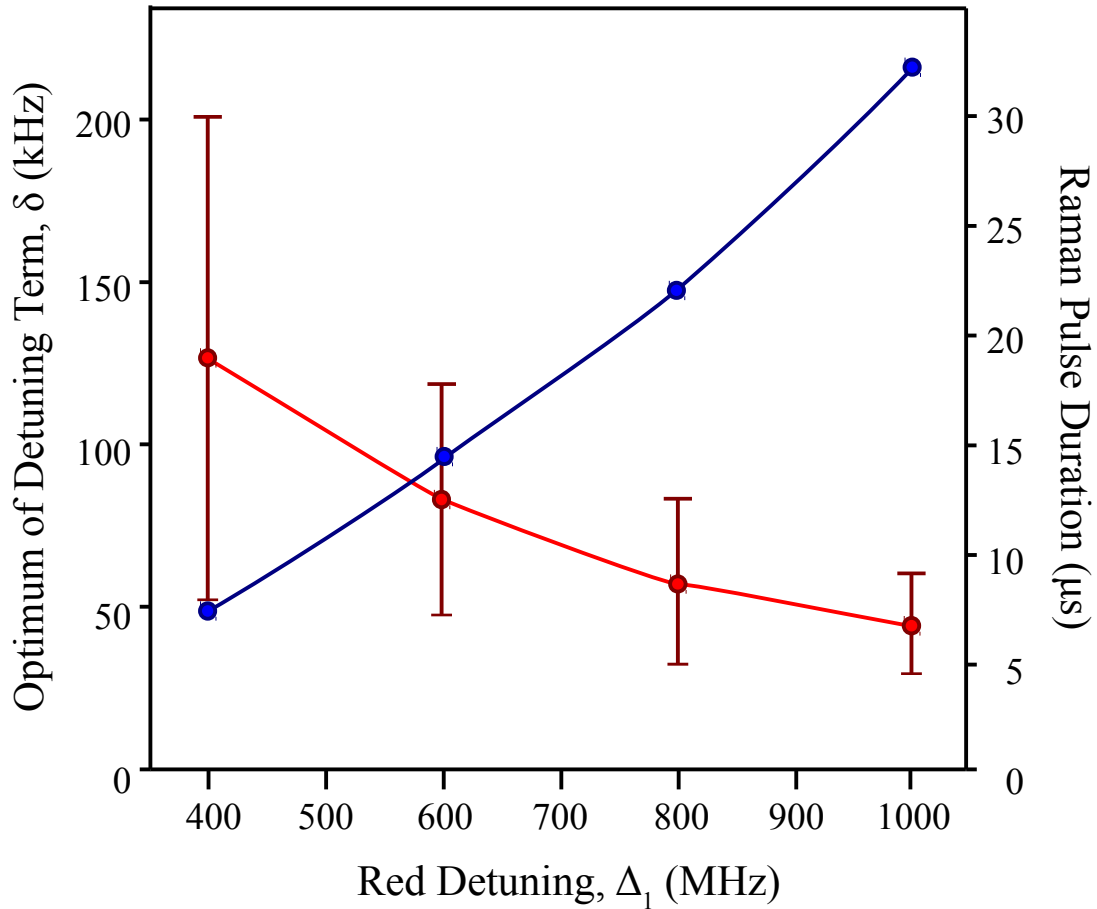
Figure B.5 Numerical Raman Pump Simulation Trends.
Behavior of the optimum setting of δ (red) and Raman pulse length (blue) as the detuning Δ_1 is changed. At these settings, total population transfer is predicted. The "error bars" on the δ points indicate how much variation reduces to about half population transfer. Throughout this range losses were consistently about 8% of the initial population. The lines are guides for the eye.

and pulse timings with acceptable loss rates. The precise detuning used will have to be determined experimentally since the exact shifts in energy in the trapping region due to the light fields is unknown. However, the numerical results indicate that spin polarizing ^{85}Rb using Raman pulses is a promising prospect.

Reference for Appendix B

[1] K. Moler, D. Weiss, M. Kasevich and S. Chu, Phys. Rev. A **45**, 342-348 (1992).

Appendix C: Additional Experimental Components

While the experimental apparatus was undergoing upgrades in anticipation of CAZ cooling (immediately following the experiments described in chapter 4), several modifications were made which were not documented in chapter 3. These modifications were not critically necessary for the initial observation of CAZ cooling, but were made in anticipation of additional CAZ cooling work where they may become useful. This appendix describes these upgrades as well as some of the physics and rationale for their implementation.

C.1 Adjustable Aspect Ratio FORT

Typically the confining potential of a red-detuned optical trap is the result of a focused TEM_{00} Gaussian laser beam which is cylindrically symmetric. Although this standard trapping potential is easy to setup and work with, inevitably there are many more experiments which can be performed with a controllable trap geometry. Evaporative cooling in a non-standard geometry however, can be quite difficult. Both the loading efficiency from a MOT and small trap volumes may pose a problem for cooling in traps of non-standard geometries. To avoid this, standard traps are loaded first then either transferred or deformed into the non-standard geometry. Both processes are likely to induce heating and/or loss of the atoms. Since CAZ cooling does not require a trap of a given geometry, it can be used to actively cool atoms as they are transferred/deformed into the non-standard geometry. This should allow a relaxation of the requirements for such processes since heat can be removed without atom loss, facilitating quicker performance and better phase-space densities once completed.

Given that both novel and adjustable traps should benefit from CAZ cooling, the FORT had been upgraded so that it has the ability to produce such a controllable trap. This was done so that CAZ cooling could be evaluated in different geometries as well as during the trap deformation. However, due to experimental limitations this upgrade never reached its full

capability. The primary reason the upgrade did not perform to full capability was a poor FORT laser beam quality. The following analysis and results presented in this section are for future reference for potential improvements to the system.

The upgrade to the FORT focusing setup consisted of using two cylindrical lenses with orthogonal axes instead of a single spherical lens. This makes the spatial beam profile along the orthogonal transverse directions, each parallel to one of the cylindrical lenses, different and (mostly) independent. In addition, one of the cylindrical lenses is mounted on a motorized translation stage [1] which allows the aspect ratio of the trap to be adjusted. As the relative spacing between cylindrical lenses changes, both the volume and depth of the trap will change. The trap can thus be adjusted from a prolate (cigar-shaped) shaped trap to an oblate (pancake-shaped) geometry continuously and smoothly. Therefore the effective dimensionality of the trap can be changed or the aspect ratio may be set to a point that maximizes transfer to another trap.

A two lens system also makes it possible to compress or expand the atom cloud in a way that changes the density and temperature of the atoms within the trap. This provides advantages for the CAZ cooling process itself. The trap can start in a configuration with a large trapping volume which permits more atoms to be initially loaded into the FORT [2]. Then the trap can be adiabatically compressed so as to increase the density of trapped atoms, which is advantageous since a higher density will cause a higher spin-exchange collision rate and thus a higher cooling rate. Conversely, if reabsorption effects become severe, the adjustable trap can be expanded to reduce the cloud density and make it more transparent. Furthermore, it has been shown that trap geometry can be used to mitigate reabsorption [3,4] by using an aspect ratio that provides one or more directions in which scattered photons can escape.

The original FORT was a 120 μK deep trap produced by a 24 W beam focused down to ~100 μm through a 5.08 cm spherical lens using one-to-one imaging into the vacuum chamber.

196

This trap could be reliably loaded with roughly 2×10^6 atoms of both ^{85}Rb and ^{87}Rb simultaneously held at a temperature of 15 μK. For the adjustable aspect ratio trap, the 5.08 cm spherical lens was replace with two cylindrical lenses (see figure C.1 for layout), an 8.89 cm lens focusing in the vertical direction and a 5 cm lens focusing in the horizontal direction.

The goal of the upgrade was to produce a FORT that behaved roughly the same as during the loading stage before the lens swap, but still had room to be adjusted to compress the trap volume. This means that when the foci of the two new lenses are displaced by some amount (on the order of one millimeter is reasonable for our system), the trap should be about 120 μK deep. With the horizontal and vertical focuses at the same location in space, the trap depth would then be greater. Predicting the behavior of the beam after the upgrade can be done using the *ABCD* law of Gaussian beam propagation. The *ABCD* law uses matrix elements of the ray tracing *ABCD* matrix to determine how the complex beam parameter changes. In matrix ray tracing, a ray passes an input plane and an output plane which are both perpendicular to the optical axis (generally denoted as the *z*-axis). At each plane, the ray is described by its position away from the optical axis, *x*, and its angle to the optical axis, *θ*. How these parameters change between planes is given by the matrix relation:

$$\begin{bmatrix} x_{out} \\ \theta_{out} \end{bmatrix} = \begin{bmatrix} A & B \\ C & D \end{bmatrix} \begin{bmatrix} x_{in} \\ \theta_{in} \end{bmatrix} \tag{C.1}$$

where the subscripts "in" and "out" denote the input and output planes respectively. The letters in the *ABCD* matrix describe how the change occurs. Each optical component (distance through free-space, lens, surface, etc.) has its own *ABCD* matrix, and traveling through multiple components can be described by a single matrix found by the matrix multiplication of all the individual component matrices. The two most commonly used matrices for beam behavior are those of free-space propagation and a thin lens:
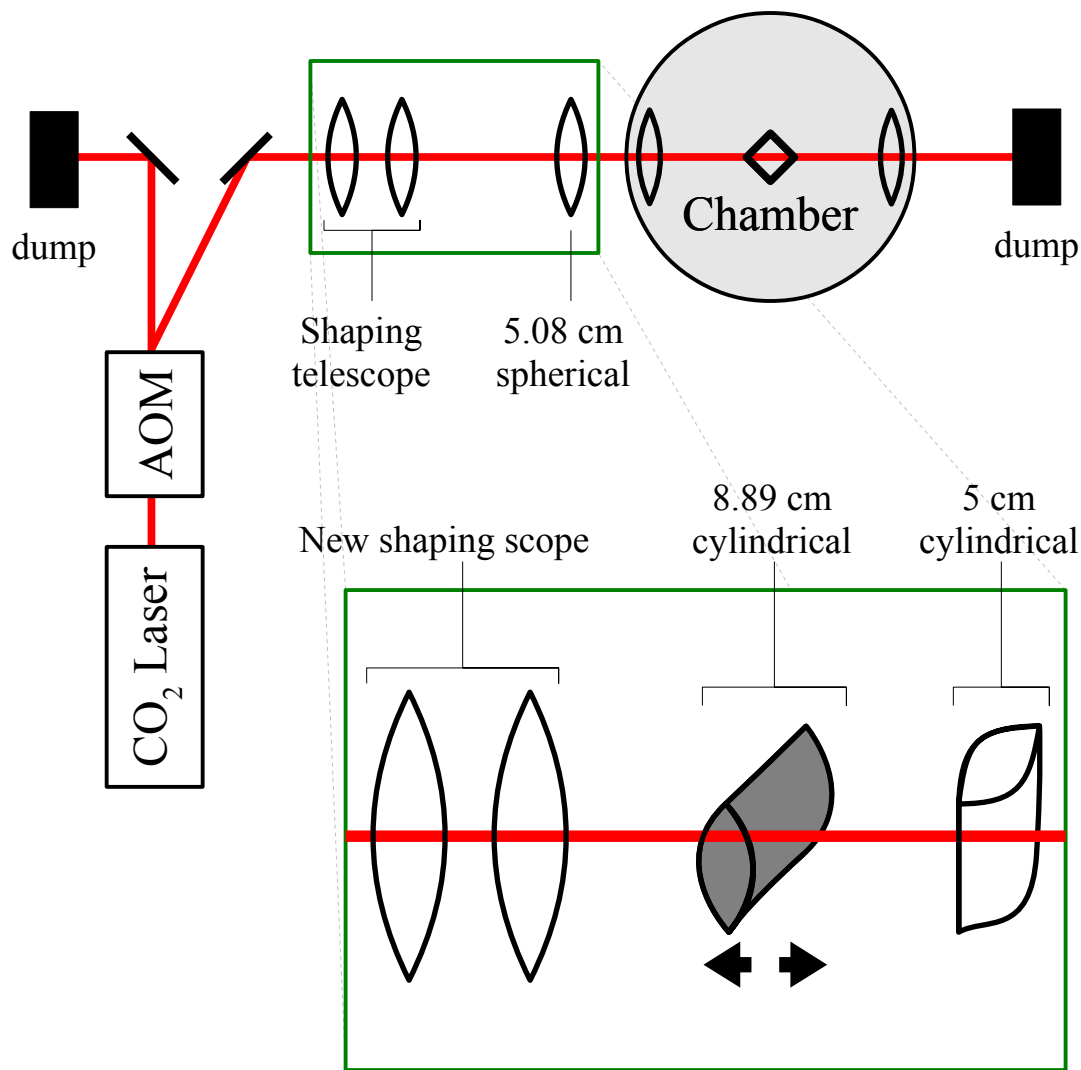
Figure C.1 Schematic of Far Off Resonant Trap Configuration.
CO_2 laser beam path indicated in red. When the FORT is off, the AOM does not deflect, sending all laser light into a beam dump. The AOM deflects the beam when on, with the deflected beam being shaped by a telescope and focused with a 5.08 cm lens prior to the chamber. A lens internal to the vacuum chamber is designed for one-to-one imaging of the external focus and provides the trap potential inside the chamber (diamond indicates trap region). The beam exits and is sent to another dump. The inset shows the region of the beam path (green) where upgrades were performed. The 5.08 cm lens is replaced by a pair of crossed-axes cylindrical lenses, one of which (shaded gray) is on a motorized translation stage. A different beam shaping scope is used to make the new trap parameters as close as possible to those prior to the upgrade.

$$T_{space} = \begin{bmatrix} 1 & d \\ 0 & 1 \end{bmatrix}, \qquad T_{lens} = \begin{bmatrix} 1 & 0 \\ -\dfrac{1}{f} & 1 \end{bmatrix} \qquad \text{(C.2)}$$

where T_{space} is the *ABCD* matrix for free-space propagation of a distance d, and T_{lens} is the *ABCD* matrix of a thin lens of focus f. Most optics textbooks cover further information on *ABCD* matrix analysis.

The complex beam parameter defines the Gaussian beam parameters as a function of propagation along the z-axis. The complex beam parameter and its reciprocal, which is useful for calculations, are given by:

$$q(z) = z + i\, z_0 \qquad \text{(C.3)}$$

$$\frac{1}{q(z)} = \frac{1}{R(z)} - i\,\frac{\lambda_0}{\pi n w(z)^2} \qquad \text{(C.4)}$$

where $R(z)$ is the radius of curvature of the beam and the other beam parameters are those discussed earlier. For completeness, the radius of curvature can be given in terms of the other beam parameters:

$$R(z) = z\left[1 + \left(\frac{z_0}{z}\right)^2\right] \qquad \text{(C.5)}$$

It should be noted that for all the beam propagation equations $z = 0$ is defined as the point of minimum spot size. Thus to make calculations in any arbitrary z-coordinate, the substitution $z \to z - z'$ where z' is the position of minimum spot size, should be made. Finally the *ABCD* law of Gaussian beam propagation is given by:

$$\frac{1}{q_{out}} = \frac{C + D(1/q_{in})}{A + B(1/q_{in})} \qquad \text{(C.6)}$$

where q_{in} is the complex beam parameter prior to propagating through optical element(s) with *ABCD* matrix and emerging with complex beam parameter q_{out}.

In estimating beam behavior for the adjustable aspect-ratio trap, the orthogonal directions of the beam were treated independently. However, this is only approximately correct [5]. While the beams discussed here are indeed solutions to equation (3.3), it is possible for them to have more complex structures and coupling between the two directions. Thus, for some beam configurations the beam propagation is not separable. However, due to the orthogonality of the focusing lens axes, treating the two directions as independent should be a good approximation of the actual beam in the experiment. Furthermore, the treatment here can be used to examine the physics of an adjustable aspect-ratio trap in general.

Figure C.2 shows predicted trap depth as a function of the separation of the two cylindrical lenses. The first prediction (blue) assumes that the 24 W beam has an M^2 of 1 and has been collimated and resized to a beam width of 6 mm prior to going through the cylindrical lenses. This prediction is overly optimistic for several reasons. First, we know the M^2 of our beam is more than one. In the past, it was measured to be 1.6 along the vertical direction and 1.35 along the horizontal direction. The calculations can be done again using these M^2 values for each coordinate separately which generates the second prediction (red). For reference a trap depth of 120 μK is marked (yellow) as well. The second prediction is actually of limited value since the M^2 of the new setup is likely different. This is because the beam passes through different optics and the laser itself has likely changed as a decrease in output power has been observed over a long period of time.

With the two cylindrical lens system in place, the behavior in figure C.3 was observed. The fact that it deviates significantly from the predictions of figure C.2 is unfortunate, but upon reflection there are several reasons why it could be so. For one, the usable power of the FORT laser had already dropped to around 20 Watts. For reasons not entirely known, the FORT laser power has had a long-time degradation in power. This likely indicates that the M^2 of the beam is
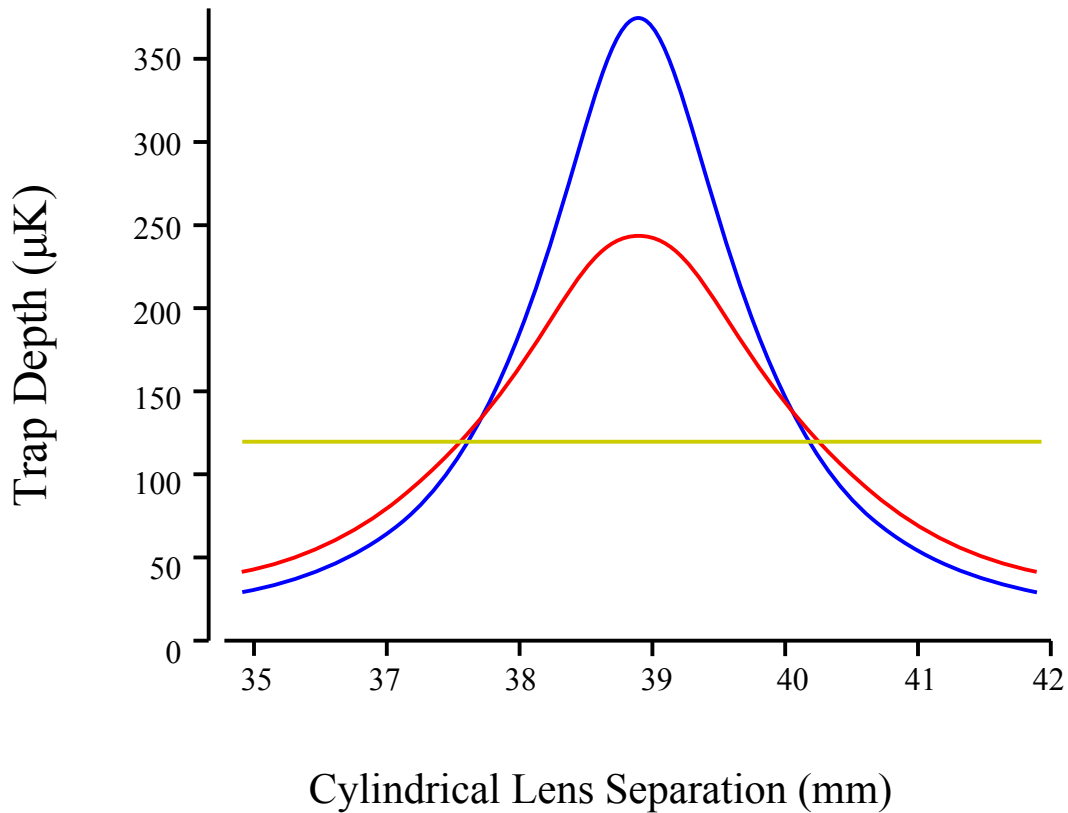
Figure C.2 Predicted Trap Depths of 2 Lens Adjustable FORT.
Predicted behavior of an adjustable aspect ratio two cylindrical lens FORT generated by a 24 W 10.6 μm laser beam sent through an 8.89 cm cylindrical lens followed by a 5 cm cylindrical lens with orthogonal axes. Shown is the trap depth for Rb atoms as a function the separation distance between the two cylindrical lenses. The blue curve assumes that the beam has an M^2 of 1. The red curve uses M^2 values measured in the past, that is 1.6 in the vertical direction and 1.35 in the horizontal direction. The yellow line denotes a trap depth of 120 μK, which was the depth of the trap prior to the upgrade. The idea is that if the cylindrical lens trap is set to have this depth, loading should exhibit familiar behavior and confinement can be improved by changing the lens separation toward the greater trap depth.
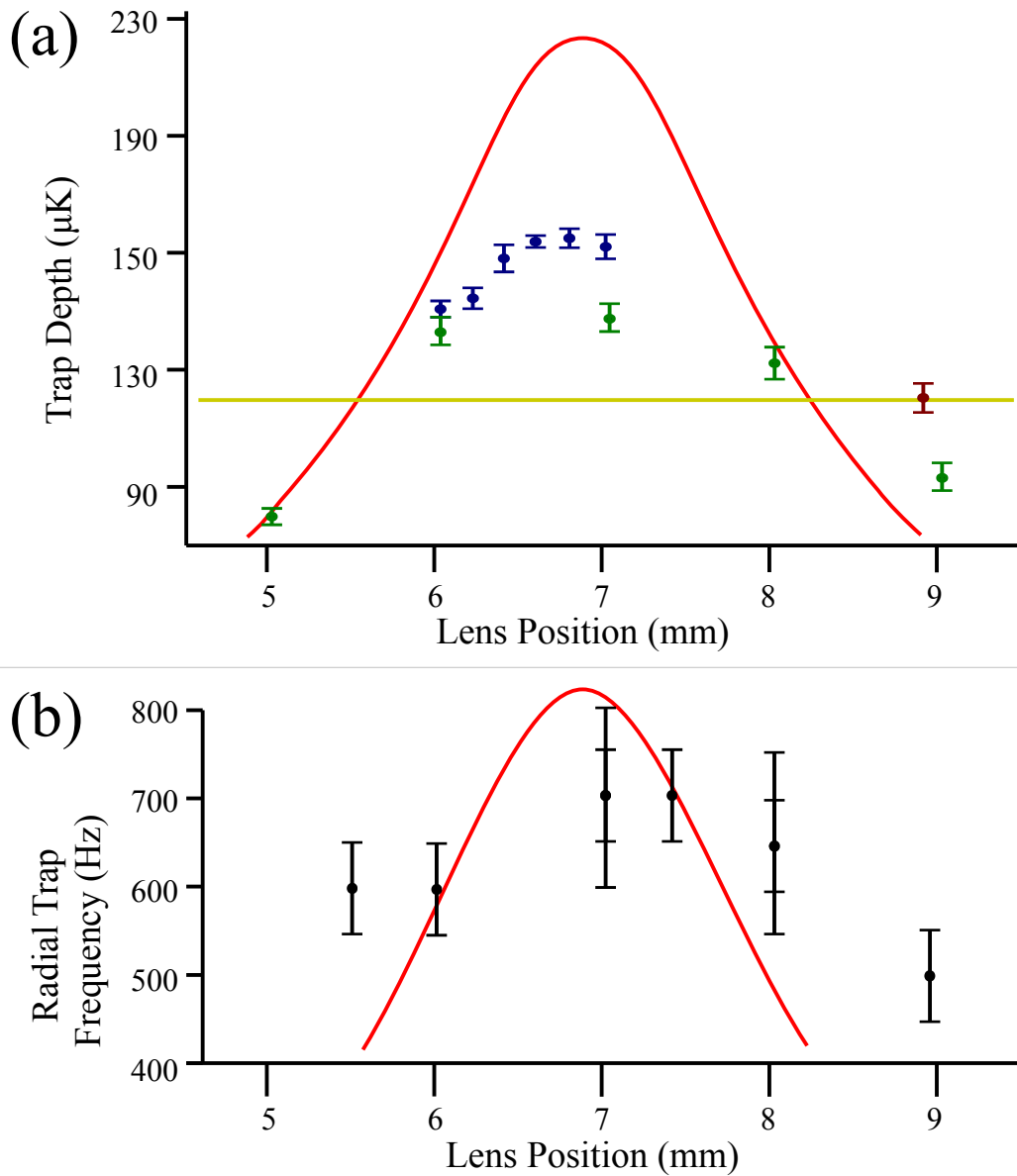
Figure C.3 Measured Behavior of Two Lens Adjustable FORT.
Measured trap depth **(a)**, and radial trap frequency **(b)**, of the adjustable aspect ratio FORT. Trap depth data taken on different days appear as different colors. The predicted depth (red curve) and previous depth (yellow line) from figure C.2 are included for comparison. The corresponding predicted horizontal trapping frequency is shown (red curve) with the measured frequency data which seemed to resolve only one of the orthogonal frequencies. Deviation from the predicted behavior is expected because the M^2 of the beam is unknown and there is likely spherical aberration in the beam since it makes a relatively large spot on the beam shaping optics.

somewhat different, and the values used in the calculation are therefore slightly off. Also it is unclear how the M^2 will be affected after passing through the cylindrical lenses. In addition, due to the larger input beam size, a larger portion of the beam will pass through regions of the lenses which are further from center. This will introduce spherical aberration to the beam, causing it to be focused to a region instead of a couple of points. These reasons can also easily account for the rather weak dependence of the trapping parameters on lens separation. This behavior is likely to have an effect on the effectiveness of any adiabatic compression that may be attempted in the future.

C.2   Adiabatic Compression of the Adjustable FORT

The adjustable aspect ratio FORT is meant to take advantage of the large capture volume of a shallow trap to acquire a large number of atoms, as well as the higher collision rate of a dense sample of atoms in a deep trap. The process of changing the trap between these two configurations is done via adiabatic compression. By adiabatically compressing the optical trap the atom density can be increased at the cost of increasing the temperature of the trapped atoms. Although the increase in temperature may seem undesirable for system focused on the cooling of atoms, by doing the compression adiabatically the collision rate (and thus cooling rate for CAZ cooling) will increase without compromising the phase-space density. Phase-space density is the ultimate measure of success for cooling to degeneracy, so a process that improves the cooling rate without changing phase-space density is valuable for any cooling scheme.

In order for the compression to be adiabatic, it must be slow. First consider an isolated atom or non-interacting atoms in a harmonic potential. In this situation slow is compared to the oscillation frequency (trapping frequency) of the atom in the potential. This requires that:

$$\frac{d\omega}{dt}\frac{1}{\omega^2} \ll 1 \qquad\qquad (C.7)$$

for the rate of change of the trap frequency ω during the compression. Extending to three spatial dimensions can be done by considering the trapping frequencies in orthogonal directions independently. For each coordinate axis, atoms will have an elliptical orbit in x-p phase-space. To preserve entropy, and thus be adiabatic, the area of this orbit will be constant throughout the transformation of the trap.

$$A_{\text{phase-space}} = \pi \, x_{\max} \, p_{\max} = \pi \left(\sqrt{\frac{2E}{m}} \, \frac{1}{\omega} \right) \left(\sqrt{2mE} \right) = \frac{2 \pi E}{\omega} = const. \qquad \text{(C.8)}.$$

For equation (C.8), the ellipse in phase-space is found from the maximum position and momentum of a harmonic oscillator of mass m and energy E oscillating at frequency ω. Clearly as the frequency of the trap is increased, so is the energy of the atom in order to maintain a constant area of phase space. The change in energy occurs through work done on the atoms by the changing potential. Since energy is directly proportional to temperature, a change in trap frequency will correlate to a proportional change in the temperature. In the case where the orthogonal harmonic oscillators are uncoupled, the temperature in each direction is independent. Thus the ratio of the average oscillation frequency to the average temperature is constant during the adiabatic ramp:

$$\frac{\left(\dfrac{\omega_x + \omega_y + \omega_z}{3} \right)}{T_{avg}} = const. \qquad \text{(C.9)}.$$

Equation (C.9) does not hold at all times. After the ramp, collisions occur that redistribute energy to eliminate any imbalances in average energy between the x, y, and z directions. These collisions have important implications for the adiabaticity of the transformation because they couple together the energy in each orthogonal direction. In order for the trap deformation to be adiabatic, the change in the trap frequency must also be slow as compared to the collision rate:

$$\frac{d\omega}{dt}\frac{1}{\omega}\frac{1}{n\sigma\langle v\rangle}\ll 1 \qquad\qquad (C.10)$$

where n is the density of the atoms, σ is the collisional cross-section, and $\langle v\rangle$ is the average velocity of the atoms, the product of all three is the collision rate. In this sort of situation, the ratio of the geometric mean of the oscillation frequencies to the temperature is kept constant through adiabatic processes:

$$\frac{\left(\omega_x\omega_y\omega_z\right)^{1/3}}{T}=\frac{\omega_{GM}}{T}=const. \qquad\qquad (C.11).$$

Here we have simplified the relation with ω_{GM} to denote the geometric mean of the oscillation frequencies of the trap. In order that a process in an optical trap be truly adiabatic, the compression must be slow with respects to both the trap frequencies and the collision rate.

Collisions also have important implications when the compression is non-uniform. For example, consider a doubling of all the trap frequencies. In this case, we see from both equations (C.9) & (C.11), that the temperature of the trapped gas would also double. Now instead consider the doubling of the radial trapping frequencies (ω_x and ω_y) while keeping the axial trapping frequency constant. This time the change in temperature is different between the two adiabatic cases. For non-interacting atoms, we find an increase in temperature of (2+2+1)/3 = 1.67, from equation (C.9). While from equation (C.11), we find that processes with collisions present, the temperature of the gas increases by a factor of $(2 \times 2 \times 1)^{1/3} = 1.59$, which is slightly less. Thus an asymmetric adiabatic compression of colliding atoms responds differently than a compression in the absence of collisions.

However, as mentioned earlier, it is not the temperature, but the phase-space density that signifies success in cooling experiments. It is therefore worthwhile to see if the phase-space density changes as a result of compression. More specifically, we will look at the peak phase-

space density. To start, the density of the atoms can be found using the Maxwell-Boltzmann spatial distribution, normalized to the number of atoms in the trap:

$$\frac{\sqrt{2}\,N\,\omega_x\,\omega_y\,\omega_z}{4}\left(\frac{m}{\pi k_B T}\right)^{3/2}\exp\left(\frac{-m\left(\omega_x^2 x^2+\omega_y^2 y^2+\omega_z^2 z^2\right)}{2k_b T}\right) \tag{C.12}.$$

Here, N is the total number of atoms of mass m and at temperature T, the ω terms are the trapping frequencies, and k_B is the Boltzmann constant. From this, the peak density can be found (at the center of the trap) to be:

$$\frac{\sqrt{2}\,N\,\omega_x\,\omega_y\,\omega_z}{4}\left(\frac{m}{\pi k_B T}\right)^{3/2} \tag{C.13}.$$

The peak density times the cube of the thermal de Broglie wavelength,

$$\lambda=\frac{h}{\sqrt{2\pi m k_B T}} \tag{C.14},$$

gives the peak phase-space density:

$$\frac{N\,\omega_x\,\omega_y\,\omega_z\,h^3}{8\left(\pi k_b T\right)^3} \tag{C.15}.$$

Note that this scales as the product of the trapping frequencies divided by the temperature cubed. As the atoms are compressed adiabatically, there would be ideally no change in phase-space density. And in fact when the compression is symmetric, this is the case (for example, doubling all the trap frequencies also doubles the temperature for no net change to equation (C.15)). However, this is not necessarily the case when performing an asymmetric transformation. Consider again the case where the radial frequency is doubled and the axial frequency remains the same. Assuming that the compression is adiabatic in the presence of collisions, we see that the phase-space density changes by $(2 \times 2 \times 1) / ((2 \times 2 \times 1)^{1/3})^3 = 1$. Thus the transformation is truly adiabatic. However, if the transformation is done faster than rethermalizing collisions can occur but still slow compared to the trapping frequency then the temperature scales as equation

(C.9), and the phase-space density changes by a factor of $(2 \times 2 \times 1) / (5/3)^3 = 0.864$. This is less than one, and can be understood by realizing that the temperatures in each trap direction will be unequal after the transformation. The temperature will then equalize through random collisional processes which increase the entropy of the gas. The increase in entropy results in a decrease in phase-space density.

A decrease in phase-space density may not be a total loss for a collision based cooling scheme. This is because one of the primary motivations for pursuing an adjustable trap is that it can be used to exercise some control over the collision rate of the atoms in the trap. This is of particular interest since the collision rate determines the cooling rate in CAZ cooling or any other collision based cooling. To get some idea as to how the compression will affect the cooling, we will take a look at how the collision rate scales as the trap is compressed. For this treatment we will consider elastic collisions with a cross-section that is assumed to be constant with collision energy. This is for simplicity and because the theory is more straightforward. The results carry over to the inelastic spin-exchange collisions needed for CAZ cooling which scale the same way at temperatures that are sufficiently cold. Begin with the collision rate, given by:

$$n\sigma\langle v \rangle \tag{C.16}$$

where n is the density of the atoms, σ is the collision cross-section, and $<v>$ is the average velocity. The average velocity is given by:

$$\langle v \rangle = \sqrt{\frac{16 k_B T}{\pi m}} \tag{C.17}.$$

This scales as the square root of the temperature. Meanwhile, the root mean squared spatial extent of a gas in equilibrium with respects to a single spatial dimension is given by:

$$\sigma_x = \frac{1}{\omega}\sqrt{\frac{k_B T}{m}} \tag{C.18}.$$

Given that the density will scale as one over all three spatial extents, we find that the collision rate in equation (C.16) with constant cross-section will scale as:

$$\frac{\omega_x}{\sqrt{T}} \frac{\omega_y}{\sqrt{T}} \frac{\omega_z}{\sqrt{T}} \times \sqrt{T} \;\; = \;\; \frac{\omega_x \omega_y \omega_z}{T} \tag{C.19}.$$

Thus in the earlier example where the phase-space density decreased by a factor of 0.864, we find that the collision rate increases by a factor of $(2 \times 2 \times 1)/(5/3) = 2.4$ which is a substantial increase. So even in a situation where the compression is slightly diabatic, there is still the potential for improved overall cooling performance.

When the compression is entirely adiabatic, equation (C.19) predicts a scaling proportional to the square of the geometric mean of the trapping frequencies. In the case of doubling the radial frequency at constant axial frequency, the increase in the collision rate is expected to be a factor of 2.52. Although this is not much better than the case in the previous paragraph, the fully adiabatic case causes no loss in phase space density due to compression.

Using an elastic collision cross-section of 3.4×10^{-12} cm^2 for Rb^{87} [6] and the known trap parameters prior to the FORT upgrade, equation (C.16) can be plotted as a function of the optical trap geometric mean. The curve shown in figure C.4 is the result of this. As a reference, the temperature of the atoms trapped in the range shown spans from about 15 μK to 45 μK, and the low point represents where the optical trap operated prior to the upgrade to the adjustable aspect-ratio FORT. The curve shown in figure C.4 assumes that the trap will exhibit behavior equivalent to that before the change; thus it only approximates how the collision rate might behave. Using numbers generated from the expected behavior of the compressible FORT (and $M^2 > 1$, that is the red curve of figure C.2), adiabatic compression from the loading setup at 120 μK to the peak trap depth would be expected to increase the collision rate by a factor of four.
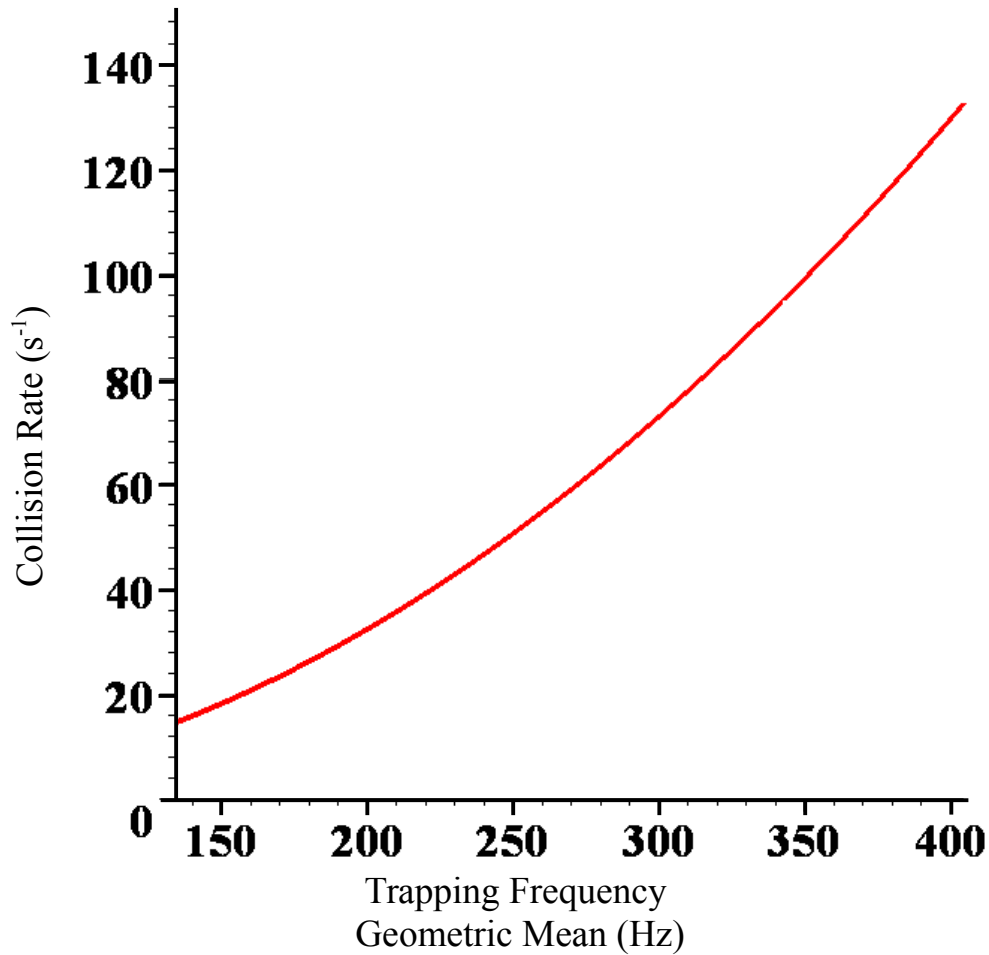
Figure C.4 Scaling of Collision Rate of [85]Rb in Adjustable Trap.
Scaling of the [85]Rb atomic collision rate as a function of the geometric mean of the FORT trapping frequencies. As the FORT is compressed, the trapping frequency of the trap will increase. This results in an increase in both the atom temperature and the atom density, with a net effect of a quadratic increase in the collision rate between atoms. The numbers used to generate this curve start with the measured properties of the FORT at the beginning of this work (450 Hz + 450 Hz + 12 Hz trap frequencies, 120 μK trap depth, 2×10^6 atoms) and assumes scaling with only the geometric mean of the trap. For reference, the plotted domain spans atom temperatures of 15 μK to 45 μK.

There are a couple of obstacles that will likely limit the performance of the adiabatic compression. First of all, additional heating could be induced by vibrational coupling induced by the moving optics during the compression sequence. This heating is harmful since entropy of the system increases as a result. Heating can be induced by either the trap potential wobbling (parametric heating), or by physical translational jumps of the potential. It is difficult to quantify the magnitude of the temperature increase as a result of vibrational coupling as such a calculation would require knowledge of the vibrational coupling constants of the system. However, it is expected that vibrational heating will not be a limiting factor in the experiment based on the induced heating effects in experiments conducted by other groups with similar setups (but moving spherical lenses as opposed to cylindrical) [7]. The mechanical heating effects are further mitigated by the use of lenses, since motion on or of the lens will be small at the focus where the atoms are trapped. Most vibrational effects should wash out with the exception of oscillations around resonant frequencies of the trap. Should there be any vibrational frequencies near the resonant frequencies of the trap, it should be possible to damp or remove them by applying additional weight to the moving parts. Another potential setback to the adiabatic compression is the anharmonicity of the optical trap due to spherical aberration or thermal lensing of the optical trap beam. The fact that the M^2 of the beam is not one implies that these effects will likely cause the adiabatic compression to perform less than anticipated. In fact, judging by the rather mellow performance of the adjustable aspect ratio trap shown in figure C.3, beam quality issues will likely need to be addressed prior to pursuing the adiabatic compression in future CAZ cooling sequences.

C.3 In Situ Control of the Magnetic Field

Spin-exchange collisions will remove kinetic energy from the system most efficiently when the magnetic field strength is set near an optimum value (equation (3.81)). As the atoms are cooled, the optimum magnetic field strength decreases. Thus to maintain an optimal cooling configuration, the magnetic field must be reduced. Fortunately a uniform magnetic field is easily controlled with a direct current. Since the maintaining of optimal magnetic field was not actually done as part of the CAZ cooling presented in this thesis, only the equipment needed to do so will be discussed here and not the details in refining the use of this equipment. These magnetic field control upgrades were used, but only in separate diagnostic experiments. Maintaining the optimal field strength will be a goal of future work.

The coils in our system are turned off and on by a FET capable of handling the 20 A while on and with a high enough breakdown voltage not to be damaged while off. Traditionally the FET gate had been controlled by TTL allowing for only two states: on and off. Meanwhile the power supply of the coils is set to run at the current limit to ensure a constant field. While in section 3.3.1 it was shown that it is simple enough to step the current down from a level for MOT operation to a level appropriate for CAZ cooling, the large inductance of the coils makes it difficult to control the current on the small timescales of the experiment. Adjusting the current limit on the power supply is not sufficient since it takes some time before the current settles at its limiting value. However, the FET can be used to control current in a configuration where the power supply is voltage limited. This is done by applying intermediate gate voltages to the FET instead of the full TTL on/off voltages. This allows the FET to be only partially on in a controlled manner. Care must be taken to avoid too much power from being dumped into the FET (when the FET is only partially on there is a voltage drop across the source and drain so when current flows through the device leading to power dissipation), so it is important that this

configuration is only used when the power supply is set to the relatively low output power settings used for CAZ cooling and not the high output settings used for the MOT.

As power is dumped into the FET while the gate is at an intermediate voltage, it will heat up and the electrical properties of the device will change. Thus it is not enough to use a constant gate voltage to maintain a constant current. However, by externally monitoring the current running through the coils and sending that signal into an electronic servo circuit, necessary adjustments can be made to maintain a constant current with a sufficient control bandwidth. Of course the device must be calibrated and the gains set properly, but that can be done with little difficulty. The set point of the FET gate circuit can then be adjusted to provide different levels of current through the coils. The use of an arbitrary waveform generator (AWG) served to control the set point of our circuit. A calibrated waveform could be programmed into the AWG to set the current to the desired setting and activated by a TTL signal. When the AWG is not active, the FET needs to be able to turn on and off normally. This is done by combining the original TTL signal to the FET with the output of the servo circuit (the servo circuit provides a negative voltage to drop below the FET on voltage). The completed circuit replaces a direct TTL signal sent to the FET gate control shown in figure 3.4. Once a constant current is possible, resonant microwave spectroscopy can then be used on trapped Rb atoms to determine the calibration of current to magnetic field strength at the region of the atoms.

The magnetic field control setup and calibration not only allows the magnetic field to be set and adjusted in order to maintain the optimal magnetic field strength for CAZ cooling, but a precisely controlled magnetic field also makes it possible to do additional diagnostics. For example, applying a ramp to the magnetic field in the presence of a constant microwave field enables adiabatic rapid passage of atoms between different hyperfine states of specific magnetic sub-levels. This enables us to probe the m_F state distribution of ^{85}Rb which is particularly useful

since it gives us a means to confirm the effectiveness of the spin-polarization. The benefit of this technique is that with a sufficient ramp size, the microwave signal need not be carefully set. This type of diagnostic is the subject of section 3.6. With this magnetic control setup it is possible to ramp the field to a constant non-zero value as well as providing control of the ramp speed.

References for Appendix C

[1] D. J. Han, Marshall T. DePue, and David S. Weiss, Phys. Rev. A **63**, 023405 (2001).

[2] P. Ahmadi, B. Timmons, and G. Summy, Phys. Rev. A **72**, 023411 (2005).

[3] V. Vuletic *et al.*, Phys. Rev. Lett. **81**, 5768-5771 (1998).

[4] M. Vengalattore, W. Rooijakkers, R. Conroy, and M. Prentiss, Phys. Rev. A **67**, 063412 (2003).

[5] J. Arnaud, and H. Kogelnik, Appl. Opt. **8**, 1687-1693 (1969).

[6] James Burke, Ph. D. Thesis, University of Colorado, (1999).

[7] T. Kinoshita, T. Wenger, and D. Weiss, Phys. Rev. A **71**, 011602 (2005).